DEPARTAMENT DE ÒPTICA

COHERENCE IN ULTRASHORT LIGHT PULSES AND
APPLICATIONS IN TEMPORAL OPTICS

VÍCTOR TORRES COMPANY

UNIVERSITAT DE VALÈNCIA
Servei de Publicacions
2008

Aquesta Tesi Doctoral va ser presentada a València el dia 26 de juny de 2008 davant un tribunal format per:

- D. Vicent Climent Jordà
- D. Ari T. Friberg
- D. Juan Pérez Torres
- D. Zbigniew Jaroszewicz
- D. Carlos Rodríguez Fernández-Pousa

Va ser dirigida per:
D. Jesús Lancis Sáez

Vniver§itat ᵈᴱ Valéncia — Facultat de Física

Coherence in ultrashort light pulses and applications in temporal optics

Memoria presentada por
Víctor Torres Company
Para optar al título de
Doctor en Física
MAYO 2008

D. Jesús LANCIS SÁEZ, Profesor Titular del Departament de Física de la Universitat Jaume I de Castelló,

CERTIFICA que la presente memoria: "**Coherence in ultrashort light pulses and applications in temporal optics**", resume el trabajo de investigación realizado, bajo su dirección, por D. Víctor TORRES COMPANY y constituye su tesis para optar al título de Doctor en Física.

Y para que así conste, y en cumplimiento de la legislación vigente, firma el presente certificado en Valencia, a 1 de abril de dos mil ocho.

Fdo: Dr. Jesús Lancis Sáez

To Ana

Acknowledgments

I would have not been able to follow this way without the support and help of many special people to whom I owe an explicit acknowledgment, at least.

I'm specially indebted to my thesis supervisor, Jesús Lancis, who has guided me during these years. I am sincerely grateful for all the freedom and confidence he has put on me. Nothing of this would have been possible without him. As close as him is Pedro Andrés, who always has offered me his enthusiasm, good advices and friendship.

I am also very grateful to Ari Friberg, who kindly received me at his Optics group in the KTH, Stockholm, during the summer of 2006. A considerable part of the work presented in this Thesis comes from the fruit of that collaboration. There I met good friends, Per Martinson, Sebastien Ricciardi, Hanna Lajunen... I owe Hanna a beer (maybe two) for the TEXpertise in the writing of this Thesis.

One year later, Idelfonso Tafur and Palle Jeppessen received me at COM·DTU, Copenhaguen, during the summer months, and helped me in this kind of "research tourism" around the northern countries. Apart from meeting really good friends like (and specially) Kamau Prince, Ji Hua, Darko Zivar, Jorge Seoane, Anders Clausen, Rasmus Kjær, Leif Oxenløwe,... I was introduced the poison of the fiber lab in the soul. Some nice experiments presented in this Thesis would have not been possible without the patience they had with me at the laboratory.

Lawrence Chen is sincerely acknowledged for inviting Pedro and me to spend some weeks in his Photonics group at McGill University, Montreal, during November, 2007. Apart from a few centimeters of snow in town (cool!), we also had the opportunity to test experimentally some of our ideas. These experiments are also included in this work. There are no enough beers to pay his efficient help at the lab.

I wish to express my gratitude to the rest of the people from the GROC-UJI research team in Castellón: Gladys Mínguez, Lluis Martínez, Vicente Durán, Merche Fernández, Enrique Tajahuerce, Vicent Climent and Omel Mendoza. I have never seen such a friendly atmosphere in a research team. Let's keep it!

The great friends from the real world who keep me locked to the Earth must be acknowledged for the "dinner and chat" we had and those that not yet: Javi, Bea, Alba, Rafa, Álex, Vero, Domi, Karton, Enric, Agus, Lorena, Ana, Salva, Pablo, Andreu, Julia, Elies, and many more.

Finally, it is great to have this family who always support me in this mad way. I am specially grateful for all the love, loyalty and friendship from my lovely Ana. Thanks for remaining always at my side.

Less important things must be mentioned in this page too. I'm grateful to the Spanish ministry of Education for this PhD FPU fellowship. It has paid my life expenses (vices included) and research (tourism) travel grants these last years. It sounds weird, but I am very grateful to the excellent Spanish railway system which has allowed me to travel every day from Valencia to Castellón. That's been the key for having a 350 references work.

Well, I wouldn't define this as "funny" but I hope you to enjoy it.

Abbreviations

1D	One dimensional
2D	Two dimensional
ASE	Amplified Spontaneous Emission
AWG	Arbitrary Waveform Generation
CPA	Chirped Pulse Amplification
CSDF	Cross-Spectral Density Function
CW	Continuous Wave
DC	Direct Current
DCF	Dispersion-Compensating Fiber
DFB	Distributed Feedback
DST	Direct Space-to-Time
D-WDM	Dense-Wavelength-Division Multiplexing
EAM	Electroabsorption Modulator
EDFA	Erbium-Doped Fiber Amplifier
EOM	Electro-Optic Modulator
EOPM	Electro-Optic Phase Modulator
ES	Energy Spectrum
ESA	Electrical Spectrum Analyzer
FCC	Federal Communication Commission
FWHM	Full-Width at Half Maximum
GDD	Group-Delay Dispersion
GSMP	Gaussian Schell-Model Pulse
GVD	Group-Velocity Dispersion
LCA	Lightwave component analyzer
LCFG	Linearly Chirped Fiber Grating
LED	Light-Emitting Diode
MCF	Mutual Coherence Function
MZI	Mach-Zehnder Interferometer
MZM	Mach-Zehnder Modulator
OCT	Optical Coherence Tomography
O/E	Optoelectronic
OSA	Optical Spectrum Analyzer
OTDM	Optical Time-Division Multiplexing
PD	Photodiode
RF	Radio Frequency
rms	Root-mean square
RTFT	Real-Time Fourier Transformer

S-LED	Superluminiscent Light-Emitting Diode
SIS	Spectral Imaging System
SMF	Single-Mode Fiber
SOA	Semiconductor Optical Amplifier
SPDC	Spontaneous Parametric Down Conversion
SSB	Single-Side Band
SLM	Spatial Light Modulator
SVEA	Slowly Varying Envelope Approximation
TESE	Transport-of-Energy-Spectrum Equation
TIE	Transport-of-Intensity Equation
TIS	Temporal Imaging System
Ti:Sa	Titanium:Saphire
TOD	Third-Order Dispersion
UWB	Ultra Wideband
WDM	Wavelength-Division Multiplexing
XGM	Cross-gain modulation
XPM	Cross-Phase Modulation

CONTENTS

Introduction

In the last decades, the generation of pulsed beams with pulse durations in the order of pico and femtosecond has constituted an important research topic for the Physics and Engineering communities. The characteristics of this kind of optical radiation, broadband spectrum, enormous temporal resolution, high peak-power with low energy average, potentially high repetition-rate, and high spatial coherence make it an indispensable tool in order to develop many applications in different fields of science and technology [1].

The development of the passive mode-locking technique in Titanium:Sapphire (Ti:Sa) lasers has produced ultrashort pulses with a duration corresponding to a few oscillations of the electric field in the near infrared, at repetition rates on the order of tenths of MHz to few GHz [2]. Alternatively, mode-locking in semiconductor lasers has allowed the achievement of pulse trains with repetition rates higher than $160 \, \mathrm{GHz}$, which constitutes a major goal for optical communications technology [3].

Ultrafast pulses have the inherent capability of resolving process in time with high resolution. At the end of the 80's, this suscitated the development of a new branch of studies in chemistry, named femtochemistry [4], where some molecular processes could be analyzed and controlled with femtosecond resolution in determined pump–probe configurations. It must be mentioned that Prof. A. H. Zewail was awarded with the Nobel prize in Chemistry in 1999 for these studies.

The enormous bandwidth, together with the high spatial coherence and peak power made ultrafast pulses to open new possibilities in optical coherence tomography (OCT), where superluminescent light emitting diodes (S-LEDs) were been commonly used. OCT is a high resolution, non-contact imaging technique for cross-sectional imaging of inhomogeneous samples, with applications ranging from imaging of biological tissues to material research [5]. In this technique, the axial resolution is inversely proportional to the spectral bandwidth of the optical source, and Ti:Sa laser pulses provide axial resolutions $\sim 1 \, \mu\mathrm{m}$.

The development of the chirped pulse amplification (CPA) technology lead to the achievement of extremely high power optical radiation [6]. This laser technology has allowed for the observation of new nonlinear phenomena [7], and the development of tabletop laser-driven accelerators [8]. The CPA technique, combined with the broadband few-cycle Ti:Sa technology, are the main ingredients to obtain new coherent radiation at shorter harmonic wavelengths with pulse durations in the sub-femtosecond regime. Attoscience is expected to open new insights in atomic-scale physics [9], and the measurement and

control of attosecond pulses is a current great challenge for the physical community [10]. Such an ultrashort pulses are created from the interaction of matter with few-cycle light pulses. The generation of higher harmonics is strongly dependent on the absolute phase of the optical field. Therefore, it is very important to control the phase difference between two neighbor pumping pulses, that appears due to the difference between the group and phase velocities in the laser cavity. It is important to note that the control in the time domain of this phase slip in a pulse train leads inherently to have a frequency comb with equally spaced frequencies shifted by a known quantity from the zero offset [11]. Thus, the control of this phase difference naturally leads to the control and stabilization of a broad set of mutually coherent single frequencies, i.e., a femtosecond frequency comb. Frequency combs have lead to impressive advances in lightwave and optical metrology applications [12, 13]. It should be mentioned that Profs. T. W. Hänsch and J. L. Hall were awarded with half of the Physics Nobel prize in 2005 for the development of this new technology.

In a different context, the so-called Space–Time analogy refers to the fact that the mathematical equations that govern the spreading of short light pulses in linear first-order dispersive media and the paraxial diffraction of monochromatic light beams are essentially the same [14]. The key of this connection is that it allows to adapt and interpret different phenomena in the temporal domain from the well-known results of diffractive optics [15]. This analogy has become particularly relevant for the optical communications community, in view of the current need of new photonic processing schemes [16].

Nevertheless, in most of the aforementioned phenomena and applications of ultrafast and temporal optics, it is widely assumed that the pulses are temporally fully coherent [17]. However, most of the real physical phenomena are subject to stochastic fluctuations and the pulses belonging to a train usually vary from one to another. In the last years there have been some research efforts centered on the development of a formal theory capable to describe these phenomena basing on coherence concepts [18].

The aim of this Thesis is to provide new insights in the description of partially coherent ultrashort light pulses from both a fundamental and applied perspective. We restrict ourselves to the scalar and plane-wave approximation, and in particular, we focus our attention on the spreading of partially coherent light pulses in first-order dispersive media. Chapter II is devoted to summarize the basic generalities of the scalar coherence theory used throughout this Thesis. Chapter III focuses on the mathematical description and experimental realization of partially coherent pulses obeying some specific models. Chapter IV provides a theory describing mathematically the deterioration of the frequency comb structure due to noise. In Chapter V we make use of the Space–Time analogy to propose new coherent pulse processing schemes. Then, we extend the analogy further to the partially coherent regime, which allows us to describe the pernicious effects of the finite source linewidth in lightwave communication systems in terms of coherence concepts. In Chapter VI we propose the use of broadband incoherent light as fundamental source in an original pulse shaping scheme. Chapter VII aims to give particular guidelines in order to measure properly partially coherent light pulses. In Chapter VIII we provide both theoretical and experimental verification of new coherent and incoherent techniques aimed to generate and process radio-frequency (RF) signals in the optical domain. In Chapter IX we point out a formal similitude between partially coherent light pulses and temporally

entangled photons. Finally, in Chapter X we summarize briefly the main achievements exposed in this Thesis.

Part of the results appearing in this Thesis have already been presented in the following original articles:

1. J. Lancis, V. Torres-Company, E. Silvestre, and P. Andrés, "Space-time analogy for partially coherent plane-wave-type pulses," *Optics Letters* **30**, 2973–2975 (2005).

2. V. Torres-Company, J. Lancis, and P. Andrés, "Unified approach to describe optical pulse generation by propagation of periodically phase-modulated CW laser light," *Optics Express* **14**, 3171–3180 (2006).

3. V. Torres-Company, G. Mínguez-Vega, J. Lancis, E. Silvestre, and P. Andrés, "Source linewidth effects in temporal imaging of Gaussian Schell-model pulses," *Optics Communications* **267**, 40–43 (2006).

4. V. Torres-Company, M. Fernández-Alonso, J. Lancis, J. C. Barreiro, and P. Andrés, "Millimeter-wave and microwave signal generation by low-bandwidth electro-optic phase modulation," *Optics Express* **14**, 9617–9626 (2006).

5. V. Torres-Company, J. Lancis, and P. Andrés, "Arbitrary waveform generator based on all-incoherent pulse shaping," *IEEE Photonics Technology Letters* **18**, 2626–2628 (2006).

6. V. Torres-Company, J. Lancis, and P. Andrés, "Incoherent frequency-to-time mapping: application to incoherent pulse shaping," *Journal of the Optical Society of America A* **24**, 888–894 (2007).

7. V. Torres-Company, J. Lancis, P. Andrés, and M. A. Muriel, "Real-time optical spectrum analyzers operating with spectrally incoherent broadband continuous-wave light source," *Optics Communications* **273**, 320–323 (2007).

8. A. T. Friberg, H. Lajunen, and V. Torres-Company, "Spectral elementary-coherence-function representation for partially coherent light pulses", *Optics Express* **15**, 5160–5165 (2007).

9. J. Lancis, V. Torres-Company, P. Andrés, and J. Ojeda-Castañeda, "Side-lobe suppression in electro-optic pulse generation," *Electronics Letters* **43**, 414–415 (2007).

10. V. Torres-Company, H. Lajunen, and A. T. Friberg, "Effects of partial coherence on frequency combs," *Journal of the European Optical Society–Rapid Publications* **2**, 07007 (2007).

11. V. Torres-Company, H. Lajunen, and A. T. Friberg, "Coherence theory of noise in ultrashort-pulse trains", *Journal of the Optical Society of America B* **24**, 1441–1450 (2007).

12. V. Torres-Company, G. Mínguez-Vega, J. Lancis, and A. T. Friberg, "Controllable generation of partially coherent light pulses with direct space-to-time pulse shaper", *Optics Letters* **32**, 1608–1610 (2007).

13. V. Torres-Company, J. Lancis, and P. Andrés, "Spectral imaging system for scaling the power spectrum of optical waveforms," *Optics Letters* **32**, 2849–2851 (2007).

14. V. Torres-Company, J. Lancis, and P. Andrés, "Flat-top ultra-wideband photonic filters based on mutual coherence function synthesis," *Optics Communications* **281**, 1438–1444 (2008).

15. V. Torres-Company, K. Prince, and I. T. Monroy, "Fiber transmission and generation of ultrawideband pulses by direct current modulation of semiconductor lasers and chirp-to-intensity conversion," *Optics Letters* **33**, 222–224 (2008).

16. V. Torres-Company, H. Lajunen, J. Lancis, and A. T. Friberg, "Ghost interference with classical partially coherent light pulses," *Physical Review A* **77**, 043811 (2008).

17. V. Torres-Company, I. T. Monroy, J. Lancis, and P. Andrés, "All-fiber incoherent frequency-to-time mapping method for microwave signal generation with baseband transmission and multicasting support," *Optics Communications* **281**, 3965 (2008).

18. V. Torres-Company, J. Lancis, L. R. Chen, and P. Andrés, "Reconfigurable RF-waveform generator based on incoherent-filter design," *Journal of Lightwave Technology* (in press, 2008).

19. V. Torres-Company, K. Prince, and I. T. Monroy, "Ultra-wideband pulse generation based on overshooting effect in gain-switched semiconductor laser," *IEEE Photonics Technology Letters* (in press, 2008).

20. V. Torres-Company, H. Lajunen, and A. T. Friberg, "Nonlocal dispersion cancellation with classical light and its application to remote spectral transfer," *Physical Review Letters* (submitted, 2008).

In addition, the following work based on the results presented in this Thesis is under preparation:

1. V. Torres-Company, J. Lancis, H. Lajunen, and P. Andrés, "Non-interferometric characterization of partially coherent pulses".

Throughout this Thesis these works can be identified with the reference numbers [19–38].

Scalar coherence theory

In order to describe the light properties accurately, the stochastic behavior of the radiation must be taken into account. In a laser, for example, fluctuations are caused either by the spontaneous emission process in the amplifier medium; thermal or mechanical variations in the cavity; or by instabilities in the pumping mechanism. Optical coherence theory takes into account all these stochastic phenomena on the basis of classical statistical theory of random signals through the so-called correlation functions. The modern formulation of optical coherence theory was developed in the 1950's with the Wolf's pioneer works [39]. Since then, the research has been mainly focused on the case of statistically stationary light fields, for which the averaged light intensity remains constant in time. This model is suitable to describe the coherence properties of thermal light, like that emitted by light emitting diodes (LEDs) or amplified spontaneous emission (ASE) sources. However, it fails to deal with the coherence properties of pulsed radiation. For this aim, optical coherence theory has been recently extended to the nonstationary case [18, 26, 29, 40–47].

The aim of this Chapter is to introduce briefly some basic results of scalar optical coherence theory that will be used throughout this Thesis. Some excellent textbooks are [15, 48], from which we will follow the nomenclature.

2.1 Random processes. Stationarity and ergodicity

We call $U(t)$ a random process of t if U does not depend on t in a deterministic manner. The quantity that contains the highest degree of information of the random process is the n-fold joint probability density $p_n(U_1, U_2, ...U_n; t_1, t_2, ..., t_n)$. The quantity $p_n(U_1, U_2, ...U_n; t_1, t_2, ..., t_n) \mathrm{d}U_1 \mathrm{d}U_2 ... \mathrm{d}U_n$ gives the probability that at time t_1 the random variable has a value between U_1 and $U_1 + \mathrm{d}U_1$, that at time t_2 has a value between U_2 and $U_2 + \mathrm{d}U_2$, and so on [48]. Obviously, the information is complete for $n \to \infty$.

Once p_n is known, the nth-order statistical moments can be calculated. For example, the first-order moment is

$$\langle U(t) \rangle = \int U p_1(U; t) \mathrm{d}U, \tag{2.1}$$

for which p_1 is only required.

Alternatively, we may consider the set of all possible realizations of the random process $\{U_r\}$. We can then form the average or expectation of U at time t by averaging over the

ensemble of all these realizations

$$\langle U(t)\rangle = \lim_{N\to\infty} \frac{1}{N} \sum_{r=1}^{N} U_r. \tag{2.2}$$

This equation is equivalent to Eq. (2.1) and defines the action of the operator $\langle\rangle$, usually known as *ensemble average*.

Following the same reasoning as before, we can define the second-order moment or temporal autocorrelation function

$$\Gamma(t_1, t_2) \equiv \langle U^*(t_1)U(t_2)\rangle = \int U_1^* U_2 \, p_2(U_1, U_2; t_1, t_2) \mathrm{d}U_1 \mathrm{d}U_2, \tag{2.3}$$

where the asterisk denotes complex conjugate. Note that in this case the second-order probability density is required.

According to [15], when the probability density function is independent on the time origin, i.e., $p_n(U_1, U_2, ...U_n; t_1, t_2, ..., t_n) = p_n(U_1, U_2, ...U_n; t_1 - T, t_2 - T, ..., t_n - T)$ $\forall T$, the random process is referred as stationary in strict sense. If the above equality is only satisfied for $n = 2$, the process is said to be stationary in a wide sense. In this case, Eq. (2.3) reduces to a function depending only on the time difference coordinate $\tau = t_2 - t_1$. Note that as long as we restrict ourselves to second-order coherence functions, there is no need to clarify whether we mean a stationary process in a wide or strict sense.

For a nonstationary process the temporal autocorrelation function is not a function that depends on the time difference anymore, but on the specific time instants t_1 and t_2. For example, the continuous-wave (CW) laser emission fits well to a stationary process when the spontaneous emission effects are taken into account. As an example of a nonstationary process, we mention the pulsed operation of a continuously operating mode-locked laser when there are nondeterministic variations from pulse to pulse.

Finally, a stochastic process is said to be ergodic when a single sample already contains all the statistical information of the ensemble. Therefore, the ensemble average operator can be replaced by a temporal average. According to this definition, stationarity does not necessarily imply ergodicity and vice versa.

2.2   Correlation functions

2.2.1   Analytic signal representation

Most of the physical variables in optics are described by real functions. However, it may be of practical interest to define a complex function associated with the real scalar optical field, $\amalg(\mathbf{r}, t)$. Assuming that $\amalg(\mathbf{r}, t)$ is square-integrable, the complex function associated with this field can be obtained as[1]

$$U(\mathbf{r}, t) = \frac{1}{2\pi} \iint \amalg(\mathbf{r}, t')\theta(\omega) \exp[i\omega(t' - t)]\mathrm{d}t'\mathrm{d}\omega. \tag{2.4}$$

Here $\theta(\omega) = 1$ for $\omega > 0$ and null for the rest. The function $U(\mathbf{r}, t)$ is known as the complex analytic signal associated with $\amalg(\mathbf{r}, t)$. Then, the real signal can be recovered just by $\amalg(\mathbf{r}, t) = 2\Re[U(\mathbf{r}, t)]$.

---

[1] In this Thesis, unless it is specified explicitly, the integration limits range from $-\infty$ to ∞.

Throughout this Thesis, we will be interested in quasi-monochromatic fields. This means that the positive-frequency content of $\text{II}(\mathbf{r}, t)$ is confined to a spectral range, $\Delta\omega$, much smaller than the carrier frequency of light, ω_0. Such fields may be described as $\text{II}(t) = \psi(t)\cos[\omega_0 t + \varphi(t)]$, where the explicit dependence with $\mathbf{r}$ has been omitted for simplicity. Although, in general, there is a broad set of pairs of $[\psi(t), \varphi(t)]$ leading to the same $\text{II}(t)$, only the analytic signal representation defines a complex envelope unambiguously as

$$U(t) = \frac{1}{2}\psi(t)\exp\{-i[\omega_0 t + \varphi(t)]\}. \tag{2.5}$$

2.2.2 Mutual coherence function

In the space–time domain, the coherence properties of fluctuating light fields can be described through the so-called mutual coherence function (MCF)

$$\Gamma(\mathbf{r}_1, \mathbf{r}_2; t_1, t_2) = \langle U^*(\mathbf{r}_1, t_1)U(\mathbf{r}_2, t_2)\rangle. \tag{2.6}$$

Here, $U(\mathbf{r}, t)$ represents the analytic signal of the random field realizations. Thus, the MCF determines the cross-correlations of the field at positions $\mathbf{r}_1$ and $\mathbf{r}_2$ at time instants t_1 and t_2. By setting $\mathbf{r}_1 = \mathbf{r}_2 = \mathbf{r}$ and $t_1 = t_2 = t$, from the above equation we get the function

$$I(\mathbf{r}, t) = \Gamma(\mathbf{r}, \mathbf{r}; t, t) = \langle |U(\mathbf{r}, t)|^2\rangle, \tag{2.7}$$

which corresponds to the intensity at $\mathbf{r}$ and time instant t averaged over the field realizations.

It is also useful to define the normalized version of the MCF,

$$\gamma(\mathbf{r}_1, \mathbf{r}_2; t_1, t_2) = \frac{\Gamma(\mathbf{r}_1, \mathbf{r}_2; t_1, t_2)}{\sqrt{I(\mathbf{r}_1, t_1)I(\mathbf{r}_2, t_2)}}, \tag{2.8}$$

known as complex degree of coherence. By invoking the Schwartz inequality, it can be shown that $0 \leq |\gamma(\mathbf{r}_1, \mathbf{r}_2; t_1, t_2)| \leq 1$. When the lower limit is satisfied, the field realizations at spatiotemporal points $(\mathbf{r}_1, t_1)$ and $(\mathbf{r}_2, t_2)$ are uncorrelated, and the field is said to be fully incoherent. The upper limit indicates that the field is fully coherent and therefore complete correlation between such particular spatiotemporal points appears. Realistic optical fields lie in between those extreme cases and are called partially coherent.

Following [43], it is possible to define the coherence time at position $\mathbf{r}$, $t_c(\mathbf{r})$, of an optical field as

$$t_c(\mathbf{r})^2 = \frac{\iint (t_2 - t_1)^2 |\gamma(\mathbf{r}, \mathbf{r}, t_1, t_2)|^2 \mathrm{d}t_1 \mathrm{d}t_2}{\iint |\gamma(\mathbf{r}, \mathbf{r}, t_1, t_2)|^2 \mathrm{d}t_1 \mathrm{d}t_2}. \tag{2.9}$$

This definition is valid for both cases, stationary and nonstationary. We must highlight that there are many other possible definitions for the measurement of the coherence time [48].

2.2.3 Cross-spectral density function

Alternatively, the coherence properties of the optical fields can be described in the space–frequency domain. For this aim, we take the Fourier transform of the analytic signal of

the fluctuating field,

$$\tilde{U}(\mathbf{r}, \omega) = \frac{1}{2\pi} \int U(\mathbf{r}, t) \exp(i\omega t) \mathrm{d}t. \tag{2.10}$$

Then we define the following function

$$W(\mathbf{r}_1, \mathbf{r}_2; \omega_1, \omega_2) = \langle \tilde{U}^*(\mathbf{r}_1, \omega_1) \tilde{U}(\mathbf{r}_2, \omega_2) \rangle, \tag{2.11}$$

which is known as the cross-spectral density function (CSDF). It represents the field correlations at positions $\mathbf{r}_1$ and $\mathbf{r}_2$ at angular frequencies ω_1 and ω_2. We can particularize this equation to $\mathbf{r}_1 = \mathbf{r}_2 = \mathbf{r}$ and $\omega_1 = \omega_2 = \omega$, which leads to the spectral density function or energy spectrum (ES)

$$S(\mathbf{r}, \omega) = \langle |\tilde{U}(\mathbf{r}, \omega)|^2 \rangle \tag{2.12}$$

Physically, this function represents a measure of the energy per unit of frequency [43].

We can now introduce the normalized version of the cross-spectral density function, i.e., the complex degree of spectral coherence

$$\mu(\mathbf{r}_1, \mathbf{r}_2; \omega_1, \omega_2) = \frac{W(\mathbf{r}_1, \mathbf{r}_2; \omega_1, \omega_2)}{\sqrt{S(\mathbf{r}_1, \omega_1) S(\mathbf{r}_2, \omega_2)}}. \tag{2.13}$$

As in the case of the complex degree of coherence, it satisfies the inequalities $0 \leq |\mu(\mathbf{r}_1, \mathbf{r}_2; \omega_1, \omega_2)| \leq 1$. The upper and lower limits are reached by a spectrally fully correlated or uncorrelated field, respectively. Intermediate cases deal with spectrally partially coherent fields. We must note that there could be a field with some degree of temporal coherence but full spectral uncorrelation. Therefore it is important to specify the domain in which the coherence properties are defined.

From Eq. (2.13), it is possible to define a spectral correlation width at position $\mathbf{r}$, $\delta\omega(\mathbf{r})$, in complete analogy with Eq. (2.9),

$$\delta\omega(\mathbf{r})^2 = \frac{\iint (\omega_2 - \omega_1)^2 |\mu(\mathbf{r}, \mathbf{r}, \omega_1, \omega_2)|^2 \mathrm{d}\omega_1 \mathrm{d}\omega_2}{\iint |\mu(\mathbf{r}, \mathbf{r}, \omega_1, \omega_2)|^2 \mathrm{d}\omega_1 \mathrm{d}\omega_2}. \tag{2.14}$$

This magnitude determines the maximum spectral portion of the energy spectrum, $S(\mathbf{r}, \omega)$, in which two different frequencies, ω_1 and ω_2, remain relatively correlated.

2.3   Wiener–Khintchine theorem

The mutual coherence and cross-spectral density functions form a Fourier transform pair,

$$\Gamma(\mathbf{r}_1, \mathbf{r}_2; t_1, t_2) = \iint W(\mathbf{r}_1, \mathbf{r}_2; \omega_1, \omega_2) \exp[i(\omega_1 t_1 - \omega_2 t_2)] \mathrm{d}\omega_1 \mathrm{d}\omega_2 \tag{2.15}$$

and

$$W(\mathbf{r}_1, \mathbf{r}_2; \omega_1, \omega_2) = \frac{1}{4\pi^2} \iint \Gamma(\mathbf{r}_1, \mathbf{r}_2; t_1, t_2) \exp[-i(\omega_1 t_1 - \omega_2 t_2)] \mathrm{d}t_1 \mathrm{d}t_2. \tag{2.16}$$

This means that the space–frequency and space–time domains are connected. These equations can be considered as the generalization of the Wiener–Khintchine theorem to nonstationary fields.

In the limit of a stationary field, the MCF verifies

$$\Gamma(\mathbf{r}_1, \mathbf{r}_2; t_1, t_2) = \Gamma_s(\mathbf{r}_1, \mathbf{r}_2; \tau = t_2 - t_1), \tag{2.17}$$

and, accordingly,

$$W(\mathbf{r}_1, \mathbf{r}_2; \omega_1, \omega_2) = W_s(\mathbf{r}_1, \mathbf{r}_2; \omega_1)\delta(\omega_2 - \omega_1), \tag{2.18}$$

where $\delta()$ denotes the Dirac's delta function. This result establishes that, in a stationary process, two frequencies become fully uncorrelated. In this case, from Eqs. (2.15) and (2.16) we get

$$\Gamma_s(\mathbf{r}, \tau) = \int S_s(\mathbf{r}, \omega) \exp(-i\omega\tau)\mathrm{d}\omega \tag{2.19}$$

and

$$S_s(\mathbf{r}, \omega) = \frac{1}{2\pi} \int \Gamma_s(\mathbf{r}, \tau) \exp(i\omega\tau)\mathrm{d}\tau, \tag{2.20}$$

where $S_s(\mathbf{r}, \omega) = W_s(\mathbf{r}, \mathbf{r}, \omega)$ and $\Gamma_s(\mathbf{r}, \tau) = \Gamma(\mathbf{r}, \mathbf{r}; \tau)$. This result represents the Wiener–Khintchine theorem as it is known in its most common version.

2.4 Cross-correlation functions

There are some physical phenomena that involve the interaction of N different random processes. In order to describe this situation, it can be useful to define a $N \times N$ random matrix known as cross-correlation matrix, with elements

$$\Gamma_{ij}(\tau) = \langle U_i^*(t)U_j(t + \tau)\rangle, \tag{2.21}$$

where $i, j = 1, ..., N$. For simplicity, we have omitted the $\mathbf{r}$ dependence and assumed explicitly that the N different random processes $U_j(t)$ are jointly stationary. Whenever $\Gamma_{ij}(\tau)$ is different from zero there will be some kind of correlation between the i and j random processes.

The cross-spectral density matrix, $W_{ij}(\omega)$, of the jointly stationary random process gives

$$\langle \tilde{U}_i^*(\omega)\tilde{U}_j(\omega + \omega')\rangle = W_{ij}(\omega)\delta(\omega - \omega'). \tag{2.22}$$

For the case $i = j$, the cross-spectral density reduces to the spectral density function of the j random process, i.e., $W_{jj}(\omega) = S_j(\omega)$.

The elements of these different matrices form a Fourier transform pair,

$$\Gamma_{ij}(\tau) = \int W_{ij}(\omega) \exp(-i\omega\tau)\mathrm{d}\omega \tag{2.23}$$

and

$$W_{ij}(\omega) = \frac{1}{2\pi} \int \Gamma_{ij}(\tau) \exp(i\omega\tau)\mathrm{d}\tau. \tag{2.24}$$

This result is known as the Wiener-Khintchine theorem generalized to cross-correlation functions.

For the case $N = 2$, it is easy to note that the cross-correlation matrix elements satisfy the following properties

$$\Gamma_{21}(\tau) = \Gamma_{12}^*(-\tau) \tag{2.25}$$

and

$$W_{12}(\omega) = W_{21}^*(\omega). \tag{2.26}$$

With the help of this last equation, it can be shown the following inequality

$$|W_{12}(\omega)| \leq \sqrt{S_1(\omega)S_2(\omega)}. \tag{2.27}$$

2.5   Gaussian random processes

Up to now, we have carried out the analysis of some second-order coherence properties of light fields. In general, higher-order random process require the knowledge of higher-order probability density functions. An exception is the Gaussian random process. In such a case, in virtue of the Gaussian moment theorem, all the hierarchy of correlation functions can be constructed from the second-order correlation function.

Therefore, for a real Gaussian random process with a zero mean, $\amalg(t)$, the nth-order correlation function results

$$\langle \amalg(t_1)\, \amalg(t_2)... \amalg(t_n)\rangle = \begin{cases} \sum_\pi \langle \amalg(t_1)\, \amalg(t_2)\rangle \langle \amalg(t_3)\, \amalg(t_4)\rangle ... \langle \amalg(t_{n-1})\, \amalg(t_n)\rangle & n \text{ even} \\ 0 & n \text{ odd} \end{cases} \tag{2.28}$$

where π indicates the sum over all the possible $(n-1)!!$ pairs.

In particular, it will be important for us the two-time intensity correlation formula for the complex Gaussian random process $U(t)$ with zero mean,

$$\langle |U(t_1)|^2 |U(t_2)|^2 \rangle = I(t_1)I(t_2) + |\Gamma(t_1,t_2)|^2, \tag{2.29}$$

where $I(t)$ denotes the averaged intensity as defined by Eq. (2.7), and $\Gamma(t_1, t_2)$ is the MCF given by Eq. (2.6).

Some physical models and practical implementations

Although optical radiation is always partially coherent, in many experimental arrangements the assumption of full coherence can be adequate. However, there are many cases in which it is necessary, and even convenient, to deal with a stochastic description. Throughout this Thesis we will provide examples in which decoherence can be pernicious and situations where incoherent sources are preferable. It is required to have adequate mathematical tools to describe optical coherence properties as well as physical devices to generate them in a controlled way.

In the spatial domain, the so-called Schell model, proposed first it in the context of antenna radiation patterning [49], has been widely adopted. This model assumes an explicit dependence in the difference (spatial) coordinate for the complex degree of spectral coherence. The scalar diffraction properties of these primary sources with the simplification of the Gaussian intensity distribution have been widely studied and experimentally verified in the literature [50–54]. This model has been later adapted into the temporal domain to study the temporal coherence properties of ultrashort pulses [40, 41, 55], receiving the name of Gaussian Schell-model pulse (GSMP).

Experimentally, there are well-known techniques to produce partially coherent quasi-monochromatic radiation in a controlled way [56–59]. An elegant solution is to generate first a spatially incoherent beam by introducing a rotating phase diffuser in front of a monochromatic laser spot [60], and then place different spatial masks in front of the beam. A broad range of spatially partially coherent structures can be synthesized in this way [51, 61].

In the temporal domain, tailoring the intensity profile and chirp of coherent pulses is now well-established with reconfigurable devices [62]. In the last few years, these user-defined waveforms have offered unique capabilities in the control of molecular dynamics and chemical reactions [63–66]. However, only fully coherent fields are used. In contrast, several studies demonstrate the influence of pulse coherence in multiphoton ionization [67]; in the product yield of some chemical reactions in a pump–dump scenario [65, 68]; or in the supercontinuum generation [69–72]. In order to control such kind of processes, new schemes for synthesizing the MCF of the pulse, rather than the complex field, become imperative.

In this Chapter we propose some physical models to describe partially coherent pulses and discuss their possible implementation with current technology. For the sake of sim-

11

plicity, we will restrict ourselves to the temporal coherence aspects and neglect the spatial structure of the beam. This assumption will be briefly justified in Chapter V.

3.1   Non-negative definiteness property

In Chapter II we saw that the MCF and the CSDF are the physically relevant functions for describing partially coherent pulses. Following the Wiener–Khintchine theorem, these quantities are connected to each other and carry the same amount of information. Their structure must be mathematically consistent with the definitions provided by Eqs. (2.6) and (2.11). Consequently, any MCF or CSDF properly defined must satisfy inequalities

$$\iint \Gamma(t_1, t_2) f^*(t_1) f(t_2) \mathrm{d}t_1 \mathrm{d}t_2 \geq 0 \tag{3.1}$$

and

$$\iint W(\omega_1, \omega_2) g^*(\omega_1) g(\omega_2) \mathrm{d}\omega_1 \mathrm{d}\omega_2 \geq 0, \tag{3.2}$$

where $f(t)$ and $g(\omega)$ are any well-behaved functions. This result is known as the non-negative definiteness property of the correlation functions [48].

In general, it is very difficult to verify that a correlation function satisfies Eqs. (3.1) and (3.2) because they must be true for any $f(t)$ and $g(\omega)$ functions. However, there exists a sufficient condition. A correlation function A is nonnegative definite if it can be written as a superposition integral of the form

$$A(\alpha_1, \alpha_2) = \int T(x) H^*(\alpha_1, x) H(\alpha_2, x) \mathrm{d}x, \tag{3.3}$$

where α denotes t or ω, $T(x)$ is a nonnegative function, and H an arbitrary well-behaved kernel [73].

3.2   Coherent-mode representation

Based on the nonnegative definiteness property and the hermiticity properties $\Gamma(t_1, t_2) = \Gamma^*(t_2, t_1)$ and $W(\omega_1, \omega_2) = W^*(\omega_2, \omega_1)$, every genuine MCF or CSDF can be alternatively expressed as a convergent series by virtue of the Mercer's theorem [42, 48]

$$A(\alpha_1, \alpha_2) = \sum_n a_n \phi_n^*(\alpha_1) \phi_n(\alpha_2), \tag{3.4}$$

where a_n and $\phi(\alpha)$ are the eigenvalues and eigenfunctions of the integral equation

$$\int A(\alpha_1, \alpha_2) \phi_n(\alpha_1) \mathrm{d}\alpha_1 = a_n \phi_n(\alpha_2). \tag{3.5}$$

It can then be shown [42] that the eigenvalues are real and nonnegative, and the eigenfunctions $\phi_n(\alpha)$ satisfy the orthogonality relation

$$\int \phi_n^*(\alpha) \phi_m(\alpha) \mathrm{d}\alpha = \delta_{mn}, \tag{3.6}$$

where δ_{mn} denotes the Kronecker's delta. We should note that the structure of the modes $\phi_n^*(\alpha_1)\phi_n(\alpha_2)$ in Eq. (3.4) can be interpreted as the correlation function of a fully coherent field. Therefore, Eq. (3.4) indicates that any MCF (or CSDF) can be constructed as an incoherent superposition of temporally (or spectrally) fully coherent fields. This coherent mode representation was adapted first to Optics considering quasimonochromatic stationary light fields [74]. Experimentally, Gase demonstrated the superposition of the transversal modes from a high-power solid-state laser resonator as a way to achieve a Gaussian Schell-model beam. In the temporal domain, this coherent mode representation has been recently extended to non-stationary pulsed plane-wave [42] and beams [45].

3.3 Independent-elementary-pulse representation model

3.3.1 Frequency domain

MATHEMATICAL FRAMEWORK

Let us assume a CSDF with a structure as

$$W(\omega_1, \omega_2) = \int S_s(\omega')\tilde{M}^*(\omega_1 - \omega')\tilde{M}(\omega_2 - \omega')\mathrm{d}\omega', \tag{3.7}$$

where $S_s(\omega)$ is a real nonnegative function and $\tilde{M}(\omega)$ is a well-behaved function. We note that this is a particular case of the structure given by Eq. (3.3). Then, the consistency with the nonnegative definiteness condition is guaranteed. Such a CSDF is constructed by spectrally shifting a basic coherent source with CSDF $W_b(\omega_1, \omega_2) = \tilde{M}^*(\omega_1)\tilde{M}(\omega_2)$, and weighting it with a function given by $S_s(\omega)$. The energy spectrum can be easily calculated by $\omega_1 = \omega_2 = \omega$

$$S(\omega) = S_s(\omega) \otimes |\tilde{M}(\omega)|^2, \tag{3.8}$$

which is just the convolution between the weighting function $S_s(\omega)$ and the energy spectrum of the spectrally coherent basis, $|\tilde{M}(\omega)|^2$.

The special structure given by Eq. (3.7) leads to the following MCF

$$\Gamma(t_1, t_2) = \Gamma_s(t_2 - t_1)m^*(t_1)m(t_2), \tag{3.9}$$

where $m(t)$ and $\Gamma_s(\tau = t_2 - t_1)$ are the inverse Fourier transform of $\tilde{M}(\omega)$ and $S_s(\omega)$, respectively. From this equation we can note that the complex degree of coherence is

$$\gamma(t_1, t_2) = \frac{\Gamma_s(t_2 - t_1)}{\Gamma_s(0)} \exp\{i[\varphi_m(t_2) - \varphi_m(t_1)]\}, \tag{3.10}$$

where $\varphi_m(t)$ is the phase of $m(t)$. By substituting Eq. (3.10) into Eq. (2.9), we conclude that the $m(t)$ function does not affect the coherence time of the pulse.

POSSIBLE EXPERIMENTAL ARRANGEMENT

Although Eqs. (3.7) and (3.9) are fully equivalent, it is perhaps more useful to think in terms of (3.9) to get a clear picture of its possible implementation.

Such a structure can be easily achieved by temporally modulating a stationary light source, $\Gamma_s(t_2 - t_1)$, with a temporal modulator providing a deterministic complex pulse

$m(t)$ [55]. Stationary light sources can be obtained, e.g., from an SLED, or by the ASE noise from the gain spectrum of some fiber amplifiers. According to Eq. (2.19), the ES of the source gives $\Gamma_s(t_2 - t_1)$ through inverse Fourier transformation. Coherence times as short as hundreds of femtoseconds can be achieved with Erbium-doped fiber amplifiers (EDFAs) [75]. On the other hand, temporal modulators providing pulse shapes $m(t)$ are widely employed in telecommunications. As an example, LiNbO$_3$ electro-optic intensity or phase modulators can work at speeds > 100 Gb/s, and electroabsorption modulators (EAMs) can achieve even ~ 1 ps temporal pulse durations [3].

For instance, the model described by Eq. (3.9) accounts for the effects of the source linewidth in wavelength-division-multiplexing (WDM) communication systems [76]. In such a case, the linewidth limits the transmission speed of the channel [77]. Some research works [78] have followed the stochastic analysis of the pioneer woks of Miyagi [79] and Marcuse [80], but recent papers have recognized that the light emerging from the modulator can be written in terms of MCFs [55, 75, 81, 82], so that coherence theory concepts provide a much richer interpretation [19]. In the case that the spectral line shape and the temporal modulation are Gaussian distributed, the emerging partially coherent pulse acquires a Gaussian Schell-model structure [55].

Finally, we remark that any MCF structure built as Eq. (3.9) has two degree of freedom. One is the coherence time, given by the shape of energy spectrum of the light source, and the other is the temporal intensity duration, given by the modulator. Then, within this precise model, the global degree of coherence, measured as the ratio between the coherence time and the temporal intensity width, can be arbitrarily set by selecting the appropriate photonic devices.

3.3.2   Time domain

MATHEMATICAL FRAMEWORK

Recently, Vahimaa and Turunen have reported the dual representation of the above model [46]. Let us assume a MCF constructed as

$$\Gamma(t_1, t_2) = \int f(t')e^*(t_1 - t')e(t_2 - t')\mathrm{d}t', \tag{3.11}$$

with $f(t)$ an arbitrary real and positive well-behaved function. This equation has the same mathematical structure as Eq. (3.3), ensuring is nonnegative definite. Following the same reasoning as before, Eq. (3.11) is performed by time shifting a fully coherent pulse with complex envelope $e(t)$ and weighting it with a function $f(t)$.

The CSDF can be calculated to give

$$W(\omega_1, \omega_2) = \tilde{F}(\omega_2 - \omega_1)\tilde{E}^*(\omega_1)\tilde{E}(\omega_2), \tag{3.12}$$

where $\tilde{F}(\omega)$ and $\tilde{E}(\omega)$ denote the Fourier transform of the weighting function and the complex envelope, respectively. Note that this equation corresponds to the dual representation of Eq. (3.9). The complex degree of spectral coherence can be calculated as

$$\mu(\omega_1, \omega_2) = \frac{\tilde{F}(\omega_2 - \omega_1)}{\tilde{F}(0)} \exp\{i[\varphi_e(\omega_2) - \varphi_e(\omega_1)]\}, \tag{3.13}$$

with $\varphi_e(\omega)$ being the phase of $\tilde{E}(\omega)$. Again, the mathematical structure is formally identical to that of Eq. (3.10). We note that the spectral correlation width is fixed by the weight function $f(t)$ only.

Analogally to Eq. (3.8), the average intensity is just given by

$$I(t) = f(t) \otimes |e(t)|^2, \tag{3.14}$$

i.e., the convolution between the intensity of the input coherent pulse and the weighting function.

Unlike in the temporal modulation of stationary light sources, here the global degree of coherence cannot be set arbitrarily. This is because it is not possible to set independently the complex degree of coherence and the averaged intensity distribution.

POSSIBLE EXPERIMENTAL ARRANGEMENT

A simple way to achieve the physical structure provided by Eq. (3.11) is by introducing a slight modification in the direct space-to-time (DST) pulse shaper. The DST pulse shaper may operate at mid infrared [83] or telecom wavelengths [84], and has been mainly employed for RF applications [85]. We note that such a device has the inherent capability to transfer the spatial coherence properties of a beam to the temporal domain. In consequence, by controlling the spatial coherence of the input pulsed field, a user-defined partially coherent output light pulse can be synthesized [30].

The operation of the DST pulse shaper has been described in detail in [86]. Briefly, a spatially patterned mask is disposed at the surface of a kinoform diffraction grating. The different spectral components are diffracted and focused on the Fourier plane of a lens with focal length f (see Fig. 3.1). At the output, at a distance f from the lens, a thin slit filters the dispersed spectrum. As a result, in the ideal case, a spatially uniform pulse is obtained whose analytic signal, aside from an irrelevant constant factor, is given by

$$U_{\mathrm{out}}(t) = e_{\mathrm{in}}(t) \otimes h[(\beta/\gamma)t]. \tag{3.15}$$

Here $e_{\mathrm{in}}(t)$ is the complex input field and the function $h(x)$ incorporates the spatial mask, $M(x)$, and the input field profile. The term $\gamma/\beta = \lambda_0/(cd\cos\theta_i)$ is a scaling factor, with λ_0 being the carrier wavelength, c the speed of light in vacuum, θ_i the angle of incidence of the input beam onto the diffraction grating of period d, and $\beta = \cos\theta_i/\cos\theta_d$, where θ_d is the diffraction angle. For an input Gaussian beam $h(x) = M(x)\exp(-x^2/4w^2)\exp(ikx^2/2R)$, with $k = 2\pi/\lambda_0$, w the root-mean-square (rms) intensity width, and R the radius of curvature. In what follows we write $h(x) = M(x)b(x)$ for convenience.

Let us now assume that the input beam is fully coherent temporally, but spatially partially coherent. In this case the spatial structure is not deterministic anymore and $h(x)$ must be replaced by a randomly varying function, say $h'(x)$. Then, the MCF of the output pulse, $\Gamma_{\mathrm{out}}(t_1, t_2) = \langle U_{\mathrm{out}}^*(t_1)U_{\mathrm{out}}(t_2)\rangle$, is given by

$$\Gamma_{\mathrm{out}}(t_1, t_2) = \iint e_{\mathrm{in}}^*(t_1 - t')e_{\mathrm{in}}(t_2 - t'') \, \langle h'^*[(\beta/\gamma)t']h'[(\beta/\gamma)t'']\rangle \, \mathrm{d}t'\mathrm{d}t''. \tag{3.16}$$

Equation (3.16) implies that the effects of partial coherence in the space domain are readily transferred to the temporal domain.
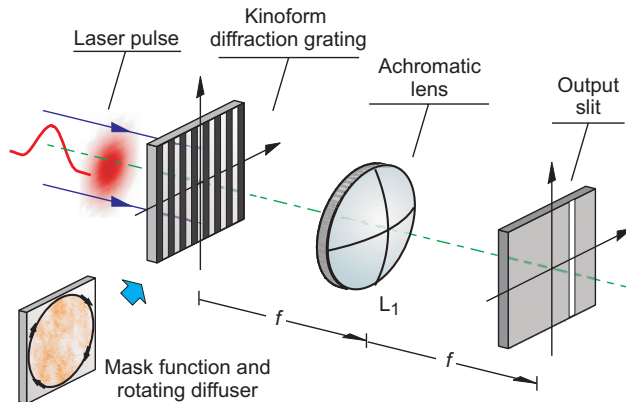
Figure 3.1: Scheme of the modified DST pulse shaper. In this case $\theta_i = 0$.

We emphasize that Eq. (3.16) corresponds to a general case of the transfer of the coherence properties from the spatial to the temporal domain. When the scaling factor γ/β is large enough so that the incoming light field can be considered as a Dirac delta function, the MCF of the output light pulse simply takes on the form $\Gamma_{\text{out}}(t_1, t_2) \approx \langle h'^*[(\beta/\gamma)t_1]\, h'[(\beta/\gamma)t_2]\rangle$. In this case the output MCF is a direct mapping of the pulse's coherence properties from the spatial to the temporal domain.

Commercially available femtosecond laser oscillators are light sources with high spatial and temporal coherence. While it is relatively easy to modify the spatial coherence of laser beams in a controlled way [48,51], let us next particularize Eq. (3.16) to the case of a spatially totally incoherent pulsed field. As illustrated in Fig. 3.1, this can be achieved if a spatially and temporally fully coherent pulsed input beam is passed through a rotating phase diffuser placed in front of the spatial mask of the DST pulse shaper. Due to the diffuser we obtain

$$\langle h'^*(x_1)\, h'(x_2)\rangle = |h(x_1)|^2\, \delta(x_2 - x_1). \tag{3.17}$$

The effect of the phase diffuser is just to de-correlate the fields at any two spatial points in the beam. By substituting Eq. (3.17) into Eq. (3.16) we find

$$\Gamma_{\text{out}}(t_1, t_2) = (\beta/\gamma) \int e_{\text{in}}^*(t_1 - t') e_{\text{in}}(t_2 - t') \big| h[(\beta/\gamma)t'] \big|^2 \, \mathrm{d}t'. \tag{3.18}$$

Equation (3.18) shows that a partially coherent pulse is obtained as an incoherent superposition of time-shifted replicas of a fully coherent pulse, $e_{\text{in}}(t)$, weighted by the (real and positive) function $|h[(\beta/\gamma)t]|^2$. The structure of Eq. (3.18) corresponds precisely to the mathematical model given by Eq. (3.11). Here, the role of the real nonnegative function $f(t)$ is played by the spatially shaped intensity profile, and the elementary coherent pulse is given by the laser pulse shape.

The averaged output intensity is, of course, $I_{\text{out}}(t) = |e_{\text{in}}(t)|^2 \otimes |h[(\beta/\gamma)t]|^2$, i.e., the convolution of the input intensity with the system's impulse response, $|h[(\beta/\gamma)t]|^2$. The complex degree of coherence then is found as $\gamma_{\text{out}}(t_1, t_2) = \Gamma_{\text{out}}(t_1, t_2)[I_{\text{out}}(t_1) I_{\text{out}}(t_2)]^{-1/2}$. This indicates that it is impossible to control simultaneously and independently both the averaged intensity and the temporal coherence of the emerging pulse.

Physically, every laser shot corresponds to a single realization. Each pulse "freezes" a different spatial structure given by the rotating phase diffuser and the mask, which is transferred to the time domain by the space-to-time conversion. The incoherent superposition is due to the rotating phase diffuser, whereas the coherent elementary pulse is the input pulse itself. If we consider a spatially and temporally Gaussian pulsed input and set $M(x) = 1$, the output rms temporal intensity width, σ_{out}, is given by $\sigma_{\text{out}} = (\sigma_0^2 + \sigma^2)^{1/2}$, where σ_0 is the rms temporal width of the input pulse and $\sigma = (\gamma/\beta)w$. From Eq. (3.18), the coherence time of the pulse can be calculated as $t_{c,\text{out}} = 2\sigma_0(1 + \sigma_0^2/\sigma^2)^{1/2}$. Note that σ_{out} accounts for the maximum temporal window of the output signal. If a binary mask function is inserted, due to the serial-to-parallel conversion of the DST pulse shaper, THz repetition rate bursts of coherence-controlled femtosecond pulses can be achieved. As a numerical example, let us consider a 50 fs rms input intensity duration centered on 850 nm and $w = 1$ mm, with a DST pulse shaper configured with a realistic value of $\gamma/\beta = 30$ ps/mm, we obtain an output GSMP with 30 ps rms intensity width and 100 fs coherence time.

As expected from Eq. (3.12), the CSDF gives

$$W_{\text{out}}(\omega_1, \omega_2) = (\beta/\gamma)\,\tilde{E}_{\text{in}}^*(\omega_1)\tilde{E}_{\text{in}}(\omega_2)\widetilde{H}_I(\omega_2 - \omega_1), \tag{3.19}$$

where $\tilde{E}_{\text{in}}(\omega)$ and $\widetilde{H}_I(\omega)$ are the Fourier transforms of $e_{\text{in}}(t)$ and $|h[(\beta/\gamma)t]|^2$, respectively. Hence the energy spectrum of the output pulse corresponds to that of the input field, $S_{\text{out}}(\omega) = |\tilde{E}_{\text{in}}(\omega)|^2$. We can then synthesize in a continuous way the coherence time of the source without affecting the energy spectrum. This is an important requisite in multi-photon ionization processes [67].

Let us comment about the inherent limitations of the system. We consider Gaussian distributions for the incoming pulsed beam, the mask function, and the aperture slit function, $a(x/x_0)$, of rms width x_0. This analytic case is proved to be useful for the determination of the efficiency and aperture effects in the DST system [86]. The aperture makes the output beam spatially non-uniform. However, when the on-axis far field is of interest [86], the output MCF is

$$\Gamma_{\text{out}}(t_1, t_2) \propto \int e_{\text{in}}^*(t_1 - t')e_{\text{in}}(t_2 - t')\big|A[(kx_0/\gamma f)t']\,h[(\beta/\gamma)t']\big|^2 \, dt'. \tag{3.20}$$

The slit modifies the system's impulse response, which now is multiplied by a scaled version of the modulus squared of the slit function's Fourier transform, $A(u)$. Accordingly, the global degree of coherence is

$$r = 2\sigma_0\left(\frac{\beta}{\gamma}\right)\left[\frac{1}{w^2} + \frac{1}{w_m^2} + \left(\frac{x_o k}{f\beta}\right)^2\right]^{1/2}, \tag{3.21}$$

where w_m is the rms width of the pattern mask. In Fig. 3.2 we show the resulting inverse of the global degree of coherence for a Gaussian input pulse of 50 fs (green dashed line) and 200 fs (red dashed line) rms intensity width. The mask function is set to 1 and typical values of $\gamma = 30$ ps/mm, $\beta = 1$, $w = 1$ mm, $f = 100$ mm, and $\lambda_0 = 850$ nm are assumed. For decreasing slit sizes the pulse becomes globally increasingly incoherent, a feature more notable for shorter pulses. For slit sizes narrower than $10\,\mu$m, its effect can

be neglected and the global degree of coherence is determined by the mask function $m(x)$ only.

It is important to note that the same figure of merit for the energy efficiency than in the coherent case can be employed in the partially coherent regime [86],

$$\eta = \frac{\iint |H(\frac{2\pi x}{\beta \lambda_0 f} - \frac{\gamma \omega}{\beta})\tilde{E}_{\text{in}}(\omega)a(\frac{x}{x_0})|^2 \mathrm{d}x \mathrm{d}\omega}{\iint |H(\frac{2\pi x}{\beta \lambda_0 f} - \frac{\gamma \omega}{\beta})\tilde{E}_{\text{in}}(\omega)|^2 \mathrm{d}x \mathrm{d}\omega}, \tag{3.22}$$

where $H(u)$ denotes the Fourier transform of $h(x)$. Figure 3.2 also plots the resulting system efficiency for the two different values of the input pulse width. It reveals that the efficiency increases linearly with the slit width, and the system operates more efficiently for longer pulses.
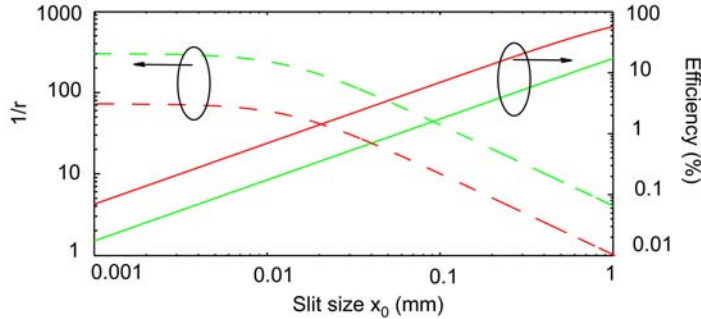

Figure 3.2: Inverse of the output global degree of coherence (dashed curves) for two different Gaussian input pulses of 50 fs (green line) and 200 fs (red line) vs. the slit size x_0. Energy efficiency (solid curves) in terms of the slit size for the same input pulses.

With this simple modification in the DST pulse shaper, it is still possible the development of genetic algorithms that control the product yield in chemical reactions, which is an important feature in femtochemistry [66]. This is achieved by measuring the yield and providing a control signal that feedbacks the spatial light modulator. Even more, in order to achieve a more compact device, the phase diffusor pattern could be implemented directly with the spatial light modulator [87]. In this case, the speed of the spatial light modulator should be refreshed at the repetition rate of the laser. Currently, this can be done at 100 kHz rates [88], which suits fine for femtosecond Ti:Sa-laser pulses that are amplified after the output of the oscillator.

Finally, it should be pointed out that some studies about using spatial speckle patterns for pulse shaping exist [89, 90], but nothing related to the coherence theory and the independent-elementary-pulse representation model. It is important to remark that within this model, fully arbitrary MCFs cannot be achieved [46]. In our experimental proposal in particular, this originates from the restriction of the shaping process given by Eq. (3.15), which is just a spectral filtering operation. Arbitrary chirping cannot be achieved since the input spectral bandwidth imposes the ultimate physical limit. However, many other situations are included in this model [46].

3.3.3 Partially coherent basis

We have seen that it is possible to construct partially coherent light pulses by continuous superposition of a temporally (or spectrally) shifted and weighted fully coherent light pulse. However, it is also possible to achieve a properly defined partially coherent light pulse by continuous superposition of a temporally (or spectrally) shifted and weighted basic *partially coherent* light pulse [26].

   With this aim, let us assume an elementary spectral coherence function as $W_{\mathrm{pc}}(\omega_1, \omega_2) = \langle \tilde{U}_{\mathrm{pc}}^*(\omega_1)\tilde{U}_{\mathrm{pc}}(\omega_2)\rangle$, where $\tilde{U}_{\mathrm{pc}}(\omega)$ is a field realization of a non-stationary ensemble that is described by the CSDF $W_{\mathrm{pc}}(\omega_1, \omega_2)$. Then, instead of the model presented in Eq. (3.7), we can construct a more general CSDF as

$$W(\omega_1, \omega_2) = \int S_s(\omega)W_{\mathrm{pc}}(\omega_1 - \omega, \omega_2 - \omega)\mathrm{d}\omega. \tag{3.23}$$

This model does not fit the structure of Eq. (3.3). However, assuming the weight function $S_s(\omega)$ to be real and nonnegative, it is possible to show that this CSDF also satisfies inequality (3.2) [26]. Equation (3.8) remains valid in this case, i.e., the energy spectrum is a convolution between the weight function and the energy spectrum of the basic pulse, $W_{\mathrm{pc}(\omega,\omega)}$.

   The MCF function is calculated to be

$$\Gamma(t_1, t_2) = \Gamma_s(t_2 - t_1)\Gamma_{\mathrm{pc}}(t_1, t_2), \tag{3.24}$$

where $\Gamma_{\mathrm{pc}}(t_1, t_2)$ is the MCF corresponding to the CSDF of the partially coherent basic ensemble $W_{\mathrm{pc}}(\omega_1, \omega_2)$. Equation (3.24) can be interpreted as a generalization of Eq. (3.9) to the case in which the modulation $m(t)$ is not deterministic anymore, but partially coherent. Therefore, this apparently more complicated situation appears in a natural way when the timing jitter or any other random pulse shape variations in the modulator are taken into account. It is clear from Eq. (3.24), that the averaged intensity is uniquely set by the averaged intensity of the modulator.

   Finally, the complex degree of coherence is

$$\gamma(t_1, t_2) = \frac{\Gamma_s(t_2 - t_1)}{\Gamma_s(0)}\gamma_m(t_1, t_2) \tag{3.25}$$

where $\gamma_m(t_1, t_2)$ denotes the complex degree of coherence of the modulator. This implies that the modulator may change the temporal coherence of the output pulse. However, since $0 \leq \gamma_m \leq 1$, it can just reduce the coherence time of the radiation.

Effects of partial coherence on frequency combs

Optical frequency combs have provided impressive advances in ultra-high resolution metrology [12,13], optical atomic clocks [11,91], extreme nonlinear optics [7,92], lightwave communications [93–95] and molecular sensing [96,97]. The central concept to these advances is that a pulse train corresponds to a comb regularly spaced in frequency by a quantity equal to the repetition rate.

The idea that a frequency comb could be used for exciting narrow resonances was first realized by Hänsch more than 30 years ago [98]. By then, the optical bandwidth available from ultrashort-pulse lasers was about hundreds of GHz and there was still the need to lock the frequency comb to a stable optical reference. Alternative procedures to achieve frequency combs by electro-optic periodic modulation of a CW stable laser were considered [99–101]. In such a case, the repetition rate can be easily locked to a microwave reference signal and the comb may be tuned independently by selecting properly the CW laser frequency. However, even for the case of the lowest V_π voltage modulators, the available optical bandwidth is around a few THz [93]. With the development of the Ti:Sa laser technology in the 90's [2], ultra-short laser pulses corresponding to less than two cycles of the carrier frequency were achieved [102, 103]. In this case, the relative phase between the peak of the pulse envelope and the underlying electric-field carrier is not constant from pulse to pulse because of the difference between the group and phase velocity inside the laser cavity. Although before 2000 there were techniques to measure this phase slip in the temporal domain [104], active feedback was not employed to control it, and therefore rapid dephasing took place because of pulse energy fluctuations and other stochastic phenomena.

Later, the key development of microstructured fibers with zero-dispersion wavelength close to 800 nm permitted the generation of a broad spectrum outside the cavity spanning more than an octave[1] [105] . With such a broad spectrum, it was finally possible to generate a frequency comb locked to a microwave reference signal without the need of any additional reference CW laser [106, 107]. Currently, octave-spanning spectra can be generated directly from the cavity by exciting nonlinear phenomena in the oscillator [108] or by four-wave mixing interactions with microresonators pumped with a high-power CW

---

[1]We refer by octave spanning spectrum when there is, at least, a factor of 2 between the minimum and maximum available optical frequencies. The minimum and maximum frequencies are usually taken as those at the -20 dB level.

laser [109].

  To be able to use this property for high-precision measurements, one has to make sure that this simple intuitive picture is correct with a high degree of accuracy. It is important then to address the question of how does this frequency comb model deteriorates when pulse-to-pulse fluctuations in energy, chirping, timing and phase jitter appear, i.e., the pulse train is partially coherent.

4.1 Fully coherent description

In order to understand the mode structure of a femtosecond frequency comb, let us consider the situation depicted in Fig. 4.1. Due to the difference between the group and phase velocities inside the laser cavity, the carrier shifts with respect to the envelope a constant phase, $\Delta\varphi$, every round trip. In consequence, the pulse train at the output of the oscillator is periodic in the envelope, $\psi(t)$, but not in the complex electric field, $U(t)$. Physically, the comb structure is achieved thanks to the constructive interference among successive pulses. Including the phase slip, the interference takes place at angular frequencies, ω, satisfying $\omega T_r - \Delta\varphi = 2\pi n$, where T_r denotes the period of the pulse envelope and n is a very large integer number. Thus, the angular frequencies of the comb are

$$\omega = \omega_r n + \omega_{\mathrm{CEO}}. \tag{4.1}$$

This equation indicates that the resonant frequencies are a multiple of the train repetition rate, $\omega_r = 2\pi/T_r$, but shifted a quantity dependent on the phase slip, $\omega_{\mathrm{CEO}} = \Delta\varphi/T_r$. Usually, both frequencies ω_r and ω_{CEO} lie in the microwave range.
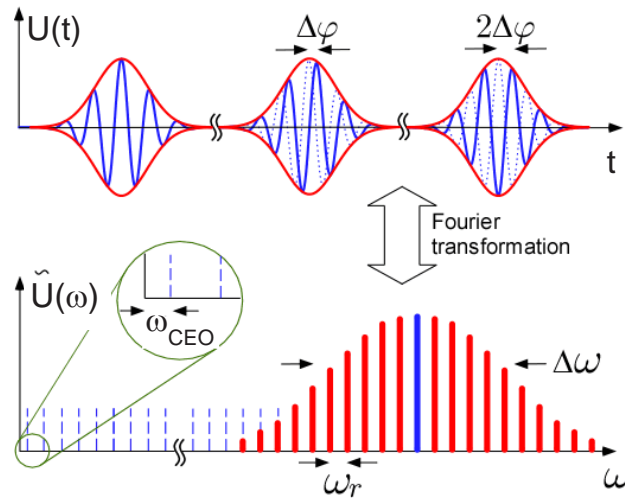

Figure 4.1: Fully coherent pulse train and its corresponding frequency comb structure. The entire comb is offset from multiple integers of the train repetition rate.

  By the SI definition of the second, a frequency is called absolute when it is referred to the ground-state hyperfine splitting of the Cs atom [11]. Since this magnitude lies in the

microwave range (9.193 GHz), it is not complicated to obtain absolute references in this region. However, before the first optical frequency comb was demonstrated, to achieve optical absolute references was a difficult task. To this end, complex chains of oscillators bridging the vast gap between the microwave and optical regions were developed [110]. This was only possible in very specific laboratories. However, Eq. (4.1) links easily both domains. Optical absolute references can be readily achieved starting from microwave absolute references to which the values of ω_r and ω_{CEO} can be locked. Therefore, once ω_r and ω_{CEO} are determined with absolute precision, the optical comb acts as a frequency ruler where every frequency is labeled and can be used for absolute frequency measurements. Any external optical frequency (determined with a precision better than the half of the repetition rate) can then be measured with absolute precision by measuring the beating with the frequency comb [12].

While ω_r is accessible with a photodiode, the frequency offset ω_{CEO} requires more clever approaches. The easiest one is to broaden the optical spectrum until it spans an octave. The low-frequency content is then doubled with a second-harmonic crystal, for example, and beaten with the upper frequency part. The lowest frequency of the beating terms gives ω_{CEO}. This self-referencing approach was first realized in [106], and the technique has been later coined as f-2f [1]. Once these frequencies are measured, an error signal can be generated to feedback the laser cavity parameters, providing the stabilization of the frequency comb. Very often the locking of ω_r and ω_{CEO} leads to a practically fully coherent pulse train. However, to have a stable pulse-to-pulse phase relation and no timing jitter does not necessarily implies complete temporal coherence. Therefore, a full coherence analysis of the pulse train deviation from the ideal case provides a deeper understanding of the dynamic behavior of frequency combs and, as last term, a different way to achieve more control parameters to feedback the cavity.

4.2   Partially coherent pulse trains

Many different stochastic phenomena that alter the ideal behavior in pulsed systems exist. When thinking of mode-locked lasers, these may be caused, e.g., by gain and length fluctuations, spontaneous emission contributions in the amplifier cavity, or by fluctuations in the microwave signal modulating the losses when the laser is actively mode-locked [111, 112]. These random noise sources contribute to degrade the correlations among the different frequency components of the pulse, which manifests as random fluctuations from pulse to pulse in shape, chirping, temporal duration, repetition rate, and energy [28, 29]. It is important to establish an analytic model to account for these random phenomena in order to measure the magnitude of the fluctuations and provide some feedback into the cavity to reduce them, whenever it is possible.

The first theories to address the stochastic behavior in ultra-short pulse trains followed the pioneer work of von derLinde [113]. This model centers on the intensity and pulse-period (timing jitter) fluctuations. A key aspect is that the information of these noise sources can be obtained from the RF spectrum of the pulse train[2], easily accessible with electrical spectrum analyzers (ESAs). This model has been proved to be very useful when

---

[2]The RF spectrum is defined as the modulus square of the temporal Fourier transform of the pulse intensity.

TABLE 4.1

Scheme of the different noise theories and their descriptions

		Noise contributions				
Reference	Theory	Timing	Energy	Phase	Shape	Cross correlations
[113]	Statistical	✓	✓	NO	NO	NO
[117, 118]	Statistical	✓	✓	NO	NO	✓
[111]	Soliton	✓	✓	NO	NO	✓
[123]	Soliton	✓	✓	✓	NO	NO
[122]	Soliton	✓	✓	✓	NO	✓
[29]	Coherence	✓	✓	✓	✓	✓

applied to a broad variety of mode-locked systems [114–116], especially actively mode-locked. Later, the model had to be complemented in view of the progress in passively mode-locked lasers [111, 117]. In these systems, the statistical correlations between jitter and field amplitude fluctuations are more notable and, further, the timing jitter may also be non-stationary [111, 117, 118]. The model of Haus and Mecozzi [111] was developed in the framework of the soliton perturbation theory [119], and special attention was paid to the possible noise sources that appear in passively mode-locked lasers. The correspondence with different experimental results is excellent [111, 112, 117, 120]. The main drawback of this theory is that since it is microscopic, it needs to be reformulated specifically for every laser system.

Nevertheless, these theories deal with timing jitter and/or amplitude fluctuations only, and the effects of pulse waveform and chirping fluctuations are not taken into account or only briefly discussed. The first approach accounting analytically for the phase fluctuations in mode-locked pulse trains is found in [121]. Similar to [119], the model is microscopic and based on perturbation of the master mode-locking equation. This model has been recently extended to include timing jitter and possible noise cross-correlations [122]. They find that the ideal frequency comb distorts and spectral broadening of the different lines in the frequency comb appears.

Here we present a theory based on optical coherence concepts [29]. Specifically, we include all the possible random fluctuations in a simple manner. We also take into account the possible statistical dependence between the noise and timing jitter, corresponding to the most general case. It represents an extension to the previous models focused on the noise of mode-locked laser systems because we consider also chirp and shape fluctuations. Since it is developed entirely in statistical terms, it is not restricted to a specific technique of mode-locking. The synergy between the experiments and the theory gives rise to the specific statistical model that characterizes the pulse train. Table 4.1 summarizes the characteristics of the different theories dealing with noise-pulse-train descriptions.

Let us denote the analytic signal of a random pulse train consisting of $2L + 1$ pulses as

$$U(t) = \exp(-i\omega_0 t) N(t) \sum_{n=-L}^{L} \psi[t - nT_r - J(t)T_r] \exp\left[i(n\omega_0 T_r - n\Delta\varphi)\right], \qquad (4.2)$$

where ω_0 is the carrier frequency, $\psi(t)$ is the complex envelope. The situation is not ideal due to the contribution of the global multiplicative noise $N(t)$, which, assuming to be a statistically stationary random process with zero a mean, describes the possible pulse-to-pulse fluctuations in a global manner. The key aspect for choosing this multiplicative noise function is that, since it is complex, it can simultaneously describe all the stochastic variations, except the timing jitter [28]. The coherence time of this function will determine the coherence time of the pulse train, i.e., how many consecutive pulses can be considered similar. In this way, although the fluctuations between the neighboring pulses may be small, when averaged among all the different possible realizations (ideally infinite), they give rise to a zero-mean field. We also point out that although the assumed stationary statistics does not correspond to the most general possible type of noise in pulse trains, it is a widely used assumption [113, 117, 118] which provides a physically valid model for many practical situations, such as free-running mode-locked lasers operating in steady-state [121, 122] or pulse trains obtained by external modulation of a continuous wave laser source [93]. Here $J(t)$ is a dimensionless real random function with zero mean, assumed to be slowly varying compared to the width of a single pulse, so that it does not cause noticeable distortions onto the pulse shapes. The envelope of the nth pulse may then be expanded in a Taylor series

$$\psi[t - nT_r - T_r J(t)] \approx \psi(t - nT_r) - T_r J(t)\dot{\psi}(t - nT_r), \tag{4.3}$$

where the dot denotes temporal derivative. With this approximation, Eq. (4.2) takes on a more compact form

$$U(t) = N(t)\exp(-i\omega_0 t)\left[M(t) - T_r J(t)\dot{M}(t)\right], \tag{4.4}$$

with

$$M(t) = \sum_{n=-L}^{L} \psi(t - nT_r)\exp\left[i(n\omega_0 T_r - n\Delta\varphi)\right]. \tag{4.5}$$

The MCF of a partially coherent pulse train can be calculated, according to Eqs. (2.6) and (4.4)

$$\Gamma(t_1, t_2) = \Gamma_{\mathrm{a}}(t_1, t_2) + \Gamma_{\mathrm{b}}(t_1, t_2) + \Gamma_{\mathrm{c}}(t_1, t_2), \tag{4.6}$$

where the MCF is given by the sum of the following terms

$$\Gamma_{\mathrm{a}}(t_1, t_2) = \Gamma_N(\tau)M^*(t_1)M(t_2)\exp(-i\omega_0\tau), \tag{4.7}$$

$$\Gamma_{\mathrm{b}}(t_1, t_2) = T_r^2 \Gamma_N(\tau)\Gamma_J(\tau)\dot{M}^*(t_1)\dot{M}(t_2)\exp(-i\omega_0\tau), \tag{4.8}$$

and

$$\Gamma_{\mathrm{c}}(t_1, t_2) = T_r^2 \dot{M}^*(t_1)\dot{M}(t_2)\left[\Gamma_{NJ}(\tau)\Gamma_{NJ}^*(-\tau) + |\Gamma_{NJ}(0)|^2\right]\exp(-i\omega_0\tau). \tag{4.9}$$

Here, we denote as $\Gamma_N(\tau) = \langle N^*(t_1)N(t_2)\rangle$ the MCF of the global multiplicative noise, and $\tau = t_2 - t_1$. We have assumed the jitter to be statistically stationary, with the corresponding MCF given by $\Gamma_J(\tau) = \langle J(t_1)J(t_2)\rangle$. Additionally, we consider that the global noise $N(t)$ and jitter $J(t)$ can be correlated, which occurs whenever these random processes are

created by the same source. This results particularly relevant for passively mode-locked lasers [111]. To achieve Eq. (4.6) we have further assumed that $N(t)$ and $J(t)$ are jointly Gaussian random processes. Basing on the central limit theorem, this assumption is physically plausible whenever there are many statistically independent sources contributing to these kind of noises [48]. Based on Eq. (2.28), we get

$$\langle N^*(t_1)N(t_2)J(t_2)\rangle = 0, \tag{4.10}$$

$$\langle N^*(t_1)N(t_2)J(t_1)\rangle = 0, \tag{4.11}$$

and

$$\begin{aligned}
\langle N^*(t_1)N(t_2)J(t_1)J(t_2)\rangle &= \langle N^*(t_1)N(t_2)\rangle\langle J(t_1)J(t_2)\rangle + \langle N^*(t_1)J(t_2)\rangle\langle J(t_1)N(t_2)\rangle \\
&\quad + \langle N^*(t_1)J(t_1)\rangle\langle J(t_2)N(t_2)\rangle \\
&= \Gamma_N(\tau)\Gamma_J(\tau) + \Gamma_{NJ}(\tau)\Gamma_{NJ}^*(-\tau) + |\Gamma_{NJ}(0)|^2, \tag{4.12}
\end{aligned}$$

which leads to Eqs. (4.6)–(4.9). Mathematically, Eq. (4.6) contains the contribution of three different terms. The first one corresponds to the MCF of a pulse train affected of global multiplicative noise only. The second term mainly contains the timing jitter contribution, whereas the last term deals with the cross-correlation between timing jitter and the multiplicative noise.

From Eq. (4.6) it is possible to calculate the averaged intensity as

$$I(t) = I_a(t) + I_b(t) + I_c(t), \tag{4.13}$$

where

$$I_a(t) = \Gamma_a(t,t) = \Gamma_N(0)\left|M(t)\right|^2, \tag{4.14}$$

$$I_b(t) = \Gamma_b(t,t) = T_r^2\Gamma_N(0)\Gamma_J(0)|\dot{M}(t)|^2, \tag{4.15}$$

and

$$I_c(t) = \Gamma_c(t,t) = 2T_r^2|\Gamma_{NJ}(0)\dot{M}(t)|^2. \tag{4.16}$$

It is important to note that the global noise $N(t)$ does not affect the averaged intensity, which perfectly fits with the frequency-domain independent-elementary-pulse representation model developed in the previous chapter. According to Eqs. (4.15) and (4.16), the timing jitter contributes to enhance the averaged intensity. Physically, this is due to the contribution of arbitrarily delayed (or advanced) pulses on the averaged measurement.

In order to illustrate these effects on the MCF, we plot in Fig. 4.2 (a) the absolute value of the MCF given by Eq. (4.6) and (b) the absolute value of the corresponding complex degree of coherence (Eq. 2.8) for a train of Gaussian pulses with 10 ps rms intensity width, 15 GHz repetition rate ($T_r = 60\,\text{ps}$), and $\omega_0 T_r - \Delta\varphi = 0$. The noise coherence function is chosen to be of a monotonically decreasing Gaussian form, $\Gamma_N(\tau) = \exp(-\tau^2/2t_{\text{cn}}^2)$, with a coherence time $t_{\text{cn}} = 100$ ps. Compared with the period of the pulse train, this value establishes that the pulses are rapidly varying from one to another. The parameters for the jitter are $\Gamma_J(\tau) = \alpha\exp(-\tau^2/2t_{\text{cj}}^2)$, with a jitter coherence time of $t_{\text{cj}} = 20$ ps and the coefficient α, determining the strength of the jitter, chosen as $\alpha = 0.01$, which represents a 10% deviation from the temporal period. The noise–jitter correlation function

$\Gamma_{NJ}(\tau) = \beta \exp(-\tau^2/2t_{\mathrm{cnj}}^2)$ has a coherence time of $t_{\mathrm{cnj}} = 80$ ps and the parameter describing the strength of the noise–jitter correlation is chosen to have a relatively high value, $\beta = 0.05$. Due to the global multiplicative noise, it can be seen from the figures that as the difference between the considered time instants t_1 and t_2 increases, the pulses become temporally uncorrelated, and the complex degree of coherence depends on the exact time instants considered. Finally, due to the dependence between the noise and the jitter, some local correlations over the whole temporal range, which can be seen from Eq. (4.9), appear.
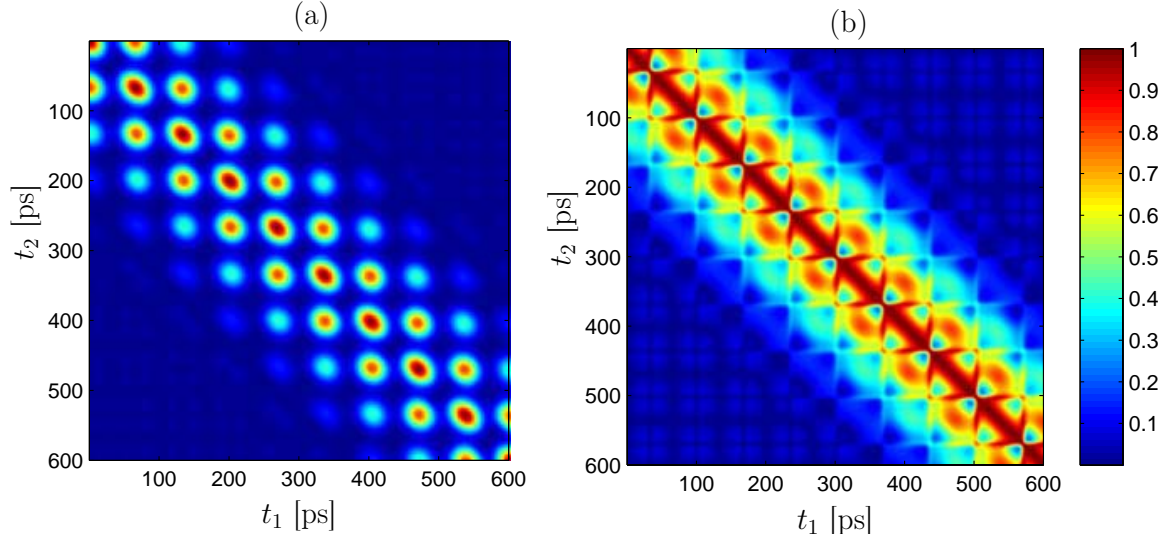

Figure 4.2: (a) Modulus of the MCF function of a partially coherent pulse train; (b) corresponding modulus of the complex degree of coherence. See text for particular settings.

From the MCF of the partially coherent pulse train, we can calculate the ES

$$S(\omega) = S_{\mathrm{a}}(\Omega) + S_{\mathrm{b}}(\Omega) + S_{\mathrm{c}}(\Omega), \tag{4.17}$$

where

$$S_{\mathrm{a}}(\Omega) = W_N(\Omega) \otimes |\tilde{M}(\Omega)|^2, \tag{4.18}$$

$$S_{\mathrm{b}}(\Omega) = (T_r\Omega)^2 \, |\tilde{M}(\Omega)|^2 \otimes W_J(\Omega) \otimes W_N(\Omega), \tag{4.19}$$

and

$$S_{\mathrm{c}}(\Omega) = (T_r\Omega)^2 \, |\tilde{M}(\Omega)|^2 \otimes \left\{ \delta(\Omega) \, |\Gamma_{NJ}(0)|^2 + W_{NJ}(\Omega) \otimes W_{NJ}^*(\Omega) \right\}. \tag{4.20}$$

Here, $\Omega = \omega - \omega_0$, and $\tilde{M}(\Omega)$, $W_N(\Omega)$, $W_J(\Omega)$, and $W_{NJ}(\Omega)$ denote the Fourier transform of $M(t)$, $\Gamma_N(\tau)$, $\Gamma_J(\tau)$, and $\Gamma_{NJ}(\tau)$, respectively.

In the limit $L \to \infty$, we achieve $\tilde{M}(\Omega) = \sum_n \delta(\Omega - n\omega_r - \omega_{\mathrm{CEO}})$. Thus, we have a comb structure but significantly modified. There appear spectral lines equally spaced by an amount corresponding to the frequency repetition rate of the pulse train and offset

by the same quantity as in the coherent case. However, according to Eq. (4.18), the global noise $N(t)$ contributes to broaden every spectral line, and this line shape effectively corresponds to the ES of the stationary noise, $W_N(\Omega)$. This line broadening has also been predicted on the framework of perturbation theories [123] and experimentally verified by several laboratories for fiber [124] and diode lasers [125]. According to Eq. (2.9), the coherence time of the pulse train can be obtained as the inverse of the line spectral width. Timing jitter distorts the comb for higher Ω components. However, for higher frequencies, there is a competition with the available energy limited by the pulse envelope. This result is mathematically similar to the distortions achieved in the RF spectrum predicted by von derLinde [113]. Additionally we find that the timing jitter does not affect the distortion of the central line. This result has been also predicted in the framework of the soliton perturbation theory [122]. Further, according to Eq. (4.20), we predict the appearance of spikes due to the possible cross correlation between the jitter and global noise. These spikes are proportionally higher for stronger cross correlations. We also note the mathematical similarity with the model developed in [117], who predicted the appearance of spikes in the RF spectrum of passively mode-locked lasers due to the correlation between the timing jitter and the amplitude noise.
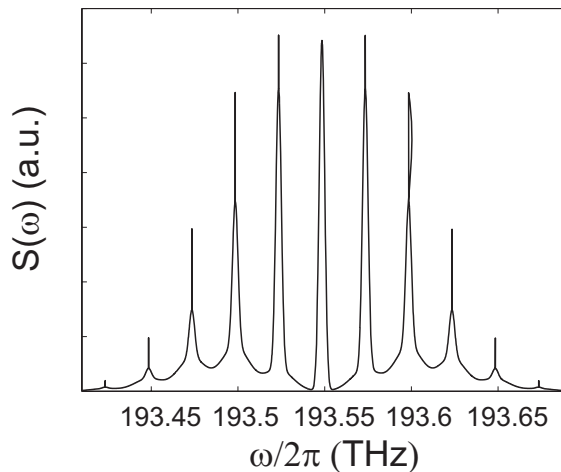

Figure 4.3: Energy spectrum (linear scale) of a pulse train affected of noise and timing jitter. See text for setting details.

We numerically illustrate the above features in Fig. 4.3, where we plot the ES of a train of 3 ps rms Gaussian pulses at 25 GHz repetition rate affected by a stationary timing jitter and noise. The ES of W_N, W_J and W_{JN} are assumed Gaussian. The coherence times of the noise and the jitter are 100 and 20 ps, respectively, and the coherence time of the correlations between the jitter and noise is 80 ps. The main frequency corresponds to 1.55μm and we have also selected $\omega_0 T_r - \Delta\varphi = 0$.

Finally, we have studied the CSDF corresponding to the MCF given by Eq. (4.6) and found the result that two frequencies are fully uncorrelated unless they differ a integral multiple of the repetition rate.

Linear distortion in dispersive media. Temporal optics

This Chapter introduces the fundamental equations describing the linear distortion of an ultrashort light pulse in a dispersive homogeneous medium. Such a basic physical problem is the cornerstone of ultrafast optical signal processing.

In this direction, the space–time analogy [126] establishes a fundamental link between the paraxial diffraction of monochromatic one-dimensional (1D) beams and the linear distortion of plane-wave pulses in first-order dispersive media. This approach has led to the achievement of several optoelectronic configurations particularly relevant in the optical communications field [16]. The field of optical pulse processing based on the space–time analogy is referred as temporal optics [127].

5.1 Pulse distortion in a linear homogeneous medium

Let us assume a scalar optical field, described by its analytic signal $U(\mathbf{r}, t')$, propagating linearly in a waveguide with translational symmetry through the propagation direction z and filled with an homogeneous lossless dispersive medium. The propagation constant is $\beta(\omega') = n(\omega')\omega'/c$, where c is the speed of light in vacuum and $n(\omega')$ the frequency-dependent refractive index. We can then write [17]

$$U(\mathbf{r}, t') = A(x, y)\psi(z, t') \exp[-i(\omega_0 t' - \beta_0 z)]. \tag{5.1}$$

Here, $\psi(z, t')$ is the pulse envelope, which modulates the monochromatic carrier wave of angular frequency ω_0; the constant $\beta_0 = \beta(\omega_0)$; and $A(x, y)$ is the transversal spatial distribution of the mode, evaluated at ω_0. Once $A(x, y)$ is calculated, we only require to know $\psi(z, t')$ in order to determine $U(\mathbf{r}, t')$ at every z position. The evolution of $\psi(z, t')$ is described by a wave equation.

Since the functional form of $\beta(\omega')$ is usually unknown, it is very useful to perform a Taylor expansion [17]

$$\beta(\omega') = \beta_0 + \beta_1(\omega' - \omega_0) + \frac{\beta_2}{2!}(\omega' - \omega_0)^2 + \frac{\beta_3}{3!}(\omega' - \omega_0)^3 + ..., \tag{5.2}$$

where $\beta_n = \mathrm{d}^n\beta(\omega')/\mathrm{d}\omega'^n|_{\omega'=\omega_0}$ are the nth-order dispersion coefficients of the waveguide, with $n = 0, 1, 2....$ From now on, we will express the temporal variations of the pulse in a reference framework moving at the group velocity of the wave packet, $t = t' - \beta_1 z$.

The wave equation describing the envelope distortion is of second order in z. In order to reduce this equation to first order, the slowly varying envelope approximation (SVEA) is usually invoked in the multi-cycle regime [17, 126]. This approximation requires first, that function $\psi(z, t)$ does not change significantly through a distance compared with the carrier wavelength, and second, the pulse duration to be much larger than the carrier oscillation period. Mathematically, it is translated into $|\partial\psi(z, t)/\partial z| << \beta_0|\psi(z, t)|$ and $|\partial\psi(z, t)/\partial t| << \omega_0|\psi(z, t)|$. Both inequalities are guaranteed whenever the optical frequency bandwidth is much less than the central frequency, $\Delta\omega << \omega_0$ [128].

Within the SVEA we have

$$i\frac{\partial\psi(z, t)}{\partial z} = H\psi(z, t), \tag{5.3}$$

where the hamiltonian operator is $H = -\sum_{n=2}^{\infty}\frac{i^n\beta_n}{n!}\frac{\partial^n}{\partial t^n}$. Alternatively, Eq. (5.3) can be rewritten in the frequency domain just by Fourier transformation,[1]

$$i\frac{\partial\tilde{\psi}(z, \omega)}{\partial z} = \tilde{H}\tilde{\psi}(z, \omega), \tag{5.4}$$

where $\tilde{\psi}(z, \omega)$ is the Fourier transform of $\psi(z, t)$, and $\tilde{H} = -\sum_{n=2}^{\infty}\frac{\beta_n}{n!}\omega^n$. This equation can be easily integrated

$$\tilde{\psi}(z, \omega) = \exp\left[i\sum_{n=2}^{\infty}\frac{\beta_n z}{n!}\omega^n\right]\tilde{\psi}(0, \omega). \tag{5.5}$$

Therefore, the dispersive medium acts as a phase-only spectral filter. Sometimes it is useful to write the dispersive terms in the more compact form $\Phi_n = \beta_n z$. In the case $n = 2$, β_2 is called the group-velocity-dispersion (GVD) coefficient, and Φ_2 the group-delay-dispersion (GDD) parameter.

In the few-cycle regime, SVEA results a rough approximation. In this case, an alternative method to achieve a first-order equation in z is the slowly evolving wave approximation [128]. However, the pulse durations used in this Thesis are suited in the multi-cycle regime, and the SVEA constitutes a fairly good approximation.

5.2 First-order approximation. Space–Time analogy

We are particularly interested in the case in which only the first term from Eq. (5.3) contributes,

$$i\frac{\partial\psi(z, t)}{\partial z} = \frac{\beta_2}{2}\frac{\partial^2\psi(z, t)}{\partial t^2}. \tag{5.6}$$

Since it implies a second-order expansion in Eq. (5.2), the medium is said to be parabolic. The first-order approximation is physically plausible whenever $\Delta\omega << 3|\beta_2/\beta_3|$. As an example, for standard single-mode fiber (SMF) and a waveform centered in the telecommunication wavelength ($\lambda_0 = 1.55\,\mu m$), the fiber coefficients are $\beta_2 = -21.68\,\text{ps}^2/\text{km}$

---

[1]In the following, the angular frequencies ω are referred at the baseband. They are related to the optical ones, ω', just by a shift equal to the carrier frequency, $\omega' = \omega + \omega_0$.

TABLE 5.1

Transfer rules connecting space and time domains

Space domain		Time domain	
position	x	t	proper time
spatial frequency	$2\pi u$	ω	angular frequency
wavenumber^{-1}	$1/k_0$	$-\beta_2$	GVD coefficient
paraxial propagation	$\exp\left(-i2\pi^2 zu^2/k_0\right)$	$\exp(i\Phi_2\omega^2/2)$	1st-order dispersion
spatial lens	$\exp\left(-i\frac{k_0 x^2}{2f}\right)$	$\exp(iKt^2/2)$	time lens

and $\beta_3 = 0.127\,\text{ps}^3/\text{km}$. The pulses should then have an optical bandwidth shorter than 80 THz. If we assume a coherent Gaussian pulse and require the above inequality to be satisfied for a 50 times shorter bandwidth, Eq. (5.6) would be valid for pulses longer than 275 fs full-width-at-half-maximum (FWHM) intensity duration.

Equation (5.6) is a Schrödinger-like equation for a free particle, present in many physical problems. In particular, this equation is mathematically identical to that describing the one-dimensional scalar diffraction of a paraxial monochromatic beam propagating in the z direction [129]

$$i\frac{\partial U_e(z,x)}{\partial z} = -\frac{1}{2k_0}\frac{\partial^2 U_e(z,x)}{\partial x^2}, \tag{5.7}$$

where $U_e(z,x)$ denotes the transversal profile of the 1D beam, and k_0 the wavenumber.

The mathematical similarity between Eqs. (5.6) and (5.7) has been known in the literature as space–time analogy. The key is that it allows the transfer of knowledge from one domain to the other. Since paraxial diffractive optics is a relatively well-established matter [129], this transfer has been usually performed from the spatial to the temporal domain [16]. Table 5.1 summarizes the transfer rules connecting both domains.

It seems that this finding was independently discovered by Akhmanov *et al.* [130], and Treacy [131] at the end of the 60's. While in the 80's there appeared some theoretical contributions based on this analogy [82, 132], it was not until the relevant works of Kolner on temporal lenses and temporal imaging systems (TISs) [14, 133] that this analogy reemerged with all its splendor.

5.3 Temporal ABCD matrix approach

The action of any linear system on the input complex envelope, $\psi_{\text{in}}(t)$, can always be written as

$$\psi_{\text{out}}(t) = \int \psi_{\text{in}}(t')K(t,t')\text{d}t', \tag{5.8}$$

where the system is described mathematically by the kernel $K(t,t')$, and $\psi_{\text{out}}(t)$ denotes the output complex envelope.

In the framework of the space–time analogy, the ABCD matrix method [134] has been verified as a powerful tool to describe those linear systems composed by cascading different quadratic elements [135, 136]. Here, the global system is characterized by a

2×2 matrix resulting from multiplying the matrix of every individual element in the appropriate order. This formalism was first adapted to the temporal domain in [135] and has been used to study actively mode-locked laser systems [136]. The kernel of an ABCD system is [137–139]

$$K(t,t') = \begin{cases} \sqrt{\frac{i}{2\pi B}} \exp\left[\frac{-i}{2B}(At'^2 + Dt^2 - 2tt')\right] & \text{if} \quad B \neq 0 \\ \sqrt{\frac{1}{A}} \exp\left[\frac{-iCt^2}{2A}\right] \delta(t' - t/A) & \text{if} \quad B = 0 \end{cases} \tag{5.9}$$

where A, B, C, and D denote the matrix coefficients. Due to the quadratic dependence of the exponential term, these linear systems are also known as Gaussian.

Let us now describe the matrix of some of the basic elements commonly employed in temporal optics.

5.3.1   Temporal lens

This element introduces a quadratic phase modulation on the input complex envelope, $\psi_{\text{out}}(t) = \exp[iKt^2/2]\psi_{\text{in}}(t)$. The effect of this quadratic modulation, or chirp, is fully analog to the action of a lens on a spatial beam. The real constant K determines the strength of the chirping. The corresponding matrix of this optical element is

$$\begin{pmatrix} A & B \\ C & D \end{pmatrix} = \begin{pmatrix} 1 & 0 \\ -K & 1 \end{pmatrix} \tag{5.10}$$

In practical terms, this operation can be implemented with electro-optic phase modulators (EOPMs) [133]; self- or cross-phase modulation (XPM) in a nonlinear fiber [140]; or with a DST pulse shaper [141]. For convenience, we are going to detail the EOPM and XPM implementations.

An EOPM is usually built with a nonlinear crystal having a high electrooptic coefficient, such as $LiNbO_3$ [126]. By applying an electrical signal on the crystal, the optical field propagating through acquires a phase proportional to the applied voltage. If the electrical field is just composed by a single-tone RF waveform, we have $\psi_{\text{out}}(t) = \exp[i\Delta\theta \cos(2\pi f_r t)]\psi_{\text{in}}(t)$, where $\Delta\theta$ is a real constant, called the modulation index, and f_r the frequency of the electrical waveform. Note that $\Delta\theta$ groups different factors depending on the crystal parameters and the maximum voltage amplitude. We have assumed the optical pulse to be synchronized with the maximum of the RF signal. If the temporal pulse width is shorter than the period, we can approximate $\psi_{\text{out}}(t) \approx \exp[i\Delta\theta] \exp[-i2\Delta\theta\pi^2 f_r^2 t^2]\psi_{\text{in}}(t)$. Then, by direct inspection we obtain $K = -4\Delta\theta\pi^2 f_r^2$.

Alternatively, a temporal lens can be achieved with a nonlinear fiber, in virtue of the XPM effect [17]. In this case, a pump signal with normalized intensity $I_p(t)$ is launched collinearly with the signal $\psi_{\text{in}}(t)$. For an adequate implementation, pump and signal should be synchronized and have nonoverlapping spectra or crossed polarization states. Then, by neglecting the dispersion in the non-linear interaction, the output complex envelope corresponding to the signal becomes $\psi_{\text{out}}(t) = \exp[i2\gamma LP_{\text{pump}}I_p(t)]\psi_{\text{in}}(t)$, where γ is the nonlinear coefficient per unit of length corresponding to the pump wavelength, P_{pump} the peak power of the pump signal, and L the fiber length. If we further consider

Gaussian intensity distribution for the pump pulse and a width larger than the signal duration, we can approximate $\psi_{\text{out}}(t) \approx \exp[i\frac{\gamma LP_{\text{pump}}t^2}{4\sigma_p^2}]\psi_{\text{in}}(t)$, where σ_p is the pump's rms intensity width. This leads to $K = \gamma LP_{\text{pump}}/(2\sigma_p^2)$. For a better performance of the XPM effect, parabolic pump pulses could be employed [142] instead.

Finally it should be reminded that in the spatial case, a spherical wavefront is obtained by diffracting the light emerging from a punctual monochromatic source [129]. This phenomenon has been analyzed in the temporal domain too [143, 144], and provided an alternative way to achieve temporal quadratic phase modulations just by launching ultra-short pulses through a dispersive medium [145].

5.3.2 Temporal Gaussian modulator

This devices filters an input signal in the temporal domain, so that the output pulse envelope is given by $\psi_{\text{out}}(t) = \exp[-\Gamma^2 t^2/2]\psi_{\text{in}}(t)$, where Γ^{-1} is a real constant related to the gate duration. The matrix associated with this element is

$$\begin{pmatrix} A & B \\ C & D \end{pmatrix} = \begin{pmatrix} 1 & 0 \\ -i\Gamma^2 & 1 \end{pmatrix} \tag{5.11}$$

This action can be readily achieved with an amplitude modulator with transform-limited Gaussian pulse modulation, like a dual-drive Mach-Zehnder modulator (MZM) [136].

5.3.3 GDD circuit

These elements are designed to achieve a quadratic phase modulation in the spectral domain, i.e., $\tilde{\psi}_{\text{out}}(\omega) = \exp[i\Phi_2\omega^2/2]\tilde{\psi}_{\text{in}}(\omega)$. Here, Φ_2 is the GDD coefficient. The matrix is

$$\begin{pmatrix} A & B \\ C & D \end{pmatrix} = \begin{pmatrix} 1 & \Phi_2 \\ 0 & 1 \end{pmatrix} \tag{5.12}$$

The most popular element is an SMF, whenever the third-order-dispersion (TOD) co-efficient can be neglected. GDD circuits can also be implemented with a dispersion compensating fiber (DCF) [77]; pairs of prisms [146]; diffraction gratings [131]; a spatial light modulator in a Fourier transform geometry with a specific phase-only profile [147]; specially designed linearly chirped fiber gratings (LCFGs) [148]; or photonic crystal fibers (PCFs) [149, 150]. A GDD circuit is fully equivalent to the action of the paraxial diffraction in free space [131, 135].

5.3.4 Spectral Gaussian filter

Such a device filters spectrally the complex field envelope as $\tilde{\psi}_{\text{out}}(\omega) = \exp[-\omega^2\Delta^2/2]\tilde{\psi}_{\text{in}}(\omega)$. In this case the corresponding matrix is

$$\begin{pmatrix} A & B \\ C & D \end{pmatrix} = \begin{pmatrix} 1 & i\Delta^2 \\ 0 & 1 \end{pmatrix} \tag{5.13}$$

Here, the real coefficient Δ^{-1} is a measure of the spectral width of the bandpass. These filters may be implemented with all-fiber devices, such as conveniently apodized Bragg gratings [136].

In the spatial domain, the action of this matrix is equivalent to place a Gaussian spatial filter at the focal plane of a 4f processing system.

5.3.5   General properties

An interesting property of Gaussian systems is that they can be described in terms of three equivalent elements: a temporal lens, a scaling system and a GDD circuit. This property is due to the fact that the elementary matrices of the constituting devices are unitary, so that any ABCD matrix can be factorized, for example, as [138]

$$\begin{pmatrix} A & B \\ C & D \end{pmatrix} = \begin{pmatrix} 1 & 0 \\ C/A & 1 \end{pmatrix} \begin{pmatrix} A & 0 \\ 0 & 1/A \end{pmatrix} \begin{pmatrix} 1 & B/A \\ 0 & 1 \end{pmatrix} \tag{5.14}$$

where the relation $AD - BC = 1$ has been used [134]. This unitary relation is only true for lossless ABCD systems. In that case, the elements described at Sects. 5.3.2 and 5.3.4 could not be used.

However, there are many other interesting characteristics that can be extracted by simple inspection of the elements of the global matrix [134]. For example, any system satisfying $B = 0$ conjugates the input and output planes, so that the output intensity profile constitutes a scaled replica of the input one, where the scale factor is given by the matrix coefficient A. When an ABCD matrix verifies $A = 0$, the system behaves as a frequency-to-time converter, i.e., the output intensity profile is a scaled version of the input ES, with the scale factor given by the coefficient B. When $C = 0$, the system is afocal.

5.4   Dual ABCD matrix approach

In temporal optics, there are some situations in which the Fourier transform of the envelope, $\tilde{\psi}(\omega)$, may be the physical magnitude of interest, rather than $\psi(t)$. Of course, they are connected to each other by a Fourier transform relation and both carry the same quantity of information.

Since any linear system in time is linear in frequency too, it is useful to provide a similar analysis of Eqs. (5.8) and (5.9) in the dual space. In the spectral domain, a temporal lens is the dual element of the GDD circuit, and the temporal Gaussian filter is the dual element of the spectral Gaussian filter [151]. By dual we mean that these devices behave mathematically identical, but their action is performed in the Fourier domain [152].

Because of linearity, we can always write

$$\tilde{\psi}_{\text{out}}(\omega) = \int \tilde{\psi}_{\text{in}}(\omega') \tilde{K}(\omega, \omega') \mathrm{d}\omega', \tag{5.15}$$

where

$$\tilde{K}(\omega, \omega') = \iint K(t', t'') \exp[i(\omega t' - \omega' t'')] \mathrm{d}t' \mathrm{d}t''. \tag{5.16}$$

In the case of a Gaussian system, by complete similarity with Eq. (5.8), we write

$$\tilde{K}(\omega, \omega') = \begin{cases} \sqrt{\frac{i}{2\pi B_\omega}} \exp\left[\frac{-i}{2B_\omega}(A_\omega \omega'^2 + D_\omega \omega^2 - 2\omega\omega')\right] & \text{if} \quad B_\omega \neq 0 \\ \sqrt{\frac{1}{A_\omega}} \exp\left[\frac{-iC_\omega \omega^2}{2A_\omega}\right] \delta(\omega' - \omega/A_\omega) & \text{if} \quad B_\omega = 0 \end{cases} \tag{5.17}$$

Here, $\{ABCD\}_\omega$ are the elements of the dual ABCD matrix system. These coefficients are not independent of the temporal ones. Their relationship is found by substituting Eq. (5.9) into Eq. (5.16) and comparing the result with Eq. (5.17), we get

$$\begin{pmatrix} A_\omega & B_\omega \\ C_\omega & D_\omega \end{pmatrix} = \begin{pmatrix} A & B \\ C & D \end{pmatrix}^{-1} = \begin{pmatrix} D & -C \\ -B & A \end{pmatrix} \tag{5.18}$$

This implies that the spectral ABCD matrix is just the inverse of the temporal one.

Mathematically, this dual analysis does not provide additional information. However, it is useful to recognize that any afocal system ($C = 0$) behaves as a spectral imaging system ($B_\omega = 0$), that is to say, the output ES is a scaled version of the input one. The scale factor will be given by the coefficient A_ω. Additionally, any system satisfying $A_\omega = 0$ corresponds to a time-to-frequency converter [153], i.e., the output ES is a scaled replica of the input temporal intensity profile. The scale factor is given by B_ω. Finally, we can easily set the requirement to have both, a temporal and spectral imaging system as $B = C = 0$. We then recover the well-known result that any scaling system produces an image in the complex field.

5.5 Some coherent ultra-high-speed optical systems

The space–time analogy has been recognized as a powerful tool for designing analog ultrafast pulse processors [16]. In this section we shall describe a few of the interesting ones for the purposes of this Thesis.

5.5.1 Real-time Fourier transformer (RTFT)

RTFTs are optical devices capable to modify the light intensity profile of an ultrashort light pulse so that the achieved shape becomes a scaled version of the input coherent ES. Two main approaches are proposed for this aim.

TEMPORAL LENS + GDD CIRCUIT

This system was originally proposed by Jannson [154], and corresponds to the temporal counterpart of the classic Fourier transformer constituted by a spatial lens and diffraction until the focal length [129], as shown in Fig. 5.1.
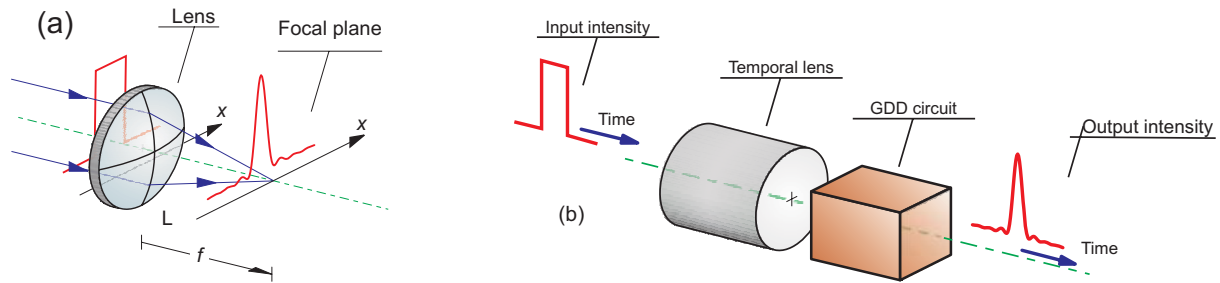

Figure 5.1: (a) spatial and (b) temporal Fourier transformer.

Using the ABCD temporal matrix approach, one calculates the matrix corresponding to the device shown in Fig. 5.1 and, by imposing $A = 0$, obtains that the chirp rate and the

GDD coefficient must satisfy $\Phi_2 K = 1$. This device can be used for measuring ES profiles in the time-domain, where the scale is fixed by the GDD parameter. The advantage of using this apparently more complicated configuration instead of an optical spectrum analyzer (OSA) is the acquisition speed. Common OSAs have a limited speed because of the mechanical sweeping elements. However, RTFTs capture the ES information in the time domain, which can be done at rates beyond MHz with current sampling oscilloscopes.

Alternatively, this device can be used to compress ultrashort pulses. In this case, the temporal width can be tuned by a proper selection of the temporal chirp and the GDD parameter. Nevertheless, the most important characteristic of this device is that the output intensity pulse is a scaled version of the ES independently of the input spectral phase. This feature has provided the key to compensate for the spectral phase distortions in ultra-high speed optical time-division multiplexing (OTDM) linear systems [142, 155].

TEMPORAL FAR-FIELD. GDD CIRCUIT

In order to achieve an RTFT, the temporal lens is not really required. In the spatial domain, it is well-known that the diffraction pattern achieved at a certain distance away from an input object, usually called the far-field distance, coalesces with the (modulus of the) Fourier transform of the object. In the temporal domain, this effect was first discovered in [156], but the connection with the the far-field condition, or Fraunhofer regime, was realized later [148, 157, 158]. In the temporal domain, this condition reads as [157]

$$\Phi_2 >> \sigma^2/(4\pi), \tag{5.19}$$

where σ is a measure of the input pulse width. When this condition is satisfied, the output intensity shape becomes a scaled replica of the input ES too. As in the previous case, the scaling factor is also given by the GDD coefficient. In general, the exact amount
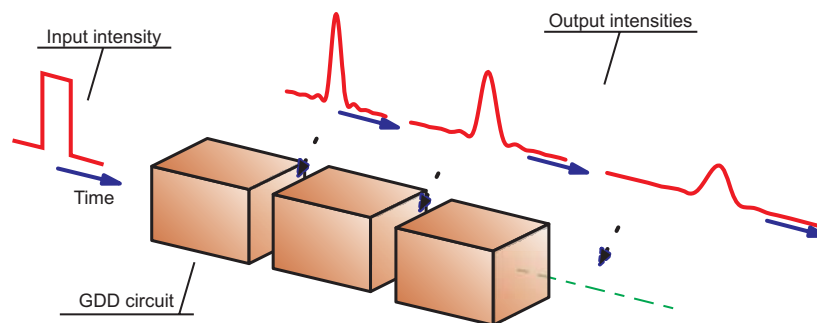

Figure 5.2: Sketch of temporal far field with a GDD circuit.

of dispersion to reach the far-field depends on the specific input pulse waveform, and Eq. (5.19) is then just a simple estimation. As sketched in Fig. 5.2, once the temporal far-field condition is practically satisfied, by adding larger dispersion amounts, the output intensity profile does not change its shape, only its scale. This means that this specific RTFT has the advantage of resolution tunability just by adding larger GDD amounts. The upper limit is just limited by absorption in the fiber and by the noise-floor level of the photodiode [159]. This has lead to the development of real-time spectroscopy [159–162]

and ultrahigh-speed optical OCT [163], where eventually highly varying spectra can be recorded in real time. Additionally, RTFTs can be used for time-domain spectral filtering in simplified 4f temporal processors [164–166].

5.5.2　Time-to-frequency converters

A time-to-frequency converter is a device operating over an incoming ultrashort pulse in such a way that the shape of the output ES is a scaled version of the input temporal intensity [153]. in this way such a device constitutes a viable alternative to measure temporal intensity waveforms with a simple OSA. It corresponds to the dual optoelectronic configuration presented at the previous section. Similarly, there are two different approaches to achieve this operation.

GDD circuit + Time lens

A time-to-frequency has a corresponding matrix whose spectral element $A_\omega = 0$. The simplest device to achieve this operation is presented in Fig. 5.3(a). Therefore, it is easy to show that the time lens and GDD parameter must satisfy the same condition as for a RTFT. However, note that the elements are disposed in reverse order. This configuration was first proposed in [153], where the time lens was implemented with an EOPM. Later, this configuration was implemented for pulses with a central wavelength centered on 800 nm, for which the time lens was implemented with sum-frequency generation [167].
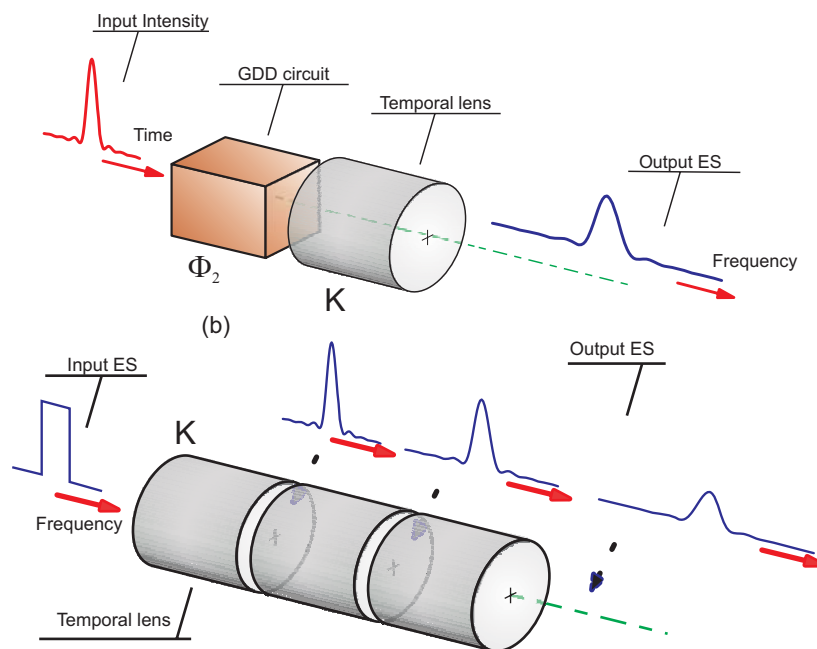

Figure 5.3: Sketch of the two different temporal devices to achieve a time-to-frequency converter (a) full configuration (b) spectral Fraunhofer-based device.

Spectral far-field. Time lens

By recalling that a time lens corresponds to the dual device of GDD circuit, it is straight-forward to note that a Fraunhofer regime also exists in the spectral domain [151]. This provides a route to achieve a simplified version of the previous time-to-frequency convert-ers by removing the input GDD parameter, as shown in Fig. 5.3(b), as long as the input pulse satisfies

$$K >> \Delta\omega^2/(4\pi), \tag{5.20}$$

where $\Delta\omega$ is a measure of the input spectral width of the pulse.

As a remark, in the same way as an RTFT implemented with a time lens + GDD circuit is independent of the spectral phase of the input light pulse, the time-to-frequency converter corresponding to Fig. 5.3(a) performs the operation independently of the input temporal phase of the pulse. Therefore, unlike the device showed in Fig. 5.3(b), the first family of time-to-frequency converters results ideal for operating with input phase fluctuating light pulses [168].

5.5.3 TIS

TISs are photonic devices that provide a scaled replica of the intensity distribution of an input short optical pulse [133]. When designed for magnifying, the output pulse duration becomes large enough to overcome the limited temporal resolution of current fast photode-tectors, acting as a temporal microscope for femtosecond waveforms [169]. Alternatively, TISs can also be applied for pulse compression while maintaining the initial intensity profile [170]. Due to the possibility to engineer the magnification factor to be negative, TISs have also been proposed for the creation of anti-correlated biphotons [171] or for compensating for the TOD effect in WDM systems [172]. The basic TIS configuration is sketched in Fig. 5.4, where two first-order dispersive elements are employed. The spatial counterpart is also sketched for comparison. The temporal imaging condition establishes a link among the chirp of the temporal lens and the GDD parameters. By calculating the ABCD matrix corresponding to the Gaussian system of Fig. 5.4(b) and imposing $B = 0$, we obtain

$$\frac{1}{\Phi_{21}} + \frac{1}{\Phi_{22}} = K. \tag{5.21}$$

The magnifying factor, m, is given by the matrix coefficient A, which under the above constraints results $m = -\Phi_{22}/\Phi_{21}$.

It should be noted that a simplified version of the system shown in Fig. 5.4(b) has also been demonstrated [173, 174], where the use of the first GDD is avoided.

5.5.4 Spectral imaging system (SIS)

We have stated in Sect. 5.4 that every temporal afocal ABCD Gaussian system behaves as an imaging system in the spectral domain, i.e., the output ES is a scaled version of the input one. The simplest temporal afocal system ($B_\omega = C = 0$) is illustrated in Fig. 5.5, where the system parameters are related through the equation

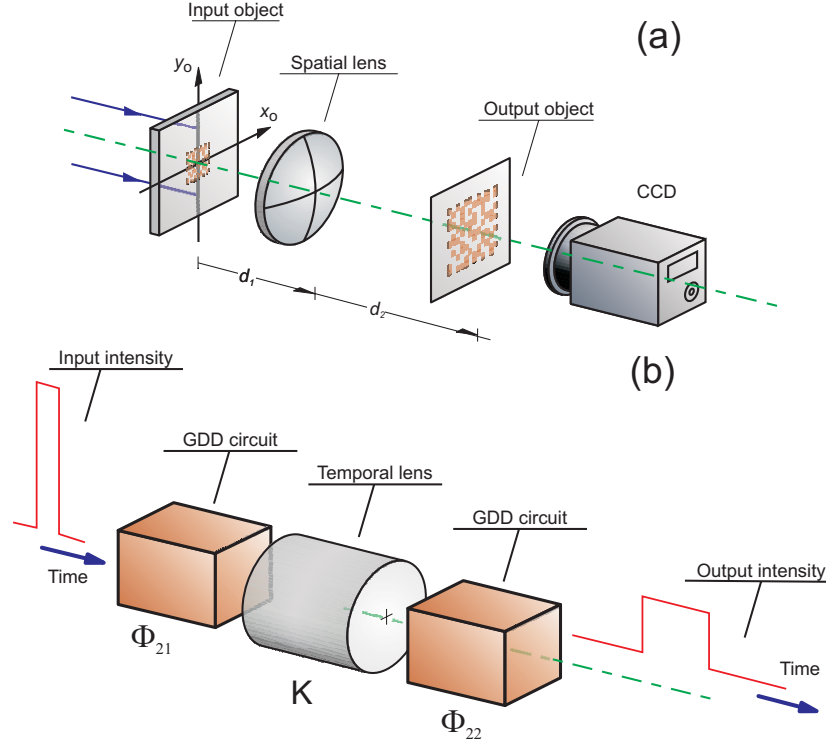$$\frac{1}{K_1} + \frac{1}{K_2} = \Phi_2. \tag{5.22}$$

Figure 5.4: Sketch of a basic (a) spatial and (b) temporal imaging system.

It is easy to note that such a configuration constitutes the dual system of the TIS of Fig. 5.4(b). In this case, the output spectral envelope is given by [31]

$$\psi_{\text{out}}(\omega) = \frac{1}{\sqrt{m_\omega}} \exp\left[i\frac{1}{2}a\omega^2\right] \psi_{\text{in}}\left(\frac{\omega}{m_\omega}\right), \qquad (5.23)$$

where $a = \Phi_2/m_\omega$ and the coefficient

$$m_\omega = 1 - \Phi_2 K_2 \qquad (5.24)$$

is the spectral scaling factor. If the system is designed for $|m_\omega| > 1$, the output ES is expanded (spectral microscope), whereas for $|m_\omega| < 1$, we have spectral compression. Another interesting feature is the fact that m_ω can be designed to be negative, which can be relevant for spectroscopy applications when input asymmetrical spectra are considered. It is important to note that Eq. (5.23) applies for both, single optical pulses and trains of finite duration, provided the time lenses operate over the complete sequence. Consequently, the proposed system does not allow the rescaling of a whole frequency comb (infinite input sequence), since it would require unreachable time lenses. However, since the proposed system is capable of rescaling the ES of every single pulse in a train, it will permit to enhance the number of lines of frequency combs (while keeping the spacing). This could provide significant advances in dense-WDM (D-WDM) systems [94] or high-resolution waveform processing [93], where it is necessary to have a large number of spectral lines.
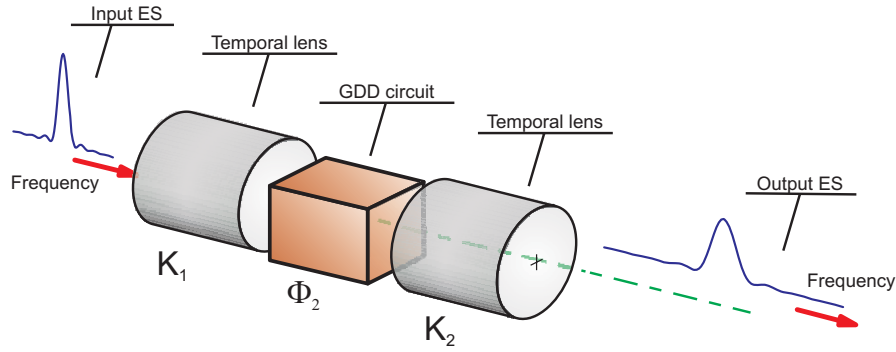
Figure 5.5: Sketch of a basic spectral imaging system.

It is important to note that these features are not achievable with a TIS because in this case, the scale tuning only operates for the intensity distribution, not for the complex field. We point out that 4f temporal processors [175, 176] can also be applied for scaling the ES of short optical pulses. These devices provide simultaneous scaling in both, time and spectral domains. However they require four dispersive elements. In contrast, our spectral imaging system, although does not lead to a scaling in the temporal domain, only uses one dispersive element, which results much better in terms of losses. Finally, the quadratic spectral phase factor in Eq. (5.23) does not allow a direct scaling of the input spectral complex envelope. However, if this was a requisite in a photonic processor, it could be removed with an additional reverse-signed GDD circuit.

TEMPORAL ABERRATIONS ANALYSIS

As in TISs, SISs are affected by some practical constraints too [177]. Three main limiting factors are highlighted. Let us denote by T_a the temporal aperture in which the device operating as time lens introduces a truly quadratic phase factor. If we think of an EOPM driven with an RF sinusoidal signal, $T_a \approx 1/\Omega_r$, where Ω_r is the angular frequency of the RF tone. So, concerning the first time lens, the first necessary condition is

$$\sigma << T_{a1}, \tag{5.25}$$

where σ is a measure of the input pulse width, and T_{a1} is the temporal window of the first time lens. The second constraint concerns the linear dispersive element. We have assumed the quadratic approximation. This assumption restricts the spectral bandwidth of the modified signal to

$$\sqrt{1/\sigma^2 + K_1^2} << 3 \left| \frac{\beta_2}{\beta_3} \right|. \tag{5.26}$$

Finally, the last constraint is related to the pulse stretching through the fiber. As for the first constraint, the pulse duration at the input of the second lens must be shorter than its temporal aperture, T_{a2}. In mathematical terms, after evaluating the width of the propagated signal

$$\sigma \sqrt{(1 - \Phi_2 K_1)^2 + (\Phi_2/\sigma^2)^2} << T_{a2}. \tag{5.27}$$

NUMERICAL EXAMPLES

Let us consider an input optical waveform consisting of two Gaussian pulses with $5\,\mathrm{ps}$ rms temporal intensity width separated by $0.2\,\mathrm{ns}$. Figure 5.6(a) plots the input ES. The oscillatory term at $5\,\mathrm{GHz}$ coming from pulse interference falls in the limit of the spectral resolution of commercial OSAs based on double-pass monochromator operating at $1.55\,\mu\mathrm{m}$.
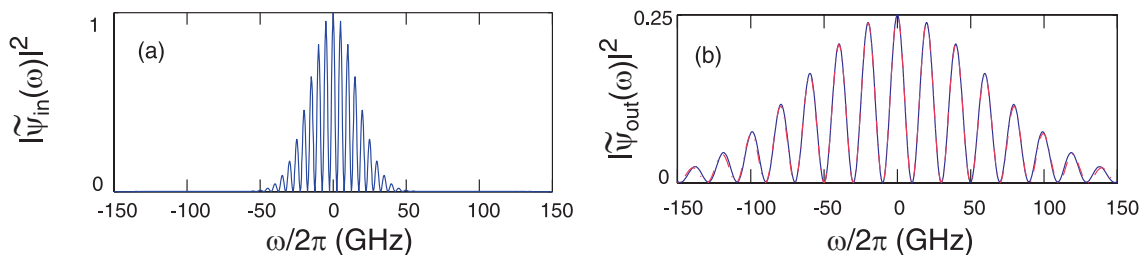

Figure 5.6: (a) Input ES (b) Output ES. A $4\times$ magnification is achieved.

With a SIS, a $4\times$ magnification can be achieved. To this end, we choose a first temporal lens implemented with an EOPM driven with a $2.5\,\mathrm{GHz}$ sinusoidal signal and $\Delta\theta = -2\,\mathrm{rad}$, giving rise to $K_1 = 493.5\,\mathrm{ns^{-2}}$. Note that, for this example, σ is nearly T_{a1} which allows us to test, for the double-Gaussian pulse, the sensibility of the technique to the first constraint. As a dispersive element we take a DCF with $\beta_2 = 21.6\,\mathrm{ps^2/km}$ and consider $\beta_3 = 0.1\,\mathrm{ps^3/km}$. Note that the second constraint is fully satisfied, since the ES at the output of the first time lens is around $40\,\mathrm{GHz}$, far from the upper limit imposed by the quadratic approximation of the fiber. To achieve a $4\times$ magnification, we need a second chirp $-4K_1$, and according to Eq. (5.22), a fiber with $z = 70.4\,\mathrm{km}$. It leads to a pulse broadening of $\sim 1\,\mathrm{ns}$ before incoming to the second lens. This would make difficult to satisfy the third constraint with an EOPM operating with a relatively low modulation index at $2.5\,\mathrm{GHz}$. Consequently, we then choose a second time lens implemented by means of the XPM effect in a nonlinear fiber pumped with a Gaussian pulse. We choose $\sigma_p = 1.8\,\mathrm{ns}$ and $\gamma L P_{\mathrm{pump}} = 3198$. Figure 5.6(b) shows the theoretical output ES from Eq. (5.22) (dashed red line) and the achieved one having into account TOD and nonparabolic chirping in the time lenses (blue solid line). Our numerical simulation shows that there are no appreciable differences from the predicted spectrum. Thus, a $4\times$ magnification can be achieved with realistic devices.

5.5.5   Repetition rate multipliers based on temporal Talbot phenomena

INTEGER TEMPORAL TALBOT PHENOMENON

As sketched in Fig. 5.7(a), the integer temporal Talbot effect or temporal self-imaging phenomenon consists on the regeneration of an input periodic pulse sequence propagating through a GDD circuit. The output pulse train is an exact replica of the input one at those GDD amounts that are a multiple integer of

$$\Phi_{2\mathrm{T}} = \frac{1}{\pi f_r^2}. \tag{5.28}$$

Here, f_r denotes the repetition rate of the pulse train. This constitutes the temporal counterpart of the well-known phenomenon in the spatial domain, sketched for illustration purposes in Fig. 5.7(b). This effect was discovered by Talbot in 1836 [178], when he realized that the diffracted field of a grating replicated itself after certain propagation distances.
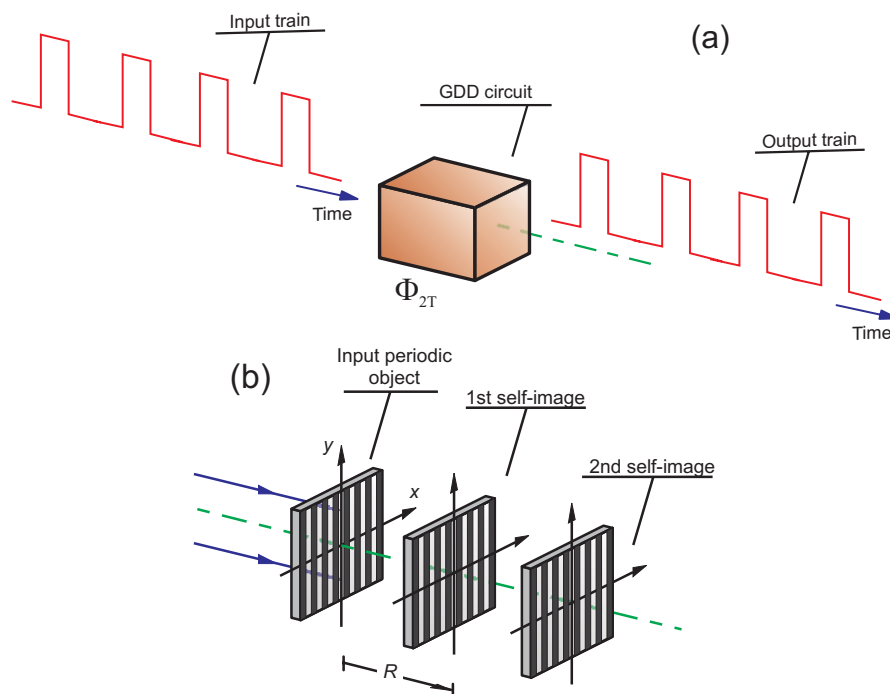

Figure 5.7: Illustration of the integer Talbot phenomenon in (a) temporal and (b) spatial domain.

Basing on the Space–Time analogy, this phenomenon was proposed in the time domain by Jannson [132], and independently verified later [179], but without pointing out any connection to self-imaging.

The temporal Talbot effect has been proposed in telecommunication systems as a simple mechanism to reduce the timing jitter of periodic pulse trains [180], as well as a clock recovery device [181]. These configurations have also been adapted to the temporal domain from their corresponding spatial counterpart phenomena [182,183]. More recently, temporal Talbot effect has been used to obtain factorial numbers in high-speed photonic computing [184].

FRACTIONAL TEMPORAL TALBOT PHENOMENON

With the ever increasing bandwidth demand in optical communications, there is a strong need on high-repetition-rate optical signals. The fractional temporal Talbot effect constitutes a simple way to achieve different clock signals from a relatively low-frequency input pulse train [185].

In the spatial domain, replicas in intensity of the input spatial distribution can be achieved at fractional distances of the fundamental one with a reduced period. In the temporal domain, this phenomenon allows us to achieve multiplication of the repetition rate of an input optical pulse train just by dispersion in a GDD circuit. The required GDD amount is

$$\Phi_2 = \frac{P}{Q}\Phi_{2\mathrm{T}} \tag{5.29}$$

where P and Q are coprime integer numbers. The output repetition rate is multiplied $Q/2$ times. This is schematically sketched in Fig. 5.8.
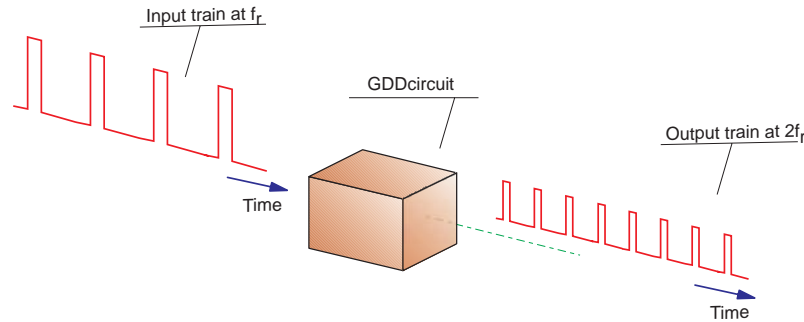

Figure 5.8: Schematic illustration of the fractional temporal Talbot effect for $\Phi_2 = \Phi_{2\mathrm{T}}/4$.

This effect was experimentally observed first in [186,187], where an SMF was employed as GDD circuit. However, the interpretation with the fractional Talbot effect was provided later [185, 188], and the use of an LCFG as GDD circuit was suggested and numerically verified. Such an experiment was later reported in [189]. Fractional Talbot effect has been verified using a spatial light modulator in a Fourier transform geometry as a GDD circuit too [147], which can provide higher bandwidths than SMFs or LCFGs. Nevertheless, it has been recently shown that Talbot effect can also take place in higher-order dispersion elements [190].

The achievement of ultra-high repetition rate pulse sequences is an important requisite in OTDM systems. What makes the fractional Talbot effect so interesting is its simplicity. However, it is important to note that, after multiplication, not every pulse has the same phase, which makes difficult to use it as an effective mechanism for OTDM applications. To overcome this problem, Atkins and Fischer demonstrated a clever method that involves the cross-gain modulation (XGM) effect in a semiconductor optical amplifier (SOA) [191].

5.5.6   Electro-optic pulse generation based on temporal array illuminators

The electro-optic pulse generation method is a technique that allows the achievement of high-repetition-rate pulse trains while preserving throughput [20, 192–194]. As sketched in Fig. 5.9, this system consists on a CW narrow-band laser modulated in phase by a periodic microwave signal. Pulsed light is achieved by temporal spreading in a GDD circuit, which converts the input phase modulation into intensity modulation.

Electro-optic phase modulation is commonly related to sinusoidal profiles only. This is because commercially available single-tone RF modulators can produce signal bandwidths >80 GHz, whereas arbitrary RF-waveform generators have a limited maximum bandwidth around $\sim 5\,\mathrm{GHz}$ [195]. Pulse generation by sinusoidal phase modulation is usually understood by means of the so-called bunching parameter [192]. This approach establishes the required GDD amount to focus the parabolic region of the sinusoidal profile. The bunching parameter is defined as the product between the chirping under the parabolic approximation, $K_{\mathrm{bunching}} = -4\Delta\theta\pi^2 f_r^2$, and the GDD coefficient. Then, it is usually accepted that the pulsed light is optimally compressed if $\Phi_2 = 1/K_{\mathrm{bunching}}$. However, as first realized in [194], this heuristic explanation has several limitations. For example, the maximum compression ratio is underestimated by the bunching-parameter value, and it cannot explain the rich panoply of achievable pulse profiles at the output of a GDD circuit, like the flat-top-pulse profile reported in [194, 196].
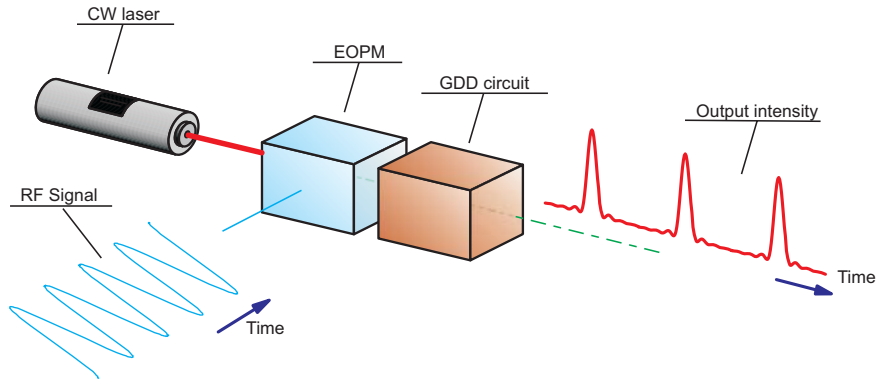

Figure 5.9: Scheme of the electro-optic pulse generation method.

On the other hand, the space–time analogy provides a nice analytic tool to tackle the problem of ultrashort light pulse generation based on propagation of periodically phase-modulated light [20]. The key relies on noticing the equivalence with the spatial diffraction of 1D phase structures. There, the so-called Fresnel array illuminators use pure-phase diffraction gratings for producing a two-dimensional (2D) array of bright spots with equal amounts of light by free-space propagation at a finite distance. In this direction a lot of research work has been devoted to understand the properties of light diffracted by periodic phase structures and above all to optimize their design in order to achieve a set of high-contrast two-level light intensity dots by diffraction [197–205].

MATHEMATICAL TREATMENT

According to the scheme of Fig. 5.9, the complex envelope at the input of the GDD circuit can be written as

$$\psi_{\mathrm{in}}(t) = \exp[iV(t)], \qquad (5.30)$$

where $V(t)$ is the periodic electrical signal driving the EOPM, with period $T_r = 1/f_r$. Consequently, the modulating envelope can be expanded as a Fourier series,

$$\psi_{\mathrm{in}}(t) = \sum_{n=-\infty}^{\infty} c_n \exp\left(-i2\pi n \frac{t}{T_r}\right), \qquad (5.31)$$

where

$$c_n = \frac{1}{T_r} \int_{-T_r/2}^{T_r/2} \exp[iV(t)] \exp(i2\pi nt) \mathrm{d}t. \tag{5.32}$$

We now propagate the signal in a GDD circuit. By substituting the matrix elements of Eq. (5.12) into Eq. (5.8), the output envelope results

$$\psi_{\mathrm{out}}(t) = \sum_{n=-\infty}^{\infty} c_n \exp\left(i\frac{2\pi^2 \Phi_2 n^2}{T_r^2}\right) \exp\left(-i2\pi n \frac{t}{T_r}\right). \tag{5.33}$$

Therefore the light intensity is

$$I_{\mathrm{out}}(t) = |\psi_{\mathrm{out}}(t)|^2 = \sum_{m=-\infty}^{\infty} C_m(\Phi_2) \exp\left(-i2\pi m \frac{t}{T_r}\right), \tag{5.34}$$

with

$$C_m(\Phi_2) = \exp\left(i2\pi m^2 \frac{\Phi_2}{\Phi_{2\mathrm{T}}}\right) \sum_{n=-\infty}^{\infty} c_n^* c_{n+m} \exp\left(i4\pi mn \frac{\Phi_2}{\Phi_{2\mathrm{T}}}\right). \tag{5.35}$$

In particular we are interested in the fractional Talbot distances [see Eq. (5.29)]. In this case, it can be verified that [185]

$$\psi_{\mathrm{out}}(t) = \sum_{L=0}^{Q-1} G(L, Q, P) \psi_{\mathrm{in}}\left(t - \frac{L}{Q} T_r\right). \tag{5.36}$$

In this case, the GDD circuit delays and weights the input periodic signal. Alternatively, any photonic processor that filters an input periodic signal in the same way as done in Eq. (5.36) will achieve the same result [206]. The weight coefficients are

$$G(L, Q, P) = \frac{1}{Q} \sum_{q=0}^{Q-1} \exp\left[-i2\pi \frac{q}{Q}(L - qP)\right]. \tag{5.37}$$

Note that we have not assumed the input light to be phase-only modulated in the above analysis, so the results remain valid for any input periodic field, disregarding if it is intensity and/or phase modulated.

Let us particularize the above analysis to the case in which the input light is phase-only modulated. Then, we can adapt well-known results from the existing bibliography in the spatial domain. Following [198, 201], we can set in Eq. (5.36) the condition $P = 1$ and $Q = 4$. The sum can be performed analytically to yield

$$I_{\mathrm{out}}(t) = 1 - \sin\left[V(t - T_r/2) - V(t)\right]. \tag{5.38}$$

This result has provided the key to explain the *a priori* counterintuitive finding reported in [194], where Komukai *et al.* achieved a flat-top-pulse profile from a sinusoidally phase-modulated CW laser [20] at a GDD amount different from the bunching condition.

With a careful insight in their experimental settings, we note they selected a GDD parameter at the one-quarter Talbot condition. By substituting $V(t) = \Delta\theta \sin(2\pi f_r t)$ in Eq. (5.38) we achieve

$$I_{\text{out}}(t) = 1 + \sin\left[2\Delta\theta \sin(2\pi f_r t)\right]. \tag{5.39}$$

This output pulse profile is schematically represented in Fig. 5.10 for $\Delta\theta = \pi/4\,\text{rad}$ and $f_r = 40\,\text{GHz}$. This waveform fits perfectly with the experimental results reported in [194, 196].
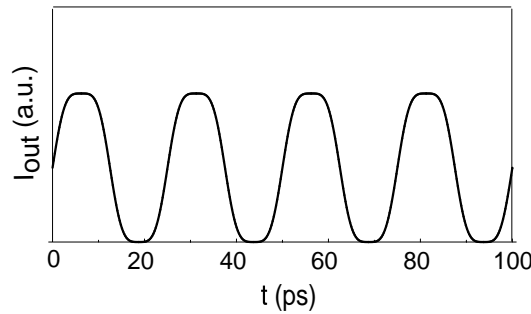

Figure 5.10: Flat-top pulse generation with the electro-optic phase modulation method (see text for numerical settings).

Finally, an analytic formula for the case $P = 1$, $Q = 3$ exists too [202],

$$
\begin{aligned}
I_{\text{out}}(t) =\ &1 + 2/3\cos\left[V(t - T_r/3) - V(t - 2T_r/3)\right] - \\
&- 2/3\sin\left[V(t) - V(t - T_r/3) + \pi/6\right] + \\
&- 2/3\sin\left[V(t) - V(t - 2T_r/3) + \pi/6\right].
\end{aligned} \tag{5.40}
$$

NUMERICAL EXAMPLES

In principle, it is not possible to synthesize any arbitrary output complex field from an arbitrary $V(t)$ and considering dispersion in a GDD circuit [203]. Nevertheless, Eqs. (5.38) and (5.40) provide a relatively easy way to determine $V(t)$ in order to achieve some interesting waveforms. Figure 5.11 plots a two-level $V(t)$ function, from which we can get an ultra-flat-top-pulse profile by dispersion in a GDD satisfying $\Phi_2 = \Phi_{2\text{T}}/4$. Such a $V(t)$ function can be provided by a bit pattern generator. With current electrical generators, the sequence can be produced at $> 40\,\text{Gb/s}$.

As illustrated in Fig. 5.12, the spacing of the ultra-flat-top-pulse profile can be tuned by changing slightly the $V(t)$ profile and setting $\Phi_2 = \Phi_{2\text{T}}/3$.

The last example concerns the generation of a sinusoidal waveform from a triangular profile at $\Phi_2 = \Phi_{2\text{T}}/4$. In this case, a triangular periodic waveform like the one presented in Fig. 5.13 will give rise to a continuous periodic sinusoidal waveform with a frequency $\Delta\theta(\pi T_r)^{-1}$, where $\Delta\theta = n\pi/2$, with n odd. Therefore, higher frequencies can be achieved just by increasing $\Delta\theta$.
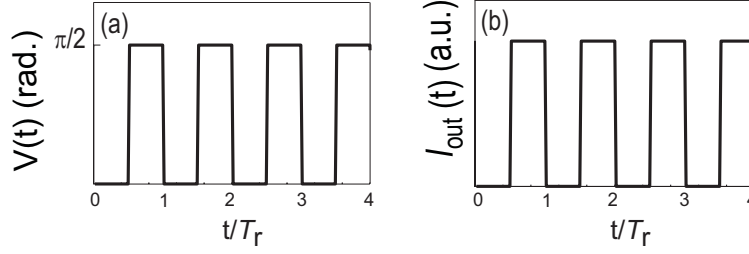
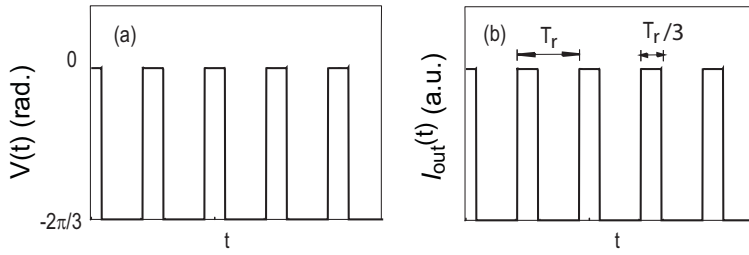**Figure 5.11**: Ultraflat-top pulse generation. (a) Required RF signal and (b) Output intensity at $\Phi_2 = \Phi_{2\mathrm{T}}/4$.

Figure 5.12: Ultraflat-top pulse generation with different duty cycle. (a) Required RF signal and (b) Output intensity at $\Phi_2 = \Phi_{2\mathrm{T}}/3$.

5.6   Space–Time analogy for partially coherent wavefields

Up to now, we have assumed that the wavefields for which the space–time analogy applies are fully coherent. In this section we extend the analogy to the partially coherent case [19]. With this aim, let us consider a plane-wave pulse with analytic signal representation, $U(z,t) = \psi(z,t) \exp[-i(\omega_0 t - \beta_0 z)]$, propagating in the z direction of an homogeneous lossless dispersive medium. Now, $\psi(z,t)$ is a nondeterministic complex envelope from a nonstationary ensemble. The associated MCF is $\Gamma(z_1, z_2; t_1, t_2) = \langle \psi^*(z_1,t_1)\psi(z_2,t_2)\rangle \exp\{-i[\omega_0\tau - \beta_0(z_2 - z_1)]\} = \Gamma_e(z_1, z_2; t_1, t_2) \exp\{-i[\omega_0\tau - \beta_0(z_2 - z_1)]\}$. Since each of the envelope realizations satisfies Eq. (5.3) in general and (5.6) in particular,
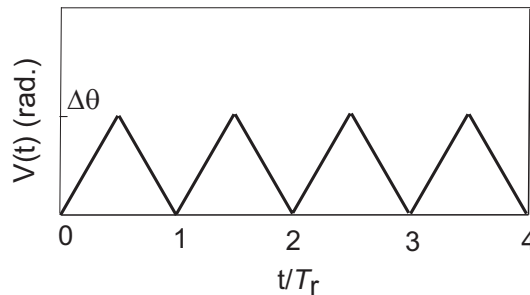

Figure 5.13: Required RF signal to achieve a sinusoidal profile at $\Phi_2 = \Phi_{2\mathrm{T}}/4$.

it is easy to show that Γ_e satisfies the following equations [19]

$$[\partial_{t_j}^2 - 2i(-1)^j \frac{1}{\beta_2} \, \partial_{z_j}]\Gamma_e(z_1, z_2; t_1, t_2) = 0, \tag{5.41}$$

where ∂_a denotes derivative with respect to the variable a, and $j = (1, 2)$.

These equations are fully equivalent to those describing free-space propagation of the envelope of a quasimonochromatic spatially partially coherent beam under paraxial approximation [39]

$$[\partial_{x_j}^2 + 2ik(-1)^j \, \partial_{z_j}]W_{s,e}(\mathbf{r}_1, \mathbf{r}_2; \omega') = 0, \tag{5.42}$$

where $\mathbf{r} = (x, z)$, $W_{s,e}(\mathbf{r}_1, \mathbf{r}_2; \omega')$ is the spatial-envelope part of the CSDF defined in Eq. (2.18), and $k = \omega'/c$ is the wave number. Equations (5.41) and (5.42) are mathematically equivalent, and the transfer rule is the same as in the coherent case (see Table 4.1).

Thanks to the extension of this analogy to the partially coherent case, we are now ready to develop new ultrashort processing schemes operating with noncoherent sources.

5.7 Partially coherent ABCD matrix approach

Let us assume a partially coherent wavefield with an MCF envelope $\Gamma_e(t_1, t_2)$ propagating in the same linear system described by the kernel $K(t, t')$ from Sect. 5.3. The relation (5.8) can be then generalized as[2]

$$\Gamma_{e,\text{out}}(t_1, t_2) = \iint \Gamma_{e,\text{in}}(t', t'')K^*(t_1, t')K(t_2, t'')\mathrm{d}t'\mathrm{d}t''. \tag{5.43}$$

Alternatively, we can formulate the problem in the spectral domain. In this case, the CSDF evolution is[3]

$$W_{b,\text{out}}(\omega_1, \omega_2) = \iint W_{b,\text{in}}(\omega', \omega'')\tilde{K}^*(\omega_1, \omega')\tilde{K}(\omega_2, \omega'')\mathrm{d}\omega'\mathrm{d}\omega'', \tag{5.44}$$

where $\tilde{K}(\omega, \omega')$ is given by Eq. (5.16). Equations (5.43) and (5.44) describe the most general case of the MCF and CSDF evolution in a linear system, respectively. For the particular case in which the system is Gaussian, $K(t, t')$ and $\tilde{K}(\omega, \omega')$ are still provided by Eqs. (5.9) and (5.17), respectively.

5.8 Effect of source linewidth in some ultra-high-speed optical systems

There are some ultrafast processors that operate with a pulsed source obtained by temporal modulation of a CW laser. Although the laser is usually assumed to be narrow-band, there are some situations in which the spectral line width is of particular concern. Equation (5.43) provides the adequate framework to deal with this problem. In this case,

---

[2]The subindex e denotes "envelope" part of the MCF. $\Gamma(t_1, t_2) = \Gamma_e(t_1, t_2) \exp(-i\omega_0\tau)$.

[3]The subindex b indicates that we deal with the baseband version of the CSDF, i.e., $W_b(\omega_1, \omega_2) = W(\omega_1' - \omega_0, \omega_2' - \omega_0)$.

we just have to substitute $\Gamma_{e,\mathrm{in}}(t_1, t_2)$ with the model from Eq. (3.9). As explained in Sect. 3.3.1, $\Gamma_s(\tau)$ is the MCF of the light source, assumed to be stationary, which is connected to the ES of the source, $S_s(\omega)$, containing the finite line shape. The role of the deterministic function $m(t)$ is played by the external modulator, which is coding the information in the time domain.

5.8.1   GSMP distortion in temporal Gaussian systems

In general, it is difficult to get an analytic expression from the integration of Eq. (5.43). However, the case of a GSMP evolving in a temporal Gaussian system described by its ABCD matrix has a compact result [21, 207].

In order to account for the finite spectral linewidth of the laser, we approximate the ES and the temporal intensity profile to Gaussian distributions. Then, the input MCF is given by $\Gamma_{\mathrm{in}}(t_1, t_2) = \Gamma_{e,\mathrm{in}}(t_1, t_2) \exp(-i\omega_0 \tau)$, where

$$\Gamma_{e,\mathrm{in}}(t_1, t_2) = I_0 \exp\left(-\frac{t_1^2 + t_2^2}{4\sigma_0^2}\right) \exp\left(-\frac{\tau^2}{2t_c^2}\right). \tag{5.45}$$

Here, I_0 is an irrelevant constant, σ_0 is the rms intensity width, and t_c determines the coherence time of the partially coherent pulse. σ_0 is given by the rms width of the modulation gate, whereas t_c is fixed by the inverse of the spectral bandwidth of the stationary light source. When this equation is inserted into Eq. (5.43) gives rise to [207]

$$\Gamma_{e,\mathrm{out}}(t_1, t_2) = \frac{I_0}{\Delta} \exp\left(-\frac{t_1^2 + t_2^2}{8\sigma_0^2 \Delta^2}\right) \exp\left(-\frac{\tau^2}{2\delta_0^2 \Delta^2}\right) \exp\left[iK(t_2^2 - t_1^2)\right]. \tag{5.46}$$

This result implies that the GSMP keeps its structure under an ABCD-type transformation. The rms intensity width and the coherence time have changed, and there has appeared a quadratic phase factor given by the matrix elements,

$$K = \frac{AC + \frac{BD}{\sigma_0^2 \delta_0^2}}{A^2 + \frac{B^2}{\sigma_0^2 \delta_0^2}}. \tag{5.47}$$

The parameter Δ is

$$\Delta^2 = A^2 + \frac{B^2}{\sigma_0^2 \delta_0^2}, \tag{5.48}$$

and $\delta_0 = 2\sigma_0(1 + 1/q_0^2)^{-1/2}$, with $q_0 = \frac{t_c}{2\sigma_0}$ being the global degree of coherence. The latter is an invariant quantity under ABCD temporal matrix transformations [21]. All these findings perfectly agree with the well-known results from the spatial domain [54].

In the case of a GDD circuit composed by an SMF, we have [81]

$$\Delta(z)^2 = 1 + \left(\frac{z\beta_2}{\sigma_0 \delta_0}\right)^2. \tag{5.49}$$

Then, it is easy to note that for a fixed σ_0 at a certain z, a decreasing in t_c (increasing of the spectral linewidth), leads to an output pulse broadening. From Eq. (5.49), any GSMP
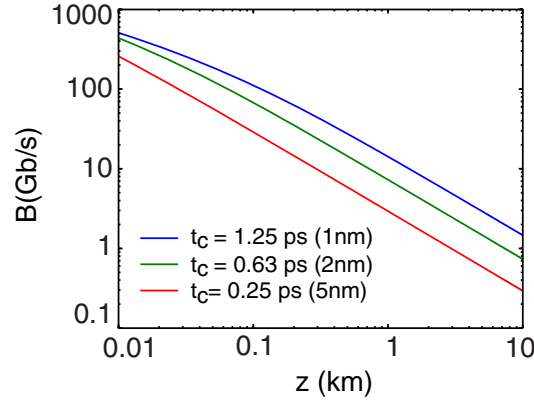
Figure 5.14: Maximum achievable bit rate for three different source linewidths.

having the same product $\sigma_0 \delta_0$ will lead to the same relative increasing, which constitutes the Collet-Wolf equivalent theorem [208] read in the temporal domain [81].

From the above equation, the input pulse width $\sigma_{0,\mathrm{opt}} = \sqrt{L|\beta_2|/2}$ minimizes the output pulse for a given fiber length L. Once the output pulse is optimized, we can estimate the maximum data transfer at the fiber link establishing the criterium that the output pulse width should be less than the quarter part of the period, i.e., $B_{\max} = (4\sigma_{0,\mathrm{opt}})^{-1}$ [77]. This determines the so-called bit-rate–distance product as

$$B_{\max} L = \sqrt{\frac{L}{4(|\beta_2| + L\beta_2^2/t_c^2)}}. \tag{5.50}$$

This is a well-known result in the field of optical communications [77], that we have recovered from the optical coherence theory concept of GSMP [19]. Figure 5.14 plots the achievable bit rate depending on the fiber link for different spectral linewidths.

5.8.2 RTFT operating with a spectrally incoherent source

Let us consider an RTFT built with a GDD only. The pulses are assumed to be launched by a modulator external to an optical source with a finite source linewidth. A sampling scope measures the average intensity after dispersion in a GDD circuit. By substituting Eq. (3.9) into Eq. (5.43) and equaling $t_1 = t_2 = t$, it can be shown that the output averaged is given by

$$I_{\mathrm{out}}(t) = S_{s,b}(t/\Phi_2) \otimes I_{\mathrm{coh}}(t), \tag{5.51}$$

where irrelevant constant factors have been dropped for clarity. Here, $S_{s,b}(\omega)$ is the ES of the source centered at the baseband and $I_{\mathrm{coh}}(t)$ is the intensity that would be achieved if the spectral source was a perfect Dirac's delta, i.e.,

$$I_{\mathrm{coh}}(t) = \left| \int \exp(i\Phi_2 \omega^2/2) \tilde{M}(\omega) \exp(-i\omega t) \mathrm{d}\omega \right|^2, \tag{5.52}$$

where $\tilde{M}(\omega)$ is the Fourier transform of the modulation $m(t)$. This general result is known as the extension of the Collett–Wolf equivalent theorem to the Fresnel region, and was

achieved first in the spatial domain in [209], and formulated recently in the temporal domain in [210]. By invoking the Fraunhofer condition (5.19) we achieve [25]

$$I_{\text{out}}(t) = S_{s,b}(t/\Phi_2) \otimes |\tilde{M}(t/\Phi_2)|^2. \tag{5.53}$$

As expected, the coherent limit is only recovered when the ES becomes a Dirac delta. Thus, in order to achieve the ES of the modulator from averaged intensity measurements, one should measure with a certain degree of accuracy the ES of the light source and perform an adequate deconvolution algorithm. However, with current laser diodes operating near 1550 nm, this effect can be disregarded, since the source linewidth can be less than 100 MHz.

5.8.3   Side-lobe suppression in electro-optic pulse generation

We already saw in Sect. 5.5.6 that the electro-optic pulse generation is a very efficient method to achieve ultrashort-pulse trains with controllable repetition rate. However, one problem with this method is the low extinction ratio. On one hand, blue-chirping and red-chirping regions repeat in every modulation period. As a result, approximately half of the energy in the input field does not contribute to the bunching and generates an undesirable direct-current (DC) floor level. On the other hand, nonlinear-chirped frequency components of sinusoidally phase-modulated light contribute to generate side lobes, so that a considerable part of the energy lies outside the main pulse [192].
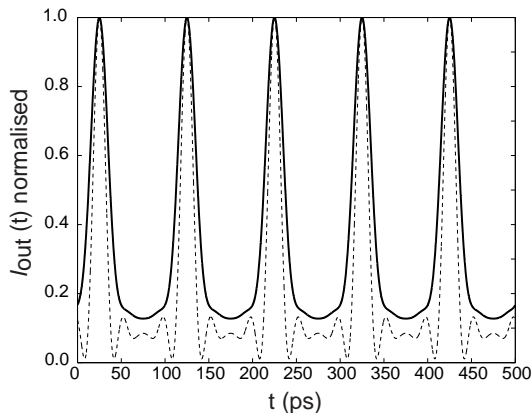

Figure 5.15: Normalized output intensity profile in electro-optic pulse generation using a CW (dashed curve) or a broadband spectrally incoherent source (solid curve).

In order to achieve highly extinctive pulse patterns, different photonic architectures have been reported. We mention the use of amplitude modulation followed by a bandwidth tunable Mach-Zehnder interferometer (MZI) [211]; dispersion-imbalanced nonlinear loop mirror [212]; high-resolution line-by-line pulse shaping [213]; cascaded uniform fibre Bragg gratings [214]; or directly modulated semiconductor laser [215]. However, in virtue of Eq. (5.51), smoothing of the high frequency components can be readily achieved just by using a broadband spectrally incoherent source [27]. To show this, we take the Fourier

transform in Eq. (5.51),

$$\tilde{I}_{\text{out}}(f) = \tilde{I}_{\text{coh}}(f)\Gamma_{s,e}(-2\pi\Phi_2 f), \tag{5.54}$$

where $\tilde{I}_{\text{coh}}(f)$ is the Fourier transform of $I_{\text{coh}}(t)$ and $\Gamma_{s,e}(\tau)$ is the inverse Fourier transform of $S_{s,b}(\omega)$. We note that the spectral filter function is just a scaled version of the MCF of the stationary light source.
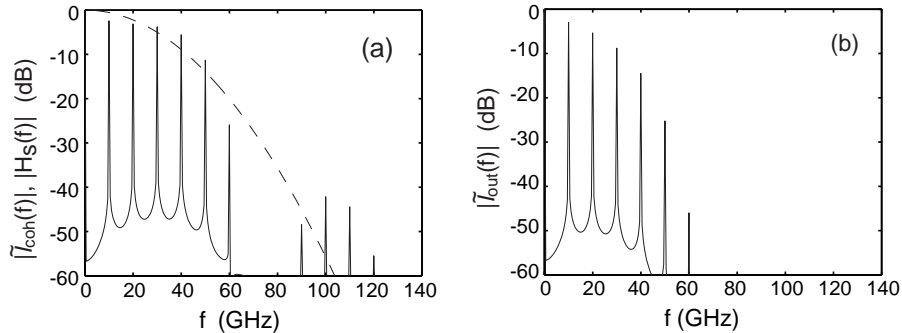

Figure 5.16: Spectral analysis of low-pass operation associated with Collett-Wolf equivalence theorem in Fresnel region for electro-optic pulse generation. See text for details.

Let us consider a practical example. Initially we consider a strictly monochromatic carrier wave at 1.55 μm. For the EOPM, we choose $f_r = 20$ GHz and $\Delta\theta = 2$ rad. For these settings, according to [194], the maximum compression is achieved at $\Phi_2 = 213.9$ ps^2/km. Such a dispersion can be implemented by means of an LCFG a few centimeters long. Fig. 5.16 shows $I_{\text{coh}}(t)$ normalized. We note the presence of main pulses in the picosecond range, approximately 40 ps width, together with undesired side lobes. The modulus of the spectrum of the intensity, $|\tilde{I}_{\text{coh}}(f)|$, is shown in Fig. 5.16[4]. This plot shows the presence of high-frequency components associated to secondary lobes. Following the previous reasoning, a low-pass filtering operation can be implemented by employing a broadband carrier wave. Here, we consider spectral filtering by means of a Gaussian ES with 12 GHz rms width. This feasible value can be obtained by means of spectral slicing an LED or an ASE source. Also in Fig. 5.15, we show in solid curve the averaged intensity output, $I_{\text{out}}(t)$, which is free from side lobes. We note a slight increment of the DC-floor level component at the output. However, zero-order frequency filtering can be easily implemented by cascading an amplitude modulator to reduce the DC-floor signal [211].

---

[4]The measurement of decibels are referred to a logarithmic scale calculated as $10\log(I/I_0)$, where log indicates common (base 10) logarithm operation and I is the magnitude to plot in intensity. When the reference I_0 is the maximum of I, the magnitude to plot is adimensional and the measurement is expressed in dB. In contrast, when the reference I_0 corresponds to 1 mW, the magnitude is expressed in dBm.

Incoherent frequency-to-time mapping and its application to incoherent pulse shaping

In the previous Chapters, we were mainly concerned about the degradation of photonic systems in view of the source spectral linewidth. Here, we take advantage of using a low-coherence source and propose a new photonic configuration to achieve arbitrary averaged intensity shaping [24]. The fundamental physical principle behind this setup is the temporal counterpart of the vanCittert–Zernike theorem [75,216] applied to quasi-stationary sources [48]. While most of the previous works to achieve user-defined intensity waveforms rely on the use of broadband coherent sources [62], our technique utilizes a spectrally incoherent light source. An experimental verification of the technique is provided in Chapter VIII, where intensity waveforms useful for RF applications are achieved.

6.1 First-order distortion of quasi-homogeneous pulses

We now proceed to propagate an arbitrary MCF into a GDD circuit. By inserting the matrix coefficients given by Eq. (5.12) into Eq. (5.43) we get

$$\Gamma_{e,\mathrm{out}}(t_1, t_2) = I_0 \exp\left(i\frac{t_1^2 - t_2^2}{2\Phi_2}\right) \iint \mathrm{d}t\mathrm{d}t' \, \Gamma_{e,\mathrm{in}}(t, t') \times$$
$$\times \exp\left(i\frac{t^2 - t'^2}{2\Phi_2}\right) \exp\left(-i\frac{tt_1 - t't_2}{2\Phi_2}\right), \tag{6.1}$$

where I_0 is an irrelevant constant. We are interested in the far-zone regime. This limit is reached when the quadratic phase factor in the integrand of Eq. (6.1) is removed. This analysis has been performed by Gori in the spatial domain [217]. Basing on the generalized space–time analogy [19], the condition to achieve the far-zone in the temporal domain reads as [24]

$$|\Phi_2| >> \frac{\sigma}{4\pi} \min[2\sigma, t_c], \tag{6.2}$$

where σ is a measure of the temporal intensity width of the input pulse, and $\min[a, b]$ means the smaller of the real numbers a and b. Equation (6.2) should be compared with the coherent result in Eq. (5.19). It can be inferred that in many cases, it is possible to achieve the far zone using a dispersive element with a lower GDD amount than in the

coherent case. Thus, when the above limit is reached, Eq. (6.1) becomes

$$\Gamma_{e,\text{out}}(t_1, t_2) = I_0 \exp\left(i\frac{t_1^2 - t_2^2}{2\Phi_2}\right) W_{b,\text{in}}\left(t_1/\Phi_2, t_2/\Phi_2\right). \tag{6.3}$$

Here, $W_{b,\text{in}}(\omega_1, \omega_2)$ is the CSDF of the input partially coherent pulse centered at baseband. Thus, apart from a quadratic phase factor, the MCF at the output is a scaled version of the CSDF at the input. This result represents a generalization of the coherent case, where, aside from a quadratic temporal phase factor, the output temporal envelope is a scale version of the input spectral envelope [148].
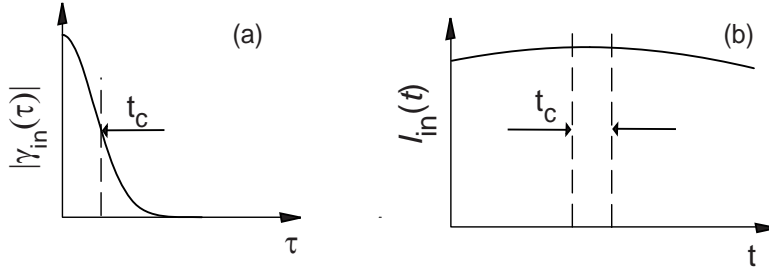

Figure 6.1: Representation of (a) the modulus of the complex degree of coherence and (b) averaged intensity for a quasi-homogeneous pulse.

Let us now assume an input quasi-homogeneous light pulse [218]. Such pulses constitute the temporal counterpart of the well-known quasi-homogeneous light sources [48]. They are characterized by a temporal intensity width much larger than the coherence time of the source, $\sigma \gg t_c$, and a complex degree of coherence depending on the time difference τ (see Fig. 6.1). In this case, the input MCF can be written as [216]

$$\Gamma_{e,\text{in}}(t_1, t_2) = I_{\text{in}}\left[(t_1 + t_2)/2\right]\gamma_{e,\text{in}}(\tau), \tag{6.4}$$

where $I_{\text{in}}(t)$ and $\gamma_{e,\text{in}}(\tau)$ denote the averaged intensity and the envelope of the complex degree of coherence of the input partially coherent light pulse. According to Eq. (6.4), this particular MCF structure leads to

$$W_{b,\text{in}}(\omega_1, \omega_2) = \tilde{I}_{\text{in}}(\omega_2 - \omega_1)\tilde{\gamma}_{e,\text{in}}\left[(\omega_1 + \omega_2)/2\right], \tag{6.5}$$

where $\tilde{I}_{\text{in}}(\omega)$ and $\tilde{\gamma}_{e,\text{in}}(\omega)$ denote the Fourier transform of $I_{\text{in}}(t)$ and $\gamma_{e,\text{in}}(\tau)$, respectively. By substituting Eq. (6.5) into Eq. (6.3) we achieve

$$\Gamma_{e,\text{out}}(t_1, t_2) = I_0 \exp\left(i\frac{t_1^2 - t_2^2}{2\Phi_2}\right) \tilde{I}_{\text{in}}(\tau/\Phi_2)\tilde{\gamma}_{e,\text{in}}\left(\frac{t_1 + t_2}{2\Phi_2}\right). \tag{6.6}$$

From this last equation, the averaged output intensity results

$$I_{\text{out}}(t) = I_0 \tilde{I}_{\text{in}}(0)\tilde{\gamma}_{e,\text{in}}(t/\Phi_2). \tag{6.7}$$

Further, taking into account the scale property of the Fourier transform, it is apparent that $\tilde{\gamma}_{e,\text{in}}$ is a slowly varying function compared with $\tilde{I}_{\text{in}}$. Therefore, the modulus of the complex degree of coherence can be approximated to

$$|\gamma_{\text{out}}(\tau)| \approx |\tilde{I}_{\text{in}}(\tau/\Phi_2)|. \tag{6.8}$$

Equations (6.7) and (6.8) constitute the temporal version of the vanCittert-Zernike theorem [75] applied to quasi-stationary light pulses [216]. It relates the output complex degree of coherence with the Fourier transform of the input light intensity. The mathematical transformations expressed by these equations are schematically represented in Fig. 6.2.
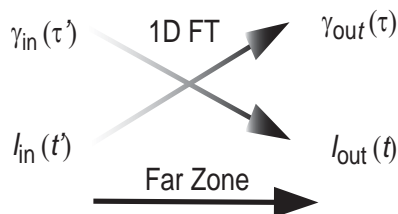

Figure 6.2: Schematic representation of the mathematical transformations involved in the temporal vanCittert–Zernike theorem. FT means Fourier transformation.

6.2   Incoherent frequency-to-time mapping

Going one step further, we focus our attention on a particular way to produce quasi-homogeneous light pulses. Following [75], these can be achieved with the model from Sect. 3.3.1, i.e., having a spectrally incoherent source, like ASE, externally modulated with a deterministic modulator. Note that, according to Eq. (3.9), a temporally modulated stationary light source does not behave, in general, as a quasi-homogeneous light pulse unless $\sigma \gg t_c$. Only in this case we can write

$$\Gamma_{e,\text{in}}(t_1, t_2) = |m[(t_1 + t_2)/2]|^2 \Gamma_{s,e}(\tau), \tag{6.9}$$

where $\Gamma_{s,e}(\tau)$ is the envelope part of the MCF of the stationary light source. Therefore, having into account Eq. (6.7) and that $\Gamma_{s,e}$, is related with the baseband ES, $S_{s,b}(\omega)$, via the Wiener–Khintchine theorem [Eq. (2.19)], the averaged output intensity becomes [75]

$$I_{\text{out}}(t) = I_0' S_{s,b}(t/\Phi_2), \tag{6.10}$$

where I_0' is an irrelevant constant. Equation (6.10) states that, after temporal modulation of a spectrally incoherent CW stationary source and subsequent first-order distortion, the output intensity profile is, independently of the temporal waveform provided by the modulator, a replica with a certain scale of the ES of the optical source. This relevant result constitutes the generalization to the partially coherent case of the well-known coherent frequency-to-time mapping technique presented in Sec. 5.5.1. It is worth mentioning that

the scale factor that finally determines the temporal width of the output pulse in intensity is conditioned by Eq. (6.2), which for a quasi-stationary light pulse reads as
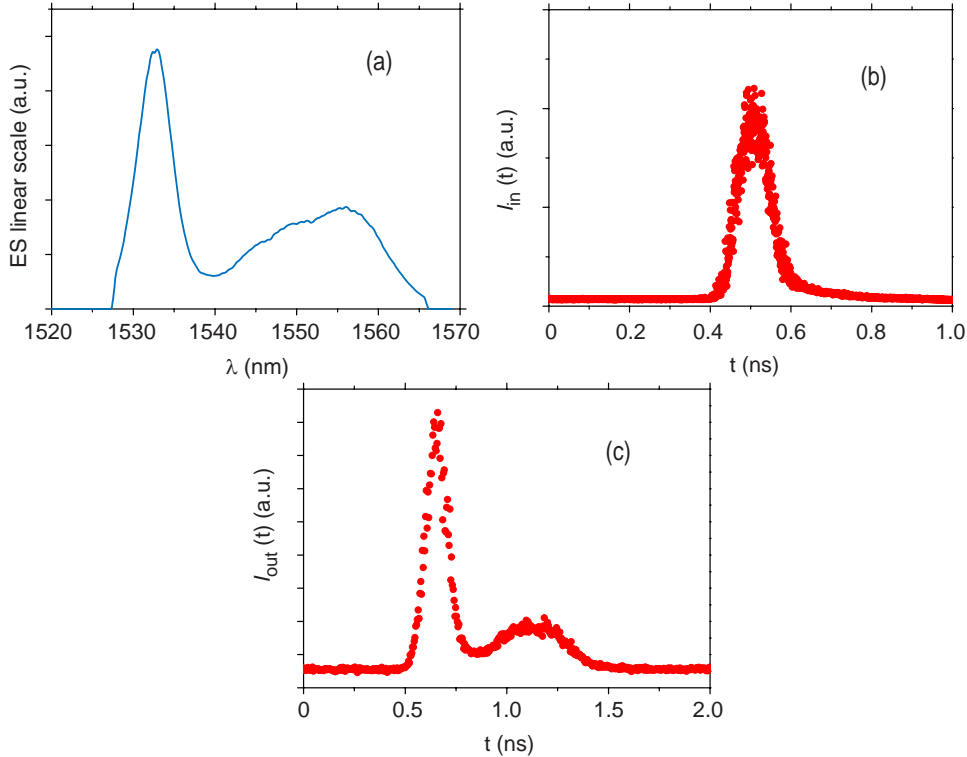
$$|\Phi_2| >> \frac{\sigma t_c}{4\pi}. \tag{6.11}$$

Figure 6.3: Generalized frequency-to-time mapping. (a) input ES (in linear scale); (b) averaged intensity at the input of the GDD; (c) averaged output intensity. The zero level for the intensities corresponds to the lowest marker in the y-scale.

Figure 6.3 represents an experimental verification of this frequency-to-time mapping operation. As spectrally incoherent source we employed the ASE from the gain spectrum of an EDFA. The ES is measured with an OSA and sketched in Fig. 6.3(a). Typical coherence time of EDFAs are around ~ 100 fs. The deterministic gate was a 10 Gb/s LiNbO$_3$ electro-optic modulator (EOM) biased at quadrature driven with a short RF Gaussian impulse. The averaged optical intensity pulse profile is measured with a 20 GHz sampling scope, and is sketched in Fig. 6.3(b). The pulse width was measured around 88 ps FWHM. In this way, the quasi-homogeneous requirement is by far reached. Finally, light is launched in an SMF of 1.44 km length. Note this GDD amount is much larger than the minimum required by condition (6.11) assuming $\beta_2 = -21.6$ ps^2/km. The output intensity shape is measured again with the same sampling scope and the result is shown in Fig. 6.3(c). The frequency-to-time mapping predicted by Eq. (6.10) is clearly achieved, in view of the waveforms from Figs. 6.3(a) and (c). The corresponding scale factor is calculated to be 0.024 ns/nm.

It should be pointed out that this generalized mapping has been achieved independently in [219]. The authors proposed to use it as an all-fiber sensor in view of the capabilities to perform quasi-real-time spectral measurements. In the following Section, we propose the use of this physical phenomenon as a way to achieve user-defined intensity profiles.

6.3   Incoherent pulse shaping

In principle, any ES shape can be synthesized just by performing a proper spectral filtering in the spectrally incoherent CW light source before entering the light into the temporal modulator. The spectral filtering operation could be experimentally achieved by using programmable pulse shapers [62, 220] or, in order to obtain all-fiber setups, by spectral slicing with fiber Bragg gratings [221]. It is very important to recognize that, after the spectral filtering stage, the resulting spectral bandwidth must remain large enough in order to satisfy the quasi-homogeneous pulse requirement. Finally, after propagation in the GDD circuit, a user-defined averaged output intensity profile is achieved. The whole setup is schematically represented in Fig. 6.4.
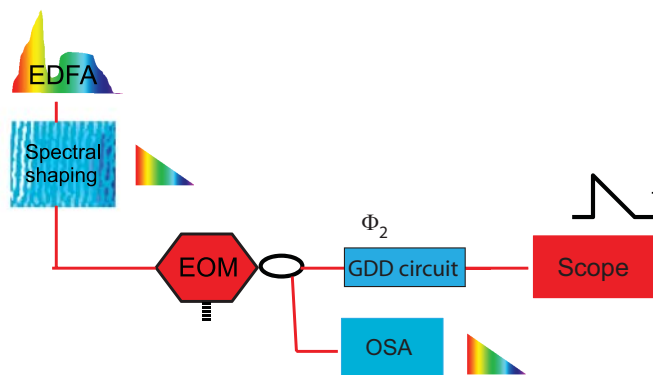

Figure 6.4: Schematic diagram of the incoherent pulse shaping technique. The spectral source is taken as the gain spectrum of an EDFA; the external modulator is assumed to be an EOM. The GDD circuit performs the incoherent frequency-to-time mapping.

It should be emphasized that, due to the incoherent nature of the optical source, only the averaged output intensity is properly shaped. This implies that some intensity fluctuations between the different practical realizations of the output shaped waveform are predicted. Although this fact is expected to seriously restrict the practical capabilities of our proposal, a coherence analysis of light fluctuations carried out in the next section shows that they can be maintained low enough in practical applications, as will be shown in the experimental verification of the technique provided in Chapter VIII.

6.4 Analysis of intensity fluctuations

Let us define the intensity fluctuations as

$$\Delta I(t) = \mathtt{I}(t) - I(t), \tag{6.12}$$

where $\mathtt{I}(t)$ is the random instantaneous intensity function associated to a particular realization of the field, $I(t) = \langle \mathtt{I}(t) \rangle$, and the angle brackets denote ensemble average. A measurement of the correlation between the intensity fluctuations at two time instants is obtained through the relative ratio,

$$r(t_1, t_2) = \frac{\langle \Delta I(t_1) \Delta I(t_2) \rangle}{I(t_1) I(t_2)}. \tag{6.13}$$

Note that this quantity reduces to the usual relative-intensity-noise figure of merit for the stationary case [77]. An analytical expression for the above quotient can be obtained when the field obeys a Gaussian statistical distribution. Having into account Eq. (2.29) and the definition of the complex degree of coherence from Eq. (2.8), we achieve [24]

$$r(t_1, t_2) = |\gamma(t_1, t_2)|^2. \tag{6.14}$$

This equation connects the correlation of the intensity fluctuations with the modulus square of the complex degree of coherence. Note that the highest intensity fluctuations correspond to the smallest value for the modulus of the complex degree of coherence.

For the case of the quasi-homogeneous pulse, and in accordance with Eq. (6.8), the coherence time at the output of the GDD circuit, $t_{c,\text{out}}$, is related to the width of the scaled Fourier transform of the input intensity modulation, $t_{c,\text{out}} = \Phi_2/\sigma$. An estimate for the improvement of the signal-to-noise ratio is roughly given by the quotient between this coherence time and the input one into the device, $t_{c,\text{in}}$. Note that $t_{c,\text{in}}$ is related to the inverse of the bandwidth of the spectrally filtered source, $\Delta\omega$. In this way we obtain,

$$\frac{t_{c,\text{out}}}{t_{c,\text{in}}} \approx \frac{\Phi_2 \Delta\omega}{\sigma}. \tag{6.15}$$

This ratio is larger for quasi-homogeneous light pulses and GDD circuits with larger amounts of dispersion. Thus, a proper choice either of the width of the input intensity or the dispersion parameter should guarantee the required value for the signal-to-noise ratio for a particular application.

Non-interferometric measurement of partially coherent light pulses

With the current diagnostic tools, it is possible the full characterization of the temporal [222–226] or spatiotemporal [227, 228] structure of coherent pulsed beams. Many of these devices need a long sequence of replicas of the pulse to be measured. This sequence is usually provided by the pulse train itself, assuming that every waveform constitutes an exact replica of its neighbors. However, this widespread procedure is not suitable when there are stochastic variations from pulse to pulse, i.e., the pulses are spectrally partially coherent.

To overcome this problem, advanced diagnostic techniques operating in a single-shot-like configuration have been developed [222, 229–232]. However, for high-repetition rates, monitoring these waveforms constitutes a great challenge [229]. Furthermore, even if the whole sequence was measured, tedious additional computation would be required for extracting the statistics of the ensemble. In order to gain access into the second-order information of the partial coherence characteristics, the MCF – or CSDF – should be the meaningful quantities to be measured instead, because they are already defined from the ensemble average [223].

Previous attempts on extracting some statistical information of fluctuating pulse trains aimed to measure the averaged intensity autocorrelation [233]; the RF-spectrum distortion [113]; the frequency dependence of the spatial-fringe visibility [234, 235]; or the linewidth in frequency combs [121, 125]. However, although these techniques provide some information about the coherence time of the pulse, no one gives direct access into the MCF or CSDF structure.

In the spatial domain, techniques for characterizing the spatial coherence properties of quasi-monochromatic light beams are now well established. They could be mainly classified into two different groups: interferometric [236–239] and non-interferometric [240–244] procedures. In the temporal domain, only interferometric approaches have been proposed for measuring either the MCF or the CSDF of the pulse [47, 245]. In this Chapter we review these advanced techniques and introduce new concepts for non-interferometric characterization of spectrally partially coherent radiation. We just consider the temporal variation of the pulse, which physically implies to particularize the measurement into a single spatial point or to have the light confined in a medium with translational symmetry. Furthermore, we also assume that we can measure: i/ the averaged ES, which results

straightforward with current OSAs, and ii/ the averaged intensity profile, which can be directly done with current sampling scopes for pulse durations around $\sim 1\,\mathrm{ps}$, or 100 fs if a magnifying TIS is utilized previous to the acquisition unit [169]. For non-telecom wavelengths, this last operation can be performed with spectro-temporal devices, like the one reported in [167].

7.1 Temporal double-slit Young experiment

The two-slit Young experiment constitutes the cornerstone in the measurement of spatial coherence [48]. In this Section we review this classic experiment in the temporal domain [246] in order to clarify further the concepts for the measurement of non-stationary partially coherent pulses. The particular experimental arrangement for this measurement was first proposed by Iaconis and Walmsley [245].

7.1.1 Time domain formulation

Let us assume a scheme like the one presented in Fig. 7.1. A partially coherent pulse, with a fluctuating electric field described by its analytic signal $U(t)$ is split and directed into the arms of a Mach-Zehnder interferometer. Each pulse traveling in the arm is optically sampled by a deterministic gate at controllable time instants t_a and t_b. This operation could be performed with a temporal modulator like the one introduced at Sect. 5.3.2, with $\Gamma^{-1} \to 0$. After the sampling, light is recombined, and the averaged ES is measured at the output with an OSA. Then, we achieve

$$S(\omega) = I(t_\mathrm{a}) + I(t_\mathrm{b}) + 2\sqrt{I(t_\mathrm{a})I(t_\mathrm{b})}|\gamma(t_\mathrm{a}, t_\mathrm{b})|\cos[\omega(t_\mathrm{a} - t_\mathrm{b}) + \varphi(t_\mathrm{a}, t_\mathrm{b})], \qquad (7.1)$$

where $\gamma(t_1, t_2)$ denotes the complex degree of coherence of the input pulse, $\phi(t_\mathrm{a}, t_\mathrm{b}) = \arg[\gamma(t_\mathrm{a}, t_\mathrm{b})]$, and $I(t) = \langle|U(t)|^2\rangle$ is the averaged input intensity. The frequency varying signal plays the role of the fringe pattern in the classical Young experiment, whereas the measurement performed with the OSA results identical to the far-field diffraction pattern. Analogously, the visibility can be defined as $V = (S_\mathrm{max} - S_\mathrm{min})/(S_\mathrm{max} + S_\mathrm{min})$,

$$V = \frac{\sqrt{I(t_\mathrm{a})I(t_\mathrm{b})}}{\left(\frac{I(t_\mathrm{a}) + I(t_\mathrm{b})}{2}\right)}. \qquad (7.2)$$

From Eq. (7.1), the real part of the complex degree of coherence [Eq. (2.8)] can be measured if one measures previously the averaged intensity of the source to be characterized. The sampling must be performed in a tunable way, so that the "temporal pinholes" can be swept by the user. We have also assumed that the optical sampling behaves as an ideal Dirac's delta function. Considering the finite shape, $m(t)$, and assuming to be much shorter than $U(t)$, Eq. (7.1) appears multiplied by the ES of the gate and results in a sinusoidal spectrally confined signal. All this together leads to a nonstraightforward method for the characterization of partially coherent pulses.

7.1.2 Spectral domain formulation

For the sake of completeness, let us formulate the spectral arrangement of the above experiment, as it is sketched in Fig. 7.2. The same partially coherent light pulse is split in
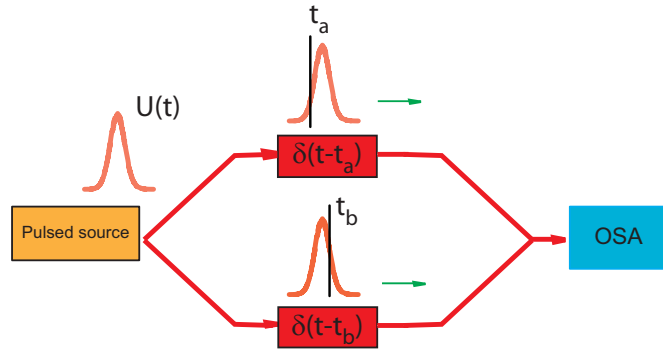
Figure 7.1: Scheme of the temporal two-slit Young experiment.

the same interferometer, but now in each arm we place different spectral filters with very narrow widths (this would be $\Delta^{-1} \to 0$ in the device described at Sect. 5.3.4), selecting the spectral components ω_a and ω_b, respectively. We recombine the pulses and measure the result with a sampling scope, which leads to the averaged intensity $I(t)$. The result becomes

$$I(t) = S(\omega_a) + S(\omega_b) + 2\sqrt{S(\omega_a)S(\omega_b)}|\mu(\omega_a,\omega_b)|\cos[(\omega_a - \omega_b)t + \varphi_e(\omega_a,\omega_b)], \quad (7.3)$$

where $S(\omega)$ is the ES of the input partially coherent pulse, $\mu(\omega_1,\omega_2)$ is the complex degree of spectral coherence [see Eq. (2.13)], and $\varphi_e(\omega_a,\omega_b) = \arg[\mu(\omega_a,\omega_b)]$. Following the same reasoning as before, by changing ω_a and ω_b we can measure the complex degree of spectral coherence [with previous knowledge of $S(\omega)$]. In practical terms, this method is more suitable than its temporal version because spectrally narrow filters are much simpler devices than external gates providing ultrashort light pulses. The resolution of the sampling scope will impose a limit on the maximum spectral separation $|\omega_a - \omega_b|$, which could be on the order of several tenths of GHz. The narrower the spectral filters are, the less energy we get into the photodiode. So, the floor-noise level of the intensity converter places the last limit into the spectral resolution of ω_a and ω_b. As in the previous case, the effect of the spectral shape of the filter, assumed to be much narrower than the Fourier transform of $U(t)$, translates into a finite sinusoidal signal, with a pulse profile given by the temporal intensity distribution of the inverse Fourier transform of the spectral complex filter shape.

7.2   Advanced interferometric characterization

The temporal version of the two-slit Young experiment is just a particular interferometric arrangement. There are more advanced implementations that could provide a faster and simpler way to achieve the second-order characterization of partially coherent light pulses. Note that in the previous configurations, a single (averaged) measurement leads to the characterization of a unique point of the MCF or CSDF 2D structure.

Spectral-phase-interferometry techniques give access into the CSDF [47, 245]. To achieve this, in the first arm of the previous interferometer it is placed a nondispersive delay line (linear spectral phase), and in the second one an element introducing a
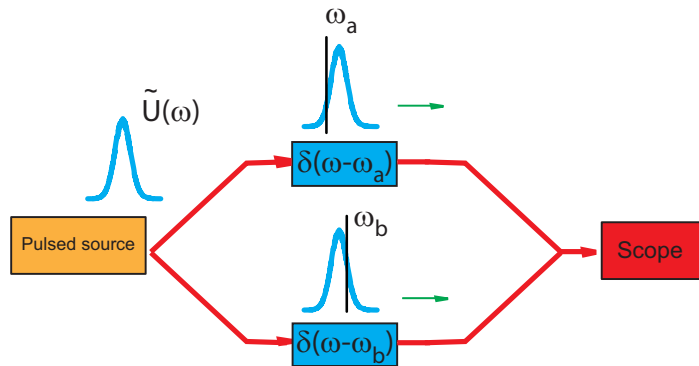
Figure 7.2: Scheme of the spectral version of the two-slit Young experiment.

temporal linear phase (time prism or spectral shear) that shifts the frequency of the pulse. At the output the averaged signal interference is recorded either in the spectral or time domain with an OSA or sampling scope, respectively. By controlling the shear, the former procedure provides a measurement of the CSDF, whereas the other one of the MCF [245].

The delay line can be easily achieved with an adjustable displacement built with mirrors, or by an in-line dispersion compensated waveguide, for example. The spectral shear can be provided with an EOPM during the zero crossing of the driving signal, which results an easy approach for telecom pulses [229]. For sub-picosecond pulses, the shear can be achieved via upconversion in a nonlinear crystal [225].

However, unlike in the coherent case, for partially coherent pulses the shear needs to be tuned over a broad range in order to measure the CSDF at different lines, which limits the applicability of the technique [47]. Finally, it should be mentioned that from the frequency-resolved optical gating method [222], it is not possible to get an obvious link between the measured averaged trace and the MCF (or CSDF) of the partially coherent pulse to be characterized, even assuming that it obeys Gaussian statistics [47].

7.3   Non-interferometric measurements

In the spatial domain, there are well-established procedures for retrieving the phase information of an input object from intensity measurements taken at two different diffraction planes [240–244, 247, 248]. These procedures are generally valid for both, coherent [248] and spatially partially coherent beams [240]. They are based on the transport-of-intensity equation (TIE) [247, 249]. This method is particularly useful because it avoids the use of any interferometer, and has been successfully applied to phase-contrast imaging with optical [250], as well as with x-ray sources [251, 252]. However, it presents some difficulties when the input light is not uniform and becomes useless when zeros appear in the intensity distribution [253]. The coherent version of the TIE has been recently adapted to the temporal domain by Dorrer, and has become a nice tool for measuring nonlinear fiber coefficients [254]. In the following, we show how the TIE can be also applied for the measurement of the MCF of partially coherent light pulses, assuming them to obey some specific model.

Before starting, it will be useful to rewrite Eqs. (2.15) and (2.16) by making the

following changes of variable

$$\bar{t} = \frac{t_1 + t_2}{2} \quad \text{and} \quad \tau = t_2 - t_1, \tag{7.4}$$

or

$$\bar{\omega} = \frac{\omega_1 + \omega_2}{2} \quad \text{and} \quad \Delta\Omega = \omega_2 - \omega_1. \tag{7.5}$$

Thus,

$$\overline{\Gamma}(\bar{t}, \tau) = \iint \overline{W}(\bar{\omega}, \Delta\Omega) \exp[-i(\bar{\omega}\tau + \Delta\Omega\bar{t})] \mathrm{d}\bar{\omega}\mathrm{d}\Delta\Omega, \tag{7.6}$$

and

$$\overline{W}(\bar{\omega}, \Delta\Omega) = \frac{1}{4\pi^2} \iint \overline{\Gamma}(\bar{t}, \tau) \exp[+i(\bar{\omega}\tau + \Delta\Omega\bar{t})] \mathrm{d}\bar{t}\mathrm{d}\tau, \tag{7.7}$$

where $\overline{\Gamma}(\bar{t}, \tau) = \Gamma(\bar{t} - \tau/2, \bar{t} + \tau/2)$ and $\overline{W}(\bar{\omega}, \Delta\Omega) = W(\bar{\omega} - \Delta\Omega/2, \bar{\omega} + \Delta\Omega/2)$.

7.3.1   Time domain approach

With this nomenclature, the averaged intensity at the output of a GDD circuit is written as

$$I(t) = \overline{\Gamma}_{e,\mathrm{out}}(t, 0) = \iint \overline{W}_{b,\mathrm{in}}(\bar{\omega}, \Delta\Omega) \exp[-i\Delta\Omega(t - \bar{\omega}\Phi_2)] \mathrm{d}\bar{\omega}\mathrm{d}\Delta\Omega. \tag{7.8}$$

Let us calculate the derivative of this function with respect to the GDD parameter,

$$\frac{\partial I(t)}{\partial \Phi_2} = i \iint \overline{W}_{b,\mathrm{in}}(\bar{\omega}, \Delta\Omega) \Delta\Omega\bar{\omega} \exp[-i\Delta\Omega(t - \bar{\omega}\Phi_2)] \mathrm{d}\bar{\omega}\mathrm{d}\Delta\Omega. \tag{7.9}$$

This equation measures the variation of the optical intensity at different GDD amounts. If we consider only those dispersive elements satisfying

$$\Phi_2 << \frac{2\pi}{\Delta\omega\delta\omega}, \tag{7.10}$$

where $\Delta\omega$ is an estimation of the spectral content of the input partially coherent pulse, and $\delta\omega$ is the spectral correlation width [Eq. (2.14)], then the exponential term in the integral can be disregarded. This can be achieved by having a GDD circuit with a small dispersion amount. So,

$$\frac{\partial I(t)}{\partial \Phi_2} \approx -\frac{\partial}{\partial t} \int \bar{\omega}\overline{W}_{\mathrm{ig,in}}(\bar{\omega}, t) \mathrm{d}\bar{\omega}, \tag{7.11}$$

where

$$\overline{W}_{\mathrm{ig,in}}(\bar{\omega}, t) = \int \overline{W}_{b,\mathrm{in}}(\bar{\omega}, \Delta\Omega) \exp(-i\Delta\Omega t) \mathrm{d}\Delta\Omega \tag{7.12}$$

is the Wigner distribution function [255] of the input partially coherent light pulse[1].

---

[1]The Wigner distribution function of a signal (coherent or not), $U(t)$, is defined as $W_{\mathrm{ig}}(\omega, t) = \int \langle U^*(t - \tau/2)U(t + \tau/2) \rangle \exp(i\omega\tau) \mathrm{d}\tau$. Further, it is verified that $W_{\mathrm{ig}}(\omega, t) = \int \langle \tilde{U}^*(\omega - \Delta\Omega/2)\tilde{U}(\omega + \Delta\Omega/2) \rangle \exp(-i\Delta\Omega t) \mathrm{d}\Delta\Omega$, where $\tilde{U}(\omega)$ is the Fourier transform of $U(t)$.

Equation (7.11) can be understood as the generalization to the partially coherent case of the TIE [240]. It relates the change of the intensity pulse profile through propagation in a GDD circuit with the first-order momentum of the Wigner distribution function [255].

However, we are interested in the characterization of the particular case of partially coherent light pulses whose MCF is described by the model presented at Sect. 3.3.1. In order to characterize fully such a concrete MCF we need to measure at least two functions: the deterministic function $m(t)$ and the weight function $S_{s,b}(\omega)$. Note that since we are dealing with the envelope part of the MCF, the weight function is defined at the baseband. The measurement of $|m(t)|$ is straightforward because we have assumed that averaged intensity measurements can be done. We should remind that $I(t) = \Gamma_{s,e}(0)|m(t)|^2$. However, we still need the characterization of the phase of $m(t)$.

With this aim we now substitute Eq. (3.7) into (7.12), and having into account the change of variables from Eqs. (7.5) we get

$$\overline{W}_{\text{ig,in}}(\bar{\omega}, t) = \iint S_{s,b}(\bar{\omega}')\tilde{M}^*(\bar{\omega} - \Delta\Omega'/2 - \bar{\omega}')\tilde{M}(\bar{\omega} + \Delta\Omega'/2 - \bar{\omega}')\times \qquad (7.13)$$
$$\times \exp(-i\Delta\Omega't)\mathrm{d}\bar{\omega}'\mathrm{d}\Delta\Omega'.$$

If we now further take into account that $\int \omega S_{s,b}(\omega)\mathrm{d}\omega = 0$ because the weight function is defined at the baseband; $\int S_{s,b}(\omega)\mathrm{d}\omega = \Gamma_{s,e}(0)$; and the relation $\iint \omega \tilde{M}^*(\omega - \Delta\Omega'/2)\tilde{M}(\omega + \Delta\Omega'/2)\exp(-i\Delta\Omega't)\mathrm{d}\Delta\Omega'\mathrm{d}\omega = \frac{\partial}{\partial t}[I(t)\frac{\partial\varphi_m}{\partial t}]$ [255], we achieve

$$\frac{\partial I(t)}{\partial \Phi_2} = -\Gamma_{s,e}(0)\frac{\partial}{\partial t}\left[I(t)\frac{\partial\varphi_m(t)}{\partial t}\right]. \qquad (7.14)$$

Here, we have taken into account that $m(t)$ can be written as $m(t) = I^{1/2}(t)\exp[-i\varphi_m(t)]$. Equation (7.14) has exactly the same structure as its spatial counterpart [247]. This important result establishes that the equation governing the intensity variations for a partially coherent pulse provided by Eq. (3.9) is exactly the same as in the coherent case [254] (for which only $m(t)$ appears), as long as the intensities are properly averaged over the ensemble. From Eq. (7.14), the phase, or more exactly the chirp, can be calculated by inverting the equation if the intensity is measured for two different GDD values. Assuming $I_1(t)$ is the averaged intensity profile measured at $\Phi_2 = 0$, and $I_2(t)$ the profile measured at Φ_2, the chirp can be recovered by calculating the derivative in the approximate way

$$\frac{\partial\varphi_m(t)}{\partial t} \approx \frac{-1}{\Phi_2 I(t)}\int_{-\infty}^{t}[I_2(t') - I_1(t')]\mathrm{d}t'. \qquad (7.15)$$

Here, we have assumed that $\Gamma_{s,e}(0) = 1$, which physically requires that the intensity measurements are properly normalized. Since, according to Eq. (7.10), the GDD amount is small, the averaged intensity distributions $I_1(t)$ and $I_2(t)$ are very similar, and then $I(t)$ in the denominator can be taken as $I_1(t)$ or $I_2(t)$, indistinctly. However, the variation is noticeable enough to extract the input chirp distribution. Finally, as can be clearly seen from Eq. (7.15), this procedure does not work for input intensity profiles having zeros. The temporal version of the TIE has proved to be a very powerful tool for measuring phase-only and phase-mostly *coherent* temporal intensity signals [254]. However, measurements for the partially coherent case in the temporal domain are not reported yet in the literature.
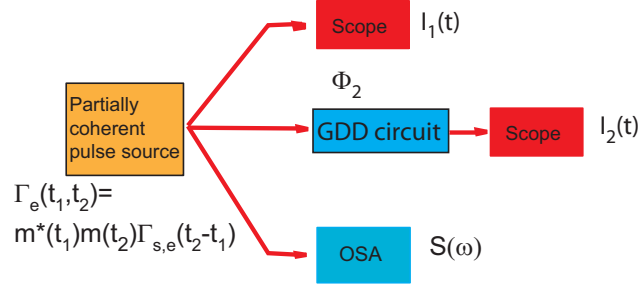
Figure 7.3: Non-interferometric characterization of partially coherent light pulses obeying the independent-elementary-pulse-representation model in the spectral domain.

With the information of the intensity and phase of the deterministic function $m(t)$, we just have to know the weight profile, $S_{s,b}(\omega)$, in order to extract the full structure of the MCF. Let us assume that we measure the ES of the partially coherent light pulse with an OSA. With the knowledge of the chirp and the intensity of $m(t)$, we can calculate its Fourier transform $\tilde{M}(\omega)$ (apart from an irrelevant phase constant). Thus, according to Eq. (3.8), $S_{s,b}(\omega)$ can be calculated by deconvolving the measured ES with the previously calculated ES of the deterministic function, $|\tilde{M}(\omega)|^2$. Once $S_{s,b}(\omega)$ is calculated, $\Gamma_{s,e}(\tau)$ is given by inverse Fourier transformation, and the complete MCF structure is achieved. Figure 7.3 summarizes the three different measurements necessary to retrieve the MCF.

This procedure was recently proposed in the spatial domain in [242]. Here, we have developed the temporal counterpart and clarified the different steps in order to characterize fully an MCF as the one provided at Sect. 3.3.1. We must emphasize that the possible experimental arrangement suggested in Sect. 3.3.1 is just a particular procedure for achieving such an MCF. In any case we mean that the model given by Eq. (3.9) is uniquely obtained by modulating a stationary source with a deterministic gate. In fact, the structure from Eq. (3.9) is in general achieved whenever we have a source of multiplicative noise obeying stationary statistics affecting a deterministic pulsed source. That is the case, for instance, in free-running passively mode-locked lasers [122].

7.3.2   Spectral domain approach

Let us now assume that we want to characterize a partially coherent light pulse for which we know it to obey the specific model presented at Sect. 3.3.2. Thus, in order to characterize fully the CSDF, we just have to know the shape of the weight function $f(t)$, and the coherent basis, $\tilde{E}(\omega)$, in amplitude and phase. Since, again, we decompose $\tilde{E}(\omega) = |\tilde{E}(\omega)| \exp[i\varphi_e(\omega)]$, and assume that measurements of the averaged ES can be readily provided, $|\tilde{E}(\omega)|$ can be measured straightforwardly. In order to extract $\varphi_e(\omega)$, we proceed to analyze the distortion of the ES of a partially coherent pulse propagating through a time lens,

$$S_{b,\text{out}}(\omega) = \frac{1}{4\pi^2} \iint \overline{\Gamma}_{e,\text{in}}(\bar{t}, \tau) \exp[i\tau(\omega + \bar{t}K)]\mathrm{d}\tau\mathrm{d}\bar{t}, \qquad (7.16)$$
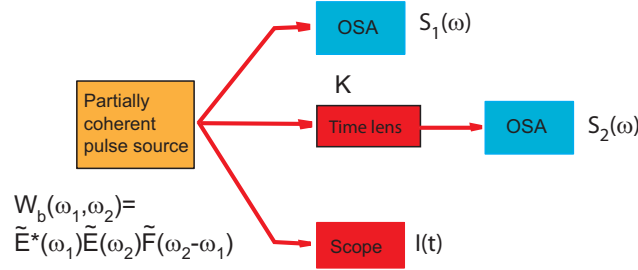
Figure 7.4: Non-interferometric characterization of partially coherent light pulses obeying the independent-elementary-pulse-representation model in the time domain.

where $\overline{\Gamma}_{e,\text{in}}(\bar{t}, \tau)$ corresponds to Eq. (3.11), and K is related with the chirp of the time lens (see Sect. 5.3.1). Note that this is exactly the dual situation described in the previous subsection.

The partial derivative of Eq. (7.17) with respect to K leads

$$\frac{\partial S_{b,\text{out}}(\omega)}{\partial K} = \frac{i}{4\pi^2} \int \bar{t} \mathrm{d}\bar{t} \frac{\partial}{\partial\omega} \left[\int \overline{\Gamma}_{e,\text{in}}(\bar{t}, \tau) \exp(i\tau\omega)\mathrm{d}\tau \right], \tag{7.17}$$

where we have assumed that the time lens satisfies

$$K << \frac{2\pi}{\sigma t_c}, \tag{7.18}$$

with σ being the temporal width of the input partially coherent pulse and t_c its coherence time. That inequality allows for removing the exponential term $\exp(i\tau K\bar{t})$ in Eq. (7.17), which is achieved with a time lens with relatively low chirping rate. Furthermore, by arbitrarily selecting the weight function with its first order moment null, $\int t f(t)\mathrm{d}t = 0$, and with the help of the relation $\iint te^*(t - \tau/2)e^*(t + \tau/2) \exp(i\omega\tau)\mathrm{d}\tau\mathrm{d}t = 4\pi^2 |\tilde{E}(\omega)|^2 \frac{\partial\varphi_e(\omega)}{\partial\omega}$, we achieve

$$\frac{\partial S_{b,\text{out}}(\omega)}{\partial K} = \tilde{F}(0)\frac{\partial}{\partial\omega} \left[|\tilde{E}(\omega)|^2 \frac{\partial\varphi_e(\omega)}{\partial\omega} \right], \tag{7.19}$$

where we are denoting $\tilde{F}(0) = \int f(t)\mathrm{d}t$. Equation (7.19) is the dual version of the TIE. It can be considered as the transport-of-energy-spectrum equation (TESE), but generalized to the partially coherent case. In the temporal domain, this equation has been already reported for fully coherent pulses only [256]. This case has been proved to be particularly useful for measuring the spectral phase of coherent ultrashort light pulses having a relatively wide and flat spectrum profile and without zeros.

In the partially coherent regime, assuming that the pulse to be measured obeys the time-domain independent-elementary-pulse representation model, we can easily calculate the spectral phase, or more exactly the delay profile, of the elementary pulse by integrating the TESE. To do this, we have to measure first the ES of the partially coherent light pulse at both the input, $S_1(\omega)$, and output, $S_2(\omega)$, of a time lens with a chirping rate satisfying Eq. (7.18). Therefore, from Eq. (7.19) we get

$$\frac{\partial\varphi_e(\omega)}{\partial\omega} \approx \frac{1}{|\tilde{E}(\omega)|^2 K} \int_{-\infty}^{\omega} [S_2(\omega') - S_1(\omega')]\mathrm{d}\omega', \tag{7.20}$$

where we have considered $\tilde{F}(0) = 1$, which implies that the ES measurements are properly normalized.

Once $\tilde{E}(\omega)$ is calculated, the weight function $f(t)$ can be calculated from Eq. (3.14). To this aim, we have to measure first the averaged intensity of the partially coherent coherent pulse to be characterized, which is mathematically given by Eq. (3.14). Following the same reasoning as before, the function $f(t)$ can be calculated by deconvolving the measured averaged intensity with the function $|e(t)|^2$, that has to be calculated from the knowledge of $\tilde{E}(\omega)$. Figure 7.4 schematically summarizes this procedure for measuring such a particular MCF.

Applications in microwave photonics

Photonic processing of microwave and RF signals is a research topic that has been explored for more than 30 years [257–259]. Indeed, microwave photonics offers many well-known advantages like reconfigurability, high bandwidth, immunity to electromagnetic interference, high-speed processing, and potential integrability with fiber optics technology [195]. These features are very difficult to achieve with electronic approaches, if not impossible. Typical microwave-photonic applications cover analog-to-digital conversion, beam-forming, filtering, and arbitrary waveform generation (AWG) [260].

In this Chapter we focus our attention on the generation and filtering of RF signals using both, coherent and incoherent techniques.

8.1 Photonically assisted filtering of RF signals

Concerning the processing of microwave signals in the optical domain, from the aforementioned advantages probably the most important ones are the flexible and reconfigurable filter design, low frequency-dependent losses, and larger bandwidth [195, 260].

In a photonic microwave filter, the input RF signal modulates an optical source, the modulated optical waveform is then processed in a photonic circuit, and finally the signal is recovered back in the electrical domain by optoelectronic (O/E) conversion [195, 260]. Usually, the use of spectrally incoherent sources is preferred because the filtering operation is more robust against environmental fluctuations [261]. It is then required that the coherence time of the optical source be shorter than the tap delay, ensuring that intensities are summed and weighted before O/E conversion. However, since intensity is always positive, the RF-filter design cannot be completely arbitrary. From a digital-filter perspective, this is because the tap weight is positive. This drawback may be solved, e.g., by employing alternative modulation formats combined with differential photodetection [262–267], or nonlinear effects in either SOAs [268] or SMFs [269, 270]. Additionally, in discrete-time processing, the resulting RF filter response is periodic [271].

Recently, it has been recognized that the use of pulse-shaping technologies provide the convenient framework for high-bandwidth, user-defined filter implementation [32, 272–275]. The spectral shapers based on spatial light modulators (SLMs) feature simultaneously reconfigurability and tunability by controlling the voltage applied on the liquid crystal. This translates into an effective way of producing a huge number of taps with

controllable weight. With such a high spectral resolution, the energy distribution can be considered as non-discrete, leading to a practically infinite free-spectral range [32, 276]. The use of spectral encoders based on SLMs [220] for RF filtering has been verified using incoherent [36, 272, 273] and coherent optical sources [274, 275].

8.1.1   Mathematical treatment

Among the existing RF-filtering architectures, we will focus our attention on the one presented at Fig. 8.1. The modulator acts as an electrical-to-optical converter. The optical source is considered to be spectrally incoherent (the gain spectrum of an EDFA in the figure), and its ES is continuously tailored by means of a SLM located in the Fourier plane of a zero-dispersion pulse shaper [62, 220]. The RF signal to be filtered comes into an external modulator, which for simplicity we will restrict to be either an EOM, EOPM, or single-sideband (SSB). After modulation, the light is launched into a GDD circuit and later is converted back to the electrical domain with a square-law photodetector. In the most general case, it is not possible to establish a simple relation between the input and output RF signals. However, if the input RF is described as a superposition of sinusoidal signals, we can then analyze the effect of a single RF tone and study under which conditions the system behaves linearly.
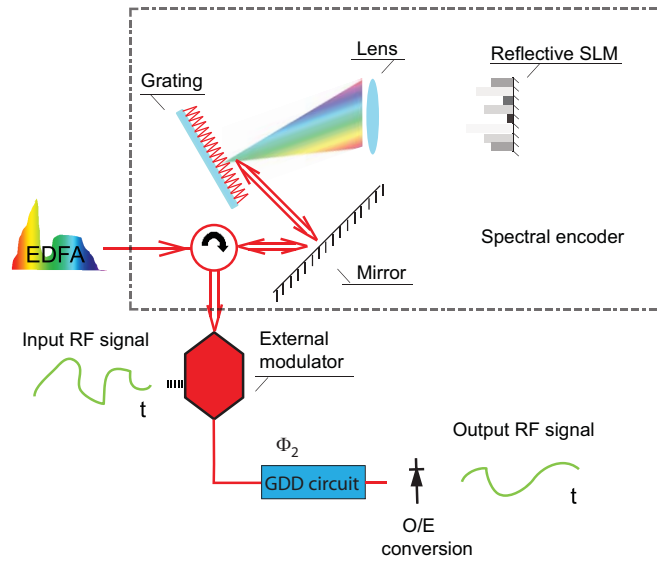

Figure 8.1: Schematic diagram of a RF photonic processor operating with an EDFA as the spectrally incoherent source. The spectral shaping is performed with a Fourier transform pulse shaping device in a reflective geometry.

We note that at the output of the photodiode (PD), the measured current will be

$$I_{\mathrm{PD}}(t) = \eta I_{\mathrm{out}}(t) \otimes R(t), \tag{8.1}$$

where η is an irrelevant constant depending on the efficiency of the photodetector, $R(t)$ is the finite temporal response of the PD, and $I_{\mathrm{out}}(t)$ is given by Eq. (5.51), with $S_{s,b}(\omega)$

being now the filtered ES of the incoherent optical source. Additionally, in our case

$$m(t) = 1 + m_1 \exp(i2\pi ft) + m_2 \exp(-i2\pi ft), \tag{8.2}$$

where the real coefficients m_1 and m_2 take into account the different modulation formats, and f is the RF. For an EOM (or double-sideband modulator), $m_1 = m_2 = \Delta\theta$; for SSB $m_1 = \Delta\theta$ and $m_2 = 0$; and for an EOPM $m_1 = J_1(\Delta\theta)$ and $m_2 = -J_1(\Delta\theta)$, where $\Delta\theta$ is the modulation index and $J_q()$ is the qth-order Bessel function of the first kind. The averaged output intensity gives rise to a DC term and two oscillatory signals at frequencies $2f$ and f. From a practical point of view, the term at $2f$ can be neglected if $\Delta\theta$ is small enough, which can be achieved by placing an RF attenuator at the input of the external modulator. Under this assumption, and neglecting the DC term (which can be achieved by placing a filter), we can define a proper normalized transfer function between the input and output single-tone RF signal, i.e., $H(f) = \tilde{I}_{\mathrm{PD}}(f)/\tilde{I}_{\mathrm{in}}(f)$, where $\tilde{I}_{\mathrm{PD}}(f)$ and $\tilde{I}_{\mathrm{in}}(f)$ are the Fourier transform of $I_{\mathrm{PD}}(t)$ and $I_{\mathrm{in}}(t)$, respectively. Here, we consider f the frequency of the signal measured in Hertz, and $I_{\mathrm{in}}(t)$ represents the electrical intensity input to the filter. Then [277, 278]

$$H(f) = H_1(f)H_2(f)H_3(f), \tag{8.3}$$

where

$$H_1(f) = \frac{\Gamma_{s,e}(-2\pi f \Phi_2)}{\Gamma_{s,e}(0)}, \tag{8.4}$$

$$H_2(f) = \begin{cases} \cos(2\Phi_2\pi^2 f^2) & \text{for} \quad \text{EOM} \\ \exp(i2\Phi_2\pi^2 f^2) & \text{for} \quad \text{SSB} \\ \sin(2\Phi_2\pi^2 f^2) & \text{for} \quad \text{EOPM} \end{cases} \tag{8.5}$$

and $H_3(f)$ is the PD transfer function, i.e., the normalized Fourier transform of $R(t)$.

This result indicates that the effective transfer function of the microwave filter can be expressed as the combination of the responses associated with the filtered ES, $H_1(f)$; the linear propagation in the GDD circuit, $H_2(f)$; and the PD response, $H_3(f)$. We note that $H_1(f)$ corresponds to a mapping of the MCF of the filtered optical source [32]. This opens the door for sculpting microwave filters by synthesizing, through an inverse problem, the ES of the source through frequency encoding. This result constitutes a generalization of those found in the context of incoherent tapped filters concerning the influence of the finite bandwidth of the spectrum slices [279, 280]. Finally, it should be mentioned that a deeper analysis of the effects of TOD on the filter characteristics can be found in [266, 278, 280].

8.1.2 Experimental results

The main problem of the device in Fig. 8.1 for implementing band-pass filtering operations is the fact that the function $H(f)$ contains a nondisregarding spectral content around $f = 0$, which is known in the literature as a baseband resonance. From Eq. (8.3), we recognize that the use of an EOPM alleviates this problem because of the notch at the DC frequency associated with $H_2(f)$ [264]. However, by properly synthesizing the MCF of the optical source, one could synthesize the RF filter even using an EOM or an SSB

modulator. This can only be done through the tailoring of the ES. Since this is a positive and real magnitude, arbitrary $H_1(f)$ functions, and therefore $H(f)$, cannot be achieved. However, a broad range of practical examples can be obtained with an adequate Fourier algorithm design [281].
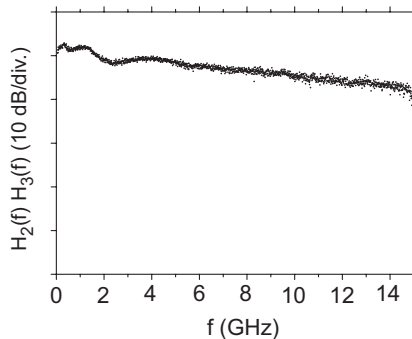

Figure 8.2: Measured filter transfer function corresponding to the terms of the PD and the EOM for an SMF of 4.6 km length.

As an example, we aimed to design an RF filter with a resonant flat bandpass at the region corresponding to 4-7 GHz, which could be interesting for ultra-wideband (UWB) applications [274]. Thus, we built the experimental setup corresponding to Fig. 8.1, where the external modulator was provided by the same 10 Gb/s LiNbO$_3$ EOM as in Sect. 6.2. Therefore, we have to prevent from the carrier suppression effect, i.e., the first zero in the cosine term in Eq. (8.5). We selected an SMF as GDD circuit with a length of 4.6 km, giving rise to an almost flat $H_2(f)$ function for the RF interval corresponding to 0-10 GHz. This would ensure us that the resulting $H(f)$ is mainly given by the $H_1(f)$ term. To test this, we first employed a narrowband CW laser and measured the corresponding filter transfer function. The measurement of the RF filter is done with a lightwave component analyzer (LCA)[1]. The measured filter transfer function is sketched in Fig. 8.2. As expected, we can see the flatness over the region of interest. Thus, by exchanging the laser with a spectrally incoherent source and keeping the same fiber length, we can stay that the new $H(f)$ will be essentially provided by a scaled version of the MCF of the synthesized optical source. Thus, we then replaced the laser with an ES provided by the gain spectrum of an EDFA, and the spectral tailoring was performed with a commercially available zero-dispersion pulse shaper. This device has been designed for controlling the channels in D-WDM communication systems, and possesses 48 channels with 100 GHz resolution spanning the whole C band and < 6 dB insertion losses (Peleton, QTM) [282]. The amplitude of each channel could be blocked fully, or reduced in increments of 0.1 dB up to a

---

[1]An LCA is an optoelectronic device that links the RF input port of the EOM with the RF signal received at the output of the PD. It launches a sweepable single tone signal at frequency f with controlled amplitude at the input. It also measures the relative ratio, in amplitude and phase, between the input signal at f and the magnitude of the same frequency measured at the output of the PD. In other words, it gives $H(f)$ over a predefined sweeping range.

maximum of 20 dB. Due to the source incoherence, the output waveform is independent of the reminiscent spectral phase of the individual channels [283]. The synthesized ES was measured with an OSA and is sketched in Fig. 8.3(a). Finally, the achieved RF filter is illustrated in Fig. 8.3(b). The group delay, i.e., the derivative of the spectral phase of $H(f)$ is also sketched for completeness in Fig. 8.3(c). Apart from the inherent baseband resonance, we achieved the desired flat-top RF filter that spans over the frequency range from 3.2 GHz to 8.8 GHz, compatible with UWB technology [274].
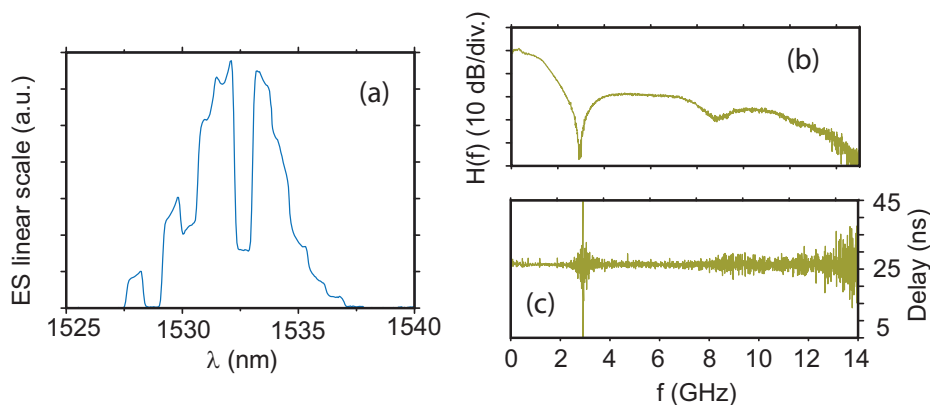

Figure 8.3: Measured filter transfer function corresponding to the terms of the PD and the EOM for an SMF of 4.6 km length.

8.2 Generation of RF and mm-wave signals

Generation, control, and distribution of microwave and millimeter-wave arbitrary signals is an important research topic due to potential applications in UWB communication systems, radar, RF communications, sensor networks, and electronic test measurements [195]. Electronic devices used to generate high-frequency complex waveforms are seriously limited by the bottleneck of digital-to-analog technology. In practice, current electronic AWGs are restricted to create RF signals with a bandwidth below ~ 5 GHz [195]. In contrast, photonically-assisted AWGs far exceed this range. In general terms, the upper limit in terms of the analog RF spectral content that can be achieved using photonic approaches is just set by the O/E conversion bandwidth. Commercially available PDs currently place this limit beyond the mm-wave region [260].

In this section we review some coherent and incoherent photonic approaches for producing high frequency electrical signals with reconfigurability capabilities.

8.2.1 Beating of coherent spectral lines

The earliest photonic approach to generate high-frequency microwave signals was achieved just by making different CW lasers to beat together and measure the temporal intensity signal with a high-bandwidth PD [284]. However, the need of phase-locked loops to control the stability of the generated signal and the impossibility to synthesize the achieved RF waveform motivated the search for alternative solutions. Wiberg *et al.* proposed a simple

approach involving the use of a single CW laser modulated with an EOM, pumping a nonlinear device in order to generate four-wave-mixing interactions. Therefore, mm-wave signals were achieved by spectral selection and beating of the generated high-frequency components [285]. Currently, with the development of stable in-fiber frequency comb generators [193, 286, 287], the beating can be achieved from different coherent lines in a comb at higher frequencies [95, 288].

8.2.2   Upshifting based on temporal imaging of virtual Talbot planes

Despite the simplicity of the previous approaches, the tunability and reconfigurability of the produced RF waveforms is still very restricted. However, with the TISs explained at Sect. 5.5.3, a scaled replica in intensity of an input coherent waveform can be easily achieved. If we focus our attention on the case of an input optical source amplitude modulated with an arbitrary RF signal, we realize that achieving a compressed replica with a TIS is synonymous to achieve an upshifted RF signal after O/E conversion with an ideal PD [289].
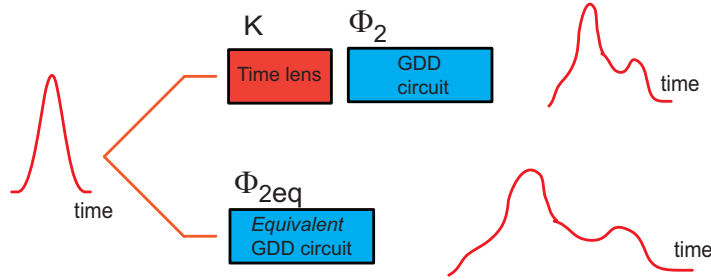

Figure 8.4: A transform-limited pulse is split in two arms. The upper arm first chirps the pulse and propagates it through a GDD circuit. The lower arm, composed by only a GDD circuit, is fully equivalent to the first arm in the sense that it may provide the same output intensity distribution as the first one, with different scale, if the GDD parameter is selected according to Eq. (8.6).

A more advanced configuration of the above proposal was later verified by Azaña *et al.* [145, 290]. To understand their procedure we should first clarify the following situation. Let us consider a coherent chirped optical pulse (a signal followed by a time lens with chirping K) propagating through a GDD circuit with Φ_2. In virtue of the property given by Eq. (5.14), the temporal transformation suffered by the chirped pulse can be rewritten in terms of the unchirped version traveling through an equivalent GDD circuit with parameter [144]

$$\Phi_{2\text{eq}} = \frac{\Phi_2}{1 - K\Phi_2}, \tag{8.6}$$

a scale factor given by

$$m_{\text{eq}} = 1 - K\Phi_2, \tag{8.7}$$

and new chirping coefficient provided by

$$K_{\text{eq}} = K/m_{\text{eq}}. \tag{8.8}$$

Therefore, according to Eq. (8.6), the temporal intensity profile achieved at Φ_2 by the chirped version is just a temporal image, with scale m_{eq}, of the one that would be achieved by the unchirped version at $\Phi_{2\text{eq}}$. This situation is schematically explained in Fig. 8.4.
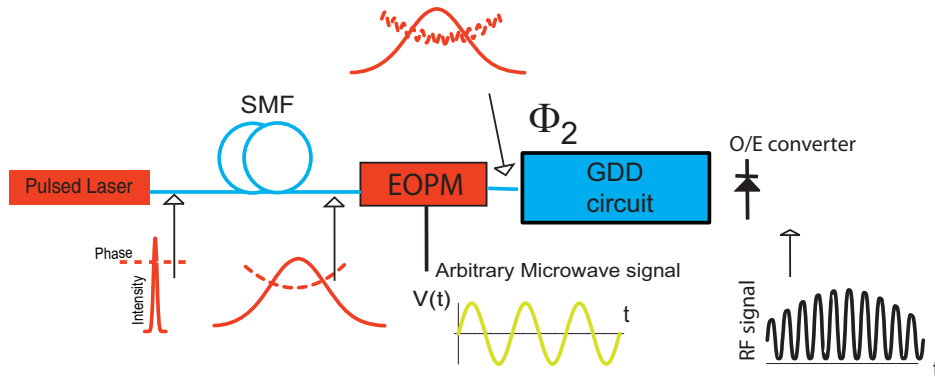

Figure 8.5: Schematic setup for mm-wave generation with a low-bandwidth RF signal driving an EOPM.

In the work reported in [145], the key to achieve the upshifting was to consider the coefficient $\Phi_{2\text{eq}}$ corresponding to the *integer* Talbot planes of an input periodic amplitude-modulated arbitrary signal. Note that the time lens must have a large temporal aperture in order to contain several periods of the initial sequence [290]. This situation was achieved by predistortion of an ultrashort pulse trough an SMF. Based on this general result, a $\sim 350\,\text{GHz}$ sinusoidal waveform with finite duration was achieved just starting from one of $40\,\text{GHz}$ [145] modulating an EOM.

A similar setup can be achieved with an EOPM, instead of an EOM, providing several advantageous features like high throughput and reconfigurability [22]. The reconfiguration is achieved by changing electrically an input low bandwidth RF periodic signal, and low losses are guaranteed by the phase modulation. In that case, the RF signal drives the EOPM, and we should consider the GDD amounts $\Phi_{2\text{eq}}$ corresponding to the *fractional* Talbot planes given by Eq. (5.29). Strictly speaking, we could not speak about "upshifting" because we are creating a different RF signal to the input one. Our setup is depicted in Fig. 8.5. The first ultrashort pulse is spread into an SMF. The acquired quadratic phase modulation is used as temporal lens with linear-chirping coefficient K. The subsequent GDD circuit is designed according to Eq. (8.6) to achieve a compressed replica that would be obtained at $\Phi_{2\text{eq}}$ if instead of the laser pulse a CW source was used. The analysis of the different intensity signals achieved at fractional Talbot planes by distortion of CW periodically phase-modulated signals has been developed in Sect. 5.5.6.

We have tested the validity of the technique through numerical simulations. The laser is assumed to provide $1\,\text{ps}$ rms width centered on $1.55\,\mu\text{m}$, leading to $\beta_2 = -21.6\,\text{ps}^2/\text{km}$ when an SMF is considered. The first example concerns the generation of a high-bandwidth flat-top–like pulse profile, for which a sinusoidal RF driving signal into the EOPM is assumed. We want to perform the image of the virtual intensity distribution that would be achieved at $\Phi_{2,\text{eq}} = \Phi_{2\text{T}}/4$, which, as explained at Sect. 5.5.6, is flat-top
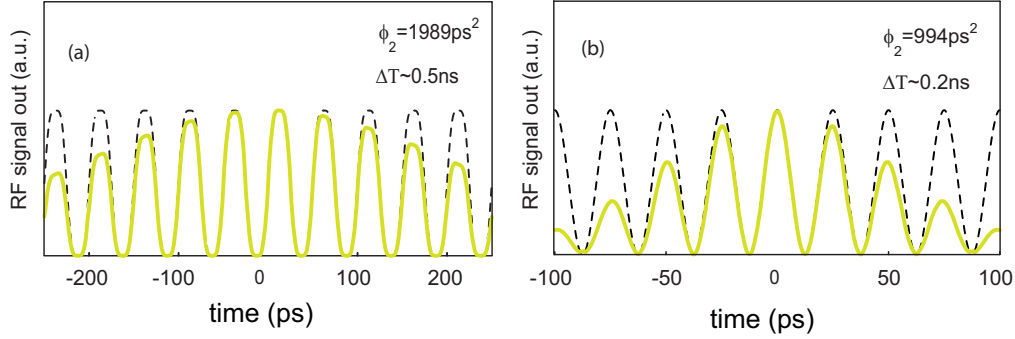
Figure 8.6: In solid line, results of numerical simulation and the case when aperture effects are neglected is plotted in each figure in dashed line. (a) Flat-top pulse RF-signal profile from a sinusoidal signal driving the EOPM at 2 GHz; (b) RF signal with sinusoidal variation obtained from an EOPM driven with a triangular profile at 2 GHz repetition rate.

for a modulation index of $\Delta\theta = \pi/4$ rad. For this aim, from Eqs. (8.6) and (8.7), we infer a fiber length of 102 km and an output GDD parameter of $\Phi_2 = 1989\,\text{ps}^2$ for a $f_r = 2\,\text{GHz}$ incoming RF signal. The resulting waveform after O/E conversion is depicted in Fig. 8.6(a), where a burst of nearly 20 GHz repetition rate is clearly achieved over a temporal aperture of 0.5 ns. In the second example we demand an output RF profile that corresponds to a single tone at 40 GHz repetition rate. As shown in Fig. 8.6 (b), this can be achieved by designing the GDD parameter to perform a temporal image of the virtual Talbot plane corresponding to $\Phi_{2,\text{eq}} = \Phi_{2\text{T}}/4$ and a triangular pulse profile like the one presented at Fig. 5.13 with $\Delta\theta = \pi/2$ at a repetition rate of $f_r = 2\,\text{GHz}$. We just need an SMF of 48 km and $\Phi_2 = 994\,\text{ps}^2$. The corresponding time aperture would be around 0.2 ns.

Finally, it must be mentioned that the first experimental verification of this technique has been recently achieved [291]. There, the flat-top pulse waveform from Fig. 8.6(a) has been reported at 18.2 GHz with a time aperture of 25 ps just starting from a sinusoidal RF tone at 3.7 GHz.

8.2.3   Fully reconfigurable generation with pulse shapers

Fully reconfigurable and nearly arbitrary RF signals can be achieved with pulse shapers and broadband coherent pulses as the optical source. With the DST pulse shaper [83], sequences of mm-wave signals are readily achieved just by designing adequate spatial masks [85, 292]. The drawback of this system, as for those proposed in the previous section, is that the generated RF signal lies only over a finite temporal aperture. However, there are many cases in which it would be of practical interest to generate continuously operating RF signals. Within the Talbot-based approaches and the DST pulse shaper, this is not possible because the generated RF signals are not wide enough to occupy a pulse period from the initial pulse train.

To overcome this problem while keeping the reconfiguration capabilities in mind, Chou
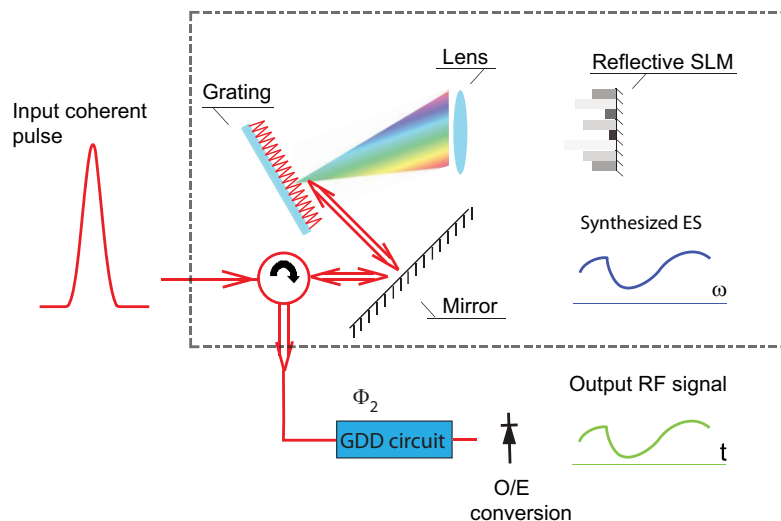
Figure 8.7: Fourier transform pulse shaper in a reflective geometry for achieving RF waveforms [293].

et al. proposed the simple yet elegant solution of using a Fourier transform pulse shaper for shaping the ES of a coherent ultrashort pulse [293]. This scheme is illustrated in Fig. 8.7. The zero dispersion pulse shaper tailors the spectrum of the incoming broadband coherent light in a user-defined fashion. Later, the pulse is launched in a GDD circuit, usually an SMF for simplicity. If the GDD parameter satisfies Eq. (5.19), with σ being the duration of the synthesized waveform at the input of the fiber, the temporal intensity profile at the output of the SMF is just a scaled version of the synthesized ES (see Sect. 5.5.1). Therefore, larger amounts of dispersion do not change the shape, only the scale of the output pulse. Then the inherent limitation of the temporal aperture is overcome just by adding a larger fiber, and continuously operating RF signals can be achieved by O/E conversion. With this system, complex waveforms [281] and closed loops for compensating for higher-order distortion can be performed to generate error signals that feedback the SLM [294].

8.2.4 Incoherent pulse shaping approach

However, despite all the benefits offered by the above mentioned coherent techniques, the high cost of pulsed sources prevent from jumping out from the research laboratories. A viable alternative could be the use of the incoherent pulse shaping technique explained at Sect. 6.3. Our numerical simulations show that using the gain spectrum of an EDFA and an EOM satisfying the quasi-homogeneous pulse conditions stayed at Chapter V, an RF-waveform generator can be achieved [23]. Even more, for some practical settings, the TOD effects can be disregarded [23].

To test experimentally this approach we have built the system corresponding to Fig. 6.4. The complete setup is depicted in Fig. 8.8. It is very similar to the device developed at Sect. 8.1 and, in fact, it is possible to show that the specific scheme for incoherent pulse shaping from Fig. 8.8 can be understood in terms of an RF filter with
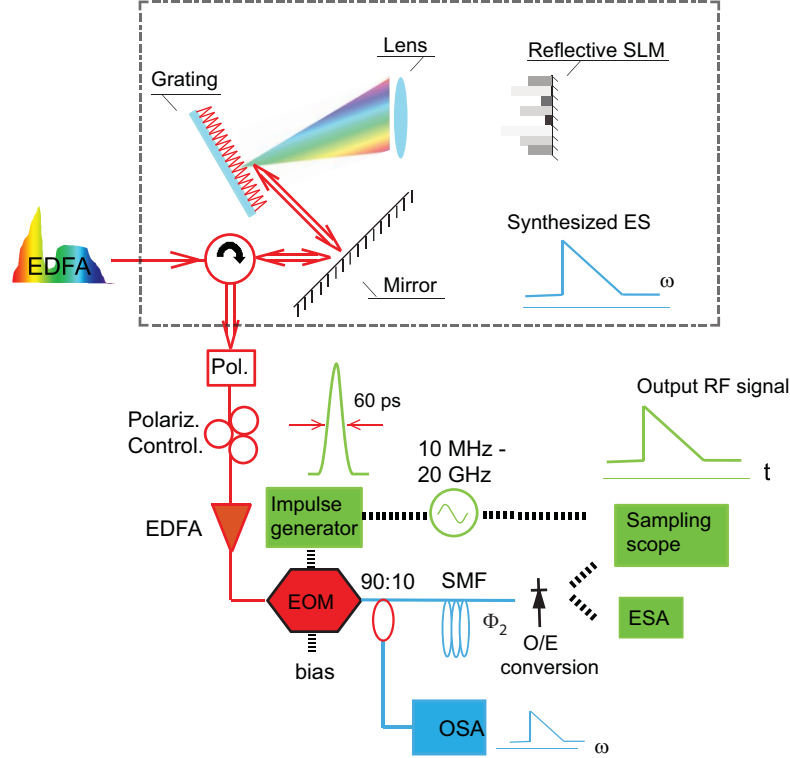
Figure 8.8: Experimental setup for achieving reconfigurable RF-waveform gener-
ator based on incoherent pulse shaping scheme of Fig. 6.4. Pol. is a polarizer.

positive coefficients [36]. As before, the spectral encoder is performed with the same
zero-dispersion Fourier-transform pulse shaper commercially available from Peleton cor-
poration [282]. The main difference with respect to the previous approach is that we now
drive the EOM with a short electrical 60 ps FWHM gaussian impulse. The repetition rate
of this gate is controlled with an RF-single tone generator with a frequency range from
10 MHz to 20 GHz, which is also used for triggering the acquisition module. The optical
averaged intensity at the input of the fiber was first measured with a 20 GHz sampling
scope and is the corresponding to Fig. 6.3(b). The slight discrepancy with the nominal
value of 60 ps is attributed to the slow response of the EOM at frequencies higher than
10 GHz. We must note that the maximum available optical spectral width of 4.8 THz
(the 48 channels on) leads to a coherence time of 33 fs, so that the quasi-homogeneous
condition specified in Fig. 6.1 is satisfied. Even for the case in which one channel is passed
and the rest are blocked, the resulting coherence time (1.6 ps) also satisfies the condition.
We selected as the GDD circuit a tandem of SMFs with different lengths (4.6 or 7.5 km).
With these values, the far-field condition stayed by Eq. (6.11) is satisfied. The control of
the ES tailoring is achieved through the software installed in a laptop connected to the
D-WDM channel controller. A screen image of the program is displayed in Fig. 8.9, which
gives an idea of the simplicity to reconfigure the ES shape.

   The first example concerns the generation of a sawtooth pulse. Such a waveform has
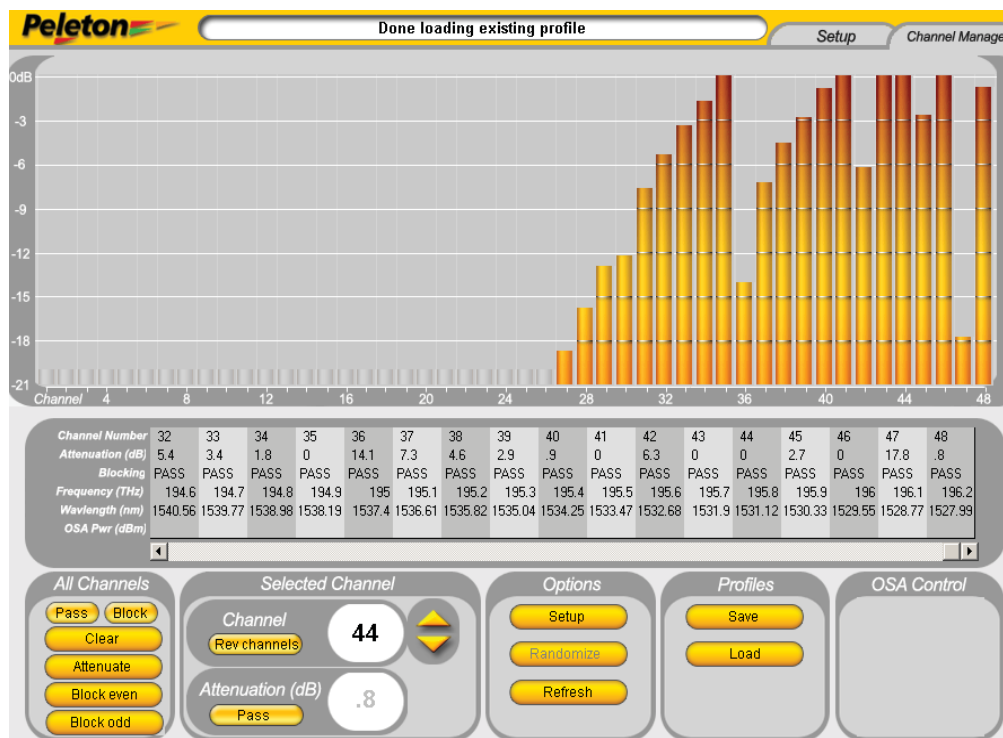
Figure 8.9: Screen image of the software utilized for tailoring the ES.

been generated previously using a Fourier-transform pulse shaper [295] or a fiber grating passive device [296]; in both of these cases, a broadband coherent pulsed source was required. Our synthesized ES was measured with an OSA after the temporal modulation, and is shown in Fig. 8.10(a). We appreciate that, according to Eq. (3.8), the ES corresponding to the modulator behaves as a Dirac's delta distribution, which is synonymous of having a quasi-homogeneous pulse at the input of the fiber. After temporal modulation and stretching in 7.6 km of SMF, the measured temporal waveform is shown in Fig. 8.10(b) and (c) in sample mode with 100 ms persistence and with four times averaging, respectively. The incoherent frequency-to-time mapping predicted by (6.10) is clearly visible. The RF spectrum obtained when using a 4.6 km length of SMF and 100 MHz repetition rate is shown in Fig. 8.10(d). The second example corresponds to the generation of a short pulse burst. The synthesized ES is shown in Fig. 8.10(e); the temporal waveform after stretching in 7.6 km of SMF is shown in Fig. 8.10(f) in sample mode and (g) with four times averaging. Figure 8.10(h) shows the measured RF spectrum when 4.6 km of SMF is used as well as a repetition rate of 300 MHz. The final example concerns the generation of a doublet-like pulse. Figure 8.10(i) shows the ES, and Figs. 8.10(j) and (k) show the temporal waveform in sample mode and with four times averaging, respectively, when using 4.6 km of SMF. The corresponding RF spectrum is shown in Fig. 8.10(l) for a repetition rate of 800 MHz.

One of the key advantages of the proposed technique is the possibility to control the repetition rate of the generated waveform in an easy way. This is achieved by changing the clock frequency that drives the electrical impulse generator. Thus, we can obtain

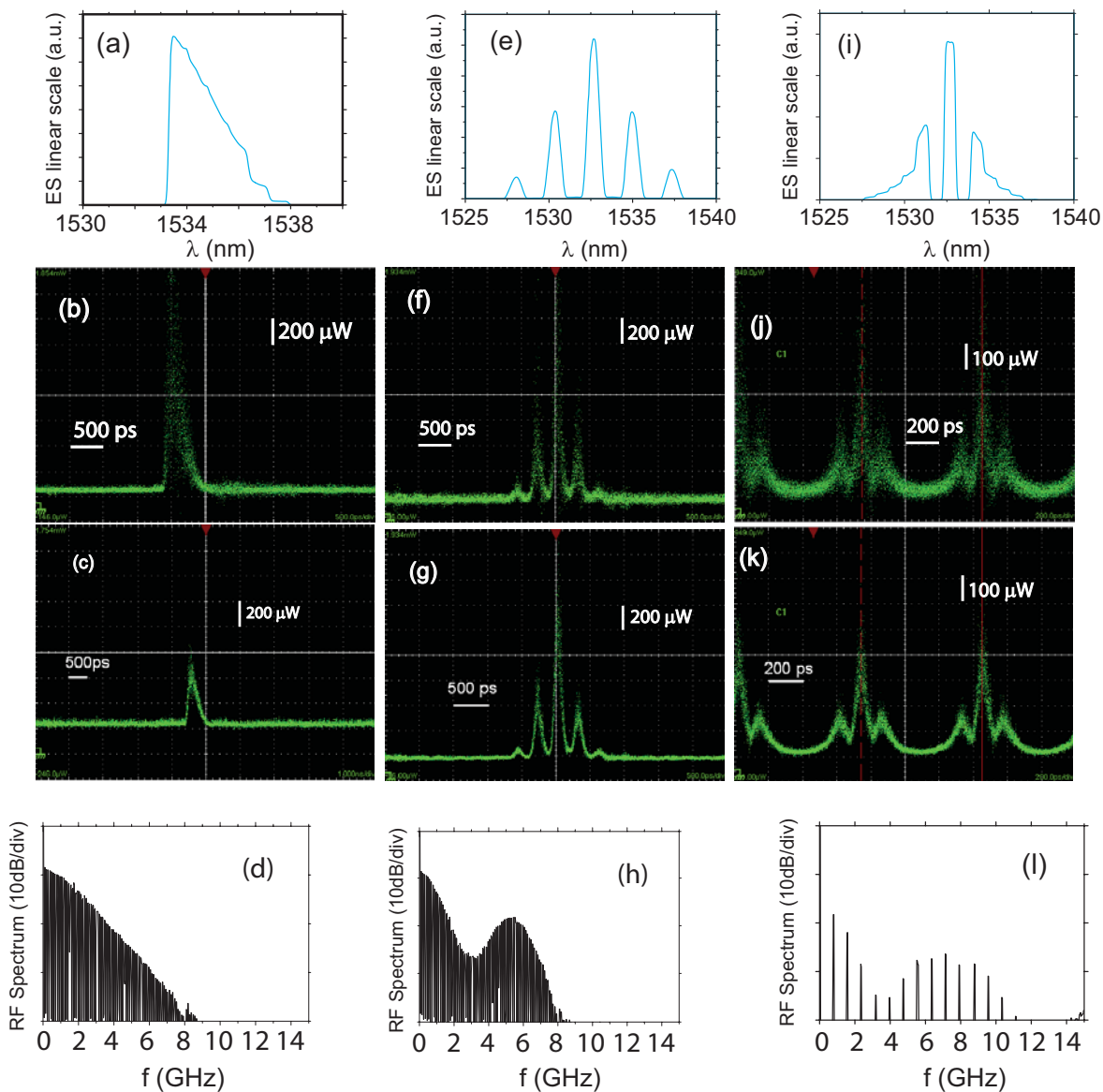**Figure 8.10**: Three different RF signals. Each example corresponds to each column. First row [(a), (e) and (i)] corresponds to the ES. Second [(b), (f) and (j)] and third rows [(c), (g) and (k)] correspond to time intensity in linear arbitrary scale in sample and four times averaged, respectively. Last row [(d), (h) and (l)] correspond to the RF spectra. The specific settings are explained in the text.
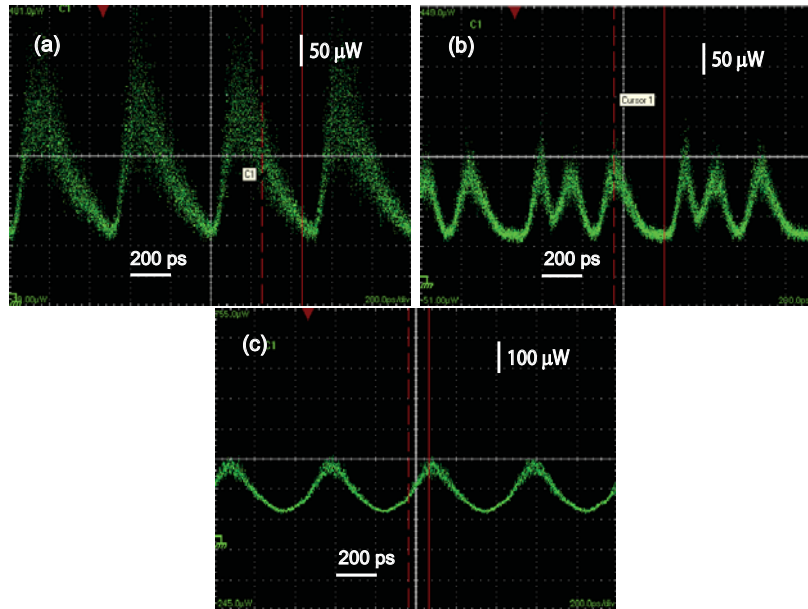
Figure 8.11: Continuous RF signal generation of: (a) sawtooth waveform (four times average); (b) linearly chirped sinusoidal profile (four times average); (c) parabolic pulse train (sixteen times average.

continuous RF waveforms. In particular, we illustrate the generation of a CW sawtooth waveform, a chirped sinusoid, and a train of parabolic pulses, in Figs. 8.11(a), (b), and (c), respectively.

As for the coherent counterpart [293], we note that once the incoherent frequency-to-time mapping is achieved, the output waveform can be scaled by increasing the amount of GDD. This leads to a decreasing of the achieved RF bandwidth. In our experiments, the upper limit is approximately 10 GHz. This limit is not a fundamental constraint and is set by both the EOM and the pulse duration provided by the electrical impulse generator. By using shorter electrical signals, a high bandwidth EAM, and the same D-WDM channel selector, our technique can be scaled up to operate in the millimeter-wave range. In particular, Fig. 8.12 gives a rough estimation of the achievable electrical bandwidth in terms of the input electrical pulse width. By using an external modulator providing < 20 ps temporal widths, it is possible to achieve operation in the mm-wave region.

8.3 UWB-over-fiber technology

In the last few years, there has been a growing interest in the generation of UWB microwave signals. The UWB RF spectrum was regulated between the 3.1 and 10.6 GHz band with a power spectral density of -41.3dBm/MHz, according to the Federal Communication Commission (FCC) of the United States. Later Asian and also European regulations have stayed similar masks [297]. Any signal to be considered as UWB must have an RF spectral bandwidth greater than 500 MHz or a fractional bandwidth greater
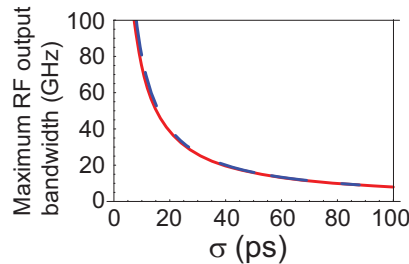
Figure 8.12: Maximum achievable RF electrical bandwidth as a function of the inpout light pulse duration. Solid curve is for a single channel on and dashed curve for all channels on.

than 20% [2]. Due to the high-data-rate capabilities, low power consumption and immunity to multi-path fading, these signals have an unprecedented opportunity to impact radio communication systems in personal area networks, and promise as well substantial applications in radar, safety, and biomedicine [298, 299]. However, such a low spectral power restricts the range of applicability of this wireless technology to several hundreds of meters. In contrast, although a large number of electronic devices for providing UWB pulses exist [297], optical approaches offer a viable alternative with several advantageous features. Indeed, all-optical schemes for UWB-signal generation constitute an ideal scenario for seamless integration and distribution of wireless communications signals over optical fiber links [300]. This is a key feature for increasing the operating range of UWB networks by several orders of magnitude compared to their counterpart electrical approaches.

Usually, monocycle and doublet waveforms are the preferred profiles for achieving UWB compliant signals [297]. These are sketched in Fig. 8.13. It is relatively easy to achieve such kind of waveforms if we realize that they correspond to the first and second-order derivative of a Gaussian pulse shape, respectively.

Previous attempts to generate UWB impulses have used the Fourier-transform geometry from Fig. 8.7 for shaping the ES of an ultrashort light pulse [281, 293, 294]. As before, the UWB signal is achieved by stretching the pulse in a fiber and subsequent photodetection. The key now is that this setup offers the possibility to achieve complex waveforms that fit more efficiently to the regulation masks than the monocycle or doublet [281]. Later, all-fiber variations of this setup have been verified, achieving the generation of monocycle, doublet [301] as well as different but more efficient shapes [302]. Zeng *et al.* also obtained UWB pulses by synthesizing a bandpass coherent microwave filter by combining an EOPM with fiber dispersion [303], acting globally as an electronic differentiator at low frequencies, but implemented in the optical domain.

The chirp-to-intensity conversion effect in spectrally linear filters has also been exploited by using XPM in either SOAs [304] or SMFs [305], or a simple EOPM pumped with a Gaussian pulse [306]. The use of nonlinear effects in SOAs to generate monocycle impulses [307, 308] has been reported too. The former approach [307] uses XGM,

---

[2]The fractional bandwidth is defined as $100 f_0/(f_{max} - f_{min})$, where f_0 is the central RF, and f_{max}/f_{min} correspond to the maximum/minimum RF values at $-10\,\mathrm{dB}$.
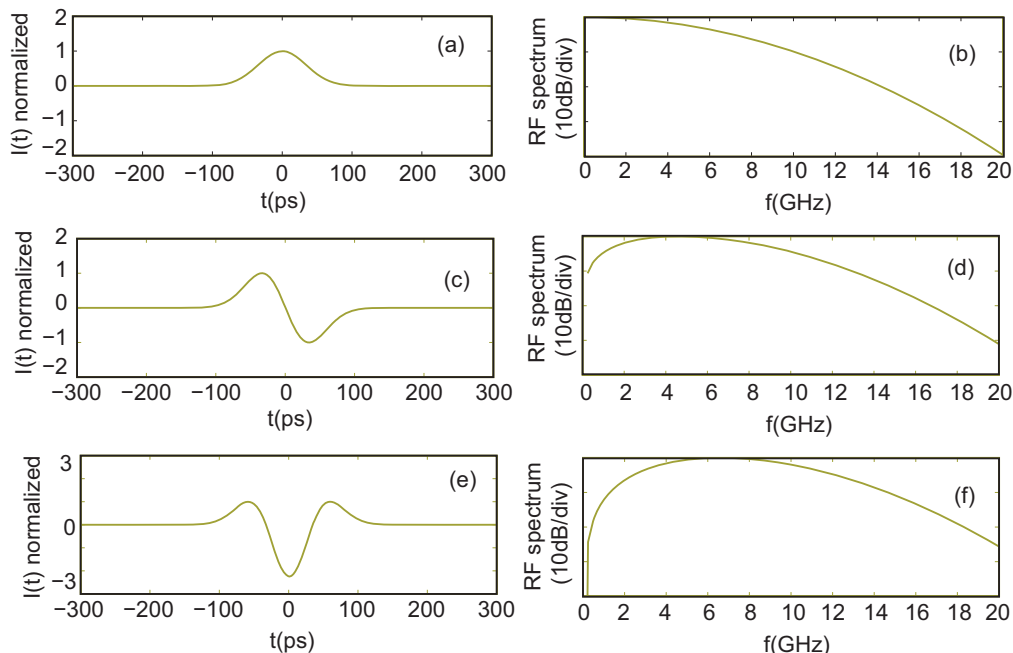
Figure 8.13: Different RF waveforms. Left column corresponds to the time domain and in right column we plot their corresponding RF spectra. (a) and (b) correspond to a Gaussian waveform of 60 ps FWHM; whereas (c) and (d) to a monocycle profile; and finally, (e) and (f) display a doublet waveform. The monocycle and doublet are achieved by first and second- order differentiation of the initial Gaussian pulse.

in which the time delay between two reversely-polarized pulses from the output of the SOA was adjusted with a pair of fiber Bragg gratings until the desired output waveform was obtained. The latter one [308] creates monocycle impulses basing on the intensity overshooting effect of optical dark pulses amplified by an SOA with unsaturated optical gain. A recent review of some of the optical approaches for generating UWB impulses is provided in [300].

The latest advances in photonically assisted UWB pulse generation include the search of alternative low-cost solutions [33,37], as well as different modulation capabilities [309, 310] like code-division multiple access or frequency-division multiplexing [293].

8.3.1 Low-cost alternatives with current-modulated semiconductor lasers

In this section we report a coherent technique to generate UWB-compliant pulses. It involves the use of a distributed feedback (DFB) coherent laser whose driving current is modulated by the electrical data signal to be transmitted [33,37]. With respect to previous approaches, our configuration offers an efficient solution in terms of power consumption and constitutes a low-cost viable alternative, since there are no optical nonlinear process involved requiring extra light sources or additional active optical devices. Our approach requires a single optical light source and avoids the use of external electro-optic modulation. It is worth mentioning that a previous reported work [311] used a current modulated

Fabry-Perot laser for the generation of UWB signals. However, unlike in our approach, the frequency chirp was not used for achieving UWB signal generation. Instead, mono-cycle pulses were obtained by O/E conversion and subsequent differentiation performed in the electrical domain.

With our setup, monocycle or doublet pulse shapes can be achieved. Although the experimental arrangement is the same in both cases, the physical mechanism behind is different. The general setup consists on a DFB semiconductor laser, a 12.5 Gb/s bit pattern generator, and a spectral passband optical filter. The DFB laser is nominally specified for operation at 10 Gb/s, but the driving data signal was selected at the maximum bit rate. The output pulse from the laser is spectrally filtered by the passband filter, which had a Gaussian profile and a FWHM of 0.3 nm. The way of selecting the UWB-pulse shape is by playing with the bias voltage applied to the laser, the amplitude of the data driving signal and the tunable filter. There are two sets of parameters that lead to UWB compli-ant monocycle and doublet shapes. We now proceed to formulate an heuristic explanation for each of the different physical phenomenon behind this achievement.

MONOCYCLE GENERATION

In this case, the laser is forward biased far from the threshold, and a relatively low value of modulating amplitude is selected. The laser dynamics is found in the linear region of the Power–Intensity curve [77]. The key is to remind that, as a result of the changes in the carrier population, the refractive index also changes, leading to a phase-modulation changing with time [77]. Therefore, in the small-signal case the laser pulse becomes highly chirped, with an instantaneous frequency resembling the shape of a monocycle. Then, as heuristically explained in Fig. 8.14, the process of chirp-to-intensity conversion can be achieved by using a spectrally linear optical filter. This behavior is obtained approximately by placing our Gaussian bandpass filter at the linear slope region.
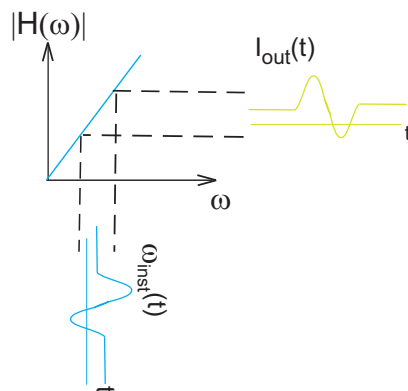

Figure 8.14: Heuristic illustration of the chirp-to-intensity conversion process. An instantaneous frequency with the profile of a monocycle comes to a filter with an linear amplitude transmission. Then, the output intensity profile follows the shape of the input chirp.

Of course, this is just an heuristic explanation and instantaneous frequencies do not

always exist in the ES of a coherent signal [312]. Even more, the case displayed at Fig. 8.14 is only valid for phase-only modulated signals. However, let us formulate mathematically our problem. The complex field of the frequency-chirped pulse is filtered by a linear optical filter $H(\omega) = A(\omega + \omega_s)$, where A is a real constant that determines the slope of the filter and ω_s denotes the vertical offset from the zero-crossing point. The temporal envelope at the output of the filter is given by

$$\psi_{\text{out}}(t) = iA\left[\psi'_{\text{in}}(t) - i\omega_s\psi_{\text{in}}(t)\right], \tag{8.9}$$

where the prime denotes temporal derivation and $\psi_{\text{in}}(t)$ is the input temporal envelope. We have taken into account that $FT^{-1}[-i\omega\tilde{\psi}_{\text{in}}(\omega)] = \psi'_{\text{in}}(t)$, where $\tilde{\psi}_{\text{in}}(\omega) = FT[\psi_{\text{in}}(t)]$, with FT and FT^{-1} denoting Fourier and inverse Fourier transformation, respectively. We can always rewrite the input envelope as $\psi_{\text{in}}(t) = I_{\text{in}}^{1/2}(t)\exp[-i\varphi_{\text{in}}(t)]$, where $\varphi_{\text{in}}(t)$ and $I_{\text{in}}(t)$ denote the phase and normalized intensity modulation, respectively. We now assume that the frequency modulation dominates respect to the intensity modulation, but its contribution value is less than the corresponding frequency offset of the filter, i.e., $|I'_{\text{in}}(t)| \ll |\varphi'_{\text{in}}(t)| \ll \omega_s$. With this assumption, and after some algebra, the optical intensity at the output of the filter can be approximated to

$$I_{\text{out}}(t) \approx 2A^2\omega_s I_{\text{in}}(t)\left[\varphi'_{\text{in}}(t) + \omega_s/2\right]. \tag{8.10}$$

The above equation establishes that the light intensity at the output of the optical filter is given essentially by the frequency chirp of the input optical pulse if the intensity profile is relatively smooth. The derivation of Eq. (8.10) accounts for the heuristic explanation provided in [304–306].
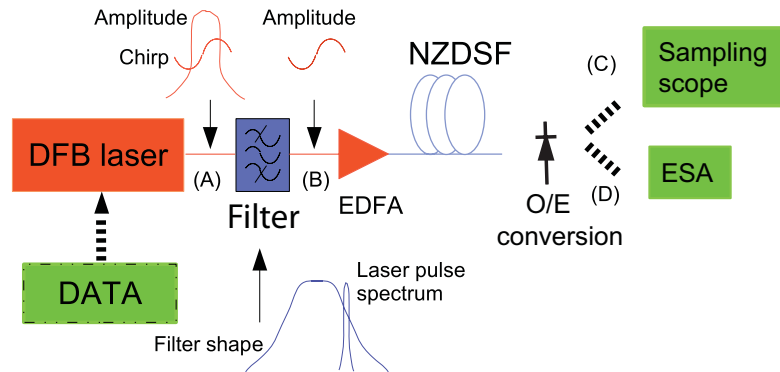
Figure 8.15: Scheme for generation and transmission of UWB monocycle pulse based on chirp-to-intensity conversion with a semiconductor laser.

To test this approach we have built the setup corresponding to Fig. 8.15. The laser was biased to $67\,\text{mA}$, a value far from the threshold of $30\,\text{mA}$, and the bit pattern generator produced a sequence of one "1" followed by seven "0" with a peak-to-peak voltage of $0.566\,\text{V}$. The measured intensity and chirp are displayed at Fig. 8.16(a) in solid and dashed line, respectively. For the measurement of the chirp we employed the TIE procedure [254], for which an SMF of $0.415\,\text{km}$ was used. We can appreciate the monocycle-like profile of

Figure 8.16: (a)Input laser intensity pulse in amplitude (solid line) and chirp (dotted line) and (b) normalized ES of laser pulse (solid line) and amplitude filter (dotted line).

Figure 8.17: UWB monocycle pulse in (a) time domain and (b) frequency domain.

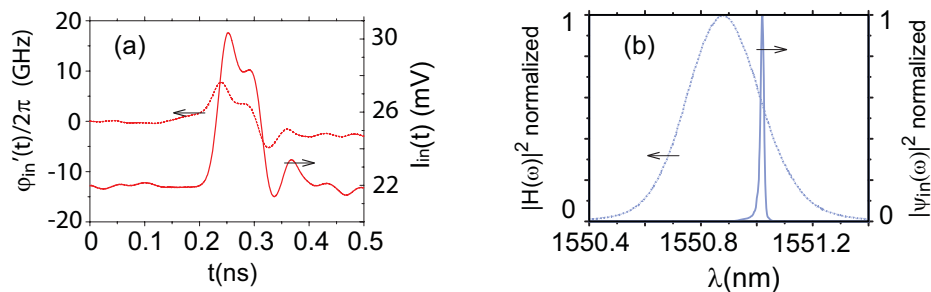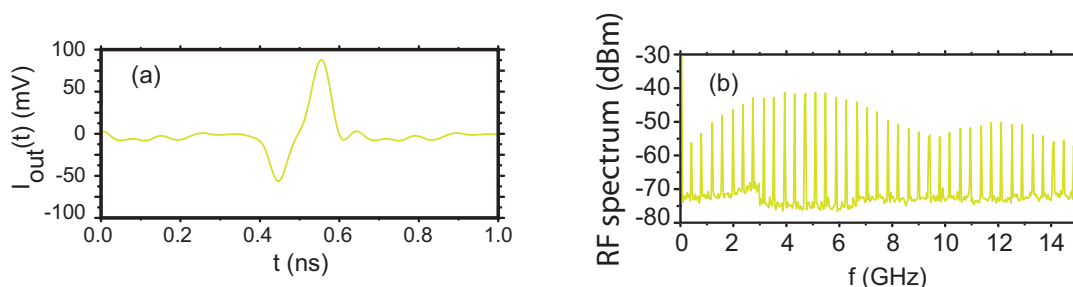the chirp. The ES corresponding to the laser and the filter, when located at the optimal point to achieve the monocycle shape, are displayed together in Fig. 8.16(b). The average optical power level before and after the filter was measured to be 5.6 dBm and −9.1 dBm, respectively.

In order to test the validity of the signal for UWB communications we performed an additional transmission experiment. The optical signal is amplified by an EDFA and propagated through 20 km of non-zero dispersion shifted fiber (NZDSF) with 4.5 dB loss and 5 ps/nm/km dispersion. This dispersion leads to a GDD parameter very low to distort in a significant way the achieved UWB pulse. The intensity waveform at the output is detected by a 10 GHz bandwidth PD which intrinsically assists in smoothing undesired high-frequency RF components that do not fall into the UWB range. The resultant electrical signal is measured in the RF domain by an ESA with a resolution of 1 MHz, and in the time domain by a sampling oscilloscope. The EDFA is adjusted so that the receiver gets an average optical input power of −0.5 dBm. Figure 8.17 shows the measured resultant UWB signal consisting of a monocycle-like pulse in time and frequency domain. For the frequency domain picture, we selected a repetition rate of 390.6 MHz (a "1" followed by 32 "0") so that the achieved spectral shape is properly sampled. As it can be appreciated, the RF spectrum spreads over the UWB region. Due to the monocycle-like waveform, a non-disregarding low-frequency content still remains, which can be minimized

by reducing the power into the photodiode with some extra attenuator.

Doublet generation

Using the same components we can also achieve a doublet UWB pulse. The physical principle behind is showed in Fig. 8.18(a). We drive the DFB laser with the electrical inverted data from the pattern generator, and forward bias it with a current close to the threshold (at 35 mA in the experiments). In the large-signal modulation regime, the laser power overshoots at the rising edge due to relaxation oscillations and then reaches the steady state [77]. We can then filter this radiation with an optical filter in order to reshape the waveform to achieve the desired doublet UWB profile.
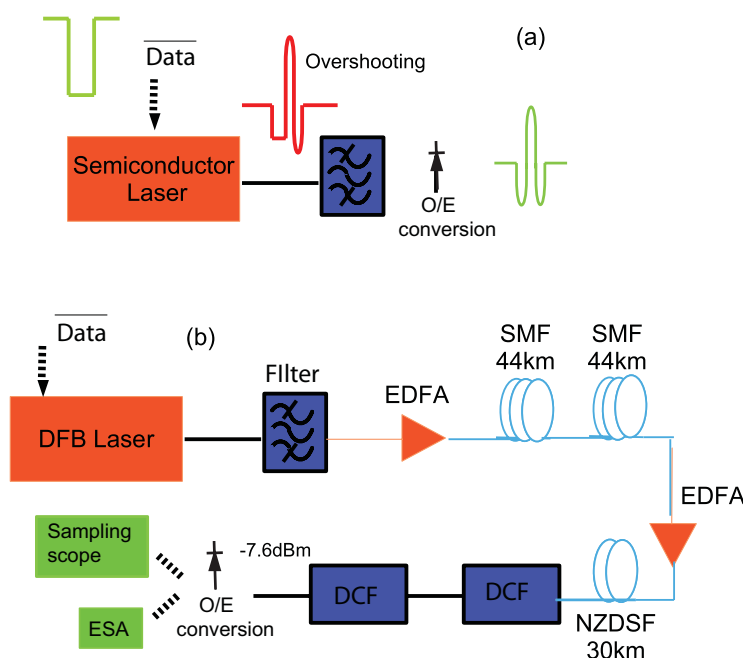
Figure 8.18: (a) Heuristic explanation of the physical principle to achieve the UWB doublet (b) Experimental setup.

Figure 8.19(a) shows the electrical data pulse (green dash-dotted line) applied to the laser, and the output optical intensity (red solid line). The overshooting effect at the trailing edge of the pulse is apparent. The power oscillates at the relaxation oscillation frequency before achieving a steady state following the shape of the driving electrical signal. We measured the RF spectrum of this waveform with the 10 GHz bandwidth PD and verified that it was not UWB compliant. However, we were able to produce the required pulse characteristics by passing this laser pulse through the same Gaussian spectral filter as before, but at different operation point. In Fig. 8.19(b) we show the output laser spectrum (blue solid line) and the filter profile placed in the optimal position to achieve the doublet shape. As we can see, the high-frequency optical components are smoothed. It should be mentioned that previously-reported approaches for optical filtering

of gain-switched lasers tried to avoid this overshooting effect and aimed to generate bell-shaped ultrashort waveforms [313,314]. Our goal here is instead to optimize the intensity profile so that this waveform can be exploited for UWB RF signal generation. After the optical filtering, we converted the optical signal into the electrical domain with a 10 GHz bandwidth PD, and succeeded in generating a doublet-like UWB impulse, as shown by the green line in Fig. 8.20(a). The RF spectrum of this pulse fits the UWB mask regulations.
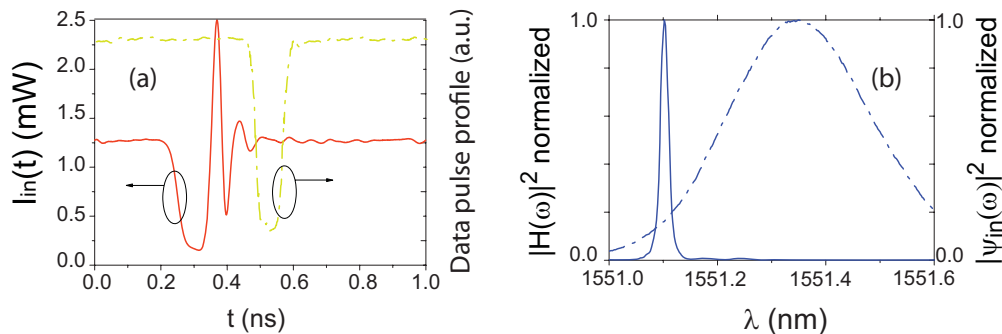

Figure 8.19: (a) Intensity laser profile (red line) and electrical data signal (green dashed line). The temporal scale has a different origin for the electrical and optical signals. (b) normalized ES of laser pulse (solid line) and amplitude filter (dotted line).

In order to verify the usefulness of this method we performed an additional experiment for propagating the signal through an optical fiber link. For this evaluation, the signal needed to be amplified after optical filtering and the O/E converter was placed at the receiver. As indicated in Fig. 8.18(b), the fiber link is comprised of two stages. We first propagated the signal through two SMF coils of 44 km length each. Then the optical signal was further amplified and propagated through 30 km of NZDSF as well as 13 km of DCF, matched to compensate for the dispersion introduced by the SMF in the first stage. This constitutes a total optical link length of 118 km, which represents the largest distance ever reported for UWB signal distribution, to the best of our knowledge. The output optical pulse is detected with the 10 GHz bandwidth photodiode and measured simultaneously in the time domain with a sampling oscilloscope, and in frequency domain with an ESA with a 1 MHz measurement resolution. The achieved signal is displayed in Figs. 8.20(b) and (c). It possesses a central frequency of 7 GHz and has a 10 dB bandwidth of 10.2 GHz, hence a fractional bandwidth of 146 %. The pulse duration was measured to be 236 ps. Comparison of Figs. 8.20(a) and (b) indicates that there is no significant distortion of the UWB pulse during propagation. From Fig. 8.20(c) we conclude that the waveform satisfies the UWB RF regulations. The spikes are due to the fact that we introduced a data sequence of one ”1” followed by sixteen ”0”, so that the RF spectrum of a single UWB pulse is conveniently sampled at 0.78 GHz for illustration purposes. We achieved higher data transmission rates with this optical pulse shape, up to a soft limit related to the output UWB pulse duration. We have successfully transmitted similar pulses at 3.12 GHz over this fiber link.
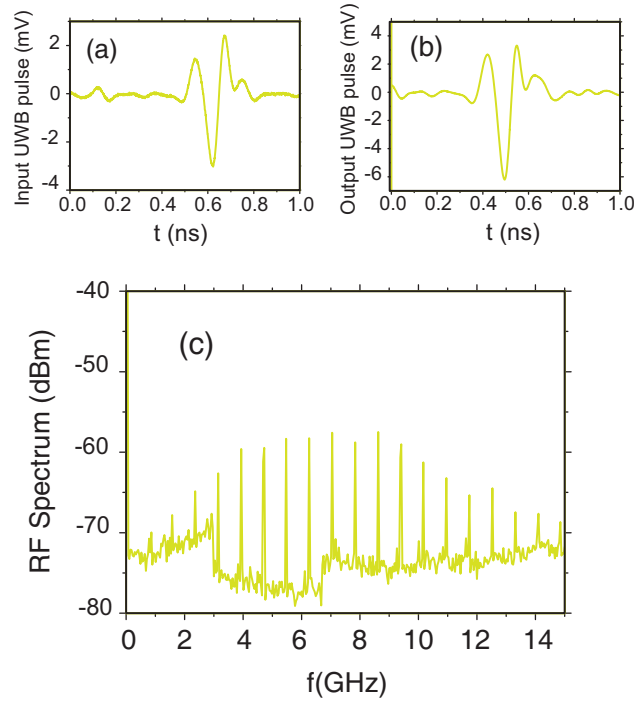
Figure 8.20: Generated UWB signal in: (a) time domain before transmission; (b) after propagation through the 118 km fiber link; (c) spectral domain.

8.3.2 Broadcasting capabilities with incoherent frequency-to-time mapping approach

While most of the previous efforts in the generation of UWB signals have been directed towards the optimization of the whole spectral range spanning the 3.1–10.6 GHz interval, UWB regulations also allow for the existence of different channels, as long as the power requirements are met.

In this Section, we propose an UWB signal generation scheme based on the incoherent pulse shaping approach presented in Chapter V, achieving also broadcasting to multiple users as illustrated in Fig. 8.21(a). Each end terminal receives the data both at the baseband and at microwave pass-band frequency within the UWB region. In our proposed method, the carrier can be easily tuned by selecting the value of the fiber length. In fact, this fiber is also the fiber link for signal transport between the central office and the remote antenna unit. We present the results corresponding to a proof-of-principle for a single-channel transmission achieving 312.5 MHz bit rate over both 22.8 and 44 km SMF length.

Let us clarify this particular setup. The ES of a spectrally incoherent source (again the ASE gain spectrum from an EDFA in the experiment) is spectrally filtered with an MZI and further smoothed with a Gaussian spectral filter, leading to a tailored ES

$$S_{s,b}(\omega) = A(\omega)[1 + \cos(\omega T)], \tag{8.11}$$

where $A(\omega)$ includes both the ES of the EDFA and the spectral response of the filter.
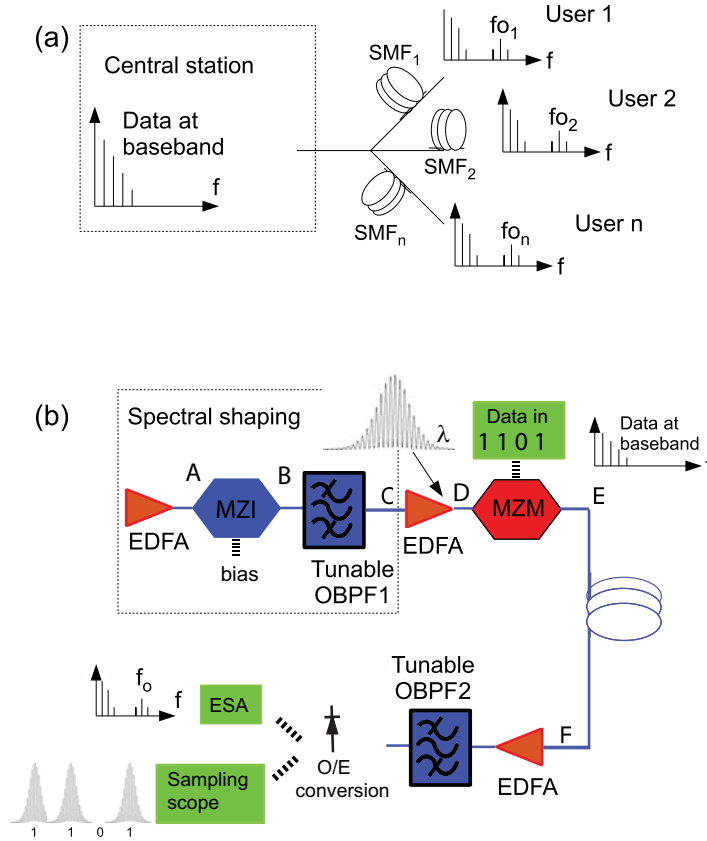
Figure 8.21: (a) UWB signal generation with broadcasting and baseband support over a passive optical network. (b) Experimental setup for the proof-of-principle using a single channel and an incoherent source.

Here, T denotes the time delay in the MZI. According to Eq. (6.10), after deterministic temporal modulation and propagation in a GDD circuit (an SMF in our case), the output temporal averaged intensity profile will resemble the shape provided by Eq. (8.11). If we assume that the spectral width of $A(\omega)$, $\Delta\omega$, is much bigger than the inverse of T (quasi-homogeneous requirement), the resulting positive RF spectrum becomes [35]

$$RF(f) = \exp[-f^2/(2\sigma_f^2)] + 1/4\exp[-(f - f_0)^2/(2\sigma_f^2)]. \qquad (8.12)$$

It is composed of two bands with identical spectral widths given by $\sigma_f = (4\pi\Phi_2\Delta\omega)^{-1}$. The second band is centered at

$$f_0 = T/(2\pi|\Phi_2|). \qquad (8.13)$$

Thus, our setup has the inherent capability to tune the band-pass frequency with the GDD coefficient and/or the temporal delay of the MZI. Larger dispersion results in a lower microwave carrier frequency. This is the key to achieve broadcasting in a passive optical network scheme as the one presented in Fig. 8.21(a). Every end terminal can obtain the data at both the baseband and the corresponding frequency band. It is interesting to note that the same theoretical results can be achieved with a fully coherent pulsed source [315].
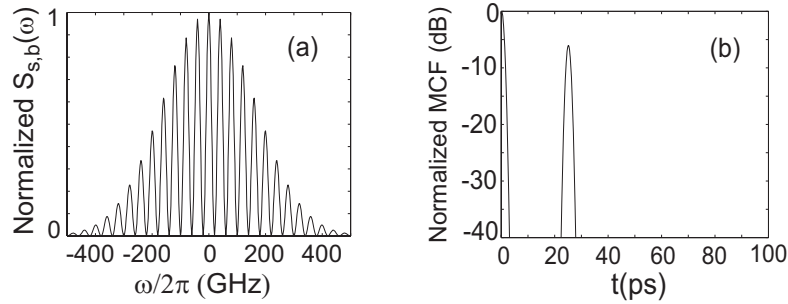
Figure 8.22: Numerical illustration of: (a) ES of a Gaussian source filtered with a MZI and (b) its corresponding MCF. See text for numerical details.

However, our setup operates based on a different physical principle, which allows us to use a fully incoherent source. Due to the restriction established by Eq. (6.11), there is a maximum achievable frequency given by $f_{0\text{max}} = 2T/(\sigma t_c)$. As a numerical example, in Fig. 8.22(a) we plot the ES at the optical baseband corresponding to a Gaussian shape with a 3 nm FWHM centered on 1532 nm and filtered with a MZI that introduces a delay of $T = 25$ ps. In Fig. 8.22(b) we plot the modulus of the corresponding MCF.
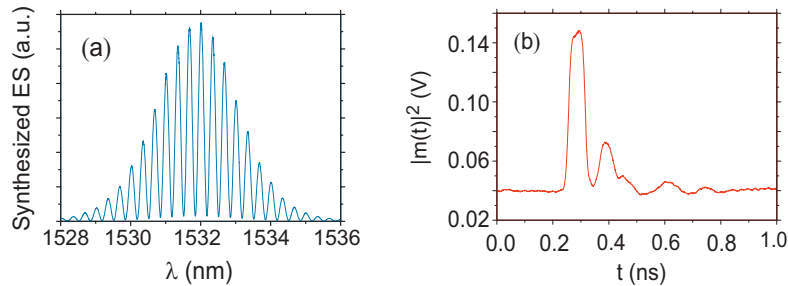
Figure 8.23: At point E in Fig. 8.21(b) we measured: (a) the synthesized ES from the MZI obtaining an average power of 4 dBm; and (b) the averaged optical intensity emerging from the modulator.

In our proof-of-principle experiment, we consider UWB signal generation and transmission between the central station and a single user. The base station is composed of an EDFA without input light, an MZI with a delay of $T = 25$ ps, an optical filter with 3 nm FWHM, and a 40 GHz bandwidth external modulator, in particular, a dual drive MZM, carrying data at 20 GHz in a bit sequence of 1 each 64 (312.5 MHz). At point C in Fig. 8.21(b) the measured average optical power was -2.7 dBm. Figures 8.23(a) and (b) show, respectively, the ES and temporal pulse profile at point E in Fig. 8.21(b). The correspondence between the measured spectrum and the numerically calculated one in Fig. 8.22(a) is excellent. This allows us to assume that the MCF of the effective source has a shape as the one in Fig. 8.22(b). According to Fig. 8.23(b), the pulse duration is around $\sigma = 200$ ps. The minimum propagation distance in the SMF to achieve the

desired mapping (18.3 km for $\beta_2 = -21.6\,\mathrm{ps}^2/\mathrm{km}$) leads, according to Eq. (6.11), to a maximum achievable frequency of $f_0 = 10\,\mathrm{GHz}$. Thus, our scheme results ideal for data up-conversion within the UWB range.

We used two different fiber lengths, 22.8 and 34 km. The achieved waveforms at point F in Fig. 8.21(b) were further optically amplified and photodetected. The measured average power before the last EDFA was $-11\,\mathrm{dBm}$ for each fiber. The second optical filter was used to avoid extra noise coming from the EDFA and was broader than the first one located between points B and C. Figure 8.24 shows the output electrical waveforms and their RF spectra measured with the 40 GHz PD and a 3 MHz resolution ESA, respectively. We recognize that the incoherent mapping is successfully achieved and the position of the transmission data in the spectrum of the resulting microwave signal appears at the expected value given by Eq. (8.13) in each case.
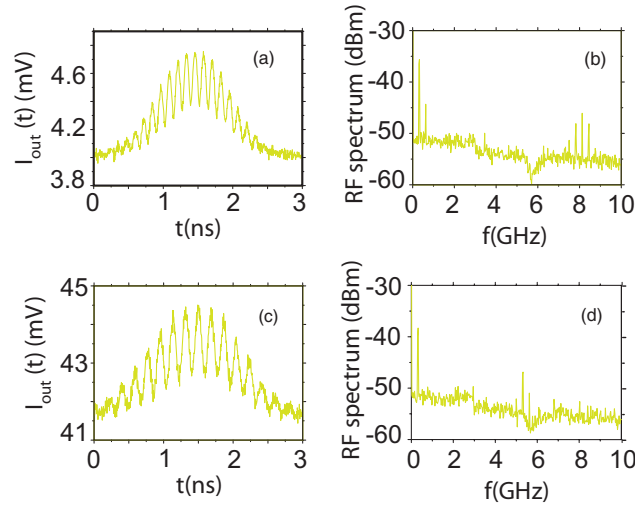
Figure 8.24: Electrical signal waveform for the 22.8 km fiber length experiment in: (a) the time domain; and (b) the RF domain. The results for the fiber length of 34 km are plotted in (c) and (d), respectively. The RF peak components come from the data pattern at 312.5 MHz.

We would like to point out that a strong DC component can be recognized at every plot in Fig. 8.24. This fact is a direct consequence of the low extinction ratio shown by the pulse provided by the MZM [see Fig. 8.23(b)]. So, the spectral correlations of the synthesized ES could not be achieved. This led to a degraded signal-to-noise ratio for the UWB up-converted signal, since the EDFA at point F increased the non-mapped noise too. We attribute this low extinction ratio to the lack of a polarizer before modulating the incoherent ES.

Mimicking temporal entanglement phenomena with partially coherent light pulses

Entanglement between particles is one of the most striking features of quantum mechanics. It has led to the resolution of the Einstein-Podolsky-Rosen paradox [316] and to demonstrations of the nonlocal character of quantum correlations. In optics, spontaneous parametric down-conversion (SPDC) has been usually the method of choice for producing entangled photon pairs (or biphotons) [317, 318]. More recently, two-photon light has been produced from semiconductor quantum wells too [319]. These photon pairs may be entangled in polarization, momentum, space, frequency, and time. Biphotons are the basic source for experiments in quantum cryptography [320], quantum imaging [321, 322], quantum teleportation [323], quantum lithography [324], quantum optical coherence tomography [325, 326], remote spectral transfer [327], and clock synchronization [328, 329].

In this Chapter we show that the two-photon temporal coincidence detection amplitude obeys a pair of equations identical to those of classical partially coherent plane-wave pulses propagating in linearly dispersive media. These equations are also the same as the paraxial Wolf equations, for both the two-photon spatial probability amplitude and the cross-spectral density function. Therefore, a four-fold analogy between space and time, as well as between quantum entanglement and partial coherence, arises. In accordance to this, we predict non-local interference structures in a fourth-order interferometric configuration with classical partially coherent pulses under the assumption of Gaussian statistics. Based on this relevant finding we provide theoretical evidence that many different experimental arrangements that hitherto are thought to need temporally entangled photon pairs can operate with classical partially coherent light pulses.

9.1 Fourfold Space–Time analogy

For light in any arbitrary quantum state, the probability of observing a photon at the space–time position $(\mathbf{r}_1, t_1)$ and another at $(\mathbf{r}_2, t_2)$ is proportional to the intensity correlation function [48, 330][1]

$$G^{(2)}(\mathbf{r}_1, t_1; \mathbf{r}_2, t_2) = \langle \Psi | \widehat{E}^-(\mathbf{r}_1, t_1) \widehat{E}^-(\mathbf{r}_2, t_2) \widehat{E}^+(\mathbf{r}_1, t_1) \widehat{E}^+(\mathbf{r}_2, t_2) | \Psi \rangle. \qquad (9.1)$$

---

[1]For convenience, optical fields are considered to be 1D, thus $\mathbf{r} = (x, z)$, with z the propagation distance.

Here, $\widehat{E}^-(\mathbf{r}, t)$ and $\widehat{E}^+(\mathbf{r}, t)$ denote the negative- and positive-frequency components of the optical-field operator at $(\mathbf{r}, t)$, and $|\Psi\rangle$ represents the state vector [48].

For the particular case of light in the two-photon state, the right hand side of Eq. (9.1) factors as [331] $\langle\Psi|\widehat{E}^-(\mathbf{r}_1, t_1)\widehat{E}^-(\mathbf{r}_2, t_2)|0\rangle\langle0|\widehat{E}^+(\mathbf{r}_1, t_1)\widehat{E}^+(\mathbf{r}_2, t_2)|\Psi\rangle$, with $|0\rangle$ being the vacuum state. Therefore,

$$G^{(2)}(\mathbf{r}_1, t_1; \mathbf{r}_2, t_2) = |G(\mathbf{r}_1, t_1; \mathbf{r}_2, t_2)|^2, \tag{9.2}$$

where

$$G(\mathbf{r}_1, t_1; \mathbf{r}_2, t_2) = \langle0|\widehat{E}^+(\mathbf{r}_1, t_1)\widehat{E}^+(\mathbf{r}_2, t_2)|\Psi\rangle \tag{9.3}$$

can be considered as the two-photon probability amplitude [317]. The two-photon probability amplitude may also be expressed in the space–frequency domain, by Fourier transforming $G(\mathbf{r}_1, t_1; \mathbf{r}_2, t_2)$ with respect to t_1 and t_2. This leads to a function $\phi(\mathbf{r}_1, \omega_1; \mathbf{r}_2, \omega_2)$. On factoring out the rapid phases as $\phi(\mathbf{r}_1, \omega_1; \mathbf{r}_2, \omega_2) = \phi_e(\mathbf{r}_1, \omega_1; \mathbf{r}_2, \omega_2)\exp[i(k_1 z_1 + k_2 z_2)]$, it can be shown that the function ϕ_e in the paraxial regime obeys the propagation equations

$$[\partial_{x_j}^2 + 2ik_j\,\partial_{z_j}]\phi_e(\mathbf{r}_1, \omega_1; \mathbf{r}_2, \omega_2) = 0, \tag{9.4}$$

where $j = (1, 2)$. Apart from a sign, these equations are identical with Eqs. (5.42). This spatial quantum–classical analogy was first analyzed in [331, 332].

Separability of the two-photon amplitude probability function means absence of entanglement, and thus minimum visibility in the fourth-order interference fringes. In contrast, separability in the mutual coherence function implies full spatial coherence, which corresponds to maximum visibility in the interference fringes in the Young's experiment. In this sense, the above mathematical similarity leads to a physical duality between the quantum and classical domains [332]. Although this similarity even holds for non-paraxial waves, we prefer to restrict ourselves to the paraxial case so as to directly connect the space duality with the following temporal analogy.

Quite recently, Tsang and Psaltis demonstrated that the equations that govern the evolution of the temporally entangled two-photon states in lossless, homogeneous, first-order dispersive media are mathematically identical to Eqs. (9.4) [171]. More specifically, if $\widehat{\psi}^+(z, t)$ is the slowly-varying plane-wave envelope operator, the envelope of the two-photon probability amplitude is $G_e(z_1, t_1; z_2, t_2) = \langle0|\widehat{\psi}^+(z_1, t_1)\widehat{\psi}^+(z_2, t_2)|\Psi\rangle$, and it satisfies the equations, for $j = (1, 2)$,

$$[\partial_{t_j}^2 - 2i\frac{1}{\beta_2}\,\partial_{z_j}]G_e(z_1, t_1; z_2, t_2) = 0, \tag{9.5}$$

where, as usual, the times t_j are measured in a coordinate frame that moves at the speed of the wave packet. The connection between Eqs. (9.5) and (9.4) can be considered as the quantum-optical version of the space–time analogy (see Sect. 5.2) that links paraxial diffraction of 1D beams with first-order temporal dispersion of short light pulses. Since, as stayed at Sect. 5.6, this analogy also exists in the classical context among spatially partially coherent beams and partially coherent plane-wave pulses [19], we point out an up-to-now overlooked analogy between quantum-mechanical two-photon-state coincidence detection and classical fluctuating optical pulses [34]. Following the same reasoning as

before, a temporally fully incoherent classical pulse corresponds to a maximum temporally entangled two-photon state. Thus, one can expect, in the same way as some quantum phenomena concerning spatial entanglement can be mimicked by spatially incoherent light, that some time-domain phenomena involving dispersion of temporal entanglement can be emulated by classical partially coherent light pulses, and vice versa.

9.2 Biphoton distortion in linear dispersive media

Let us consider now the situation depicted in Fig. 9.1(a). A source providing temporally entangled photon pairs launches each photon in the pair through a different temporal optical system. The propagation of the two-photon probability amplitude $G_{e,\text{in}}(t_1, t_2)$ is mathematically described by the Green integral equation [333]

$$G_{e,\text{out}}(z_1, t_1; z_2, t_2) = \iint G_{e,\text{in}}(t', t'') K_1(t_1, t') K_2(t_2, t'') \, \mathrm{d}t' \mathrm{d}t'', \qquad (9.6)$$

where the kernel $K_\alpha(t, t')$ describes mathematically the system through which the α photon is traveling, $\alpha = (1, 2)$. As in the coherent case (see Sect. 5.3), each temporal system can be composed by cascading spectral and amplitude filters, GDD circuits and or temporal lenses, for example. According to Eq. (9.2), the probability of observing one photon at time t_1 and the other at t_2 is given by the modulus square of Eq. (9.6).

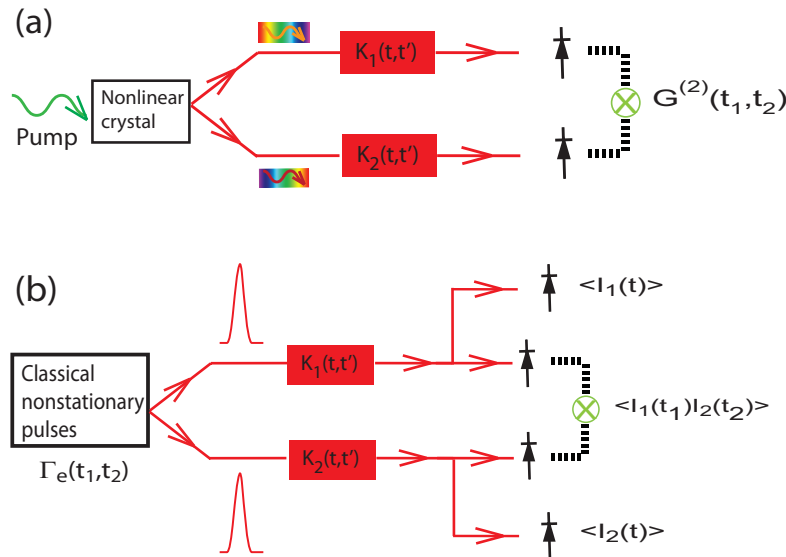**Figure 9.1**: (a) Quantum biphoton distortion in a general dispersive setup; (b) classical counterpart Hanbury Brown–Twiss interference with partially coherent light pulses.

9.3 Fourth-order interference with partially coherent pulses

In a series of experiments in 1995, light in two-photon quantum state produced by SPDC was used to achieve what was referred as the *ghost diffraction* [334] and *imaging* [322]

phenomena. In this technique, each photon from the pair travels through a different optical setup and is individually photodetected with a spatial array. By placing an object in only one of the paths, it was shown that a diffraction pattern of the object appeared by measuring coincidence counts with the scanning detector arrays. The seemingly counterintuitive finding is that the diffraction pattern was created by photons that never passed through the object. At that time, the authors suggested that "it is possible to imagine some type of classical source that could partially emulate this behavior" [322]. Later on, a comprehensive work on the formal similarities between spatial entanglement and classical spatial partial coherence was developed [332]. But the key experiment came when Bennink *et al.* performed the coincidence imaging experiment with spatially incoherent classical light [335]. In this case, apart from a background level, similar effects as in the quantum case were found. More advanced experiments involving phase-only masks have been also carried out with quantum [336] as well as classical light [337]. The mathematical foundation of these two different physical phenomena leading to practically identical results was finally clarified in [338–341]. The analogy relies on the fundamental formal similitude of Eqs. (9.4) and (5.42) [331]. Recent review papers about ghost imaging and diffraction can be found in [321, 342].

In the temporal domain, analogous ghost diffraction phenomena have recently been reported [343, 344]. These experiments consist of spectral coincidence measurements of two-photon pairs in an interferometric arrangement. By spectrally (or temporally) filtering a beam in one arm, various interference structures were obtained. The earlier work of Valencia *et al.* [344] presents temporal interferometric coincidence measurements with two-photon light. Each photon generated in the pair is focused into a different SMF placed in each arm of the interferometer. More advanced configurations may use a high flux of two-photon light and SLMs [345]. In this Section we show that similar experiments can be carried out by using classical partially coherent pulses instead of temporally entangled two-photon quantum light.

9.3.1   Mathematical formulation

Let us consider a device as the one depicted in Fig. 9.1(b). A light source produces partially coherent light pulses described by Γ_e, that are later split in two arms. Each arm is composed by the same system as in Fig. 9.1(a). At the end of each arm, we assume that a fast photodiode detects the radiation instantaneously. Then, the signal is further carried to a coincidence circuit that produces the average $\langle I_1(t_1)I_2(t_2)\rangle$, where $I_\alpha(t)$ is the instantaneous intensity arriving at detector from arm α,

$$I_\alpha(t) = \left| \int \psi_{\text{in}}(t')K_\alpha(t,t')\,\mathrm{d}t' \right|^2. \tag{9.7}$$

Here $\psi_{\text{in}}(t)$ is the slowly-varying envelope of a random realization of the input light [171]. The average $\langle I_1(t_1)I_2(t_2)\rangle$ can be implemented with a time-to-amplitude converter followed by a multichannel analyzer. In [344], this operation is performed with a temporal resolution on the order of hundreds of picoseconds. It is important to note that we are dealing with the two-time intensity correlation function, not with an integrated version. Taking into account Eq. (9.7), and exchanging the order of integration and ensemble

averaging, we obtain

$$\langle I_1(t_1)I_2(t_2)\rangle = \int \mathrm{d}t_1'\mathrm{d}t_2'\mathrm{d}t_1''\mathrm{d}t_2''\,\langle\psi_{\mathrm{in}}^*(t_1')\psi_{\mathrm{in}}^*(t_1'')\psi_{\mathrm{in}}(t_2')\psi_{\mathrm{in}}(t_2'')\rangle \qquad (9.8)$$
$$\times\, K_1^*(t_1,t_1')K_2^*(t_2,t_1'')K_1(t_1,t_2')K_2(t_2,t_2'').$$

This fourth-order correlation can further be simplified by assuming the random input light to obey Gaussian statistics [48]. Therefore, using Eq. (2.28), $\langle\psi_{\mathrm{in}}^*(t_1')\psi_{\mathrm{in}}^*(t_1'')\psi_{\mathrm{in}}(t_2')\psi_{\mathrm{in}}(t_2'')\rangle = \Gamma_e(t_1',t_2')\Gamma_e(t_1'',t_2'') + \Gamma_e(t_1',t_2'')\Gamma_e(t_1'',t_2')$, where $\Gamma_e(t_1,t_2) = \langle\psi_{\mathrm{in}}^*(t_1)\psi_{\mathrm{in}}(t_2)\rangle$. Then, we find that

$$\langle I_1(t_1)I_2(t_2)\rangle = \langle I_1(t_1)\rangle\langle I_2(t_2)\rangle + \left|\Delta G(t_1,t_2)\right|^2, \qquad (9.9)$$

where

$$\Delta G(t_1,t_2) = \int \Gamma_e(t_1',t_2')K_1^*(t_1,t_1')K_2(t_2,t_2')\,\mathrm{d}t_1'\mathrm{d}t_2'. \qquad (9.10)$$

Clearly, $|\Delta G|^2$ is responsible for the interference effect. The connection between Eqs. (9.10) and (9.6) is clear. $|\Delta G|^2$ plays the role of two-photon coincidence probability given by Eq. (9.2). Apart from a conjugate, these two equations are formally identical and therefore, classical partially coherent light pulses might achieve the same results than temporal entanglement phenomena provided that the Gaussian statistics assumption holds. The discrepancy in the kernel is present in the differential equations (9.5) and (5.41), and is fundamentally due to the definition of the MCF and the two-photon temporal amplitude probability [compare Eq.(2.6) with (9.3)].

Our result in Eq. (9.9) is due to the Hanbury Brown–Twiss interferometer [48] in Fig. 9.1(b), operating with non-stationary light pulses. In a practical configuration, the background terms $\langle I_\alpha(t)\rangle$ can be independently measured, e.g., with a sufficiently fast oscilloscope, and then subtracted from Eq. (9.9) [346]. We would like to emphasize that ΔG does not satisfy Eqs. (5.41), only Γ_e does. However, the Gaussian statistics allow one to rewrite the fourth-order correlation in terms of second-order correlations. Only in this case do the analogies in fourth-order interferometry between the quantum and classical domains emerge [338].

We can define a visibility parameter as [342]

$$V = \max\left[\frac{\Delta G(t_1,t_2)}{\langle I_1(t_1)I_2(t_2)\rangle}\right]. \qquad (9.11)$$

Therefore, using Schwartz inequality, we can see that if the background term is included, the maximum achievable visibility is 50%. This is in clear distinction with the quantum case, where, in the small photon-number regime, the visibility approaches the theoretical limit of 100% [338].

9.3.2 Classical temporal ghost diffraction phenomenon

Let us now apply the scheme in Fig. 9.1(b) to the particular case of Fig. 9.2. In arm 1, we place a temporal modulator providing a deterministic gate $m(t)$. Before and after it we have two GDD circuits (SMFs for simplicity) with Φ_{21b} and Φ_{21a} the corresponding GDD parameters. In arm 2, we place another SMF characterized by Φ_{22}. The source
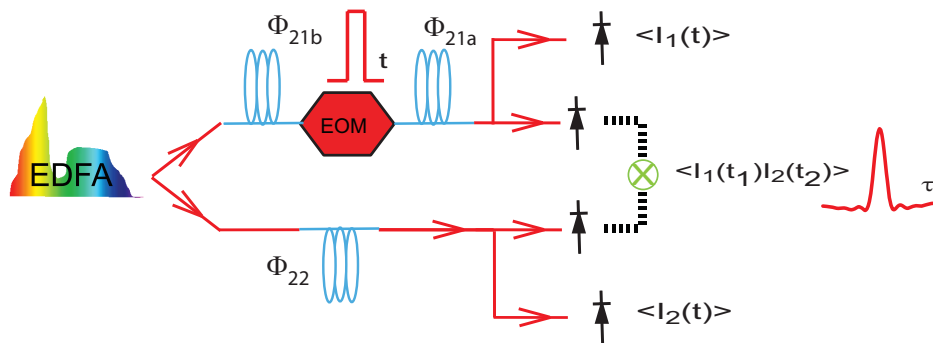
Figure 9.2: Classical version of the temporal ghost diffraction phenomenon.

is temporally incoherent and can be implemented by ASE. In practice, the condition of temporal incoherence is satisfied when the coherence time of the ASE source is short enough compared with the PD resolution and the pulse width of the temporal window of $|m(t)|^2$. We then have $\Gamma_e(t_1, t_2) \propto \delta(t_2 - t_1)$. Then, by substituting the corresponding kernel into Eq. (9.10) and further selecting the fibers to match $\Phi_{22} = \Phi_{21b} + \Phi_{21a}$, we find that

$$|\Delta G(t_2 - t_1)|^2 \propto \left| \tilde{M} \left(\frac{t_2 - t_1}{\Phi_{21a}} \right) \right|^2, \tag{9.12}$$

where $\tilde{M}(\omega)$ is the Fourier transform of $m(t)$. In close analogy with the spatial case [322, 335, 340], this situation thus leads to the temporal Fraunhofer pattern of the gate function, where here the temporal gate function corresponds to the object.

9.4   Nonlocal dispersion cancelation with classical pulses

Nonlocal dispersion cancelation is a quantum phenomenon that relies on the use of a quantum light source providing temporally entangled photon pairs, usually obtained from SPDC [347]. Each photon from the pair propagates through a dispersive medium with suitable dispersion properties. Then, the dispersion experienced by one photon can cancel out the dispersion of the other one, so that their intensity coincidence probability remains unaffected. This effect was experimentally demonstrated by Steinberg *et al.* in a configuration based on a Hong-Ou-Mandel interferometer [348] in which only one dispersive medium is needed, and the even-order dispersion terms are naturally canceled out [349, 350]. Nonlocal dispersion cancelation has triggered important applications in quantum information science, like quantum optical coherence tomography [326], distant clock synchronization [327] and remote transfer of spectral amplitude functions [329].

9.4.1   Mathematical formulation

In this Section we show that dispersion cancelation is not a genuine quantum phenomenon and it can take place with classical stationary light obeying Gaussian statistics.

We start with the quantum case corresponding to Fig. 9.3(a) with a different SMF placed at each arm. This corresponds to the initial configuration of the nonlocal dispersion cancelation scheme reported by Franson [347]. If the detectors were ideal, the coincidence
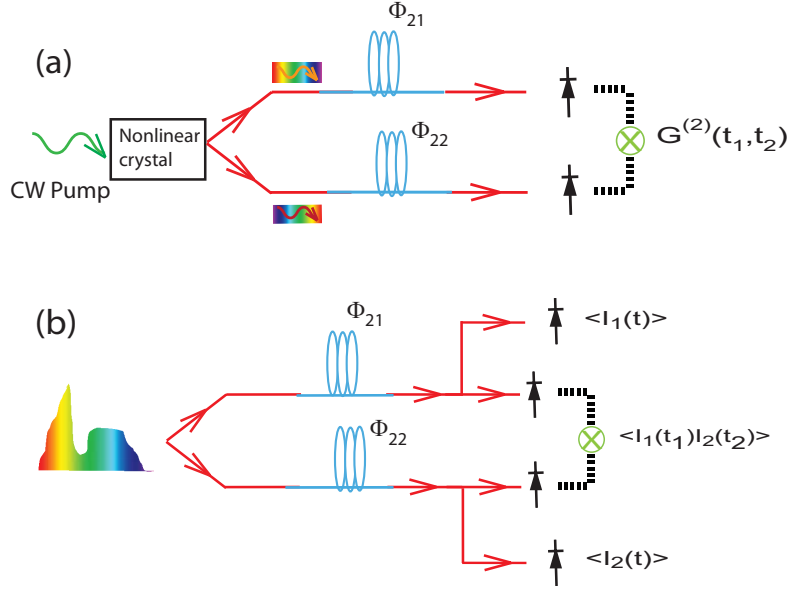
Figure 9.3: (a) Quantum and (b) classical scheme for nonlocal dispersion cancelation.

circuit would give a quantity proportional to the second-order correlation function (9.3) [48, 344]. The output $G^{(2)}$ function can be calculated by introducing the corresponding kernel expressions from Sect. 5.3.3 into Eq. (9.6), leading to

$$G^{(2)}(t_1, t_2) \propto \left| \iint \phi_e(\omega_1, \omega_2) \right. \tag{9.13}$$

$$\left. \times \prod_{n=2}^{N} \exp\{i[\omega_1^n \Phi_{n1} + \omega_2^n (-1)^n \Phi_{n2}]/n!\} \exp[-i(\omega_1 t_1 + \omega_2 t_2)]\mathrm{d}\omega_1 \mathrm{d}\omega_2 \right|^2 .$$

Here, $\phi_e(\omega_1, \omega_2)$ is the two-dimensional Fourier transform with respect to t_1 and t_2 of the two-photon probability amplitude at the input state, $G_{e,\mathrm{in}}(t_1, t_2)$, and Φ_{na} the nth-order dispersion parameter of the SMF at arm a. For the case of an SPDC process operating with CW pumping, signal and idler photons are initially entangled with negative-frequency correlation, i.e.,

$$\phi_e(\omega_1, \omega_2) = F(\omega_1)\delta(\omega_1 + \omega_2), \tag{9.14}$$

where the function $F(\omega)$ represents the spectral amplitude of the SPDC process centered at the baseband, which is determined by the wave-vector phase matching in the nonlinear crystal [317]. Thus, Eq. (9.13) leads to

$$G^{(2)}(t_2 - t_1) \propto \left| \int \mathrm{d}\omega F(\omega) \exp[-i\omega(t_2 - t_1)] \right. \tag{9.15}$$

$$\left. \times \prod_{n=2}^{N} \exp\{i\omega^n[\Phi_{n1} + (-1)^n \Phi_{n2}]/n!\} \right|^2 ,$$

Therefore, unless one has two dispersive media adjusted to satisfy $\Phi_{n1} = (-1)^{n+1}\Phi_{n2}$ $\forall n$, the effect of dispersion is to broaden the second-order correlation function [344, 347]. In the case of first-order dispersion ($N = 2$) and when the fibers are not matched, Eq. (9.15) becomes a Fresnel integral [344]. Interestingly, one can achieve a far-field condition whenever $\Phi_{21} + \Phi_{22} >> \pi\sigma_c^2$, where σ_c is the coherence time of the SPDC process, roughly given by the inverse of the bandwidth of the function $F(\omega)$. Then, a frequency-to-time mapping takes place, and the output $G^{(2)}$ resembles the shape of $F(\omega)$ [317, 344]. This result can be understood as the biphoton temporal version of the vanCittert–Zernike theorem [332].

Let us now consider a modified Hanbury Brown–Twiss interferometer [48] as the one shown in Fig. 9.3(b) with the same two SMFs as before. However, now the light source is assumed to be temporally partially coherent and obeying Gaussian statistics. Again, at the output of each arm the light intensity is photodetected and carried to a coincidence circuit. As usual, we assume that the averaged intensity can be independently measured at each arm and then subtracted from the intensity correlation. This leads to

$$\Delta G(t_1, t_2) = \left| \iint d\omega_1 d\omega_2 W_{b,\text{in}}(\omega_1, \omega_2) \right. \tag{9.16}$$
$$\left. \prod_{n=2}^{N} \exp\{-i[\omega_1^n \Phi_{n1} - \omega_2^n(-1)^n \Phi_{n2}]/n!\} \exp[i(\omega_1 t_1 - \omega_2 t_2)] \right|^2 .$$

Here, $W_{b,\text{in}}$ is the CSDF centered at baseband corresponding to the input partially coherent light pulse. For the stationary case given by Eq. (2.18), we get

$$\Delta G(t_2 - t_1) = \left| \int S_{s,b}(\omega) \exp[-i\omega(t_2 - t_1)] \prod_{n=2}^{N} \exp[i\omega^n(\Phi_{n2} - \Phi_{n1})/n!] \, d\omega \right|^2 . \tag{9.17}$$

Here, $S_{s,b}(\omega)$ represents the ES of the light source centered at the baseband. We note that it is possible to achieve all-order dispersion cancelation with classical light too by selecting the different fibers to satisfy $\Phi_{n2} = \Phi_{n1}$ $\forall n$.

By comparing Eq. (9.17) with Eq. (9.15) we note that $S_{s,b}(\omega)$ plays the role of the spectrum of the SPDC process, $F(\omega)$ [317]. In each case, the spectral width of the corresponding function determines the coherence time of the random field or two-photon light. The first-order coherence properties of each beam (quantum or classical) traveling individually in each arm are not affected by the dispersion [283, 344]. The coherence time is roughly given by the spectral structure of $F(\omega)$ (in the quantum case) [317] or $S_{s,b}(\omega)$ (classical) [48] and the dispersive effects are only notable in fourth-order interference [344]. For this reason, already in the Appendix of the original work of nonlocal cancelation, Franson pointed out that with stationary light, the intensity coincidence detection could be affected by dispersion, but any nonlocal cancelation achieved by matching the dispersive coefficients should not be considered as such because the correlation time of each beam is unaffected with propagation [347]. However, that is indeed the case in the quantum regime too: the first-order correlation function of the idler (signal) from the SPDC process results unaffected by the dispersion, and only $G^{(2)}$ does broaden [317, 344]. Nevertheless, there is a sign difference in the dispersion compensation laws for the classical and the quantum case. As briefly commented in the previous section, the origin of this

discrepancy is two-fold. First, due to the definition of the first-order coherence functions, there is a difference in the Green propagators in Eqs. (9.13) and (9.16). Second, the signal and idler photons in the case of the SPDC process are initially negative-frequency anti-correlated, whereas the stationary case corresponds to fully de-correlated frequencies. This has lead to the nonlocal dispersion cancelation with a classical source, though with different dispersion requirements [38].

9.4.2 Application to remote spectral transfer

As a first application, we next propose a configuration for a remote spectrometer as the one reported in [327], but here operating with a classical stationary source. In practical terms, such light source could be provided by an ASE source. While spectral measurements based on intensity correlations have been known for decades [351], the special feature of the remote set-up is that the needed information can be transferred long distances undistorted, relying on the nonlocal cancelation of dispersion.
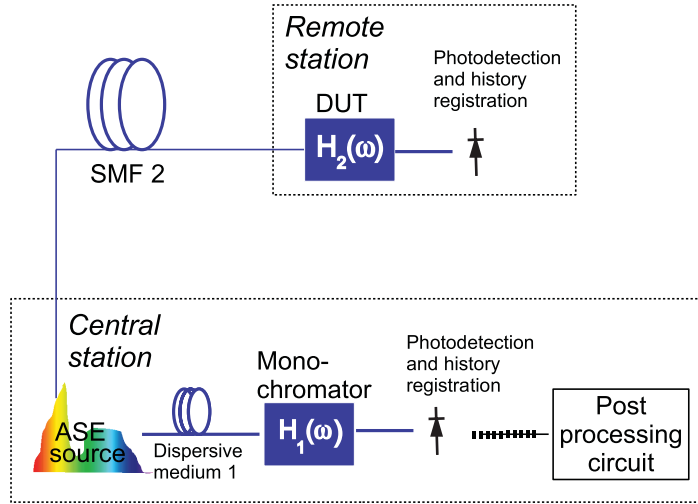
Figure 9.4: Remote spectral transfer scheme.

With this aim, let us assume a configuration as the one presented in Fig. 9.4. A static base station is provided of an ASE source, a monochromator, and a dispersive medium 1. This base station is connected with an optical fiber (SMF2) to a remote station which has a spectral device with a spectral amplitude transfer function to be measured. The benefit of this technique is that it does not require any OSA in the remote station and the resolution of the spectrometric measurement is only limited by the scanning monochromator.

The remote measurement is performed by sweeping the monochromator in the base station and recording the light intensity with two photodetectors at each station, that also memorize the event history. When the sweeping is finished, the information from both stations is shared (through a classical or quantum information channel) in order to perform *a posteriori* the joint detection coincidence rate in a post-processing circuit. Mathematically, this translates into the calculation of [327]

$$R_c = \frac{1}{T_R T} \int_{-T/2}^{T/2} \mathrm{d}t_1 \int_{-T_R/2}^{T_R/2} \Delta G(t_1, t_1 + \tau) \mathrm{d}\tau. \tag{9.18}$$

Here T_R is the temporal response of the photodiode and T is the average time. Both times are usually much longer than the coherence time of the source that can be on the order of hundreds of femtoseconds, which allows us to extend the integral limits from $-\infty$ to $+\infty$.

The intensity interference term corresponding to the example in Fig. 9.4 is

$$\Delta G(t_1, t_2) = \left| \int d\omega \, S_{s,b}(\omega) H_1^*(\omega) H_2(\omega) \right.$$
$$\left. \times \prod_{n=2}^{N} \exp[i\omega^n(\Phi_{n2} - \Phi_{n1})/n!] \exp[-i\omega(t_2 - t_1)] \right|^2 . \qquad (9.19)$$

Here $H_1(\omega)$ and $H_2(\omega)$ represent the spectral transfer function at the baseband of the monochromator and the device under test (DUT), respectively. We also observe the need of the dispersive medium 1 to match the dispersion introduced by SMF2 in order to minimize the distortions in ΔG. Further, we assume that the monochromator has a sufficiently sharp bandpass function around the tunable frequency ω_m, so that $H_1(\omega) \approx \delta(\omega - \omega_m)$. We then get $R_c \approx |H_2(\omega_m) S_{s,b}(\omega_m)|^2$. If the spectrum of the ASE noise is flat enough in the spectral band of $H_2(\omega)$, the coincidence rate will provide the spectral shape function of the filter by sweeping the frequency of the monochromator. We would achieve then the same result as in [327] but without any quantum source [38]. However, unlike in the quantum case, in our scheme the measurable spectral range is limited to the spectral bandwidth of the source. But our setup has the advantage that it allows for all-order dispersion cancellation by selecting identical pair of fibers. And further, since broadband ASE sources operating in the $1.55 \, \mu$m telecom window are well-established, our method would avoid the intermodal distortion present in the original configuration [327], which uses visible light, allowing for larger interconnection distances.

Conclusions

The Space–Time analogy establishes a formal link between the diffraction of 1D paraxial monochromatic coherent beams and the temporal dispersion of coherent plane-wave pulses in first-order dispersive media. Far from being just a simple curiosity, this connection has triggered important applications in ultrashort-pulse processing by transferring results from diffractive optics that have been known for decades.

In this Thesis, we have proposed the temporal counterpart of an afocal system. In the temporal domain, this system has the capability of scaling the energy spectrum of ultrashort optical waveforms, and results completely feasible with current technology. Additionally, the analogy has also been used to propose the temporal counterpart of the Fresnel array illuminators. In this way, we have been able to reformulate the problem of temporal distortion of continuous-wave periodically phase-modulated light in terms of the Fresnel images of a phase grating. Our results perfectly match those previously achieved by different groups and opens the door to obtain highly repetitive ultrashort pulses with a high degree of flatness, with potential applications in optical-time-division multiplexing as well as in millimeter-wave photonics.

We have pointed out that it is necessary to take into account the stochastic nature of the light in order to have a more accurate description of ultrashort optical pulses affected by noise. In this Thesis, the description has been adapted from the previous results on optical coherence theory, in the framework of nonstationary statistics. In particular, we have developed a simple theory that simultaneously include the effects of amplitude, phase, and timing noise in ultrashort pulse trains. This theory has been shown to result particularly relevant to have a complete description of noisy frequency combs.

Additionally, we have reported the route to achieve, in a user-defined way, partially coherent pulses that obey the so-called independent-elementary-pulse representation. This model describes partially coherent pulses as an incoherent continuous superposition of a fully coherent ensemble of pulses. Further, we have extended the model to consider the elementary basis as partially coherent. This sophistication of the theory appears natural when one considers nondeterministic pulses modulating stationary sources.

The Space–Time analogy has also been shown to appear between partially coherent wavefields, with the same transfer rules than in the coherent case. Within this framework, we have studied the problem of having non-monochromatic incoherent sources in different systems widely used in temporal optics. In particular, real-time Fourier transformers have

been shown to degrade when operating under broadband spectrally incoherent sources. However, there are many optical systems that offer a better performance with incoherent sources. We have shown numerically that the electro-optic pulse generation technique can be ripple-free when a broadband source is used. Additionally, we have proposed and demonstrated experimentally a new technique for pulse shaping which is based on the quasistationary vanCittert–Zernike theorem in the time domain. In this technique, one filters spectrally an incoherent source and achieves a frequency-to-time mapping just by temporal modulation and dispersion in a group-delay-dispersion circuit. The technique has been shown particularly promising for radio-frequency arbitrary waveform generation because its performance can be understood as an incoherent microwave photonic filter.

There is a current trend to achieve low-cost alternatives to ultra-wideband pulse generation and fiber transmission. In this Thesis, we have experimentally reported several solutions based on current modulation of semiconductor lasers, as well as on the aforementioned technique of incoherent pulse shaping.

Finally, we have further extended the Space–Time analogy into the quantum–classical domain, thus establishing a fourfold connection. In particular, we have shown that the spreading in first-order dispersive media of temporally entangled two-photon light is identical (apart from a sign in the fundamental equations) to the spreading of partially coherent light pulses. Based on this new analogy, we have claimed that some previously reported effects that were achieved with temporally entangled two-photon light are not genuinely quantum and can be mimicked with partially coherent classical pulses. We have focused on the cases of ghost interference and nonlocal dispersion cancelation.

Further studies and experiments might be developed in the future. The experimental implementation of the proposed technique for achieving partially coherent pulses in a user-defined fashion seems particularly promising for some current femtochemistry applications where stochastic pulses are on demand.

The implementation of the incoherent pulse shaping technique using shorter pulse gates and/or different photonic architectures opens the door to truly arbitrary radio-frequency generation in the millimeter-wave domain. This could trigger several low-cost devices easily feasible in every fiber-optics laboratory.

Finally, the recently developed spatiotemporal quantum-classical analogy is expected to have some impact in quantum information science. Whether partially coherent pulses can always be used to emulate the effects of temporal entanglement is an open question that needs to be answered.

Durante las últimas décadas, la generación de haces ópticos pulsados con una duración temporal del orden del pico y femtosegundo ha constituido uno de los temas de investigación más candentes en el ámbito de la Física y la Ingeniería. Las características de este tipo de radiación, alta resolución temporal, elevada coherencia espacial, gran ancho de banda y potencialmente alta intensidad, la hacen sumamente útil para desarrollar numerosas aplicaciones en distintos campos de la ciencia y la tecnología [1].

Los láseres que poseen un amplio conjunto de modos longitudinales constituyen los mejores candidatos para la obtención de este tipo de radiación [112]. Para conseguir el régimen pulsado es necesario que todas estas componentes frecuenciales se superpongan con una fase determinada, para lo cual se han venido desarrollando diferentes técnicas, comúnmente denominadas bajo el apelativo de anclaje de modos ("mode locking" en inglés). De manera general es posible afirmar que existen dos mecanismos para el anclaje de modos, el activo y el pasivo. El primero ha permitido desarrollar dispositivos todo-fibra, y por tanto muy compactos, de enorme interés en el ámbito de las telecomunicaciones [3]. Típicamente la longitud de onda central se sitúa en la ventana de $1.55\,\mu$m y la duración temporal de los pulsos suele ser de 100 fs. El mecanismo de anclaje se consigue insertando en la cavidad un modulador electroóptico, de amplitud o de frecuencia, con lo que el tren de pulsos puede alcanzar una tasa de repetición de unas pocas decenas de GHz. Por otro lado, el anclaje de modos pasivo, obtenido mediante el efecto no lineal de focalizacin tipo Kerr en los cristales de Ti:Sa, ha permitido el desarrollo de sistemas comerciales capaces de ofrecer los pulsos más cortos ($<$ 10 fs) para longitudes de onda centradas en el infrarrojo [2]. Usualmente, la frecuencia de repetición, igual al rango espectral libre de la cavidad láser, es de algunas decenas de MHz.

Cabe destacar que los láseres de modos anclados sufren ciertas carencias, como la elevada sensibilidad a las condiciones ambientales reales o su enorme coste econmico, lo cual dificulta, a día de hoy, su incorporación al mercado en algunas de sus potenciales aplicaciones. Existen sistemas alternativos para la producción de radiación ultracorta. En el sector de las telecomunicaciones, por ejemplo, dicha generación se puede llevar a cabo utilizando moduladores de electroabsorción o mediante la técnica electroóptica [3]. En ambos métodos la tasa de repetición del tren es de decenas de GHz, pero la duración de los pulsos suele ser de unos pocos picosegundos.

Una de las potencialidades más interesantes de los sistemas ultrarrápidos es la de resolver procesos en el tiempo. El principio de operación es análogo al utilizado para captar imágenes del movimiento de ciertos procesos macroscópicos con flashes electrónicos [1]. Así nace la femtoquímica, que ha permitido el análisis y control en el régimen del femtosegundo de ciertas reacciones químicas fotoinducidas [4]. Mediante una configuracin bombeo-prueba se han podido determinar procesos químicos intermedios en reacciones qumicas de interés biológico e industrial. Cabe mencionar que estas investigaciones le valieron el premio Nobel de Química al profesor A. H. Zewail en 1999.

El enorme ancho de banda que presentan los pulsos ultracortos, junto con la alta potencia y elevada coherencia espacial, abre nuevas posibilidades en el campo de la tomografía de coherencia óptica y la metrología de superficies, donde usualmente se vienen empleando LEDs superluminiscentes como fuentes ópticas de baja coherencia temporal. Al sustituir este tipo de diodos por un láser de femtosegundo se consigue incrementar sustancialmente la resolución axial, es decir, en profundidad, de estos sistemas interferométricos [1].

Los pulsos de femtosegundo pueden alcanzar una potencia de pico muy alta, lo que permite la generación de procesos multifotón. Esto ha abierto nuevas posibilidades en el campo de la microscopía no lineal, ya que la región de fluorescencia se concentra ahora en un volumen focal mucho menor que el alcanzado mediante métodos convencionales, lo que en definitiva incrementa la capacidad de seccionado óptico. Esto, combinado con el hecho de que la potencia promedio es lo suficientemente baja como para no dañar determinadas muestras biológicas, ofrece interesantes aplicaciones en el campo de la biomedicina [1].

La generación de pulsos cuya duración temporal ocupa sólo unos pocos ciclos de oscilación de la frecuencia óptica principal, combinado con la tecnología CPA, ha permitido la obtención de haces de radiación de extremada potencia de pico, abriendo nuevas líneas de investigación en el ámbito de la interacción radiación-materia, como la física no lineal extrema o la fusión nuclear inducida por láser [7]. Uno de los fenómenos no lineales extremos que está suscitando un mayor interés en la comunidad científica es la generación de radiación de longitudes de onda harmónicas inferiores mediante pulsos láser de femtosegundo. En este caso se pueden conseguir pulsos con duración subfemtosegundo. La creación, manipulación y caracterización de estos pulsos constituye un reto para la comunidad científica y sin duda será uno de los campos más prometedores de la Física en los próximos aos [10]. Al igual que la femtoquímica permitió el estudio de la dinámica de las moléculas, la denominada attofísica, debido a la escala temporal del pulso empleado, permitirá el estudio dinámico del movimiento de los electrones en el átomo. Es muy importante destacar que para la generación de secuencias de pulsos de attosegundo es necesario obtener previamente un tren de pulsos ópticos de unos pocos femtosegundos con elevada estabilidad [13]. Esto quiere decir que la variación aleatoria tanto de la envolvente, como de la fase relativa entre la envolvente y la portadora entre pulso y pulso, debe ser controlada. En otras palabras, la coherencia del tren de pulsos debe ser total. En el dominio frecuencial esta afirmacin equivale a tener un peine de frecuencias de extremadamente alta definición. Para conseguirlo, se han adaptado y perfeccionado técnicas empleadas en espectroscopía láser de alta resolución para la estabilización del espectro de modos longitudinales del láser [11]. De esta manera, el láser de modos anclados estabilizado constituye una potente herramienta de precisión con una resolución sin precedentes, lo que ha revolucionado el sector de la metrología de frecuencias ópticas [12],

con aplicaciones que van desde la determinación de compuestos moleculares [97] hasta la síntesis de señales necesarias en telecomunicaciones [93]. Finalmente, es necesario destacar que los profesores T. W. Hänsch y J. L. Hall fueron galardonados en 2005 con la mitad del premio Nobel de Física por el desarrollo de esta tecnología.

Respecto a las aplicaciones comerciales de los sistemas ultrarrápidos, cabe mencionar que la corta duración de los pulsos permite su utilización para el control de calidad de sistemas electrónicos de alta velocidad, ya que los dispositivos usualmente empleados para este fin son más lentos que los sistemas electrónicos más avanzados [195]. De hecho, la energía que posee un solo pulso se concentra en una duración temporal mucho menor que el tiempo de difusión térmica de muchos materiales, lo que permite por ejemplo, la fabricación de guías de onda y la realización de cortes y perforado de alta precisión con mínima afectación térmica sobre diferentes tipos de sustrato [1]. Cabe destacar que una de las aplicaciones de la excitación multifotón mediante pulsos ultracortos es la fabricación de objetos tridimensionales de dimensiones reducidas mediante la polimerización a dos fotones que tiene lugar en determinados tipos de resina. El potencial de esta técnica para aplicaciones biomédicas reside en el hecho de que las piezas fabricadas poseen el mismo tamaño que un glóbulo rojo, lo que sugiere la creación y empleo de microsensores o micromáquinas para determinados tratamientos clínicos [1]. Otras aplicaciones potenciales de los láseres de femtosegundo en biomedicina pasan por la obtención de radiografías sin radiación ionizante, nuevas técnicas de cirugía no térmica de la córnea, incisiones en el esmalte dental o el desarrollo de nuevos marcadores de células cancerosas [1].

Finalmente, en el sector de las comunicaciones por fibra óptica, un láser de 100 fs posee un ancho de banda espectral comparable al ancho total de su ventana de pérdidas mínimas. De esta manera, para sistemas avanzados que operan mediante multiplexado denso por división de longitud de onda, donde cada canal de información se implementa mediante un láser de semiconductor, es posible sustituir todos los canales por un solo láser pulsado, aprovechando en definitiva el ancho de banda global de la fibra óptica [94]. Para sistemas que operan mediante multiplexado óptico por división temporal, se ha demostrado experimentalmente la transmisión de datos a una tasa de 1.28 Tb/s [3]. Por otro lado, en el ámbito del procesado fotónico de señales de microondas, las técnicas de conformado de alta resolución de pulsos ultracortos por medio de conversores espacio-tiempo han permitido la generación de señales de perfil arbitrario de decenas de GHz, que actualmente resultan imposibles de realizar mediante métodos electrónicos convencionales [85]. En este mismo sector, mediante el empleo de láseres de fibra pulsados, también se ha conseguido aumentar la frecuencia de señales de microondas cosenoidales [145].

Por otro lado, en óptica temporal es un hecho bien conocido que la ecuación que describe la distorsión de la envolvente de un pulso en el seno de un medio dispersivo cuadrático es formalmente idéntica a la que gobierna la difracción paraxial de un haz coherente unidimensional monocromático [14]. Esta conexión se conoce como analogía Espacio-Tiempo y constituye una herramienta muy potente, pues permite la transferencia de resultados y la profundización en la comprensión física de ciertos fenómenos que necesariamente tienen lugar en ambos dominios. Por nombrar sólo unos ejemplos, la implementación de sistemas de formación de imágenes temporales ha permitido cambiar la escala temporal de la intensidad de pulsos ópticos, sin distorsinar la forma, hasta hacerla accesible a la resolución temporal de los aparatos de medida electrónicos con-

vencionales [169]; el efecto Talbot temporal entero ha sido propuesto, por ejemplo, para mitigar el denominado "timing jitter" [180]; el efecto Talbot fraccional ha servido para la multiplicación totalmente óptica de la tasa de repetición en intensidad de trenes de pulsos [158]; y la adaptación del formalismo matricial ABCD ha permitido reformular de una manera más simple el mecanismo de anclaje de modos activo en una cavidad láser [136]. La analogía Espacio–Tiempo también ha sido aplicada para definir el régimen de Fraunhofer temporal en medios dispersivos [157] y su aplicación para el diseño de analizadores espectrales en tiempo real, identificar el homólogo temporal de la acción de la iluminación esférica [143]; seguido de un largo etcétera.
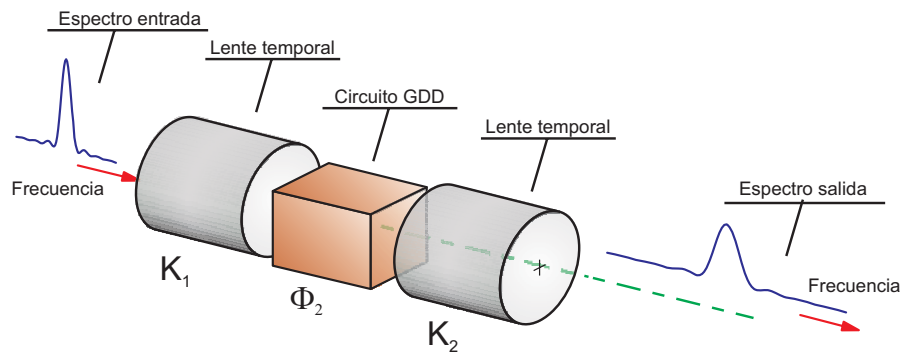

Figura 1. Esquema de un sistema formador de imágenes espectral. El espectro del pulso de salida constituye una réplica escalada del de entrada si se establece la siguiente relación $K_1^{-1} + K_2^{-1} = \Phi_2$, donde K_i es la tasa de chirp de la lente i y Φ_2 es la cantidad de dispersión introducida por el circuito de retardo de grupo (circuito GDD).

Dentro de la mencionada analogía, en el Capítulo V de esta Tesis hemos demostrado que cualquier sistema afocal se comporta como un sistema formador de imágenes en el dominio espectral. Esto implica que podemos diseñar sistemas fotónicos capaces de escalar el espectro de potencia de un pulso de entrada, tal y como se ilustra en la Fig. 1. La implementación práctica de este tipo de dispositivos se realiza mediante dos lentes temporales separadas de un medio dispersivo lineal. Las simulaciones presentadas demuestran que, mediante un tándem formado por una lente temporal implementada mediante un modulador electroóptico de fase, una fibra monomodo y una fibra no lineal bombeada con un pulso Gaussiano, es posible obtener el deseado sistema. En concreto, se puede diseñar el sistema para superar la resolución actual de los analizadores ópticos espectrales comerciales.

Asimismo, también hemos adaptado al dominio temporal los famosos "iluminadores Talbot" [201]. Mientras que el fenómeno Talbot fraccional ha sido utilizado para alcanzar altas frecuencias de repetición a partir de un tren de pulsos con bajo factor de llenado; los iluminadores de Talbot tratan de obtener una secuencia de pulsos, de alta tasa de repetición y perfil arbitrario, a partir del diseño de un perfil de fase adecuado y su distorsión en el seno de un medio linealmente dispersivo que satisface la condición de Talbot fraccional. Para la implementación práctica de este tipo de dispositivos, únicamente es necesario un láser de onda continua; un modulador electroóptico de fase; una señal de radiofrecuencia que conduce el modulador; y una fibra óptica monomodo como medio

dispersivo, tal y como muestra la Fig. 2. Por un lado, nuestro análisis ha proporcionado soporte teórico a los experimentos publicados recientemente en la literatura donde se conseguían secuencias de pulsos de perfil plano [194]. Por otro lado, la adaptación de iluminadores Talbot al dominio temporal ha permitido la predicción teórica de nuevos perfiles de enorme utilidad para el demultiplexado de señales de alta tasa de repetición. Finalmente, al utilizar una fuente óptica pulsada en lugar de un láser de onda continua, es posible conseguir señales comprimidas en el tiempo que, al ser detectadas por un fotodiodo ideal, generan corrientes eléctricas con un contenido espectral en el rango de las ondas milimétricas. Dichas señales pueden ser útiles en el campo de la transmisión de señales inalámbricas por redes de fibra óptica [195].
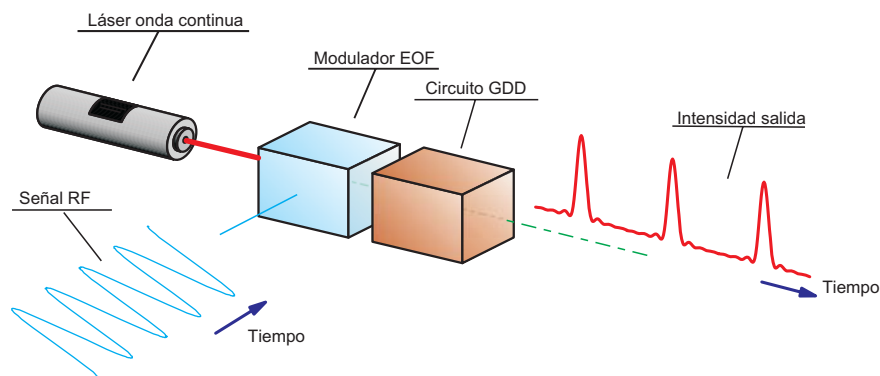

Figura 2. Esquema para la generación de iluminadores Talbot en el dominio temporal. Un láser de onda continua es modulado por un modulador electro-óptico de fase (EOF), que a su vez es ocnducido por una señal periódica y arbitraria de radio frecuencia (RF). El perfil de esta señal eléctrica se transfiere a la fase óptica del láser. Al dispersar la onda por un medio dispersivo cuadrático es posible obtener determinados patrones de intensidad mediante el correcto diseño de la señal de RF.

No obstante, en la mayoría de los fenómenos y aplicaciones anteriores se asume que los pulsos son totalmente coherentes. Sin embargo, la mayoría de los fenómenos físicos reales están sujetos a fluctuaciones aleatorias y, en un caso práctico real, la envolvente de los pulsos que conforman el tren varía, en cierta medida, aleatoriamente de pulso a pulso [48]. Esto se debe a que la superposición de las distintas componentes frecuenciales no se realiza con una fase determinada. En el ámbito de la óptica temporal, este hecho cobra especial relevancia dada la influencia de los fenómenos de emisión espontánea en dispositivos tales como los láseres de semiconductor, las fuentes de emisión espontánea amplificada o los diodos emisores de luz, entre muchos otros [77]. La contribución de estos efectos, de origen puramente aleatorio, se refleja en un ensanchamiento de la línea óptica espectral, lo que no puede ser ignorado en muchas aplicaciones.

En este contexto, el método desarrollado por Marcuse [76] ha sido ampliamente utilizado para estudiar la propagación de pulsos Gaussianos parcialmente coherentes emitidos por moduladores externos a la fuente óptica real o para diseñar filtros transversales para aplicaciones en sistemas de radiofrecuencia sobre fibra [78]. Por otro lado, la teoría de la coherencia óptica fue desarrollada en el marco de la difracción de haces parcialmente coherentes espacialmente, pero constituyendo en sí misma un tratamiento más riguroso y

potente para describir los efectos estadísticos en sistemas ópticos [48]. Esta teoría tiene en cuenta los fenómenos estocásticos a través de las funciones de correlación, que tienen su fundamento matemático en el marco de la teoría clásica de señales aleatorias. Sin embargo, su empleo en el dominio de la óptica temporal ha sido más bien escaso. Saleh empleó este formalismo para tratar el mismo problema que Marcuse, pero restringiéndose a primer orden en la distorsión [81]. Ya destacó que algunos de los resultados obtenidos se encontraban estrechamente ligados con sus problemas homólogos espaciales, pero sin establecer un vínculo formal entre los mismos.

Recientemente ha habido un renovado interés en el estudio teórico de este tipo de radiación desde la perspectiva de la teoría de la coherencia óptica. Específicamente, se ha introducido la definición rigurosa de un pulso Gaussiano parcialmente coherente y sus características [41], su implementacin experimental [55] y su propagación en sistemas matriciales ABCD temporales [207], así como la reformulación del teorema de vanCittert-Zernike en el dominio temporal y su aplicación para medir los parámetros de dispersión cromática de medios dispersivos arbitrarios [75]. Cabe destacar que para la medida experimental de pulsos parcialmente coherentes, en principio no se requieren nuevos dispositivos, pero sí un conjunto amplio de muestras con el fin de poder llevar a cabo cálculos estadísticos [245].

El objetivo principal de esta Tesis ha sido el de estudiar, desde una perspectiva tanto práctica como aplicada, los efectos aleatorios en pulsos ópticos, y en especial en pulsos ultracortos dado su enorme interés actual. Para ello hemos empleado el formalismo de la coherencia óptica. Nos hemos restringido al caso escalar, lo que equivale a asumir un estado de polarización determinista e invariable. El Capítulo II recoge brevemente los resultados más importantes de esta teoría que han sido necesarios para entender los principales resultados expuestos a lo largo de la Tesis. En él se destacan brevemente, por un lado el caso de estadística estacionaria, que fue adaptada a la óptica a mitades del siglo XX con los trabajos pioneros de Wolf [48] y que, aunque resulta particularmente adecuada para describir luz de tipo térmica, tal como la de un diodo emisor de luz o una fuente de radiación del tipo emisión espontánea, resulta imprecisa a la hora de describir pulsos ultracortos que poseen una variación promedio de la intensidad que no es constante en el transcurso del tiempo. Así pues el Capítulo II también recoge por otro lado, a modo de resumen, la extensión del formalismo de funciones de correlación al caso en el que la intensidad promedio es una función dependiente del tiempo, esto es, el caso no estacionario. En particular, se estudia el teorema de Wiener–Khintchine generalizado, que conecta las funciones de correlación en el dominio espacio–tiempo y espacio–frecuencia en su expresión más general. Por último, se realiza un análisis de funciones de correlación de orden superior asumiendo estadística Gaussiana. En este caso, toda la jerarquía de funciones de correlación es susceptible de ser expresada en términos de funciones de correlación de segundo orden.

El Capítulo III estudia algunos modelos particulares de funciones de correlación. Por un lado, estos modelos constituyen herramientas matemáticas adecuadas a la hora de describir las propiedades de coherencia de pulsos ultracortos, y por otro, dan una idea física clara y concisa a la hora de generar en el laboratorio este determinado tipo de radiación. En particular, se estudia la representación de pulsos coherentes independientes. Básicamente, este modelo asume que se puede generar determinados tipos de funciones de
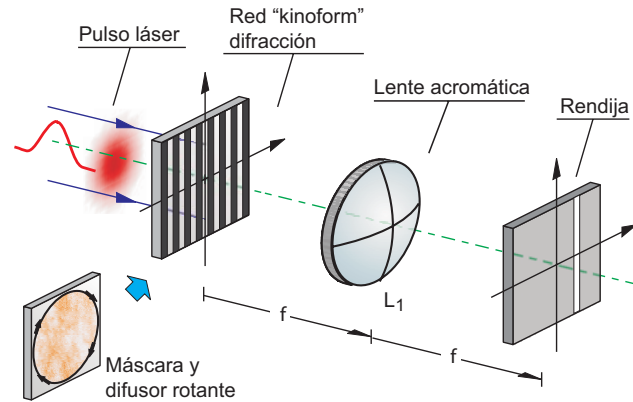
Figura 3. Esquema para la síntesis de pulsos parcialmente coherentes mediante el modelo de superposición incoherente de pulsos elementales coherentes. Un haz pulsado espacial y temporalmente coherente incide sobre un conformador de pulsos tipo espacio a tiempo. La clave está en insertar un difusor rotante junto a la máscara de síntesis. De esta manera, el pulso óptico de salida resulta espectralmente parcialmente coherente y posee una función de correlación correspondiente al modelo de superposición continuo e incoherente.

correlación mediante superposición incoherente de pulsos totalmente coherentes [46]. El modelo puede ser expresado tanto en el dominio temporal como en el espectral. Ambos son completamente compatibles con las definiciones rigurosas de no negatividad [73]. Experimentalmente, el primer modelo puede ser construido mediante modulación determinista de una fuente spectralmente incoherente con un determinado ancho de banda [55]. El segundo modelo se puede implementar mediante un esquema como el de la Fig. 3. Un haz pulsado totalmente coherente pasa por un difusor rotante. El difusor induce coherencia espacial en el haz, que a su vez pasa por un conformador de pulsos de traslación directa espacio-tiempo. En esta Tesis hemos demostrado que en este caso, las propiedades de coherencia temporal pueden ser controladas a través del control de las propiedades de coherencia espacial y que la función de coherencia mutua se corresponde con el modelo de superposición de pulsos elementales coherentes en el dominio espectral. Cabe destacar que la utilización de pulsos parcialmente coherentes con coherencia controlada puede dar lugar a un nuevo grado de libertad en el control de la producción de productos en ciertas reacciones químicas [68].

Finalmente, en el Capítulo III también extendemos el modelo de superposición al dominio parcialmente coherente. En este caso la base elemental ya no es un conjunto de pulsos totalmente coherentes sino parcialmente coherentes. Esta sofisticación de la teoría es perfectamente válida a la hora de considerar modulaciones no deterministas de fuentes estacionarias.

El Capítulo IV estudia los efectos de coherencia temporal en trenes de pulsos ultracortos. A diferencia de los anteriores capítulos, consideramos la coherencia de trenes de pulsos y no pulsos individuales. Este hecho permite desarrollar un modelo basado en conceptos de coherencia que incluye los efectos de "timing jitter" de una manera simple y analítica. Asimismo, nuestro modelo permite predecir las distorsiones aparentes en las correlaciones espectrales de un peine de frecuencias [122]. En particular encontramos que

los efectos de coherencia parcial (modelizada como ruido estacionario multiplicativo) contribuyen en ensanchar cada una de las líneas espectrales del peine. Cuando se considera el espectro de energía en su conjunto, las líneas se ubican en la misma posición que en el caso coherente. El timing jitter contribuye a ensanchar las líneas más alejadas de la frecuencia central de manera cuadrática. Finalmente, dos frecuencias aparecen descorrelacionadas entre sí de no ser que su diferencia sea un múltiplo entero de la frecuencia de repetición del tren.

El Capítulo V constituye el núcleo del trabajo. En él estudiamos la propagación en medios linealmente dispersivos de pulsos de tipo onda plana parcialmente coherentes. Mediante la formulación de la teoría de la coherencia óptica, hemos reconocido que la analogía Espacio–Tiempo también se establece entre campos ondulatorios parcialmente coherentes. Este resultado clave permite extender los resultados conocidos durante décadas referentes a haces parcialmente coherentes espacialmente a pulsos temporalmente parcialmente coherentes. En particular, hemos recuperado las leyes de evolución de un pulso parcialmente coherente Gaussiano [207] a partir de los resultados en el dominio espacial [54], y reconocido que los efectos del ancho de línea de la fuente óptica en sistemas linealmente dispersivos pueden tratarse matemáticamente en términos de una simple convolución entre el espectro de energía de la fuente con la intensidad resultante de la propagación de a señal coherente. Esta potente herramienta constituye el homólogo temporal del teorema de equivalencia de Collet–Wolf en la región de Fresnel [209] y ha servido para analizar la influencia del ancho de línea en sistemas transformadores de Fourier en tiempo real. Por último, el teorema de Collet–Wolf en la región de Fresnel nos permite reconocer que el espectro de energía de la fuente actúa como un filtro pasa-baja para la intensidad [210]. Así pues, por el hecho de utilizar una fuente espectralmente incoherente con un determinado ancho de banda, se puede eliminar los efectos perniciosos que induce la modulación de alta frecuencia en los sistemas generadores de pulsos por el método electroóptico [192].
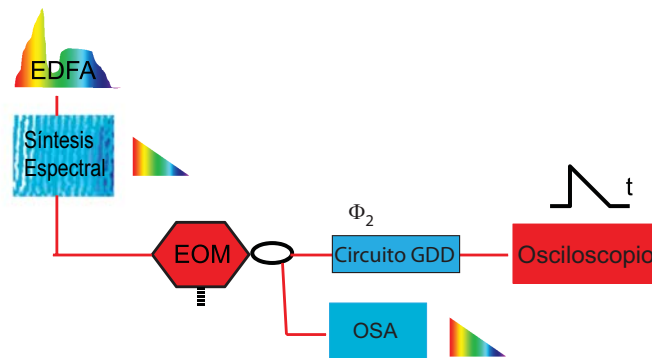
Figura 4. Diagrama para la generación arbitraria de perfiles de intensidad promedio. La fuente espectral incoherente se toma de un amplificador de fibra dopada con Erbio (EDFA) y se perfila adecuadamente; la modulación externa determinista se realiza con un modulador electroóptico (EOM). Finalmente, el circuito de dispersión realiza la conversión frecuencia tiempo.

El Capítulo VI recoge una técnica original para la generación de perfiles temporales de intensidad arbitrarios, basada en el teorema de van Cittert–Zernike para pulsos cuasi-homogéneos en el dominio temporal [75]. La técnica está ilustrada en la Fig. 4. Una

fuente óptica espectralmente incoherente se filtra con un perfil definido por el usuario. Después la fuente se modula externamente con un modulador determinista, pero de tal manera que el espectro óptico de energía no cambie significativamente. Al propagar la señal por un medio dispersivo de primer orden (como una fibra óptica) con una cantidad mínima de dispersión (fijada por la condición de campo lejano parcialmente coherente), la intensidad promedio del pulso a la salida constituye una réplica escalada del perfil sintetizado de la fuente.

En el Capítulo VII proponemos dos técnicas para la medida de pulsos parcialmente coherentes mediante métodos no interferenciales. El primero asume que el pulso parcialmente coherente se puede decribir como un pulso coherente afectado de ruido multiplicativo y estacionario en el tiempo. Para caracterizar este tipo de radiación, se requieren únicamente tres medidas. Dos medidas del perfil de intensidad promedio, una antes y otra después de propagación en un medio dispersivo de primer orden. Finalmente, una medida del espectro de energía da lugar a una caracterización completa de la función de coherencia mutua del pulso. Por otro lado, el segundo modelo, dual del primero, asume que el pulso parcialmente coherente puede ser descrito como un pulso coherente afectado de ruido multiplicativo en el dominio espectral. También se requieren tres medidas: el espectro de energía del pulso a la entrada y la salida de una lente temporal y el perfil de intensidad promedio del pulso. Con este procedimiento, la función de correlación cruzada espectral queda caracterizada completamente.

El Capítulo VIII recoge diversas técnicas fotónicas de aplicación en el ámbito del procesado y generación de señales de radiofrecuencia. Hemos demostrado teórica y experimentalmente que un la función de transferencia en un filtro transversal incoherente de microondas se compone de la mulltiplicación de tres términos. El primero corresponde al efecto del tipo de conversor eléctrico-óptico, el segundo a la respuesta frecuencial del conversor óptico-eléctrico y el tercero y más importante, una versión escalada de la función de coherencia mutual de la fuente espectralmente incoherente de banda ancha utilizada. Hemos demostrado que, en determinadas circunstancias se puede conseguir que este término domine sobre los demás, lo que implica que el filtro se puede reconfigurar al filtrar adecuadamente el espectro de la fuente óptica y a través de él, la función de coherencia mutua de la fuente. En el ámbito de la generación de señales de radio-frecuencia, el sistema de la Fig. 4 ha resultado adecuado para la generación de señales arbitrarias en el rango 0–10 GHz. Dentro del rango de banda ultra amplia (3.1–10.6 GHz) [300], hemos demostrado que se pueden emplear láseres semiconductor como alternativa de bajo coste, aprovechando las operaciones inherentes de conversión frecuencia–intensidad y "sobredisparo" [77].

Finalmente, en el Capítulo IX, hemos extendido la analogía Espacio–Tiempo al caso cuántico. Hemos demostrado que las ecuaciones que las ecuaciones que describen la distorsión temporal de un sistema de fotones entralazados en medios dispersivos de primer orden [171] son formalmente idénticas, a parte de un signo, a las que describen la distorsión de pulsos clásicos parcialmente coherentes. Este hecho sugiere que algunos sistemas interferenciales de cuarto orden donde se utilizan fuentes cuánticas pueden operar con fuentes clásicas, pero parcialmente coherentes, tal y como se muestra en la Fig. 5. En particular, hemos formulado el fenómeno de la difracción fantasma [342] en el dominio temporal y demostrado que puede ser conseguido mediante pulsos parcialmente coherentes. Final-
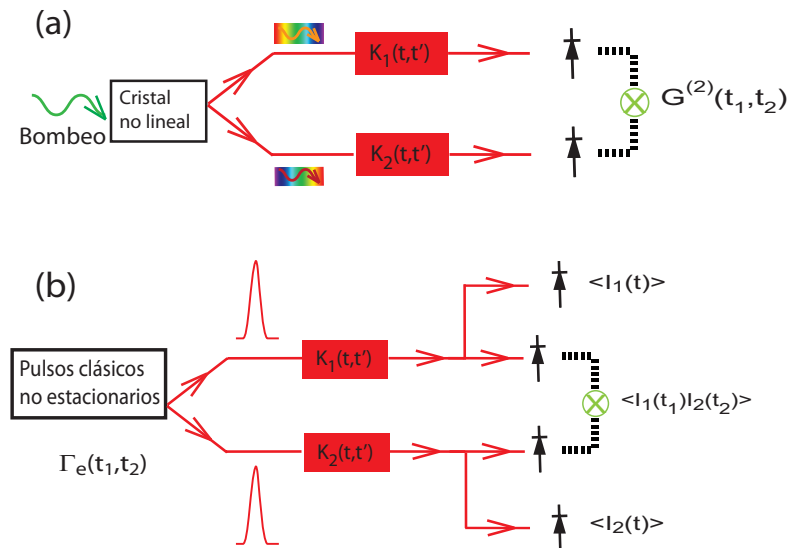
Figura 5. (a) Sistema cuántico que describe la distorsión temporal de dos fotones entrelazados en un medio dispersivo general; (b) Sistema clásico que opera con pulsos parcialmente coherentes. En ambos se miden coincidencias en intensidad. En el caso cuántico estas coincidencias son proporcionales al módulo cuadrado de la amplitud de probabilidad mientras que en el caso clásico el resultado es proporcional a la función de correlación de cuarto orden.

mente, hemos desmostrado teóricamente que el fenómeno de cancelación no local de la dispersión [347] puede ser emulado con fuentes clásicas estacionarias, lo que ha permitido proponer un sistema para la transferencia remota de funciones espectrales [329] que opera sin luz cuántica.

[1] M. E. Fermann, A. Galvanauskas, and G. Sucha, eds., *Ultrafast Lasers. Technology and Applications* (Marcel Dekker, New York, 2003).

[2] G. Steinmeyer, D. H. Sutter, L. Gallmann, N. Matuschek, and U. Keller, "Frontiers in ultrashort pulse generation: pushing the limits in linear and nonlinear optics," *Science* **286**, 1507–1512 (1999).

[3] H.-G. Weber and M. Nakazawa, eds., *Ultrahigh–Speed Optical Transmission Technology* (Springer Verlag, New York, 2007).

[4] A. H. Zewail, "Femtochemistry: Atomic-scale dynamics of the chemical bond," *J. Phys. Chem. A* **104**, 5660–5694 (2000).

[5] A. F. Fercher, W. Drexler, C. K. Hitzenberger, and T. Lasser, "Optical coherence tomography - principles and applications," *Rep. Prog. Phys.* **66**, 239–303 (2003).

[6] M. D. Perry and G. Mourou, "Terawatt to Petawatt Subpicosecond Lasers," *Science* **264**, 917–924 (1994).

[7] T. Brabec and F. Krausz, "Intense few-cycle laser fields: Frontiers of nonlinear optics," *Rev. Mod. Phys.* **72**, 545–591 (2000).

[8] G. A. Mourou, T. Tajima, and S. V. Bulanov, "Optics in the relativistic regime," *Rev. Mod. Phys.* **78**, 309–371 (2006).

[9] P. H. Bucksbaum, "The future of attosecond spectroscopy," *Science* **317**, 766–769 (2007).

[10] E. Goulielmakis, V. S. Yakovlev, A. L. Cavalieri, M. Uiberacker, V. Pervak, A. Apolonski, R. Kienberger, U. Kleineberg, and F. Krausz, "Attosecond control and measurement: lightwave electronics," *Science* **317**, 769–775 (2007).

[11] S. T. Cundiff and J. Ye, "Colloquium: Femtosecond optical frequency combs," *Rev. Mod. Phys.* **75**, 325–342 (2003).

[12] T. Udem, R. Holzwarth, and T. W. Hänsch, "Optical frequency metrology," *Nature* **416**, 233–237 (2002).

[13] J. Ye and S. T. Cundiff, eds., *Femtosecond Optical Frequency Comb Technology. Principle, Operation and Application* (Springer Verlag, New York, 2005).

[14] B. H. Kolner, "Space–time duality and the theory of temporal imaging," *IEEE J. Quantum Electron.* **30**, 1951–1963 (1994).

[15] J. W. Goodman, *Statistical Optics* (John Wiley and Sons, New York, 1985).

[16] J. van Howe and C. Xu, "Ultrafast optical signal processing based upon space–time dualities," *J. Lightwave Technol.* **24**, 2649–2662 (2006).

[17] G. P. Agrawal, *Nonlinear Fiber Optics* (Academic Press, San Diego, 2007).

[18] M. Bertolotti, L. Sereda, and A.Ferrari, "Application of the spectral representation of stochastic processes to the study of nonstationary light radiation: a tutorial," *J. Eur. Opt. Soc. A* **6**, 153–171 (1997).

[19] J. Lancis, V. Torres-Company, E. Silvestre, and P. Andrés, "Space-time analogy for partially coherent plane-wave-type pulses," *Opt. Lett.* **30**, 2973–2975 (2005).

[20] V. Torres-Company, J. Lancis, and P. Andrés, "Unified approach to describe optical pulse generation by propagation of periodically phase-modulated CW laser light," *Opt. Express* **14**, 3171–3180 (2006).

[21] V. Torres-Company, G. Mínguez-Vega, J. Lancis, E. Silvestre, and P. Andrés, "Source linewidth effects in temporal imaging of Gaussian Schell-model pulses," *Opt. Commun.* **267**, 40–43 (2006).

[22] V. Torres-Company, M. Fernández-Alonso, J. Lancis, J. C. Barreiro, and P. Andrés, "Millimeter-wave and microwave signal generation by low-bandwidth electro-optic phase modulation," *Opt. Express* **14**, 9617–9626 (2006).

[23] V. Torres-Company, J. Lancis, and P. Andrés, "Arbitrary waveform generator based on all-incoherent pulse shaping," *IEEE Photon. Technol. Lett.* **18**, 2626–2628 (2006).

[24] V. Torres-Company, J. Lancis, and P. Andrés, "Incoherent frequency-to-time mapping: application to incoherent pulse shaping," *J. Opt. Soc. Am. A* **24**, 888–894 (2007).

[25] V. Torres-Company, J. Lancis, P. Andrés, and M. A. Muriel, "Real-time optical spectrum analyzers operating with spectrally incoherent broadband continuous-wave light source," *Opt. Commun.* **273**, 320–323 (2007).

[26] A. T. Friberg, H. Lajunen, and V. Torres-Company, "Spectral elementary-coherence-function representation for partially coherent light pulses," *Opt. Express* **15**, 5160–5165 (2007).

[27] J. Lancis, V. Torres-Company, P. Andrés, and J. Ojeda-Castañeda, "Side-lobe suppression in electro-optic pulse generation," *Electron. Lett.* **43**, 414–415 (2007).

[28] V. Torres-Company, H. Lajunen, and A. T. Friberg, "Effects of partial coherence on frequency combs," *J. Eur. Opt. Soc. R.P.* **2**, 07007 (2007).

[29] V. Torres-Company, H. Lajunen, and A. T. Friberg, "Coherence theory of noise in ultrashort-pulse trains," *J. Opt. Soc. Am. B* **24**, 1441–1450 (2007).

[30] V. Torres-Company, G. Mínguez-Vega, J. Lancis, and A. T. Friberg, "Controllable generation of partially coherent light pulses with direct space-to-time pulse shaper," *Opt. Lett.* **32**, 1608–1610 (2007).

[31] V. Torres-Company, J. Lancis, and P. Andrés, "Spectral imaging system for scaling the power spectrum of optical waveforms," *Opt. Lett.* **32**, 2849–2851 (2007).

[32] V. Torres-Company, J. Lancis, and P. Andrés, "Flat-top ultra-wideband photonic filters based on mutual coherence function synthesis," *Opt. Commun.* **281**, 1438–1444 (2008).

[33] V. Torres-Company, K. Prince, and I. T. Monroy, "Fiber transmission and generation of ultrawideband pulses by direct current modulation of semiconductor lasers and chirp-to-intensity conversion," *Opt. Lett.* **33**, 222–224 (2008).

[34] V. Torres-Company, H. Lajunen, J. Lancis, and A. T. Friberg, "Ghost interference with classical partially coherent light pulses," *Phys. Rev. A* 043811 (2008).

[35] V. Torres-Company, I. T. Monroy, J. Lancis, and P. Andrés, "All-fiber incoherent frequency-to-time mapping method for microwave signal generation with baseband transmission and multicasting support," *Opt. Commun.* (in press, 2008).

[36] V. Torres-Company, J. Lancis, P. Andrés, and L. R. Chen, "Reconfigurable RF-waveform generation based on incoherent-filter design," *J. Lightwave Technol.* (in press, 2008).

[37] V. Torres-Company, K. Prince, and I. T. Monroy, "Ultra-wideband pulse generation based on overshooting effect in gain-switched semiconductor lasers," *IEEE Photon. Technol. Lett.* (in press, 2008).

[38] V. Torres-Company, H. Lajunen, and A. T. Friberg, "Nonlocal dispersion cancellation with classical light and its application to remote spectral transfer," *Phys. Rev. Lett.* (submitted, 2008).

[39] M. Born and E. Wolf, *Principles of Optics* (Cambridge University Press, Cambridge, 2000).

[40] I. P. Christov, "Propagation of partially coherent light pulses," *Optica Acta* **33**, 63–72 (1986).

[41] P. Pääkkönen, J. Turunen, P. Vahimaa, A. T. Friberg, and F. Wyrowski, "Partially coherent Gaussian pulses," *Opt. Commun.* **204**, 53–58 (2002).

[42] H. Lajunen, J. Tervo, and P. Vahimaa, "Overall coherence and coherent-mode expansion of spectrally partially coherent plane-wave pulses," *J. Opt. Soc. Am. A* **21**, 2117–2123 (2004).

[43] S. A. Ponomarenko, G. P. Agrawal, and E. Wolf, "Energy spectrum of a nonstationary ensemble of pulses," *Opt. Lett.* **29**, 394–396 (2004).

[44] H. Lajunen, J. Turunen, P. Vahimaa, J. Tervo, and F. Wyrowski, "Spectrally partially coherent pulse trains in dispersive media," *Opt. Commun.* **255**, 12–22 (2005).

[45] H. Lajunen, P. Vahimaa, and J. Tervo, "Theory of spatially and spectrally partially coherent pulses," *J. Opt. Soc. Am. A* **22**, 1536–1545 (2005).

[46] P. Vahimaa and J. Turunen, "Independent-elementary-pulse representation for nonstationary fields," *Opt. Express* **14**, 5007–5012 (2006).

[47] B. J. Davis, "Observable coherence theory for statistically periodic fields," *Phys. Rev. A* **76**, 043843 (2007).

[48] L. Mandel and E. Wolf, *Optical Coherence and Quantum Optics* (Cambridge University Press, Cambridge, 1995).

[49] A. C. Schell, "Technique for the determination of the radiation pattern of a partially coherent aperture," *IEEE Trans. Anten. Prop.* **AP-15**, 187–188 (1967).

[50] J. T. Foley and M. S. Zubairy, "Directionality of Gaussian Schell-model beams," *Opt. Commun.* **26**, 297–300 (1978).

[51] P. DeSantis, F. Gori, G. Guattari, and C. Palma, "An example of a Collett–Wolf source," *Opt. Commun.* **29**, 256–260 (1979).

[52] E. Collett and E. Wolf, "Beams generated by a Gaussian quasi-homogeneous sources," *Opt. Commun.* **32**, 27–31 (1980).

[53] A. T. Friberg and R. J. Sudol, "Propagation parameters of Gaussian Schell-model beams," *Opt. Commun.* **41**, 383–387 (1982).

[54] A. T. Friberg and J. Turunen, "Imaging of Gaussian Schell-model sources," *J. Opt. Soc. Am. A* **5**, 713–720 (1988).

[55] H. Lajunen, J. Tervo, J. Turunen, P. Vahimaa, and F. Wyrowski, "Spectral coherence properties of temporally modulated stationary light sources," *Opt. Express* **11**, 1894–1899 (2003).

[56] J. Turunen, E. Tervonen, and A. T. Friberg, "Acousto-optic control and modulation of optical cohernece by elecronically synthesized holographic gratings," *J. Appl. Phys.* **67**, 49–59 (1990).

[57] D. Mendlovic, G. Shabtay, and A. W. Lohmann, "Synthesis of spatial coherence," *Opt. Lett.* **24**, 361–363 (1999).

[58] Z. Zalevsky, J. García, P. García-Martínez, and C. Ferreira, "Spatial information transmission using othogonal mutual coherence coding," *Opt. Lett.* **30**, 2837–2839 (2005).

[59] M. Takeda, W. Wang, Z. Duan, and Y. Miyamoto, "Coherence holography," *Opt. Express* **13**, 9629–9635 (2005).

[60] W. Martienssen and E. Spiller, "Coherence and fluctuations in light beams," *Am. J. Phys.* **32**, 919–926 (1964).

[61] E. Baleine, A. Dogariu, and G. S. Agarwal, "Correlated imaging with shaped spatially partially coherent light," *Opt. Lett.* **31**, 2124–2126 (2006).

[62] A. M. Weiner, "Femtosecond pulse shaping with spatial light modulators," *Rev. Sci. Inst.* **71**, 1929–1960 (2000).

[63] A. M. Weiner, D. E. Leaird, G. P. Wiederrecht, and K. A. Nelson, "Femtosecond pulse sequences used for optical manipulation of molecular motion," *Science* **247**, 1317–1319 (1990).

[64] W. S. Warren, H. Rabitz, and M. Dahleh, "Coherent control of quantum dynamics – The dream is alive," *Science* **259**, 1581–1589 (1993).

[65] M. Shapiro and P. Brumer, "Coherent control of molecular dynamics," *Rep. Prog. Phys.* **66**, 859–942 (2003).

[66] A. Assion, T. Baurmert, M. Bergt, B. Kiefer, V. Seyfried, M. Strehle, and G. Gerber, "Control of chemical reactions by feedback-optimized phase-shaped femtosecond laser pulses," *Science* **282**, 919–922 (1998).

[67] J.-C. Diels and J. Stone, "Multiphoton ionization under sequential excitation by coherent pulses," *Phys. Rev. A* **31**, 2397–2402 (1985).

[68] X. P. Jiang, M. Shapiro, and P. Brumer, "Pump-dump coherent control with partially coherent laser pulses," *J. Chem. Phys.* **104**, 607–615 (1996).

[69] J. M. Dudley and S. Coen, "Coherence properties of supercontinuum spectra generated in photonic crystal and tapered optical fibers," *Opt. Lett.* **27**, 1180–1182 (2002).

[70] J. M. Dudley and S. Coen, "Numerical simulations and coherence properties of supercontinuum generation in photonic crystal and tapered optical fibers," *IEEE J. Sel. Top. Quantum Electron.* **8**, 651–659 (2002).

[71] J. W. Nicholson and M. F. Yan, "Cross-coherence measurements of supercontinua generated in highly-nonlinear, dispersion shifted fiber at 1550 nm," *Opt. Express* **12**, 679–688 (2004).

[72] J. M. Dudley, G. Genty, and S. Coen, "Supercontinuum generation in photonic crystal fiber," *Rev. Mod. Phys.* **78**, 1135–1184 (2006).

[73] F. Gori, "Devising genuine spatial correlation functions," *Opt. Lett.* **32**, 3531–3533 (2007).

[74] E. Wolf, "New spectral representation of random sources and of the partially coherent fields that they generate," *Opt. Commun.* **38**, 3–6 (1981).

[75] C. Dorrer, "Temporal van Cittert-Zernike theorem and its application to the measurement of chromatic dispersion," *J. Opt. Soc. Am B* **21**, 1417–1423 (2004).

[76] D. Marcuse, "Pulse distortion in single-mode fibers," *Appl. Opt.* **19**, 1653–1660 (1980).

[77] G. P. Agrawal, *Fiber-Optics Communication Systems* (John Wiley and Sons, New York, 2002).

[78] J. Capmany, D. Pastor, S. Sales, and M. A. Muriel, "Pulse distortion in optical fibers and waveguides with arbitrary chromatic dispersion," *J. Opt. Soc. Am. B* **20**, 2523–2533 (2003).

[79] M. Miyagi and S. Nishida, "Pulse spreading in single-mode optical fiber due to third-order dispersion: effect of optical source bandwidth," *Appl. Opt.* **18**, 2237–2240 (1979).

[80] D. Marcuse, "Propagation of pulse fluctuations in single-mode fibers," *Appl. Opt.* **19**, 1856–1861 (1980).

[81] B. E. A. Saleh and M. I. Irshid, "Collett-Wolf equivalence theorem and propagation of a pulse in a single-mode optical fiber," *Opt. Lett.* **7**, 342–343 (1982).

[82] B. E. A. Saleh and M. I. Irshid, "Transmission of pulse sequences through monomode fibers," *Appl. Opt.* **21**, 4219–4222 (1982).

[83] D. E. Leaird and A. M. Weiner, "Femtosecond optical placket generation by a direct space-to-time pulse shaper," *Opt. Lett.* **24**, 853–855 (1999).

[84] J. D. McKinney, D. S. Seo, and A. M. Weiner, "Direct space-to-time pulse shaping at 1.5 μm," *IEEE J. Quantum Electron.* **39**, 1635–1644 (2003).

[85] J. D. McKinney, D. E. Leaird, and A. M. Weiner, "Millimeter-wave arbitrary waveform generation with a direct space-to-time pulse shaper," *Opt. Lett.* **27**, 1345–1347 (2002).

[86] D. E. Leaird and A. M. Weiner, "Femtosecond direct space-to-time pulse shaping," *IEEE J. Quantum Electron.* **37**, 494–504 (2001).

[87] Conversation with Prof. Weiner.

[88] E. Frumker and Y. Silberberg, "Femtosecond pulse shaping using a two-dimensional liquid-crystal spatial light modulator," *Opt. Lett.* **32**, 1384–1386 (2007).

[89] M. A. Webster, T. D. Gerke, A. M. Weiner, and K. J. Webb, "Spectral and temporal speckle field measurements of a random medium," *Opt. Lett.* **29**, 1491–1493 (2004).

[90] E. Tal and Y. Silberberg, "Transformation from an ultrashort pulse to a spatiotemporal speckle by a thin scattering surface," *Opt. Lett.* **31**, 3529–3531 (2006).

[91] S. A. Diddams, T. Udem, J. C. Bergquist, E. A. Curtis, R. E. Drullinger, L. Hollberg, W. M. Itano, W. D. Lee, C. W. Oates, K. R. Volges, and D. J. Wineland, "An optical clock based on a single trapped $^{199}Hg^+$ ion," *Science* **293**, 825–828 (2001).

[92] G. G. Paulus, F. Grasbon, H. Walther, P. Villoresi, M. Nisoli, S. Stagira, E. Priori, and S. D. Silvestri, "Absolute-phase phenomena in photoionization with few-cycle laser pulses," *Nature* **414**, 182–184 (2001).

[93] Z. Jiang, C. B. Huang, D. E. Leaird, and A. M. Weiner, "Optical arbitrary waveform processing of more than 100 spectral comb lines," *Nature Photon.* 463–467 (2007).

[94] T. Ohara, H. Takara, H. Masuda, T. Morioka, M. Abe, and H. Takahashi, "Over-1000-channel ultradense WDM transmission with supercontinuum multicarrier source," *J. Lightwave Technol.* **24**, 2311–2317 (2006).

[95] P. J. Delfyett, S. Gee, M. T. Choi, H. Izadpanah, W. Lee, S. Ozharar, F. Quinlan, and T. Yilmaz, "Optical frequency combs from semiconductor lasers and applications in ultrawideband signal processing and communications," *J. Lightwave Technol.* **24**, 2701–2719 (2006).

[96] M. J. Thorpe, K. D. Moll, R. J. Jones, B. Safdi, and J. Ye, "Broadband cavity ringdown spectroscopy for sensitive and rapid molecular detection," *Science* **311**, 1595–1599 (2006).

[97] S. A. Diddams, L. Hollberg, and V. Mbele, "Molecular fingerprinting with the resolved modes of a femtosecond laser frequency comb," *Nature* **445**, 627–630 (2007).

[98] R. Teets, J. Eckstein, and T. W. Hänsch, "Coherent two-photon excitation by multiple light pulses," *Phys. Rev. Lett.* **38**, 760–764 (1977).

[99] T. Kobayashi, T. Sueta, Y. Matsuo, and Y. Cho, "High-repetition-rate optical pulse-generator using a Fabry-Perot electrooptic modulator," *Appl. Phys. Lett.* **21**, 341–343 (1972).

[100] M. Kourogi, K. Nakagawa, and M. Ohtsu, "Wide-span optical frequency comb generator for accurate optical frequency difference measurement," *IEEE J. Quantum Electron.* **29**, 2693–2701 (1993).

[101] D. S. Kim, M. Arisawa, A. Morimoto, and T. Kobayashi, "Femtosecond optical pulse generation using quasi-velocity-matched electrooptic phase modulator," *IEEE J. Sel. Top. Quantum Electron.* **2**, 493–499 (1996).

[102] U. Morgner, F. X. Kärtner, S. H. Cho, Y. Chen, H. A. Haus, J. G. Fujimoto, E. P. Ippen, V. Scheuer, G. Angelow, and T. Tschudi, "Sub-two cycle pulses from a Kerr-lens mode-locked Ti:sapphire laser," *Opt. Lett.* **24**, 411–413 (1999).

[103] D. H. Sutter, G. Stenmeyer, L. Gallmann, N. Matuschek, F. Moreier-Genoud, U. Keller, V. Scheuer, G. Angelow, and T. Tschudi, "Semiconductor saturable-absorber mirror-assited Kerr-lens mode-locked Ti:sapphire laser producing pulses in the two-cycle regime," *Opt. Lett.* **24**, 631–633 (1999).

[104] L. Xu, C. Spielmann, A. Poppe, T. Brabec, F. Krausz, and T. W. Hänsch, "Route to phase control of ultrashort light pulses," *Opt. Lett.* **21**, 2008–2010 (1996).

[105] J. K. Ranka, R. S. Windeler, and A. J. Stentz, "Visible continuum generation in air-silica microstructure optical fibers with anomalous dispersion at 800 nm," *Opt. Lett.* **25**, 25–27 (2000).

[106] D. J. Jones, S. A. Diddams, J. K. Ranka, A. Stentz, R. S. Windeler, J. L. Hall, and S. T. Cundiff, "Carrier-envelope phase control of femtosecond mode-locked lasers and direct optical frequency synthesis," *Science* **104**, 635–639 (2000).

[107] R. Holzwarth, T. Udem, T. W. Hänsch, J. C. Knight, W. J. Wadsworth, and P. S. J. Russell, "Optical frequency synthesizer for precision spectroscopy," *Phys. Rev. Lett.* **85**, 2264–2267 (2000).

[108] R. Ell, U. Morgner, F. X. Kärtner, J. G. Fujimoto, E. P. Ippen, V. Scheuer, G. Angelow, T. Tschudi, M. J. Lederer, A. Boiko, and B. Luther-Davies, "Generation of 5-fs pulses and octave-spanning spectra directly from a Ti : sapphire laser," *Opt. Lett.* **26**, 373–375 (2001).

[109] P. Del'Haye, A. Schliesser, T. Wilken, R. Holzwarth, and T. J. Kippenberg, "Optical frequency comb generation from a monolithic microresonator," *Nature* **450**, 1214–1217 (2007).

[110] H. Schnatz, B. Lipphardt, J. Helmcke, R. Riehle, and G. Zinner, "First phase-coherent frequency measurement of visible radiation," *Phys. Rev. Lett.* **76**, 18–21 (1996).

[111] H. A. Haus and A. Mecozzi, "Noise of mode-locked lasers," *IEEE J. Quantum Electron.* **29**, 983–996 (1993).

[112] H. A. Haus, "Mode-locking of lasers," *IEEE J. Sel. Top. Quantum Electron.* **6**, 1173–1185 (2000).

[113] D. von derLinde, "Characterization of the noise in continuously operating mode-locked lasers," *Appl. Phys. B* **39**, 201–217 (1986).

[114] M. Guina, N. Xiang, A. Vainionpää, O. G. Okhotnikov, T. Sajavaara, and J. Keinonen, "Self-starting stretched-pulse fiber laser mode locked and stabilized with slow and fast semiconductor saturable absorbers," *Opt. Lett.* **26**, 1809–1811 (2001).

[115] J. E. Malowicki, M. L. Fanto, M. J. Hayduk, and P. J. Delfyett, "Harmonically mode-locked glass waveguide laser with 21-fs timing jitter," *IEEE Photon. Technol. Lett.* **17**, 40–42 (2005).

[116] H. Tsuchida, "Timing noise measurement of 320 GHz optical pulses using an improved optoelectronic mixer," *Opt. Lett.* **31**, 628–630 (2006).

[117] D. Eliyahu, R. A. Salvatore, and A. Yariv, "Effect of noise on the power spectrum of passively mode-locked lasers," *J. Opt. Soc. Am. B* **14**, 167–174 (1997).

[118] D. Eliyahu, R. A. Salvatore, and A. Yariv, "Noise characterization of a pulse train generated by actively mode-locked lasers," *J. Opt. Soc. Am. B* **13**, 1619–1626 (1996).

[119] H. A. Haus, J. G. Fujimoto, and E. P. Ippen, "Structures for additive pulse mode locking," *J. Opt. Soc. Am. B* **8**, 2068–2076 (1991).

[120] A. Poppe, L. Xu, F. Krausz, and C. Spielmann, "Noise characterization of sub-10-fs Ti:sapphire oscillators," *IEEE J. Sel. Top. Quantum Electron.* **4**, 179–184 (1998).

[121] P. T. Ho, "Phase and amplitude fluctuations in a mode-locked laser," *IEEE J. Quantum Electron.* **QE-21**, 1806–1813 (1985).

[122] F. X. Kärtner, U. Morgner, T. Schibli, R. Ell, H. A. Haus, J. G. Fujimoto, and E. P. Ippen, "Few-cycle pulses directly from a laser," *Top. Appl. Phys.* **95**, 73–136 (2004).

[123] D. W. Rush, G. L. Burdge, and P. T. Ho, "The linewidth of a modelocked semiconductor laser caused by spontaneous emission: experimental comparison to single-mode operation," *IEEE J. Quantum Electron.* **QE-22**, 2088–2091 (1986).

[124] F. K. Fatemi, J. W. Lou, and T. F. Carruthers, "Frequency comb linewidth of an actively mode-locked fiber laser," *Opt. Lett.* **29**, 944–946 (2004).

[125] K. Haneda, M. Yoshida, M. Nakazawa, H. Yokohama, and Y. Ogawa, "Linewidth and relative intensity noise measurements of longitudinal modes in ultrahigh-speed mode-locked laser dioses," *Opt. Lett.* **30**, 1000–1002 (2005).

[126] A. Yariv, *Optical Electronics in Modern Communications* (Oxford University Press, New York, 1997).

[127] D. M. Bloom, *New Light Sources and Concepts in for Electro-Optic Sampling* (Final technical report to the Air Force Office of scientific research, Contract F49620-92-J-0099, Edward L. Ginzton Laboratory, Stanford University, 1994).

[128] T. Brabec and F. Krausz, "Nonlinear optical pulse propagation in the single-cycle regime," *Phys. Rev. Lett.* **78**, 3282–3285 (1997).

[129] J. Goodman, *Introduction to Fourier Optics* (McGraw-Hill, New York, 1968).

[130] S. A. Akhmanov, A. S. Chirkin, K. N. Drabovich, A. I. Kovrigin, R. V. Khokhlov, and A. P. Sukhorukov, "Nonstationary nonlinear optical effects and ultrashort light pulse formation," *IEEE J. Quantum Electron.* **QE-4**, 598–605 (1968).

[131] E. B. Treacy, "Optical pulse compression with diffraction gratings," *IEEE J. Quantum Electron.* **QE-5**, 454–458 (1969).

[132] T. Jannson and J. Jannson, "Temporal self-imaging effect in single-mode fibers," *J. Op. Soc. Am.* **71**, 1373–1376 (1981).

[133] B. H. Kolner and M. Nazarathy, "Temporal imaging with a time lens," *Opt. Lett.* **14**, 630–632 (1989).

[134] A. E. Siegman, *Lasers* (University Science Books, Mill Valley, 1985).

[135] S. P. Dijaili, A. Dienes, and J. S. Smith, "ABCD matrices for dispersive pulse propagation," *IEEE J. Quantum Electron.* **26**, 1158–1164 (1990).

[136] M. Nakazawa, H. Kubota, and K. Tamura, "Time-domain ABCD matrix formalism for laser mode-locking and optical pulse transmisison," *IEEE J. Quantum Electron.* **34**, 1075–1081 (1998).

[137] S. A. Collins, "Lens-system diffraction integral written in terms of matrix optics," *J. Opt. Soc. Am.* **60**, 1168–1174 (1970).

[138] C. Palma and V. Bagini, "Extension of the Fresne transform to ABCD systems," *J. Opt. Soc. Am. A* **14**, 1774–1779 (1997).

[139] J. Caraquitena, *PhD Thesis* (University of Valencia, Valencia, 2004).

[140] S. Mookherjea and A. Yariv, "Analysis of optical pulse propagation with two-by-two (ABCD) matrices," *Phys. Rev. E* **64**, 016611 (2001).

[141] D. E. Leaird and A. M. Weiner, "Chirp control in the direct space-to-time pulse shaper," *Opt. Lett.* **25**, 850–852 (2000).

[142] T. Hirooka and M. Nakazawa, "Optical adaptive equalization of high-speed signals using time-domain optical Fourier transformation," *J. Lightwave Technol.* **24**, 2530–2540 (2006).

[143] J. Azaña and L. R. Chen, "General temporal self-imaging phenomena," *J. Opt. Soc. Am. B* **20**, 83–90 (2003).

[144] J. Lancis, J. Caraquitena, P. Andrés, and M. A. Muriel, "Temporal self-imaging effect for chirped laser pulse sequences: Repetition rate and duty cycle tunability," *Opt. Commun.* **253**, 156–163 (2005).

[145] J. Azaña, N. K. Berger, B. Levit, V. Smulakovsky, and B. Fischer, "Frequency shifting of microwave signals by use of a general temporal self-imaging (Talbot) effect in optical fibers," *Opt. Lett.* **29**, 2849–2851 (2004).

[146] R. L. Fork, O. E. Marínez, and J. P. Gordon, "Negative dispersion using pairs of prisms," *Opt. Lett.* **9**, 150–152 (1984).

[147] J. Caraquitena, Z. Jiang, D. E. Leaird, and A. M. Weiner, "Tunable pulse repetition-rate multiplication using phase-only line-by-line pulse shaping," *Opt. Lett.* **32**, 716–718 (2007).

[148] J. Azaňa and M. A. Muriel, "Real-time optical spectrum analysis based on the space–time duality in chirped fiber gratings," *IEEE J. Quantum Electron.* **36**, 517–526 (2000).

[149] A. Ferrando, E. Silvestre, J. J. Miret, and P. Andrés, "Nearly zero ultraflattened dispersion in photonic crystal fibers," *Opt. Lett.* **25**, 790–792 (2000).

[150] W. H. Reeves, J. C. Knight, P. S. J. Russell, and P. J. Roberts, "Demonstration of ultra-flattened dispersion in photonic crystal fibers," *Opt. Express* **10**, 609–613 (2002).

[151] J. Azaňa, N. K. Berger, B. Levit, and B. Fischer, "Spectro-temporal imaging of optical pulses with a single time lens," *IEEE Photon. Technol. Lett.* **16**, 882–884 (2004).

[152] A. Papoulis, "Dual optical systems," *J. Opt. Soc. Am.* **58**, 653–654 (1968).

[153] M. T. Kauffman, W. C. Banyai, A. A. Godil, and D. M. Bloom, "Time-to-frequency converter for measuring picosecond optical pulses," *Appl. Phys. Lett.* **64**, 270–272 (1994).

[154] T. Jannson, "Real-time Fourier transformation in dispersive optical fibers," *Opt. Lett.* **8**, 232–234 (1983).

[155] M. Nakazawa, T. Hirooka, F. Futami, and S. Watanabe, "Ideal distortion-free transmission using optical Fourier transformation and Fourier transform-limited optical pulses," *IEEE Photon. Technol. Lett.* **16**, 1059–1061 (2004).

[156] Y. C. Tong, L. Y. Chan, and H. K. Tsang, "Fiber dispersion or pulse spectrum measurement using a sampling oscilloscope," *Electron. Lett.* **33**, 983–985 (1997).

[157] M. A. Muriel, J. Azaňa, and A. Carballar, "Real-time Fourier transformer based on fiber gratings," *Opt. Lett.* **24**, 1–3 (1999).

[158] J. Azaňa, L. R. Chen, M. A. Muriel, and P. W. E. Smith, "Experimental demonstration of real-time Fourier transformation using linearly chirped fibre Bragg gratings," *Electron. Lett.* **35**, 2223–2224 (1999).

[159] D. R. Solli, J. Chou, and B. Jalali, "Amplified wavelength-time transformation for real-time spectroscopy," *Nature Photon.* **2**, 48–51 (2008).

[160] P. V. Kelkar, F. Coppinger, A. S. Bhushan, and B. Jalali, "Time-domain optical sensing," *Electron. Lett.* **35**, 1661–1662 (1999).

[161] J. Chou, Y. Han, and B. Jalali, "Time-wavelength spectroscopy for chemical sensing," *IEEE Photon. Technol. Lett.* **16**, 1140–1142 (2004).

[162] J. Hult, R. S. Wyatt, and C. F. Kaminski, "High bandwidth absorption spectroscopy with a dispersed supercontinuum source," *Opt. Express* **15**, 11385–11395 (2007).

[163] S. Moon and D. Y. Kim, "Ultra-high-speed optical coherence tomography with a stretched pulse supercontinuum source," *Opt. Express* **14**, 11575–11584 (2006).

[164] P. C. Chou, H. A. Haus, and J. F. Brennan, "Reconfigurable time-domain spectral shaping of an optical pulse stretched by a fiber Bragg grating," *Opt. Lett.* **25**, 524–526 (2000).

[165] R. E. Saperstein, N. Alic, D. Panasenko, R. Rokitski, and Y. Fainman, "Time-domain waveform processing by chromatic dispersion for temporal shaping of optical pulses," *J. Opt. Soc. Am. B* **22**, 2427–2436 (2005).

[166] J. Azaña, N. K. Berger, B. Levit, and B. Fischer, "Reconfigurable generation of high-repetition-rate optical pulse sequences based on time-domain phase-only filtering," *Opt. Lett.* **30**, 3228–3230 (2005).

[167] L. K. Mouradian, F. Louradour, V. Messager, and A. B. anc C. Froehly, "Spectro-temporal imaging of femtosecond events," *IEEE J. Quantum Electron.* **36**, 795–801 (2000).

[168] C. R. Fernández-Pousa, "Temporal resolution limits of time-to-frequency transformations," *Opt. Lett.* **31**, 3049–3051 (2006).

[169] C. V. Bennett and B. H. Kolner, "Upconversion time microscope demonstrating 103x magnification of femtosecond waveforms," *Opt. Lett.* **24**, 783–785 (1999).

[170] C. V. Bennett and B. H. Kolner, "Principles of parametric temporal imaging - Part I: System configurations," *IEEE J. Quantum Electron.* **36**, 430–437 (2000).

[171] M. Tsang and D. Psaltis, "Propagation of temporal entanglement," *Phys. Rev. A* **73**, 013822 (2006).

[172] S. Kumar, "Compensation of third-order dispersion using time reversal in optical transmission systems," *Opt. Lett.* **32**, 346–348 (2007).

[173] F. Coppinger, A. S. Bhushan, and B. Jalali, "Photonic time stretch and its application to analog-to-digital conversion," *IEEE Trans. Microwave Theory Techn.* **47**, 1309–1314 (1999).

[174] J. Azaña, N. K. Berger, B. Levit, and B. Fischer, "Simplified temporal imaging systems for optical waveforms," *IEEE Photon. Technol. Lett.* **17**, 94–96 (2005).

[175] A. F. Lohmann and D. Mendlovic, "Temporal filtering with time lenses," *Appl. Opt.* **31**, 6212–6219 (1992).

[176] D. Mendlovic, O. Melamed, and H. M. Ozaktas, "Compact optical temporal processors," *Appl. Opt.* **34**, 4113–4118 (1995).

[177] C. V. Bennett and B. H. Kolner, "Aberrations in temporal imaging," *IEEE J. Quantum Electron.* **37**, 20–32 (2001).

[178] K. Patorski, "The self-imaging phenomenon and its applications," *Progr. Opt.* **27**, 3–108 (1989).

[179] P. A. Andrekson, "Linear propagation of optical picosecond pulse trains over oceanic distances," *Opt. Lett.* **18**, 1621–1623 (1993).

[180] C. R. Fernández-Pousa, F. Mateos, L. Chantada, M. T. Flores-Arias, C. Bao, M. V. Pérez, and C. Gómez-Reino, "Timing jitter smoothing by Talbot effect. I. Variance," *J. Opt. Soc. Am. B* **21**, 1170–1177 (2004).

[181] D. Pudo, M. Depa, and L. R. Chen, "Single and multiwavelength all-optical clock recovery in single-mode fiber using the temporal Talbot effect," *J. Lightwave Technol.* **25**, 2898–2903 (2007).

[182] R. U. Maheswari, N. Takai, and T. Asakura, "Talbot images by a spatially fluctuating grating," *Opt. Commun.* **81**, 259–266 (1991).

[183] A. Kalestyński and B. Smolińska, "Self-restoration of the autoidolon of defective periodic objects," *Optica Acta* **25**, 125–134 (1978).

[184] D. Bigourd, B. Chatel, W. P. Schleich, and B. Girard, "Factorization of numbers with the temporal Talbot effect: optical implementation by a sequence of shaped ultrashort pulses," *Phys. Rev. Lett.* **100**, 030202 (2008).

[185] J. Azaňa and M. A. Muriel, "Temporal self-imaging effects: Theory and application for multiplying pulse repetition rates," *IEEE J. Sel. Top. Quantum Electron.* **7**, 728–744 (2001).

[186] I. Shake, H. Takara, S. Kawanishi, and M. Saruwatari, "High-repetition-rate optical pulse generation by using chirped optical pulses," *Electron. Lett.* **34**, 792–793 (1998).

[187] S. Arahira, S. Kutsuzawa, Y. Matsui, D. Kunimatsu, and Y. Ogawa, "Repetition-frequency multiplication of mode-locked pulses using fiber dispersion," *J. Lightwave Technol.* **16**, 405–410 (1998).

[188] J. Azaña and M. A. Muriel, "Technique for multiplying the repetition rates of periodic trains of pulses by means of a temporal self-imaging effect in chirped fiber gratings," *Opt. Lett.* **24**, 1672–1674 (1999).

[189] S. Longhi, M. Marano, P. Laporta, O. Svelto, M. Belmonte, B. Agogliati, L. Arcangeli, V. Pruneri, M. N. Zervas, and M. Ibsen, "40-GHz pulse-train generation at 1.5 μm with a chirped fiber grating as a frequency multiplier," *Opt. Lett.* **25**, 1481–1483 (2000).

[190] D. Duchesne, R. Morandotti, and J. Azaña, "Temporal Talbot phenomena in high-order dispersive media," *J. Opt. Soc. Am B* **24**, 113–125 (2007).

[191] S. Atkins and B. Fischer, "All-optical pulse rate multiplication using fractional Talbot effect and field-to-intensity conversion with cross-gain modulation," *IEEE Photon. Technol. Lett.* **15**, 132–134 (2003).

[192] T. Kobayashi, H. Yao, K. Amano, Y. Fukushima, A. Morimoto, and T. Sueta, "Optical pulse compression using high-frequency electrooptic phasemodulation," *IEEE J. Quantum Electron.* **24**, 382–387 (1988).

[193] H. Murata, A. Morimoto, T. Kobayashi, and S. Yamamoto, "Optical pulse generation by electrooptic-modulation method and its application to integrated ultrashort pulse generators," *IEEE J. Sel. Top. Quantum Electron.* **6**, 1325–1331 (2000).

[194] T. Komukai, T. Yamamoto, and S. Kawanishi, "Optical pulse generator using phase modulator and linearly chirped fiber Bragg gratings," *IEEE Photon. Technol. Lett.* **17**, 1746–1748 (2005).

[195] J. Capmany and D. Novak, "Microwave photonics combines two worlds," *Nature Photon.* **1**, 319–330 (2007).

[196] N. K. Berger, B. Levit, A. Bekker, and B. Fischer, "Compression of periodic optical pulses using temporal fractional Talbot effect," *IEEE Photon. Technol. Lett.* **16**, 1855–1857 (2004).

[197] J. T. Winthrop and C. R. Worthington, "Theory of Fresnel images. I. Plane periodic objects in monochromatic light," *J. Opt. Soc. Am.* **55**, 373–381 (1965).

[198] J. P. Guigay, "On the Fresnel diffraction by one-dimensional periodic objects, with application to structure determination of phase objects," *Optica Acta* **18**, 677–682 (1971).

[199] K. Patorski and G. Parfjanowicz, "Self-imaging phenomenon of a sinusoidal complex object," *Optica Acta* **28**, 357–367 (1981).

[200] J. R. Leger and G. J. Swanson, "Efficient array illuminator using binary-optics phase plates at fractional-Talbot planes," *Opt. Lett.* **15**, 288–290 (1990).

[201] V. Arrizón and J. Ojeda-Castañeda, "Irradiance at Fresnel planes of a phase grating," *J. Opt. Soc. Am. A* **9**, 1801–1806 (1992).

[202] V. Arrizón and J. Ojeda-Castañeda, "Phase grating – analytical formulas for the near-field," *Microwave Optical Technol. Lett.* **5**, 483–486 (1992).

[203] J. Westerholm, J. Turunen, and J. Huttunen, "Fresnel diffraction in fractional Talbot planes: a new formulation," *J. Opt. Soc. Am. A* **11**, 1283–1290 (1994).

[204] V. Arrizón and J. Ojeda-Castañeda, "Multilevel phase gratings for array illuminators," *Appl. Opt.* **33**, 5925–5931 (1994).

[205] V. Arrizón, E. López-Olasagasti, and A. Serrano-Heredia, "Talbot array illuminator with optimum compression ratio," *Opt. Lett.* **21**, 233–235 (1996).

[206] J. Azaña and S. Gupta, "Complete family of periodic Talbot filters for pulse repetition rate multiplication," *Opt. Express* **14**, 4270–4279 (2006).

[207] Q. Lin, L. G. Wang, and S. Y. Zhu, "Partially coherent light pulse and its propagation," *Opt. Commun.* **219**, 65–70 (2003).

[208] E. Wolf and E. Collett, "Partially coherent sources which produce same far-field intensity distribution as a laser," *Opt. Commun.* **25**, 293–296 (1978).

[209] B. E. A. Saleh, "Intensity distribution due to a partially coherent field and the Collett-Wolf equivalence theorem in the Fresnel zone," *Opt. Commun.* **30**, 135–138 (1979).

[210] L. Chantada, C. R. Fernández-Pousa, and C. Gómez-Reino, "Theory of the partially coherent temporal Talbot effect," *Opt. Commun.* **266**, 393–398 (2006).

[211] T. Otsuji, M. Yaita, T. Nagatsuma, and E. Sano, "10-80-Gb/s highly extinctive electrooptic pulse pattern generation," *IEEE J. Sel. Top. Quantum Electron.* **2**, 643–649 (1996).

[212] S. Yang and X. Bao, "Generating a high-extinction-ratio pulse from a phase-modulated optical signal with a dispersion-imbalanced nonlinear loop mirror," *Opt. Lett.* **31**, 1032–1034 (2006).

[213] C. B. Huang, Z. Jiang, D. E. Leaird, and A. M. Weiner, "High-rate femtosecond pulse generation via line-by-line processing of phase-modulated CW laser frequency comb," *Electron. Lett.* **42**, 1114–1115 (2006).

[214] N. K. Berger, B. Levit, and B. Fischer, "Reshaping periodic light pulses using cascaded uniform fiber Bragg gratings," *J. Lightwave Technol.* **24**, 2746–2751 (2006).

[215] H. Hao, J. L. Yu, L. T. Zhang, A. X. Zhang, Y. Li, Y. Jiang, and E. Z. Yang, "Pulse source based on directly modulated laser and phase modulator," *Opt. Express* **15**, 8931–8937 (2007).

[216] H. Lajunen, A. T. Friberg, and P. Ostlund, "Quasi-stationary plane-wave optical pulses and the van Cittert-Zernike theorem in time," *J. Opt. Soc. Am. A* **23**, 2530–2537 (2006).

[217] F. Gori, "Far-zone approximation for partially coherent sources," *Opt. Lett.* **30**, 2840–2842 (2005).

[218] R. A. Silverman, "Locally stationary random processes," *IRE Trans. Inform. Theory* **3**, 182–187 (1957).

[219] Y. X. Wang, M. Han, and A. Wang, "High-speed fiber-optic spectrometer for signal demodulation of inteferometric fiber-optic sensors," *Opt. Lett.* **31**, 2408–2410 (2006).

[220] M. Kavehrad and D. Zaccarin, "Optical code-division-multiplexed systems based on spectral encoding of noncoherent sources," *J. Lightwave Technol.* **13**, 534–545 (1995).

[221] H. Venghaus, ed., *Wavelength Filters in Fibre Optics* (Springer Verlag, Heidelberg, 2006).

[222] R. Trebino, *Frequency-Resolved Optical Gating: The Measurement of Ultrashort Laser Pulses* (Kluwer Academic Publishers, Massachussets, 2000).

[223] C. Iaconis and I. A. Walmsley, "Self-referencing spectral interferometry for measuring ultrashort optical pulses," *IEEE J. Quantum Electron.* **35**, 501–509 (1999).

[224] D. J. Kane and R. Trebino, "Characterization of arbitrary femtosecond pulses using frequency-resolved optical gating," *IEEE J. Quantum Electron.* **29**, 571–579 (1993).

[225] C. Iaconis, V. Wong, and I. A. Walmsley, "Spectral phase interferometry for direct electric-field reconstruction of ultrashort optical pulses," *Opt. Lett.* **23**, 792–794 (1998).

[226] G. Stinbenz, C. Ropers, C. Lienau, C. Warmuth, A. S. W. amd I. A. Walmsley, and G. Steinmeyer, "Advanced methods for the characterization of few-cycle light pulses: a comparison," *Appl. Phys. B* **83**, 511–519 (2006).

[227] C. Dorrer, E. M. Kosik, and I. A. Walmsley, "Spatio-temporal characterization of the electric field of ultrashort optical pulses using two-dimensional shearing interferometry," *Appl. Phys. B* **74**, 209–217 (2002).

[228] P. Gabolde and R. Trebino, "Self-referenced measurement of the complete electric field of ultrashort pulses," *Opt. Express* **12**, 4423–4429 (2004).

[229] C. Dorrer, "High-speed measurements for optical telecommunication systems," *IEEE J. Sel. Top. Quantum Electron.* **12**, 843–858 (2006).

[230] P. O'Shea, M. Kimmel, X. Gu, and R. Trebino, "Highly simplified device for ultrashort-pulse measurement," *Opt. Lett.* **26**, 932–934 (2001).

[231] I. Kang and C. Dorrer, "Highly sensitive differential tomographic technique for real-time ultrashort pulse characterization," *Opt. Lett.* **30**, 1545–1547 (2005).

[232] J. Bromage, C. Dorrer, I. A. Begishev, N. G. Usechak, and J. D. Zuegel, "Highly sensitive, single-shot characterization for pulse widths from 0.4 to 85 ps using electro-optic shearing interferometry," *Opt. Lett.* **31**, 3523–3525 (2006).

[233] E. W. Van Stryland, "The effect of pulse to pulse variation on ultrashort pulsewidth measurements," *Opt. Commun.* **31**, 93–96 (1979).

[234] M. Bellini and T. W. Hänsch, "Measurement of the temporal coherence of ultrashort harmonic pulses: towards coherent spectroscopy in the extreme ultraviolet," *Appl. Phys. B* **65**, 677–680 (1997).

[235] M. Bellini and T. W. Hänsch, "Phase-locked white-light continuum pulses: toward a universal optical frequency-comb synthesizer," *Opt. Lett.* **25**, 1049–1051 (2000).

[236] C. Iaconis and I. A. Walmsley, "Direct measurement of the two-point field correlation function," *Opt. Lett.* **21**, 1783–1785 (1996).

[237] H. Arimoto and Y. Ohtsuka, "Measurements of the complex degree of spectral coherence by use of a wave-front-folded interferometer," *Opt. Lett.* **22**, 958–960 (1997).

[238] C. Dorrer and I. A. Walmsley, "High-dynamic-range measurement of the two-point field correlation function by carrier-encoded spatial shearing interferometry," *Opt. Lett.* **27**, 1613–1615 (2002).

[239] M. Santarsiero and R. Borghi, "Measuring spatial coherence by using a reversed-wavefront Young interferometer," *Opt. Lett.* **31**, 861–863 (2006).

[240] K. A. Nugent, "Partially coherent diffraction patterns and coherence measurement," *J. Opt. Soc. Am. A* **8**, 1574–1579 (1991).

[241] K. A. Nugent, "Wave field determination using three-dimensional intensity information," *Phys. Rev. Lett.* **68**, 2261–2264 (1992).

[242] C. Q. Tran and K. A. Nugent, "Recovering the complete coherence function of a generalized Schell model field," *Opt. Lett.* **31**, 3226–3228 (2006).

[243] K. A. Nugent, "X-ray noninterferometric phase imaging: a unified picture," *J. Opt. Soc. Am. A* **24**, 536–547 (2007).

[244] C. K. Aruldoss, N. M. Dragomir, and A. Roberts, "Noninterferometric characterization of partially coherent scalar wave fields and application to scattered light," *J. Opt. Soc. Am. A* **24**, 3189–3197 (2007).

[245] C. Iaconis, V. Wong, and I. A. Walmsley, "Direct interferometric techniques for characterizing ultrashort optical pulses," *IEEE J. Select. Topics Quantum Electron.* **4**, 285–294 (1998).

[246] K. C. Chu, J. P. Heritage, R. S. Grant, K. X. Liu, A. Dienes, W. E. White, and A. Sullivan, "Direct measurement of the spectral phase of femtosecond pulses," *Opt. Lett.* **20**, 904–906 (1995).

[247] M. R. Teague, "Deterministic phase retrieval – a Green-function solution," *J. Opt. Soc. Am.* **73**, 1434–1441 (1983).

[248] C. Dorrer and J. D. Zuegel, "Optical testing using the transport-of-intensity equation," *Opt. Express* **15**, 7165–7175 (2007).

[249] H. S. Green and E. Wolf, "A scalar representation of electromagnetic fields," *Proc. Phys. Soc. A* **66**, 1129–1137 (1953).

[250] T. E. Gureyev, D. M. Paganin, A. W. Stevenson, S. C. Mayo, and S. W. Wilkins, "Generalized eikonal of partially coherent beams and its use in quantitative imaging," *Phys. Rev. Lett.* **93**, 068103 (2004).

[251] S. W. Wilkins, T. E. Gureyev, D. Gao, A. Pogany, and A. W. Stevenson, "Phase-contrast imaging using polychromatic hard X-rays," *Nature* **384**, 335–338 (1996).

[252] T. E. Gureyev, S. Mayo, S. W. Wilkins, D. Paganin, and D. W. Stevenson, "Quantitative in-line phase-contrast imaging with multienergetic x rays," *Phys. Rev. Lett.* **86**, 5827–5830 (2001).

[253] F. Gori, M. Santarsiero, and G. Guattari, "Coherence and the spatial-distribution of intensity," *J. Opt. Soc. Am. A* **10**, 673–679 (1993).

[254] C. Dorrer, "Characterization of nonlinear phase shifts by use of the temporal transport-of-intensity equation," *Opt. Lett.* **30**, 3237–3239 (2005).

[255] L. Cohen, "Time–frequency distributions — a review," *Proc. IEEE* **77**, 941–981 (1989).

[256] C. Dorrer and I. Kang, "Complete temporal characterization of short optical pulses by simplified chronocyclic tomography," *Opt. Lett.* **28**, 1481–1483 (2003).

[257] K. Wilner and A. P. V. den Heuvel, "Fiber-optic delay lines for microwave signal processing," *Proc. IEEE* **64**, 805–807 (1976).

[258] K. Jackson, S. Newton, B. Moslehi, M. Tur, C. C. Cutler, J. W. Goodman, and H. J. Shaw, "Optical fiber delay-line signal processing," *IEEE Trans. Microwave Theory Techn.* **MTT-33**, 193–204 (1985).

[259] A. Seeds, "Microwave photonics," *IEEE Trans. Microwave Theory Techn.* **50**, 877–887 (2002).

[260] R. A. Minasian, "Photonic signal processing of microwave signals," *IEEE Trans. Microwave Theory Techn.* **54**, 832–846 (2006).

[261] J. Capmany, B. Ortega, D. Pastor, and S. Sales, "Discrete-time optical processing of microwave signals," *J. Lightwave Technol.* **23**, 702–723 (2005).

[262] S. Sales, J. Capmany, J. Martí, and D. Pastor, "Experimental demonstration of fiberoptic delay-line filters with negative coefficients," *Electron. Lett.* **31**, 1095–1096 (1995).

[263] J. Capmany, D. Pastor, A. Martínez, B. Ortega, and S. Sales, "Microwave photonic filters with negative coefficients based on phase inversion in an electro-optic modulator," *Opt. Lett.* **28**, 1415–1417 (2003).

[264] F. Zeng and J. P. Yao, "All-optical microwave filter based on an electro-optic phase modulator," *Opt. Express* **12**, 3814–3819 (2004).

[265] N. S. You and R. A. Minasian, "All-optical photonic signal processors with negative coefficients," *J. Lightwave Technol.* **22**, 2739–2742 (2004).

[266] J. Mora, J. Capmany, A. Loayssa, and D. Pastor, "Novel technique for implementing incoherent microwave photonic filters with negative coefficients using phase modulation and single sideband selection," *IEEE Photon. Technol. Lett.* **18**, 1943–1945 (2006).

[267] M. Sagues, R. G. Olcina, A. Loayssa, S. Sales, and J. Capmany, "Multi-tap complex coefficient incoherent microwave photonic filters based on optical single-sideband modulation and narrow band optical filtering," *Opt. Express* **16**, 295–303 (2008).

[268] F. Coppinger, S. Yegnanarayan, P. D. Trinh, and B. Jalali, "All-optical incoherent negative taps for photonic signal processing," *Electron. Lett.* **33**, 973–975 (1997).

[269] A. Loayssa, J. Capmany, M. Sagues, and J. Mora, "Demonstration of incoherent microwave photonic filters with all-optical complex coefficients," *IEEE Photon. Technol. Lett.* **18**, 1744–1746 (2006).

[270] B. Vidal, M. A. Piqueras, and J. Martí, "Tunable and reconfigurable microwave filter based on stimulated Brillouin scattering," *Opt. Lett.* **32**, 23–25 (2007).

[271] B. Vidal, M. A. Piqueras, and J. Martí, "Photonic microwave filter based on spectrum slicing with reconfiguration capability," *Electron. Lett.* **41**, 1286–1287 (2005).

[272] N. A. Riza and M. A. Arain, "Programmable broadband radio-frequency transversal filter with compact fiber-optics and digital microelectromechanical system-based optical spectral control," *Appl. Opt.* **43**, 3159–3165 (2004).

[273] J. Capmany, J. Mora, D. Pastor, and B. Ortega, "High-quality online-reconfigurable microwave photonic transversal filter with positive and negative coefficients," *IEEE Photon. Technol. Lett.* **17**, 2730–2732 (2005).

[274] S. Xiao and A. M. Weiner, "Programmable photonic microwave filter with arbitrary ultra-wideband phase response," *IEEE Trans. Microwave Theory Techn.* **54**, 4002–4008 (2006).

[275] S. Xiao and A. M. Weiner, "Coherent photonic processing of microwave signals using spatial light modulators: programmable amplitude filters," *J. Lightwave Technol.* **24**, 2523–2529 (2006).

[276] J. Mora, B. Ortega, A. Díez, J. L. Cruz, M. V. Andrés, J. Capmany, and D. Pastor, "Photonic microwave tunable single-bandpass filter based on a Mach-Zender interferometer," *J. Lightwave Technol.* **24**, 2500–2509 (2006).

[277] J. Mora, B. Ortega, M. V. Andrés, J. Capmany, J. L. Cruz, D. Pastor, and S. Sales, "Tunable all-optical negative multi-tap microwave filters based on uniform fiber Bragg gratings," *Opt. Lett.* **28**, 1308–1310 (2003).

[278] J. Mora, *PhD Thesis* (University of Valencia, Valencia, 2005).

[279] W. Zhang, I. Bennion, and J. Williams, "Chromatic dispersion effect in a microwave photonic filter using superstructured fiber Bragg grating and dispersive fiber," *Opt. Express* **13**, 6429–6437 (2005).

[280] X. Yi and R. A. Minasian, "Dispersion induced RF distortion of spectrum-sliced microwave-photonic filters," *IEEE Trans. Microwave Theory Techn.* **54**, 880–886 (2006).

[281] J. D. McKinney, I. S. Lin, and A. M. Weiner, "Shaping the power spectrum of ultra-wideband radio-frequency signals," *IEEE Trans. Microwave Theory Techn.* **54**, 4247–4255 (2006).

[282] http://www.peleton.com/Site2007/Products/DWDM.html from Peleton photonic systems (valid February, 2008).

[283] L. J. Wang, B. E. Magill, and L. Mandel, "Propagation of thermal light through a dispersive medium," *J. Opt. Soc. Am. B* **6**, 964–966 (1989).

[284] G. J. Simonis and K. G. Parchase, "Optical-generation, distribution, and control of microwave signals using laser heterodyne," *IEEE Trans. Microwave Theory Techn.* **38**, 667–669 (1990).

[285] A. Wiberg, P. Pérez-Millán, M. V. Andrés, and P. O. Hedekvist, "Microwave-photonic frequency multiplication utilizing four-wave mixing and fiber Bragg gratings," *J. Lightwave Technol.* **24**, 329–334 (2006).

[286] K. Imai, M. Kourogi, and M. Ohtsu, "30-THz span optical frequency comb generation by self-phase modulation in an optical fiber," *IEEE J. Quantum Electron.* **34**, 54–68 (1998).

[287] T. Sakamoto, T. Kawanishi, and M. Izutsu, "Asymptotic formalism for ultraflat optical frequency comb generation using a Mach-Zender modulator," *Opt. Lett.* **32**, 1515–1517 (2007).

[288] T. Yilmaz, C. M. DePriest, T. Turpin, J. H. Abeles, and P. J. Delfyett, "Toward a photonic arbitrary waveform generator using a modelocked external cavity semiconductor laser," *IEEE Photon. Technol. Lett.* **14**, 1608–1610 (2002).

[289] J. U. Kang, M. Y. Frankel, and R. D. Esman, "Demonstration of microwave frequency shifting by use of a highly chirped mode-locked fiber laser," *Opt. Lett.* **23**, 1188–1190 (1998).

[290] J. Azaña, N. K. Berger, B. Levit, and B. Fischer, "Broadband arbitrary waveform generation based on microwave frequency upshifting in optical fibers," *J. Lightwave Technol.* **24**, 2663–2675 (2006).

[291] N. K. Berger, B. Levit, B. Fischer, and J. Azaña, "Picosecond flat-top pulse generation by low-bandwidth electro-optic sinusoidal phase modulation," *Opt. Lett.* **33**, 125–127 (2008).

[292] J. D. McKinney, D. S. Seo, D. E. Leaird, and A. M. Weiner, "Photonically assisted generation of arbitrary millimeter-wave and microwave electromagnetic waveforms via direct space-to-time optical pulse shaping," *J. Lightwave Technol.* **21**, 3020–3028 (2003).

[293] J. Chou, Y. Han, and B. Jalali, "Adaptive RF-photonic arbitrary waveform generator," *IEEE Photon. Technol. Lett.* **15**, 581–583 (2003).

[294] I. S. Lin, J. D. McKinney, and A. M. Weiner, "Photonic synthesis of broadband microwave arbitrary waveforms applicable to ultra-wideband communication," *IEEE Microwave Wireless Comp. Lett.* **15**, 226–228 (2005).

[295] I. Y. Poberezhskiy, B. Bortnik, J. Chou, B. Jalali, and H. R. Fetterman, "Serrodyne frequency translation of continuous optical signals using ultra-wideband electrical sawtooth waveforms," *IEEE J. Quantum Electron.* **41**, 1533–1539 (2005).

[296] M. Shen and R. A. Minasian, "Toward a high-speed arbitrary waveform generation by a novel photonic processing structure," *IEEE Photon. Technol. Lett.* **16**, 1155–1157 (2004).

[297] (eds.) M.-G. Di Benedetto, T. Kaiser, A. F. Molish, I. Oppermann, and C. Politano, *UWB Communication Systems: A Comprehensive Overview* (Hindawi Publishing, New York, 2006).

[298] G. R. Aiello and G. D. Rogerson, "Ultra-wideband wireless systems," *IEEE Microwave Mag.* **4**, 36–47 (2003).

[299] D. Porcine, P. Research, and W. Hirt, "Ultra-wideband radio technology: potential an challenges ahead," *IEEE Commun. Mag.* **41**, 66–74 (2003).

[300] J. P. Yao, F. Zeng, and Q. Wang, "Photonic generation of ultrawideband signals," *J. Lightwave Technol.* **25**, 3219–3235 (2007).

[301] C. Wang, F. Zeng, and J. P. Yao, "All-fiber ultra wideband pulse generation based on spectral shaping and dispersion-induced frequency-to-time conversion," *IEEE Photon. Technol. Lett.* **19**, 137–139 (2007).

[302] M. Abtahi, M. Mirhshafiei, J. Magné, L. A. Rusch, and S. LaRochelle, "Ultra-wideband waveform generator based on optical pulse-shaping and FBG tuning," *IEEE Photon. Technol. Lett.* **20**, 135–137 (2008).

[303] F. Zeng and J. P. Yao, "An approach to ultrawideband pulse generation and distribution over optical fiber," *IEEE Photon. Technol. Lett.* **18**, 823–825 (2006).

[304] J. J. Dong, X. L. Zhang, J. Xu, D. X. Huang, S. N. Fu, and P. Shum, "Ultra-wideband monocycle generation using cross-phase modulation in a semiconductor optical amplifier," *Opt. Lett.* **32**, 1223–1225 (2007).

[305] F. Zeng, Q. Wang, and J. P. Yao, "All-optical UWB impulse generation based on cross-phase modulation and frequency discrimination," *Electron. Lett.* **43**, 121–122 (2007).

[306] F. Zeng and J. P. Yao, "Ultrawideband signal generation using a highspeed electrooptic phase modulator and an FBG-based frequency discriminator," *IEEE Photon. Technol. Lett.* **18**, 2062–2064 (2006).

[307] Q. Wang, F. Zeng, S. Blais, and J. P. Yao, "Optical UWB monocycle pulse generation based on cross-gain modulation in a semiconductor optical amplifier," *Opt. Lett.* **31**, 3083–3085 (2006).

[308] J. J. Dong, X. L. Zhang, J. Xu, and D. X. Huang, "All-optical ultrawideband monocycle generation utilizing gain saturation of a dark return-to-zero signal in a semiconductor optical amplifier," *Opt. Lett.* **32**, 2158–2160 (2007).

[309] Q. Wang and J. P. Yao, "Switchable optical UWB monocycle and doublet generation using a reconfigurable photonic microwave delay-line filter," *Opt. Express* **15**, 14667–14672 (2007).

[310] J. Q. Li, S. Fu, J. Wu, J. Lin, M. Tang, and P. Shum, "Ultra-wideband pulse generation with flexible pulse shape and polarity control using a Sagnac-interferometer-based intensity modulator," *Opt. Express* **15**, 18156–18161 (2007).

[311] W. P. Lin and Y.-C. Chen, "Design of a new optical impulse radio system for ultra-wideband wireless communications," *IEEE J. Sel. Top. Quantum Electron.* **12**, 882–887 (2006).

[312] L. Mandel, "Interpretation of instantaneous frequencies," *Am. J. Phys.* **42**, 840–846 (1974).

[313] M. Nakazawa, K. Suzuki, and Y. Kimura, "Transform-limited pulse generation in the gigahertz region from a gain-switched distributed-feedback laser diode using spectral windowing," *Opt. Lett.* **15**, 715–717 (1990).

[314] T. Niemi, J. G. Zhang, and H. Ludvigsen, "Effect of optical filtering on pulses generated with a gain-switched DFB laser," *Opt. Commun.* **192**, 339–345 (2001).

[315] H. Chi, F. Zeng, and J. P. Yao, "Photonic generation of microwave signals based on pulse shaping," *IEEE Photon. Technol. Lett.* **19**, 668–670 (2007).

[316] A. Einstein, B. Podolsky, and N. Rosen, "Can quantum-mechanical description of physical reality be considered complete?," *Phys. Rev.* **47**, 770–780 (1935).

[317] Y. H. Shih, "Entangled biphoton source – property and preparation," *Rep. Prog. Phys.* **66**, 1009–1044 (2003).

[318] Y. H. Shih, "Entangled photons," *IEEE J. Sel. Top. Quantum Electron.* **9**, 1455–1467 (2003).

[319] A. Hayat, P. Ginzburg, and M. Orenstein, "Observation of two-photon emission from semiconductors," *Nature Photon.* **2**, 1–3 (2008).

[320] A. K. Ekert, J. G. Rarity, P. R. Rapster, and G. M. Palma, "Practical quantum cryptography based on 2-photon interferometry," *Phys. Rev. Lett.* **69**, 1293–1295 (1992).

[321] M. D'Angelo and Y. H. Shih, "Quantum imaging," *Laser Phys. Lett.* **2**, 567–596 (2005).

[322] T. B. Pittman, Y. H. Shih, D. V. Strekalov, and A. V. Sergienko, "Optical imaging by means of 2-photon quantum entanglement," *Phys. Rev. A* **52**, 3429–3432 (1995).

[323] D. Bowmeester, J. W. Pan, K. Mattle, M. Eibl, H. Weinfurter, and A. Zeilinger, "Experimental quantum teleportation," *Nature* **390**, 575–579 (1997).

[324] A. N. Boto, P. Kok, D. S. Abrams, S. L. Braunstein, C. P. Williams, and J. P. Dowling, "Quantum interferometric optical lithography: Exploiting entanglement to beat the diffraction limit," *Phys. Rev. Lett.* **85**, 2733–2736 (2000).

[325] A. F. Abouraddy, M. B. Nasr, B. E. A. Saleh, A. V. Sergienko, and M. C. Teich, "Quantum-optical coherence tomography with dispersion cancellation," *Phys. Rev. A* **65**, 053817 (2003).

[326] M. B. Nasr, B. E. A. Saleh, A. V. Sergienko, and M. C. Teich, "Demonstration of dispersion-canceled quantum-optical coherence tomography," *Phys. Rev. Lett.* **91**, 083601 (2003).

[327] G. Scarceli, A. Valencia, S. Gompers, and Y. H. Shih, "Remote spectral measurement using entangled photons," *Appl. Phys. Lett.* **83**, 560–5562 (2003).

[328] V. Giovanetti, S. Lloyd, L. Maccone, and F. N. C. Wong, "Clock synchronization with dispersion cancellation," *Phys. Rev. Lett.* **87**, 117902 (2001).

[329] A. Valencia, G. Scarcelli, and Y. H. Shih, "Distant clock synchronization using entangled photon pairs," *Appl. Phys. Lett.* **85**, 2655–2657 (2004).

[330] R. J. Glauber, "The quantum theory of optical coherence," *Phys. Rev.* **130**, 2529–2539 (1963).

[331] B. E. A. Saleh, M. Teich, and A. V. Sergienko, "Wolf equations for two-photon light," *Phys. Rev. Lett.* **94**, 223601 (2005).

[332] B. E. A. Saleh, A. F. Abouraddy, A. V. Sirgienko, and M. C. Teich, "Duality between partial coherence and partial entanglement," *Phys. Rev. A* **62**, 04386 (2000).

[333] A. F. Abouraddy, B. E. A. Saleh, A. V. Sergienko, and M. C. Teich, "Entangled-photon Fourier optics," *J. Opt. Soc. Am. B* **19**, 1174–1184 (2002).

[334] D. V. Strekalov, A. V. Sergienko, D. N. Klyshko, and Y. H. Shih, "Observation of 2-photon ghost interference and diffraction," *Phys. Rev. Lett.* **74**, 3600–3603 (1995).

[335] R. S. Bennink, S. J. Bentley, and R. W. Boyd, ""Two-photon" coincidence imaging with a classical source," *Phys. Rev. Lett.* **89**, 113601 (2002).

[336] A. F. Abouraddy, P. R. Stone, A. V. Sergienko, B. E. A. Saleh, and M. C. Teich, "Entangled-photon imaging of a pure phase object," *Phys. Rev. Lett.* **93**, 213903 (2004).

[337] M. Bache, D. Magatti, F. Ferri, A. Gatti, E. Brambilla, and L. A. Lugiato, "Coherent imaging of a pure phase object with classical incoherent light," *Phys. Rev. A* **73**, 053802 (2006).

[338] A. Gatti, E. Brambilla, M. Bache, and L. A. .Lugiato, "Ghost imaging with thermal light: Comparing entanglement and classical correlation," *Phys. Rev. Lett.* **93**, 093602 (2004).

[339] A. Gatti, E. Brambilla, M. Bache, and L. A. .Lugiato, "Correlated imaging, quantum and classical," *Phys. Rev. A* **70**, 013802 (2004).

[340] J. Cheng and S. H. Han, "Incoherent coincidence imaging and its applicability in X-ray diffraction," *Phys. Rev. Lett.* **92**, 093903 (2004).

[341] F. Ferri, D. Magatti, A. Gatti, M. Bache, E. Brambilla, and L. A. Lugiato, "High-resolution ghost image and ghost diffraction experiments with thermal light," *Phys. Rev. Lett.* **94**, 183602 (2005).

[342] A. Gatti, M. Bache, E. Brambilla, F. Ferri, and L. A. Lugiato, "Coherent imaging with pseudo-thermal incoherent light," *J. Mod. Opt.* **53**, 739–760 (2006).

[343] M. Bellini, F. Marin, S. Viciani, A. Zavatta, and F. T. Arecchi, "Nonlocal pulse shaping with entangled photon pairs," *Phys. Rev. Lett.* **90**, 043602 (2003).

[344] A. Valencia, M. V. Chekhova, A. Trifonov, and Y. H. Shih, "Entangled two-photon wave packet in a dispersive medium," *Phys. Rev. Lett.* **88**, 183601 (2002).

[345] A. Pe'er, B. Dayan, A. A. Friesem, and Y. Silberberg, "Temporal shaping of entangled photons," *Phys. Rev. Lett.* **94**, 073601 (2005).

[346] M. L. M. Ricci, J. Mazzaferri, A. V. Bragas, and O. E. Martínez, "Photon counting statistics using a digital oscilloscope," *Am. J. Phys.* **75**, 707–712 (2007).

[347] J. D. Franson, "Nonlocal cancellation of dispersion," *Phys. Rev. A* **45**, 3126–3132 (1992).

[348] C. K. Hong, Z. Y. Ou, and L. Mandel, "Measurement of subpicosecond time intervals between 2 photons by interference," *Phys. Rev. Lett.* **59**, 2044–2046 (1987).

[349] A. M. Steinberg, P. G. Kwiat, and R. Y. Chiao, "Dispersion cancellation in a measurement of the single-photon propagation velocity in glass," *Phys. Rev. Lett.* **68**, 2421–2424 (1992).

[350] A. M. Steinberg, P. G. Kwiat, and R. Y. Chiao, "Dispersion cancellation and high-resolution time measurements in a fourth-order optical interferometer," *Phys. Rev. A* **45**, 6659–6665 (1992).

[351] M. L. Goldberg, H. W. Lewis, and K. M. Watson, "Intensity-correlation spectroscopy," *Phys. Rev.* **142**, 25–32 (1966).